Growth & Surface Characterisation Of Metal Oxide Thin Films Under UHV Conditions

Huggins, Chris

Queen Mary
University of London

Growth & Surface Characterisation Of Metal Oxide Thin Films Under UHV Conditions

By

Chris Huggins

Department of Chemistry
Queen Mary, University of London

A thesis presented for the degree of Doctor of Philosophy in the University of London

June 2005

Statement of Originality

I certify that this thesis, and the research to which it refers, are the product of my own work, and that any ideas or quotations from the work of other people, published or otherwise, are fully acknowledged in accordance with the standard referencing practices of the discipline. I acknowledge the helpful guidance and support of my supervisor, Dr. Nix.

Abstract

Thin films of a variety of technologically important oxide systems (chromium oxide, barium oxide, titanium oxide and iron oxide) have been grown under ultra-high vacuum conditions by vapour deposition techniques. The surface structure and chemistry of these oxide films have been characterised by x-ray photoelectron spectroscopy (XPS), low energy electron diffraction (LEED), reflection absorption infrared spectroscopy (RAIRS) and temperature programmed desorption spectroscopy (TPD). These studies have included investigation of both the clean oxide surface and their interaction with small molecules.

Well-defined chromium oxide films were produced and the surface structure of these films was found to be consistent with the (0001) surface of Cr_2O_3. The studies of barium oxide have revealed a complicated oxygen chemistry with transformation between different forms being brought about by different preparation conditions and post-treatments including heating and exposure to O_2, CO_2 and CO. Well-defined iron oxide films have been generated and in addition to their characterisation such films have been used as a support for the deposition of silver metal nanoparticles. The surface chemistry of this mixed metal/oxide Ag/FeO_x system has been probed in particular by the adsorption of propene at sub-ambient temperatures.

The ultimate aim of this research was to study these metal oxide thin films as a means to elucidating a deeper fundamental understanding of the surface chemistry of these systems, which is of both academic and industrial interest.

Acknowledgements

I would like to take this opportunity to thank a number of people for their support and assistance in the course of my PhD. Firstly I am very grateful to Dr. Nix for supervising this project. Our discussions on my work have been absolutely invaluable. I also greatly appreciate the guidance of Mr. Thompson and Mr. Pell with respect to a number of technical and electrical matters.

I am grateful to the UK Engineering and Physical Sciences Research Council (EPSRC), for funding the PhD by means of the Doctoral Training Grant.

There are many friends and colleagues who I would like to thank for providing a friendly atmosphere in which to work over the last few years. This includes the physical chemistry group, the organic chemists with whom I regularly played football and people from various departments with whom I went running. Finally I would like to acknowledge the support of my family throughout the course of this work.

Chris Huggins, June 2005

Contents

Chapter 1:

Introduction

1.1 UHV Surface Science Studies

1.2 Studies of Metal Oxide Surfaces

  1.2.1 Applications of Metal Oxides

  1.2.2 Properties of Metal Oxides and their Surfaces

  1.2.3 Methods used to study Metal Oxide Surfaces

1.3 Background to the Systems Studied

1.4 Aims of the Research

1.1 UHV Surface Science Studies

Surface science is the study of the structure, composition and reactivity of (commonly) low index solid surfaces in a controlled, highly idealised environment (*i.e.* ultra-high vacuum), utilising a variety of surface sensitive techniques to obtain a fundamental understanding of the properties of the solid surface. Why study surfaces and why in vacuum conditions? Solid surfaces are interesting from a purely scholastic point of view, since the surface represents a termination of the bulk structure and possesses its own unique electronic and structural characteristics, as well as being an interface with the local environment at which reactions will occur. Whereas the properties of bulk binary oxides, for example, are relatively well understood, it is only fairly recently that we have started to study their surfaces. Moreover, the findings of such studies can also be considered of great interest to application-orientated research. One of the main motivations for surface science research is to obtain a better understanding of heterogeneous catalysis, which is a major part of the chemical industry, playing a crucial role in industrial synthesis, petroleum refining and environmental applications. It is on the surface of the catalyst that the crucial reactions occur and from research on such surfaces we can gain vital clues as to the mechanistic aspects of the catalytic reactions. Many of the most important heterogeneous catalysts consist of a catalytically active metal dispersed on a support material, usually a metal oxide (see Figure 1.1).

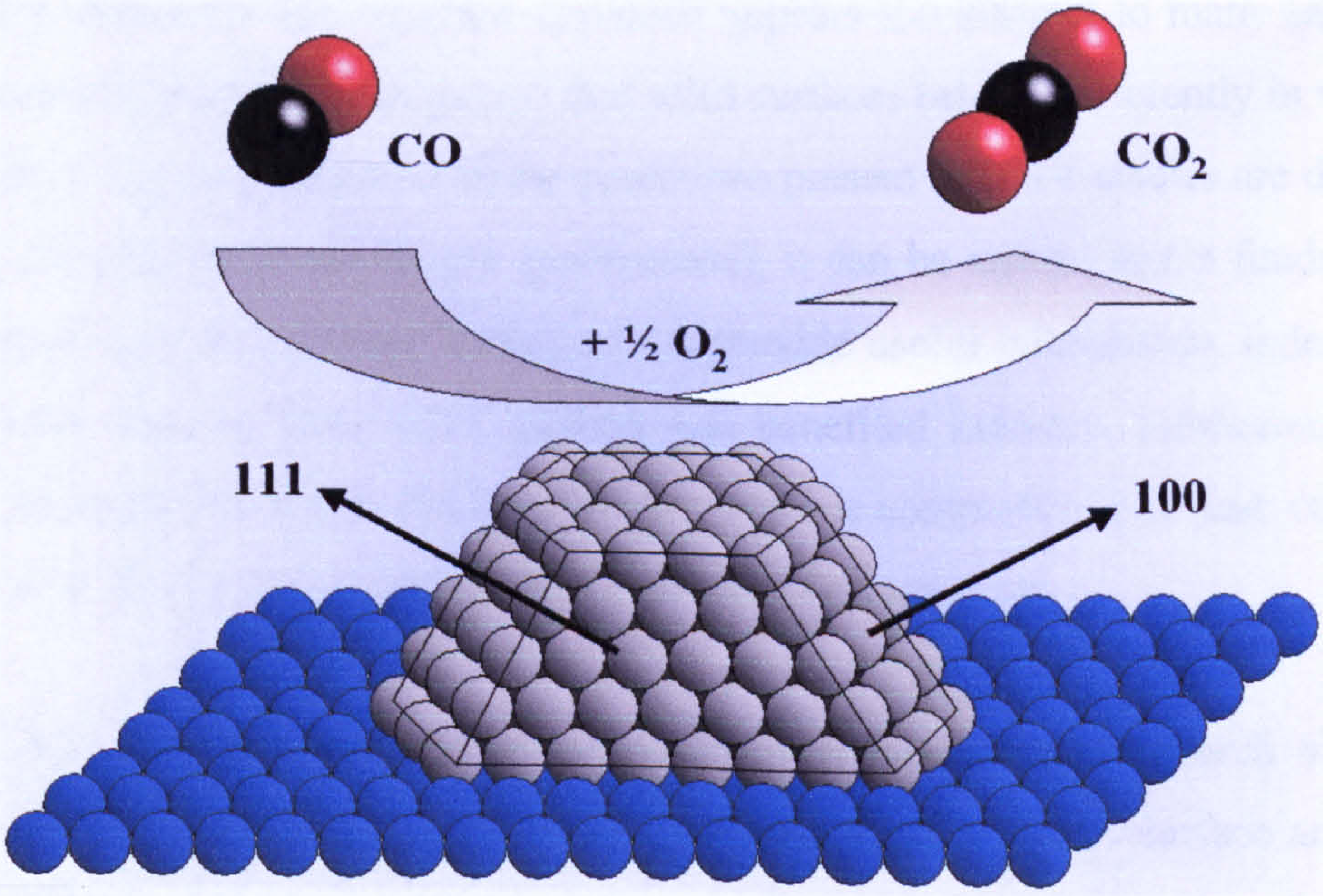

Figure 1.1: CO oxidation on a supported metal catalyst – one example of heterogeneous catalysis. Metal clusters of the sizes typically present in real catalysts expose low-index surfaces and the aim of surface science is to study these surfaces to understand better how these reactions occur.

Apart from heterogeneous catalysis, surface science has also played an important role in the development of semiconductor device technology and in areas such as corrosion control of materials. These are all technological areas where an understanding of the properties of the surface is critical.

Why study surfaces in UHV? Indeed a large proportion of catalytic research consists of studies on powdered samples in flow reactors at pressures far closer to those in the real application. Although such research provides much useful information, study under UHV conditions can offer further benefits. Firstly in UHV it is possible to employ a variety of analytical techniques which provide characterisation of the surface of the sample and which cannot operate at higher pressures - techniques that involve low-energy electrons, *e.g.* x-ray photoelectron spectroscopy (XPS), low energy electron diffraction (LEED), etc. must be carried out in high vacuum to avoid scattering of the electrons. Secondly, by studying the interaction of molecules at the highly idealised (*i.e.* clean) vacuum-solid interface we can focus on the chemistry of individual interactions in a way that is not possible in more complex realistic systems. Dispersed metal clusters on a support (as in many technologically important materials) can generally be considered as a collection of low-index crystal surfaces (see Figure 1.1). Therefore in UHV studies the aim is to characterise well-defined surfaces and to combine this with study of their individual adsorption and catalytic properties. Although this idealised approach appears too abstract to many industrial applications (it should be recognised that solid surfaces behave differently in vacuum compared to higher pressures and the conditions present in UHV studies are different from the conditions found in real applications), it can be argued that a fundamental understanding of well defined surfaces does provide useful information. Indeed such information, derived from UHV studies, has benefited industry. Furthermore, this type of research fills a gap, since in industry there is commonly little time or money invested in actually understanding how particular systems work.

In fact there has been a tremendous growth in surface science research since the 1960's. This growth has coincided with the development of many surface analytical techniques (*e.g.* XPS) and has further been facilitated by the availability of stainless steel chambers into which equipment can easily be mounted and de-mounted with stainless steel flanges sealed by copper gaskets, allowing a whole range of UHV techniques to be carried out in one system. Most of the early surface science work was carried out on well-defined metals, however the explosion in research into metal oxide systems has been phenomenal, clearly as a result of their many important technological applications (not least heterogeneous catalysis). To obviate problems associated with *in situ* cleaving and low conductivity, it is common to grow films when studying oxides. More recently the systems under study have been extended to metals dispersed on metal oxides and this is a step in the direction of modelling the typical heterogeneous catalyst, whilst still retaining the well-defined fundamental approach.

1.2 Studies of Metal Oxide Surfaces

Metal oxides are ubiquitous and are applied in a diverse range of technologies. This diversity is largely due to a number of distinct properties that they possess. In many cases understanding their surfaces and the chemical processes that occur at their surfaces is critical to targeted product design. As a consequence a number of approaches and techniques have been adopted to study metal oxide surfaces.

1.2.1 Applications of Metal Oxides

The utilisation of metal oxides in **heterogeneous catalysis** has already been mentioned in section 1.1. This is arguably the greatest motivation for surface science research. There are a multitude of catalytic reactions in which metal oxides play a role either as the catalytically active component or as the support. One of the most important examples is the use of metal oxides in three-way catalysts (TWCs) in automobiles. The purpose of these is to convert CO, NO_x and hydrocarbons (HCs) in the exhaust gas to less harmful CO_2, N_2 and H_2O, as indicated in Figure 1.2.

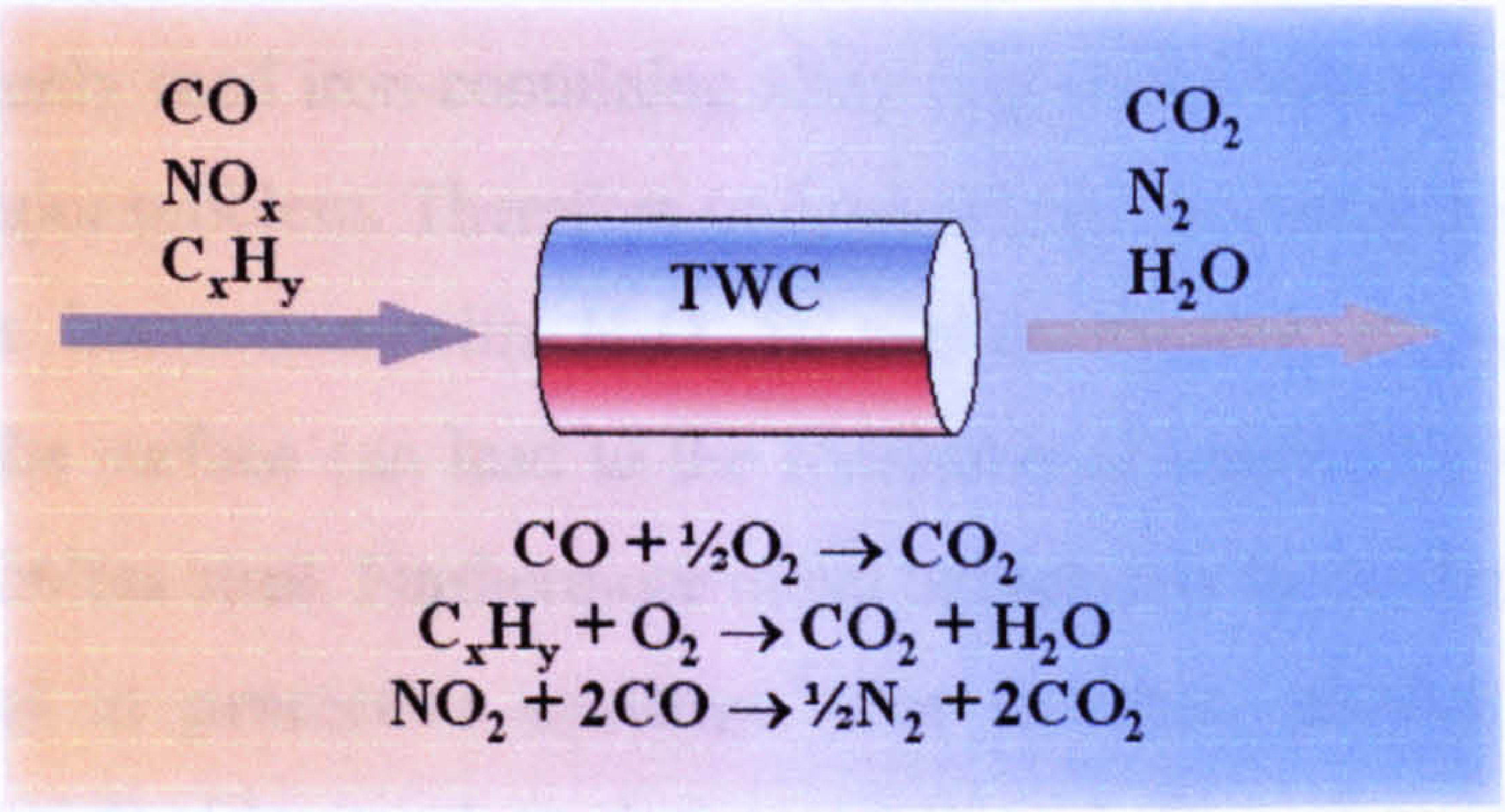

Figure 1.2: Principle reactions in a three-way catalytic converter

The catalyst typically consists of one or more metals (e.g. Pt, Rh, Pd) dispersed on an oxide support (generally Al_2O_3). Additionally the catalyst is usually modified with CeO_2 or CeO_2/ZrO_2. As will be discussed further in chapter 4, one current concern is the development of efficient catalysts for use with the economical lean-burn engines, which operate in oxygen-rich conditions and therefore make NO_x reduction more difficult. This has been addressed by the development of NO_x storage/reduction catalysts, which use BaO as the storage medium. Heterogeneous catalysis is also important in the chemical and petroleum industries, where a wide range of synthesis and rearrangement reactions are carried out in the presence of metal oxide-based catalysts. Dehydrogenation of alkanes is an alternative to thermal cracking for producing alkenes, and is carried out on a potassium-modified Cr_2O_3/γ-Al_2O_3 catalyst. Styrene synthesis by dehydrogenation of ethylbenzene is carried out industrially in the presence of steam using a potassium-promoted FeO_x catalyst. These are just a few examples of metal oxide-based catalysts used in industrial synthesis and there are many more.[1]

The application of TWCs is not the only reason why metal oxide studies are important in **environmental science.** Al_2O_3 particles in the stratosphere and mineral dust (consisting of a mixture of SiO_2, Al_2O_3, Fe_2O_3, MgO and CaO) present in the troposphere come from a number of natural sources (e.g. volcano eruptions) and anthropogenic sources (e.g. space shuttle exhaust).[2] It has been recognised that the role that these oxide surfaces play in their interactions with gases in the atmosphere (e.g. NO_2 and SO_2) is very significant to atmospheric chemistry and they have even been linked to O_3 depletion.[2]

Steel is a commonly used iron-containing alloy (*e.g.* as a construction material) and corrosion is a major problem. Therefore understanding iron oxide surface chemistry, in particular its interaction with H_2O, is useful. Natural segregation of alloy components to the surface can lead to the formation of passivating oxide layers, as illustrated by stainless steel. Furthermore metal oxides may be deliberately applied to corrosion control in **protective coatings.**[3] For example, anodising involves the formation of an Al_2O_3 film by electrolytic oxidation of the surface of an Al anode in an acidic solution.

Metal oxides are also used in a variety of electrical technologies, where both their bulk and surface properties are important. Not least is the application of insulating metal oxide **dielectric layers** in capacitors. Dielectrics improve the performance of capacitors by allowing conducting plates to be placed in close proximity without risk of contact and in addition they increase the capacitance. Typically SiO_2 has been used, but with the drive for miniaturisation and higher performance of computer and telecommunication technology, increasingly thinner dielectric materials are required and Ta_2O_5 and Nb_2O_5 have gained attention.[4] Structural defects at the surface of the layers are largely responsible for limiting their dielectric properties and therefore studies of the surfaces of these oxides are important. **High-temperature superconductors** are materials that exhibit superconductivity at liquid nitrogen temperature (77 K), as a result of having a higher critical temperature T_c than low-temperature superconductors (which require liquid helium as a coolant). The most widely studied high-temperature superconductor is yttrium-barium-copper-oxide (YBCO). Thin films of YBCO have been grown on various substrates (*e.g.* MgO and $SrTiO_3$).[5]

Many metal oxides (including oxides of chromium, iron, tin and zinc), doped and undoped, are used as **gas sensors**, which are important for pollution monitoring and detection of toxic gases (*e.g.* CO).[6] In some cases surface properties (such as surface conductivity) are responsible for their gas detection properties.

1.2.2 Properties of Metal Oxides and their Surfaces

In section 1.2.1 the diverse technological applications of metal oxides were discussed. The range of different applications is phenomenal - from catalytic oxidation to catalytic reduction, and from insulators to superconductors – and the variety of applications reflects the properties that metal oxides possess.

Many binary metal oxides are substantially ionic in nature and consist of metal cations and oxygen anions in a giant ionic lattice. Termination of this bulk structure to create a surface results in a positive contribution to the total free energy of the system, since electrostatic interactions/bonds have to be broken when a solid is split to produce a surface. Therefore all surfaces are energetically unfavourable to some extent and undergo relaxations and/or reconstructions to lower the surface energy. What properties do metal oxides posses that are relevant to their technological application?

For non-transition metal oxides, redox chemistry is not particularly important in understanding metal oxide surface chemistry since the electronic states are separated by a band gap and thus less accessible.[7] Rather it is the presence of acidic and basic sites which tend to control their surface chemistry. These arise from co-ordinative unsaturation of ions on the surface, which remain despite reconstruction. Examples of such sites are given in Figure 1.3. Various surface science studies investigate the existence of acidic and basic sites by adsorption of probe molecules.[8,9]

The presence of surface defects are also clearly an important aspect of metal oxides and their properties. It is recognised that the presence of surface defects are often responsible for catalytic activity. A common defect on oxide surfaces is the presence of anion or cation vacancies and these affect the electronic energy levels at the site. Oxide vacancies are more common than metal cation vacancies.[2] Other defects that metal oxides may possess are similar to those found on elemental surfaces, such as steps, kinks and impurity atoms. The effect of surface defects have been investigated by various researchers, often in a rather uncontrolled fashion, by sputtering metal oxide surfaces to create vacancies.[10,11]

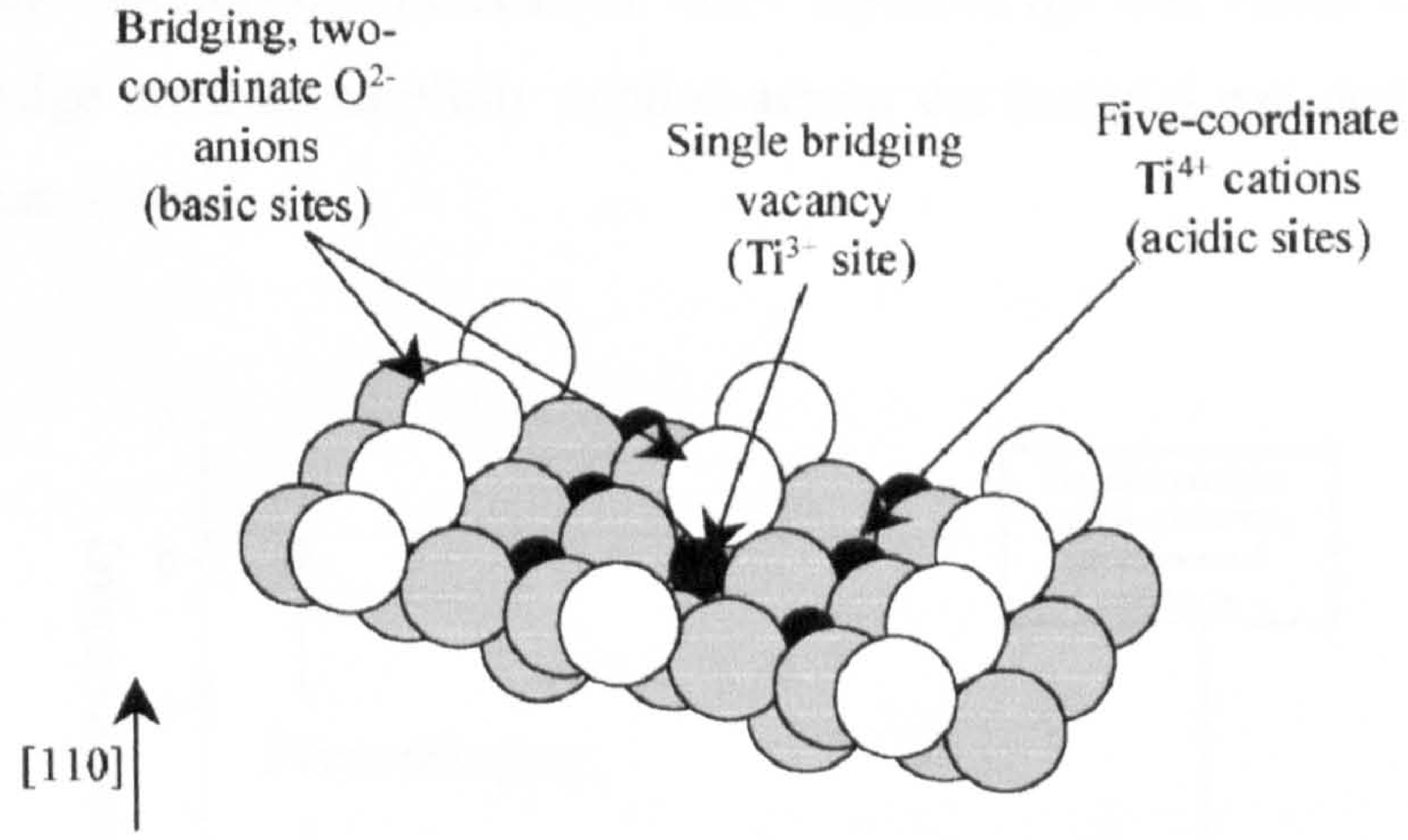

Figure 1.3: Acidic and basic sites and an oxygen vacancy on a rutile $TiO_2(110)$ surface[2]

With transition metal oxides, the ability of transition metal cations to undergo oxidation and reduction is a key property, in particular with regards to catalytic chemistry. For example iron(III) oxide, Fe_2O_3, can be reduced to Fe_3O_4 or even FeO. In the opposite direction the iron cation is oxidised. This property allows metal oxides to exchange oxygen with reacting molecules and this is especially important in catalytic oxidation and reduction. High oxygen ion mobility is also an important property that some metal oxides possess and this can have an important role in catalytic processes (*e.g.* oxygen storage by ceria in TWCs).

1.2.3 Methods used to study Metal Oxide Surfaces

As a result of the technological significance of metal oxides and their surfaces, there have been an abundance of different techniques and approaches adopted to study their surface properties and chemistry. [12-15] Despite this there are a number of problems particular to the study of oxides which need to be addressed and study of metal oxide surfaces has proved difficult. Ironically the diversity and complexity of metal oxides responsible for their technological importance is also the reason for this difficulty. For example, varying stoichiometry can make it difficult to obtain well-defined oxide surfaces. Amongst the approaches adopted it is possible to differentiate a well-defined, fundamental approach, generally under UHV conditions, from catalytic studies carried out on polycrystalline, less well-defined samples under more realistic conditions. Clearly both approaches have much to contribute to our understanding of these important materials. However, some caution is required when interpreting the findings of fundamental UHV research (as was mentioned in section 1.1). Knowledge must be carefully applied across the material gap and the pressure gap (see Figure 1.4).

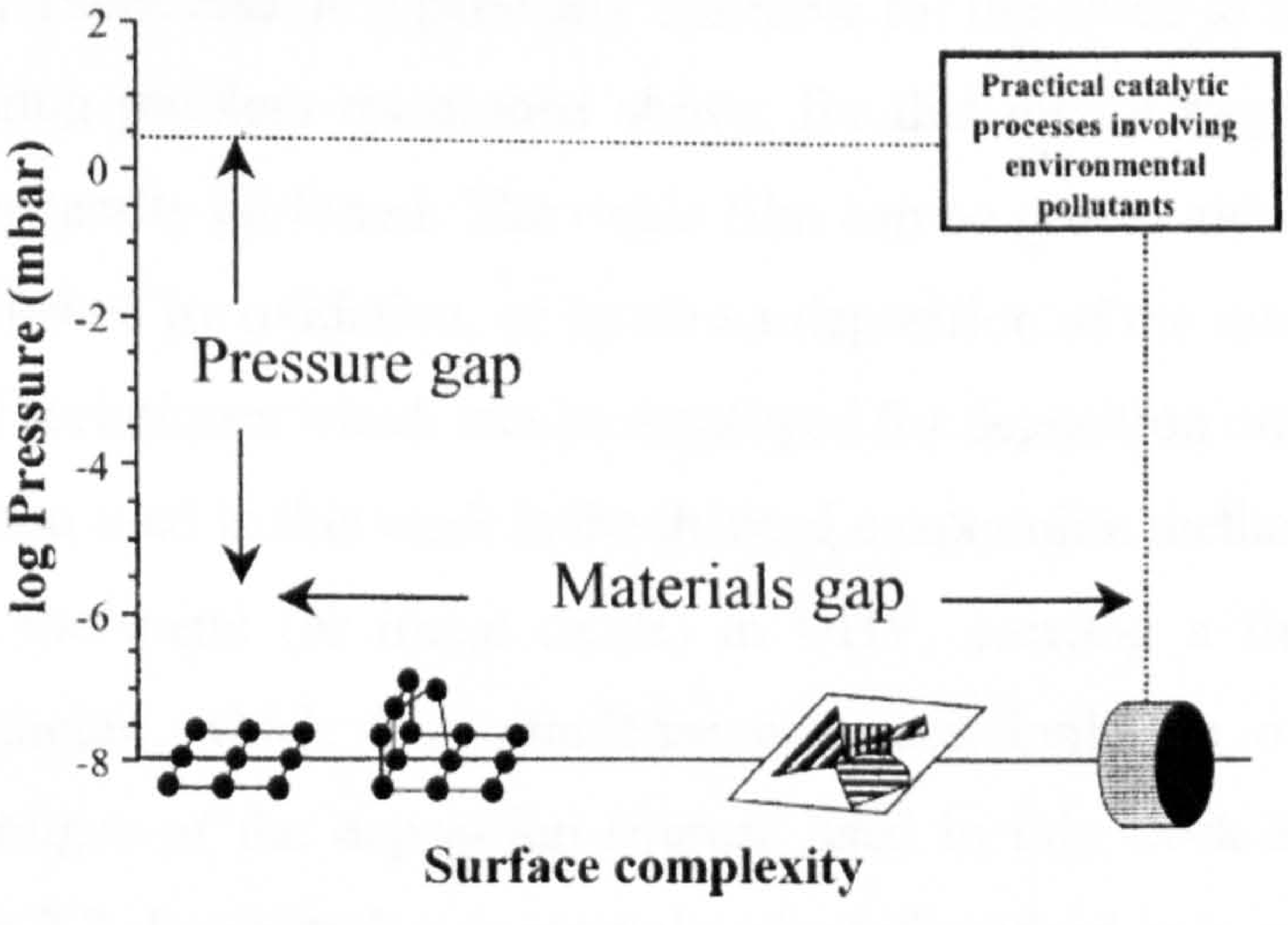

Figure 1.4: The material and pressure gaps that must be accounted for in fundamental UHV studies[2]

Additionally, when conducting more fundamental studies, surface scientists have the option of either using commercially available single crystals which are cleaved to expose the relevant surface orientation, or preparing thin films of the oxide *in situ* on an appropriate substrate, which for practical reasons is often a metallic single crystal.

A variety of **single crystal metal oxides**, cleaved to expose the relevant surface orientation, are commercially available and can be used for surface science study, *e.g.* rutile $TiO_2(110)$. A major issue here is the availability of single crystals. This can be for a number of reasons, both commercial (*e.g.* customer demand) and practical (*e.g.* difficulty in preparing the single crystals themselves, or in cleaving some materials). Additionally when available, the samples are often of rather small dimensions. There may also be issues with purity (maybe resulting in surface segregation of one impurity component) and thermal conductivity (leading to issues with the uniformity of heating). The most significant problem with most oxide single crystals however is with their low electrical conductivity. This can cause particular problems with spectroscopic techniques involving electrons and ions, where sample charging is a serious obstacle. To some extent this problem can be partially addressed by *in situ* sputtering and annealing in O_2 to create surface defects which support electrical conductivity.[16] However in so-doing one is modifying the nature of the surface which one is intending to study. Many of the problems associated with using single crystals of metal oxides can be overcome by using the **thin film approach**. This approach consists of growing a film (usually between 1 nm and 5 nm in thickness) on a substrate. It is generally desirable for the oxide to be conducting to avoid the charging problem mentioned above; for this reason single crystal metal substrates are generally preferred. The oxide film can be grown either by deposition of the metal followed by oxidation, or by direct deposition of the metal oxide. There are a number of techniques which can be employed for deposition onto a substrate in UHV. The method used in this work is the thermal evaporation method. This consists of vaporising the metal (or metal oxide) in UHV, creating a flux of atoms or molecular fragments, which then condense onto and build up on the substrate surface. The designs of the deposition sources used in this work are discussed in detail in section 2.2. In general, a commonly adopted method is to resistively heat a wire filament of the required metal by passing sufficient electrical current through it, or to resistively heat a crucible that contains the material. The evaporation deposition technique is conceptually straightforward and suitable sources can be fabricated by researchers to their own specifications. Although deposition of contaminants can arise, outgassing of the source before use significantly reduces this problem. Alternative methods of preparing thin films are sputtering, chemical vapour deposition (CVD) and molecular beam epitaxy (MBE). The thin film approach described above overcomes many of the issues associated with the poor thermal and electrical conductivity of oxides, since the films are just a few atomic layers in thickness and are in contact with a conductive metal substrate. Therefore techniques such as XPS and LEED can be used without the problems encountered with bulk single crystals. A wide range of oxide films can be grown with high purity. It should however be recognised that the structure and properties of thin films in contact with a substrate may vary from those of the bulk metal oxide. In the case of an epitaxial film, the overlayers ideally adopt the geometric structure of the substrate, but if a substrate with an appropriately-sized unit cell is not available, then the oxide film may contain a high concentration of defects or even be polycrystalline in nature. The differing properties of thin films may themselves be of technological significance, nonetheless this is a further reason why caution is required when attempting to make a connection between the findings of thin film studies and the properties of materials used in real applications. Another potential problem with this approach is with the degree (and control) of stoichiometry of the metal oxides films. Much time may be spent in refining the preparation method to generate films of the required specification (crystalline orientation, degree of order, morphology and stoichiometry). However this gives researchers tremendous scope for generating films of particular structures and properties that could not be obtained elsewhere.

In this next section, the various experimental techniques which are commonly applied to the study of oxide surfaces are discussed, with particular reference to issues that arise in the study of these surfaces.

Scanning probe techniques have revolutionised surface science, allowing routine imaging of surfaces up to atomic resolution. **Scanning tunnelling microscopy** (STM) operates by bringing a sharp conductive tip very close ($\leq$ 1 nm) to a conducting surface. A voltage difference is applied between the tip and the surface and a tunnelling current is observed between the tip and the surface. An image may be obtained by controlling and recording the height of the tip as it is scanned across the surface whilst maintaining a constant tunnelling current (using a feedback circuit). In **atomic force microscopy** (AFM) a conducting or insulating surface can be imaged by scanning a tip attached to a nonrigid cantilever. The tip experiences attractive or repulsive forces (van der Waals, chemical, magnetic or electrostatic) which causes the cantilever to bend. An image may be formed in a similar fashion to STM, by using a feedback loop to adjust the tip height. STM is not possible with bulk samples of insulating oxides, but it can be applied to some semiconducting oxide surfaces. In particular their have been extensive studies of TiO_2 single crystal surfaces.[17-20] When thin films of oxides are employed then STM may be used to image oxides of much lower conductivity as illustrated by work on oxides such as Al_2O_3 [21] and CeO_2.[22] AFM may be applied to both single crystal oxides and thin film oxides, but it doesn't generally provide atomic resolution.

Electron spectroscopic techniques are amongst the most important in surface science. These techniques frequently involve the excitation of sample atoms leading to electron emission, in which case the energy of emitted electrons is measured providing useful characterisation of the sample surface. **X-ray photoelectron spectroscopy** (XPS) is one of the techniques utilised in this study and the background to the technique is discussed in section 2.3. Basically, XPS involves the photoemission of core electrons, stimulated by irradiation of the sample by soft monochromatic x-rays. The kinetic energies of the photoelectrons are measured and correlated with binding energy of the electrons to the atom. This provides qualitative and quantitative elemental analysis along with information on chemical states (e.g. oxidation state and chemical environment). The main issue with applying XPS to the study of metal oxides is that surface charging can occur due to the inability of insulating oxides to dissipate the charge caused by the photoemission process. The positive charge on the surface results in a higher measured binding energy and can cloud judgement when extracting information on chemical states. One solution is to use a charge neutraliser.[23] Alternatively, this problem can be largely overcome by using the thin film deposition approach, since the degree of charging that can occur at the surface of very thin oxide films on metallic substrates is very small. In **ultraviolet photoelectron spectroscopy** (UPS), ultraviolet photons excite photoemission from valence levels. Therefore UPS is well-suited to the study of bonding at surfaces, providing measurements of the work function and band structure of the surface and adsorbed layers. UPS has been widely applied in the study of both single crystal and thin film oxide surfaces, since it is sensitive to the presence of surface defects (*e.g.* oxygen vacancies) and surface hydroxylation (an important issue with oxides).[24] Finally, in **Auger electron spectroscopy** (AES), an Auger transition occurs after ionisation of a core level, and a higher lying core or valence electron fills the resulting hole in a radiationless transition. This leaves the atom in an excited state, which is removed by the ejection of a second electron. Auger transitions can be excited by photons, electrons or by ion bombardment, but electron bombardment is commonly used in surface analytical AES. AES provides quantitative elemental analysis.

Another technique making use of low energy electrons is **low energy electron diffraction** (LEED) and this is also employed in this study and therefore explained in greater detail in section 2.4. In LEED electrons of a well-defined energy are back-scattered by atoms in the surface region giving rise to a diffraction pattern which is observed on a fluorescent screen. From this it is possible to extract structural information on the size and symmetry of the crystal unit cell. Furthermore LEED can be used to analyse overlayer structures formed by adsorbates. Like XPS however, LEED can be problematic with highly insulating samples. This can either be overcome by employing very low beam currents, together with high sensitivity detectors (*e.g.* channelplates) or using the thin film approach.[25,26]

Vibrational spectroscopies are amongst the most important techniques for analysing species adsorbed on oxide surfaces. The vibrations of molecules adsorbed on a surface can be probed by **reflection absorption infrared spectroscopy** (RAIRS) and this technique is discussed further in section 2.5. RAIRS is similar to conventional IR spectroscopy except the IR beam is specularly reflected off the sample. From this it is possible to identify modes of vibrational excitation of particular chemical bonds, thus providing identification of adsorbed species. In addition the dipole selection rule makes it possible to deduce the orientation of the adsorbed molecule on a metal or a thin film of an insulator (*e.g.* metal oxide) on a metallic substrate. RAIRS provides high spectral resolution and can be carried out at relatively high pressure, allowing better comparison with real conditions. However RAIRS can only be applied easily to highly reflective samples, so it is not well suited to studies of single crystal metal oxide surfaces. This problem can be overcome by depositing thin films of the metal oxide onto a metallic (and therefore reflecting) substrate, and there are now a significant number of researchers using this approach for the study of oxide surface chemistry.[27,28] Another limitation of RAIRS however is that the signal to noise ratio can be quite poor, since the amount of adsorbed molecules on the sample is very small (*e.g.* approximately 1 nanomole). Another form of vibrational spectroscopy is **electron energy loss spectroscopy** (EELS). In EELS monochromatic electrons are backscattered by the sample and the energy measured. From the energy loss vibrational and electronic transitions can be observed. Study of vibrations is often called high-resolution EELS (HREELS) and this technique is widely employed for the study of adsorbates on metal surfaces. On oxide surfaces, however, there are frequently strong signals due to the optical phonons of the oxide lattice and these can mask the signals due to adsorbates.[23]

Finally, in **temperature programmed desorption spectroscopy** (TPD), discussed in section 2.6, a gas is dosed onto the surface and then the surface is heated at a controlled rate whilst recording desorbing species (usually with a quadrupole mass spectrometer). This provides information on the surface coverage, binding energy of the molecules to the surface and kinetics of desorption. One problem with using TPD to study adsorption on single crystal metal oxide samples is with their low thermal conductivity, which can lead to issues with the uniformity of heating. The technique can, however, be readily applied to studies of adsorption on thin film oxides.[29-31]

1.3 Background to the Systems Studied

The tremendous increase in the output of surface science literature on metal oxides over the past few decades is a reflection of the importance of these materials to industry and the significance of their physical and chemical surface properties in these applications. Metal oxides are used in heterogeneous catalysis, both as the catalytically active component and as support material, in important industrial reactions (*e.g.* methanol synthesis) and for removing environmentally damaging compounds (*e.g.* catalytic converters in automobiles). Metal oxides are also used in numerous other technologies, including semiconductor devices and corrosion control. In all of these examples understanding the surface properties is essential. In the course of the work described in this thesis, studies have been carried out looking at the growth of ultra-thin (sub-nanometer and nanometer thick) layers of CrO_x, BaO_x, TiO_x and FeO_x on Cu(111) and a Ag/FeO_x model catalyst.

Chromium oxide is an important industrial catalyst used in the dehydrogenation of alkanes to alkenes[32] and oxidation of environmentally damaging compounds (CO, VOCs, *etc.*)[33,34] Resultantly there has been a great deal of surface science research into the surface chemistry of chromium oxide, the specific findings of which will be reviewed in more detail in section 3.1. Chromium oxide surfaces are quite well understood in terms of structure, but our understanding of molecular interactions with well-defined surfaces is at a somewhat rudimentary stage, with the interactions of water and oxygen with such surfaces being the most commonly studied. Considering the importance of chromium oxide to industry it is surprising that its surface chemistry has not been more extensively researched. A better understanding of how small molecules interact with well-defined chromium oxide surfaces would be an important step towards appreciating how chromia-based catalysts function. There is no published work of chromium oxide films on a Cu(111) substrate.

Barium oxide has received attention recently as a storage medium in NO_x storage/reduction catalysts for automobiles.[35] This research is reviewed in section 4.1. The majority of these studies involve the testing of prepared model catalysts in flow reactors. In contrast there is little published work on BaO surface science in UHV, despite the fact that such studies clearly have much to contribute to our understanding. There is much potential for additional research here; for example, a recent surface science study of NO_x/BaO[36] utilised XPS, but not other potentially interesting techniques (*e.g.* TPD, RAIRS). Furthermore NO_x storage/reduction catalysts used in the real world will also be exposed to other gases (*e.g.* CO_2, O_2, hydrocarbons, SO_2), and the interaction of these molecules with BaO surfaces is therefore also of interest. Yet there are no UHV studies of hydrocarbon or SO_2 interaction with BaO in the existing literature (in contrast to a fair number of studies of the effect of sulfur poisoning on NO_x trap catalysts).[37,38] Finally, there has been no published work on BaO grown on a copper substrate.

Titanium dioxide is a support material used in many important heterogeneous catalysis applications (*e.g.* selective oxidation)[39] and also has interesting photochemical properties which enable it to be used in photodegredation of harmful or unwanted compounds.[40] The importance of understanding its surface properties has led to an abundance of surface science studies, which are reviewed in section 5.1. Although TiO_2 surfaces have been extensively researched under UHV conditions, including their interaction with molecules, the majority of this research is on the readily obtainable $TiO_2(110)$ rutile surface. In fact most catalysts in industrial use consist of largely the anatase form of TiO_2 – and this is also believed to be the most catalytically active. Yet, there are only a handful of studies on well-defined anatase surfaces. There have been no reports of TiO_2 films grown on a Cu(111) substrate.

Iron oxides are to be found in many industrial catalyst applications including styrene synthesis by ethylbenzene dehydrogenation[41] and removal of environmentally unfriendly compounds.[42,43] The substantial research into iron oxide surfaces (both Fe_2O_3 and Fe_3O_4) is reviewed in section 6.1. Despite this research iron oxides are not very well understood, largely as a result of their complicated interconversion from one phase to another under oxidising and reducing conditions.

Recently surface scientists have turned their attention towards dispersed metal on metal oxide systems in an attempt to bridge the gap between single crystal surfaces and real catalysts. Noble metals, which are commonly employed as the catalytically active component on an oxide support, have received particular attention. A review of some studies of silver clusters on metal oxides is presented in section 6.4.

Dispersed **silver on iron oxide** was chosen as the focus of this research. Supported silver is known to exhibit catalytic activity, for example in three-way catalysts.[44] Additionally Ag on metal oxide systems are relevant to solid state gas sensor technology.[45] Although Ag/TiO_2 systems have been studied, no UHV studies of Ag/FeO_x have yet been published.

Despite the substantial amount of research on the metal oxides mentioned above, there is clearly still plenty of scope for further studies to enhance our understanding of these very important systems.

1.4 Aims of the Research

The previous section clearly demonstrated the technological importance of the particular oxide systems discussed and the significance of understanding their surface properties. Yet it also revealed that there are many gaps in our current understanding and much potential for UHV surface science studies. The ultimate aim of this research therefore is to elucidate a deeper understanding of the surface chemistry of these oxide systems at a fundamental level. In order to achieve this, the approach which has been adopted is to grow and characterise well-defined oxide films. For each system, the initial phase of work involves optimising the parameters for obtaining these films. X-ray photoelectron spectroscopy (XPS) and low energy electron diffraction (LEED) are the main analytical techniques in this phase. The next phase is to investigate the interaction of small molecules with these surfaces. In addition to the techniques mentioned before, reflection-absorption infrared spectroscopy (RAIRS) and temperature programmed desorption (TPD) are used to provide information on surface adsorbates and adsorption behaviour. In each case the aim is to relate information obtained on the adsorption characteristics of particular species to the surface structure elucidated in the characterisation phase.

References

1 G. Ertl, H. Knözinger and J. Weitkamp (Eds.), *Handbook of Heterogeneous Catalysis*, Wiley, Weinheim,1997.

2 H.A. Al-Abadleh, V.H. Grassian, *Surf. Sci. Rep.* 2003, **52**, 63

3 L.H. Chiu, C.C. Chen, C.F. Yang, *Surf. Coatings Tech.* 2005, **191**, 181

4 K. Kukli, M. Ritala, M. Leskela, *J. Electrochem. Soc.* 2001, **148**, F35

5 M. Ohmukai, *Appl. Surf. Sci.* 1999, **152**, 49

6 H.J. Frenck and S. Georgiou, *Surf. Sci.* 1997, **385**, 155

7 W. Weiss and W. Ranke, *Prog. Surf. Sci.* 2002, **70**, 1

8 H. Ma, Y. Berthier and P. Marcus, *Appl. Surf. Sci.* 1999, **153**, 40

9 M. Badlani, I.E. Wachs, *Catal. Lett.* 2001, **75**, 137

10 Y.D. Kim, J. Stultz and D.W. Goodman, *Langmuir*, 2002, **18**, 3999

11 R.L. Kurtz and V.E. Henrich, *Phys. Rev. B*, 1987, **36**, 3413.

12 J.M. Walls, *Methods of Surface Analysis*, 1989, Cambridge University Press

13 D.P. Woodruff and T.A. Delchar, *Modern Techniques of Surface Analysis*, 1986, Cambridge University Press

14 K.W. Kolasinski, *Surface Science Foundations of Catalysis and Nanoscience*, 2002, Wiley

15 G. Ertl and J. Küppers, *Low Energy Electrons and Surface Chemistry*, 1985, Weinheim

16 H.J Freund, *Faraday Discuss.* 1999, **114**, 1

17 U. Diebold, J. Lehman, T. Mahmoud, M. Kuhn, G. Lionardelli, W. Hebenstreit, M. Schmidt, P. Varga, *Surf. Sci.* 1998, **411**, 137

18 U. Diebold, *Surf. Sci.Rep.* 2003, **48**, 53

19 P.W. Murray, F.M. Leibsle, C.A. Muryn, H.J. Fisher, C.F.J. Flipse and G.Thornton, *Phys.Rev.Lett.* 1994, **72**, 689

20 P.W. Murray, N.G. Condon and G.Thornton, *Phys. Rev. B*, 1995, **51**, 10989

21 C. Dietrich, B. Koslowski and P. Ziemann, *J. Appl. Phys.* 2005, **97**, 083515

22 H. Nörenberg and G.A.D. Briggs, *Phys. Rev. Lett.* 1997, **79**, 4222

23 V.E. Henrich and P.A. Cox, *The Surface Science of Metal Oxides*, 1994, Cambridge University Press

24 V.E. Henrich, *Prog.Surf.Sci.* 1979, **9**, 143

25 F. Rohr, M. Bäumer, H.J. Freund, J.A. Mejias, V. Staemmler, S. Müller, L.

Hammer and K. Heinz, *Surf. Sci.* 1997, **372**, L291

26 Sh.K. Shaikhutdinov and W. Weiss, *Surf. Sci.* 1999, **432**, L627

27 U. Berner, K. Schierbaum, G. Jones, P. Wincott, S. Haq and G. Thornton, *Surf. Sci.* 2000, **467**, 201

28 H.E. Sanders, P. Gardner and D.A. King, *Surf. Sci.* 1995, **331**, 1496

29 C. Lemire, R. Meyer, V.E. Henrich, Sh. Shaikhutdinov and H.J. Freund, *Surf. Sci.* 2004, **572**, 103

30 T. Kawabe, K. Tabata, E. Suzuki, Y. Ichikawa, Y. Nagasawa, *Catal. Today*, 2001, **71**, 21

31 M. Schulze and R. Reissner, *Surf. Sci.* 2001, **482**, 285

32 C.H. Marcilly and B. Delmon, *J. Catal.* 1972, **24**, 336

33 M.I. Zaki, M.A. Hasan and L. Pasupulety, *Appl. Catal. A Gen.* 2000, **198**, 247

34 M. Kulażyński, J.G.V. Ommen, J. Trawczyński and J. Walendziewski, *Appl. Catal. B Environ.* 2002, **36**, 239

35 E. Fridell, M. Skoglundh, B. Westerberg, S. Johansson and G. Smedler, *J. Catal.* 1999, **183**, 196

36 P.J. Schmitz and R.J. Baird, *J. Phys. Chem.* 2002, **106**, 4172

37 A. Amberntsson, M. Skoglundh and M. Jonsson, et al. *Catal. Today*, 2002, **73**, 279

38 H. Mahzoul, L. Limousy, J.F. Brilhac and P. Gilot, *J. Anal. Appl. Pyrol.* 2000, **56**, 179

39 U. Diebold, *Surf. Sci. Rep.* 2003, **48**, 53

40 C.H. Ao, S.C. Lee, J.Z. Ju and J.H. Zu, *Appl. Catal.* B:Environ. 2004, **54**, 41

41 W. Weiss and W. Ranke, *Prog. Surf. Sci.* 2002, **70**, 1

42 K. Adib, N. Camillone III, J.P. Fitts, K.T. Rim, G.W. Flynn, S.A. Joyce and R.M. Osgood Jr. *Surf. Sci.* 2002, **497**, 127

43 K. Adib, D.R. Mullins, G. Totir, N. Camillone III, J.P. Fitts, K.T. Rim, G.W. Flynn, and R.M. Osgood Jr. *Surf. Sci.* 2003, **524**, 113

44 F. Bonet, S. Grugeon, R. Herra Urbina, K. Takaia-Elhsissen and J.M. Tarascon, *Solid State Sciences*, 2002, **4**, 665

45 U. Kirner, *Sens. Actuators B*, 1990, **1**, 103

Chapter 2:

Experimental Techniques

2.1 The UHV System

The experiments detailed in this report were carried out in a stainless steel ultra-high vacuum chamber (see Figure 2.1) consisting of an analytical chamber and an independently-pumped chamber for RAIRS studies. The main analytical chamber was pumped by a diffusion pump (Edwards EO4) fitted with a liquid nitrogen trap and an ion pump. Base pressures of $< 5 \times 10^{-10}$ Torr were readily achieved when pumping with the diffusion pump. The RAIRS chamber was pumped by a turbomolecular pump (Leybold, 60 ls^{-1}) backed by a rotary pump. The pressures in the main chamber and RAIRS chamber were measured by hot filament ionisation gauges. Dosing of O_2 or other gases was achieved from a gas-dosing manifold which could be evacuated with a rotary pump and a diffusion pump (Edwards EO2). The Cu(111) substrate was mounted on a sample holder attached to a high precision manipulator. Heating of the sample could be achieved by passing an electrical current through a tantalum wire which was fed through a ceramic block contained in the molybdenum holder upon which the Cu crystal was mounted. The temperature of the Cu crystal was monitored by use of a chromel/alumel thermocouple junction, which was in contact with one corner of the crystal. The sample was cleaned by argon ion sputtering, using an ion gun (VG AG5000). Following annealing the Cu(111) surface was re-ordered by annealing at 923 K for 10 minutes. Integrated in the system was an x-ray source (VG XR2E3) and an electron energy analyser (VG CLAM 2 concentric hemispherical analyser) for XPS, reverse-view low energy electron diffraction (LEED) optics for LEED, and a quadrupole mass spectrometer (VG Micromass 200D). Additionally there were several extra flanges allowing the evaporation sources (described in section 2.2) to be installed.

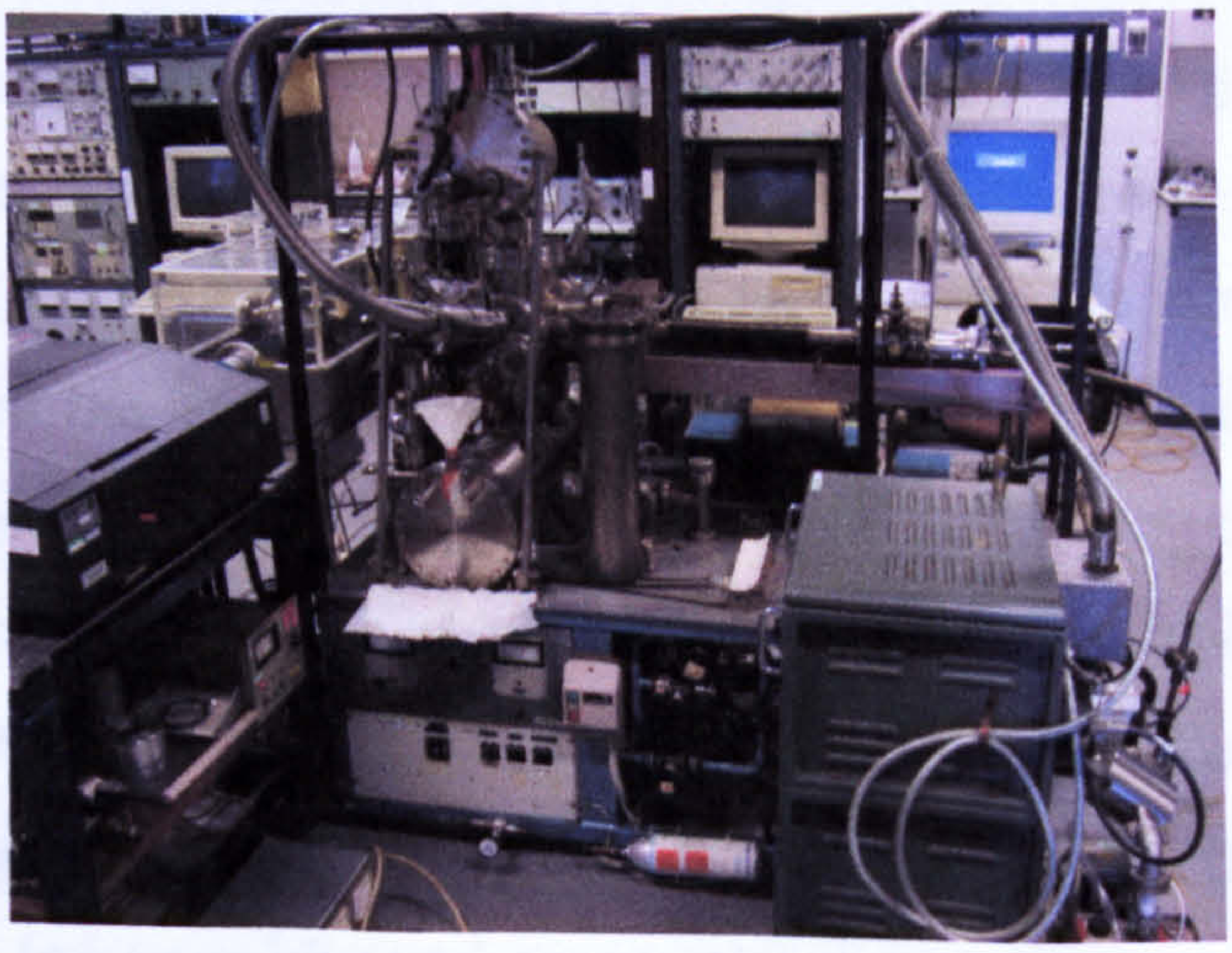

Figure 2.1: The UHV system

2.2 Fabrication of Metal / Metal Oxide Evaporation Sources

Evaporation sources were constructed to allow deposition of Cr, BaO, Ti, Fe and Ag onto the substrate. The Cr source utilised electron bombardment heating, whereas all other sources functioned by resistive heating of a filament or boat.

2.2.1 Chromium Metal Evaporation Source

The chromium evaporation source (see Figure 2.2) functioned by electron bombardment of a chromium plated tungsten wire (10 mm long, 1.8 mm diameter (1.3 mm W), from Alfa Aesar), supported in a coil of tungsten wire (0.15 mm thick).

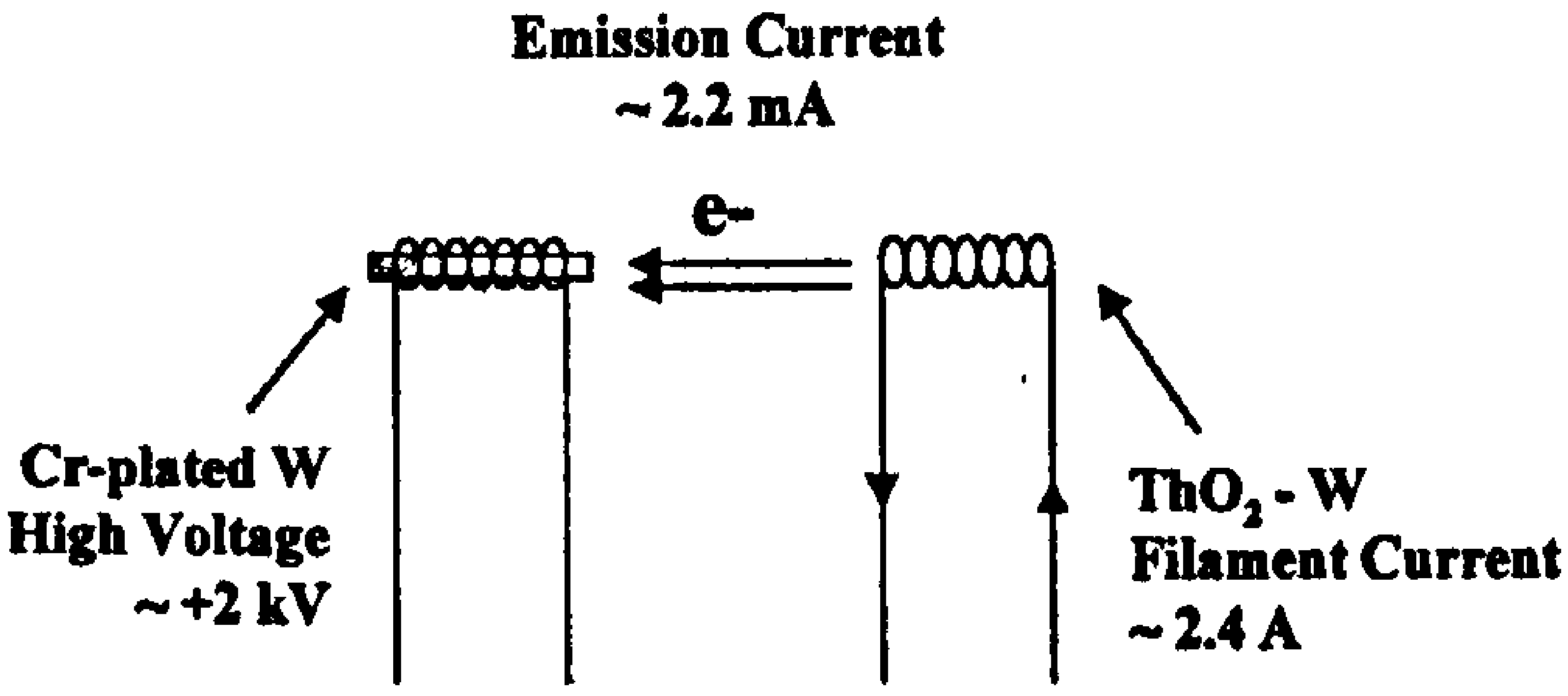

Figure 2.2: Schematic representation of the chromium evaporation source

Electrons are thermionically emitted from the filament and accelerated across the gap by a high positive potential (~ +2 kV). The heating caused by this bombardment results in evaporation of the Cr metal and thus a flux of Cr atoms.

The quadrupole mass spectrometer (located with line of sight to the source) was used to ascertain the high voltage and emission current needed to evaporate chromium. It was determined that with a high voltage of 1950 V and a filament current of 2.4 A, corresponding to an emission current of 2.2 mA chromium evaporation could be observed (*i.e.* there was an increase in the $m/z = 52$ peak). During this operation, Cr evaporation was not seen until the source had been run for ~ 30 s and a steady-state flux was not achieved until ~ 70 s. Therefore the Cr evaporation source was always run for 90 s before the sample was wound into place, to ensure consistency with different deposition times. With continued use of the evaporation source in the experiments in this report it was found that the Cr flux began to decrease gradually. This problem was solved by increasing the operational power, eventually up to 2050 V and an emission current of 2.9 mA. In normal operation the total pressure of the main chamber (measured by an ion gauge) increased from a base pressure of ~

10^{-10} Torr to a pressure of ~ 3×10^{-8} Torr during deposition. Analysis of the XPS survey scan (see Figure 2.3) showed the only impurity to be carbon, as indicated by a small C 1s signal.

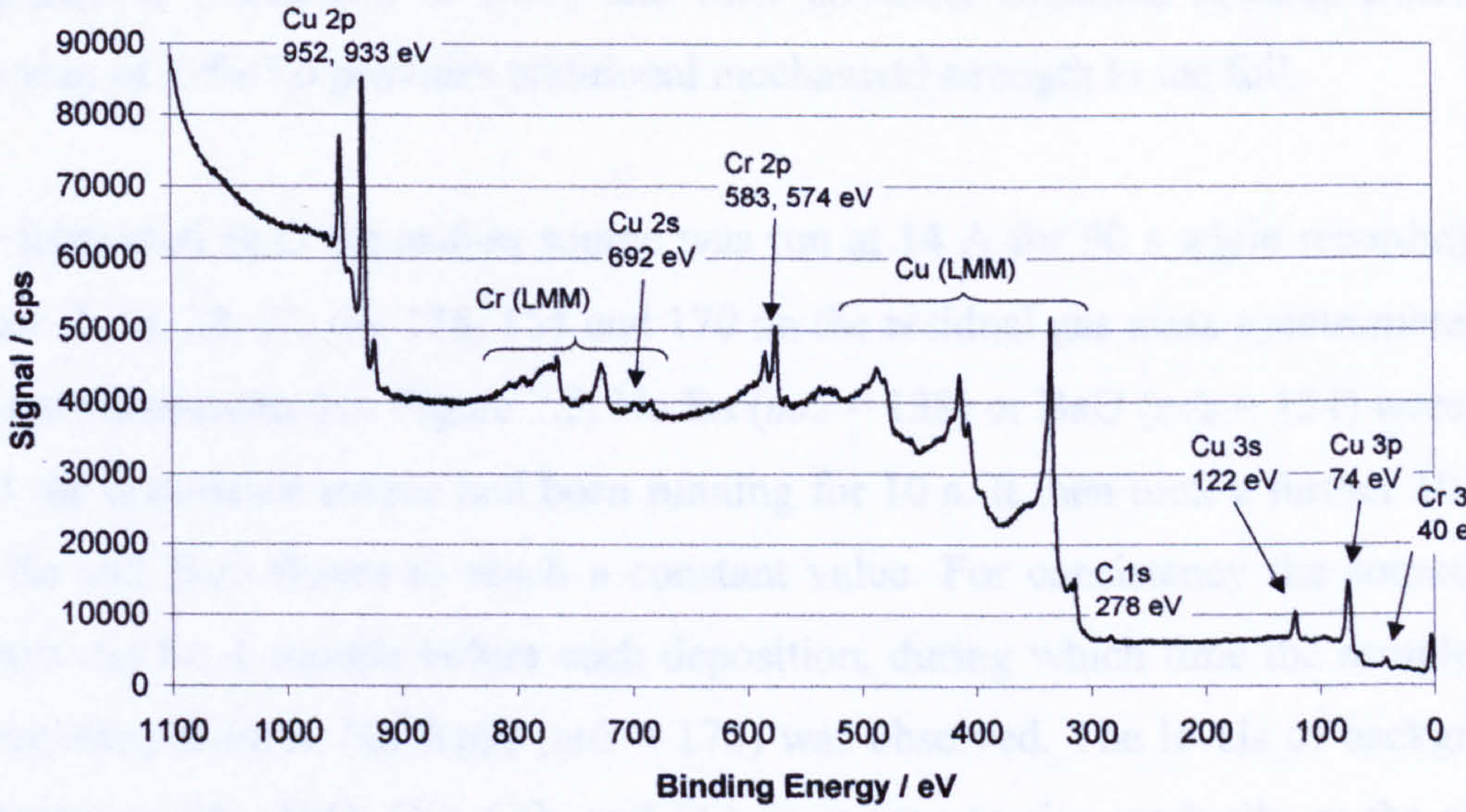

Figure 2.3: Survey spectrum for Cr deposition on a Cu(111) substrate

2.2.2 *Barium Oxide Evaporation Source*

The deposition source consisted of BaO lumps (from Fluka/Riedel-de Haën, 95% BaO, 5% BaO_2, 0.1% Cl^-, 0.05% Fe) measuring a few millimetres in diameter supported in a "boat" made by folding a piece of Pt/Rh foil into a "V" shape (Johnson Matthey, 10% Rh, 0.015 mm thick) and sealing at either end by pinching. The sample holder was joined to the electrical feedthroughs by spot-welding (see Figure 2.4).

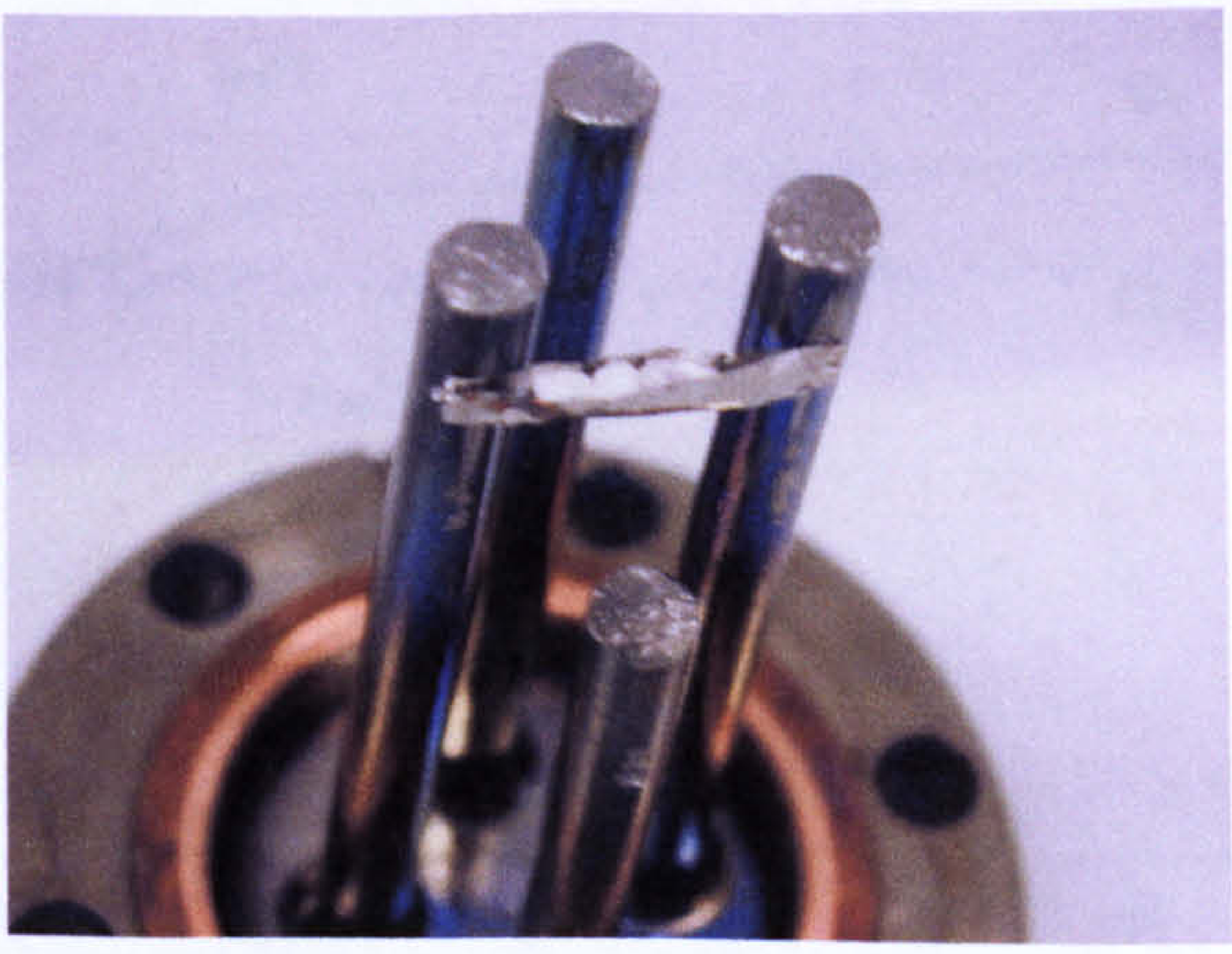

Figure 2.4: BaO evaporation source

This evaporation source works simply by the resistive heating of the foil "boat" and the transference of this heat to the BaO lumps leading to BaO evaporation. The choice of Pt and Rh was undertaken with consideration to their evaporation temperatures (compared to BaO) and their chemical inertness towards BaO. The inclusion of 10% Rh provides additional mechanical strength to the foil.

The fabricated BaO deposition source was run at 14 A for 90 s while recording *m/z* values 2, 18, 28, 32, 44, 138, 154 and 170 on the residual gas mass spectrometer and this data is presented in Figure 2.5. No Ba (*m/z* = 138) or BaO (*m/z* = 154) were seen until the deposition source had been running for 10 s. It then took a further 10 s for the Ba and BaO fluxes to reach a constant value. For consistency the source was always run for 1 minute before each deposition, during which time the sample was facing away from it. No BaO_2 (*m/z* = 170) was observed. The levels of background components (H_2, H_2O, CO, CO_2 and O_2) were seen to rise gradually as the source was run. This is the result of parts of the deposition source outgassing as they become heated. When the source was turned off the levels of Ba and BaO dropped immediately and the level of the background gases soon returned to normal.

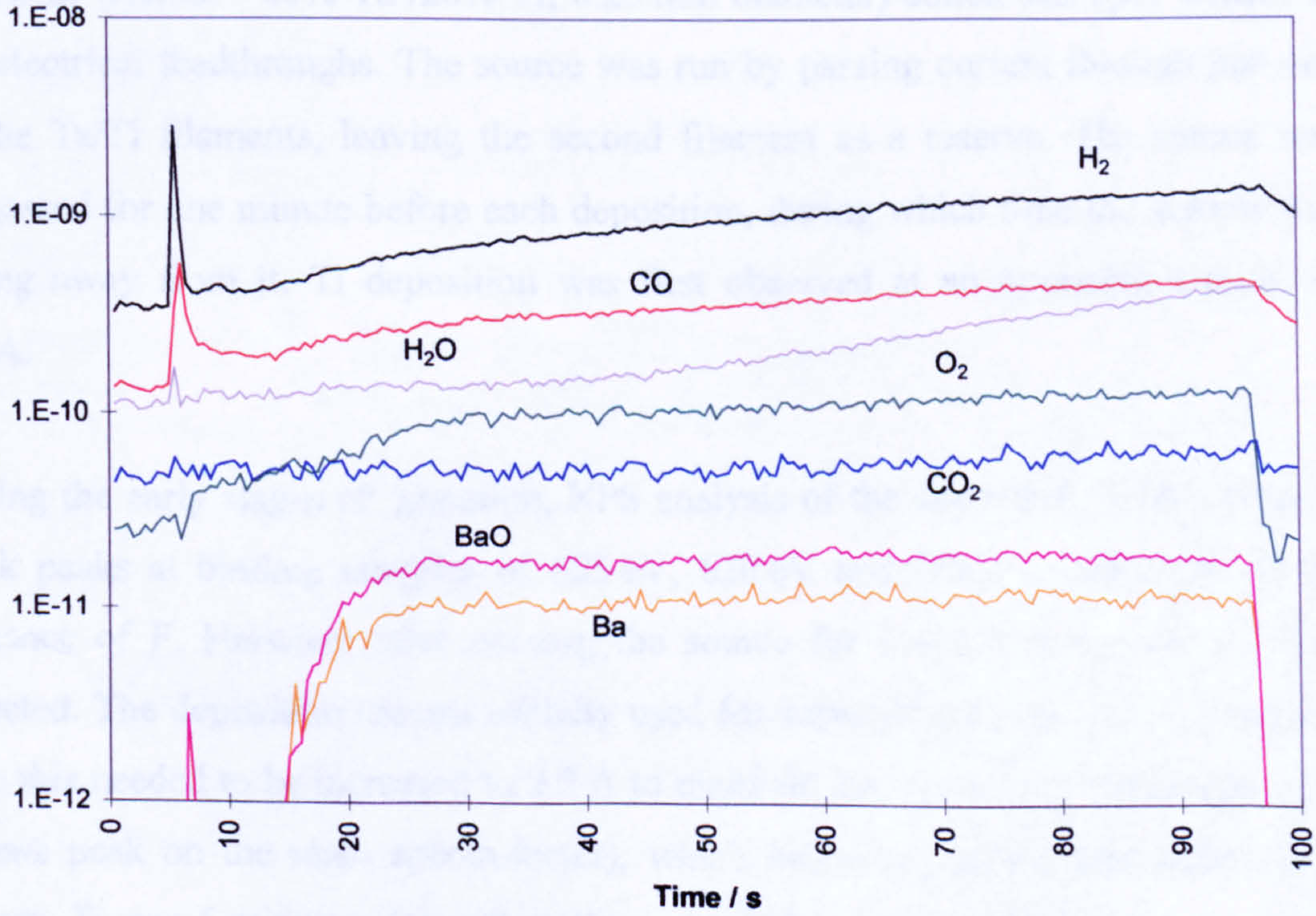

Figure 2.5: Mass spectral data recorded during operation of the BaO deposition source (the source was switched on at t ~ 5 s).

Analysis of the XPS survey scan (see Figure 2.6) showed the only impurity to be carbon, as indicated by a small C 1s signal.

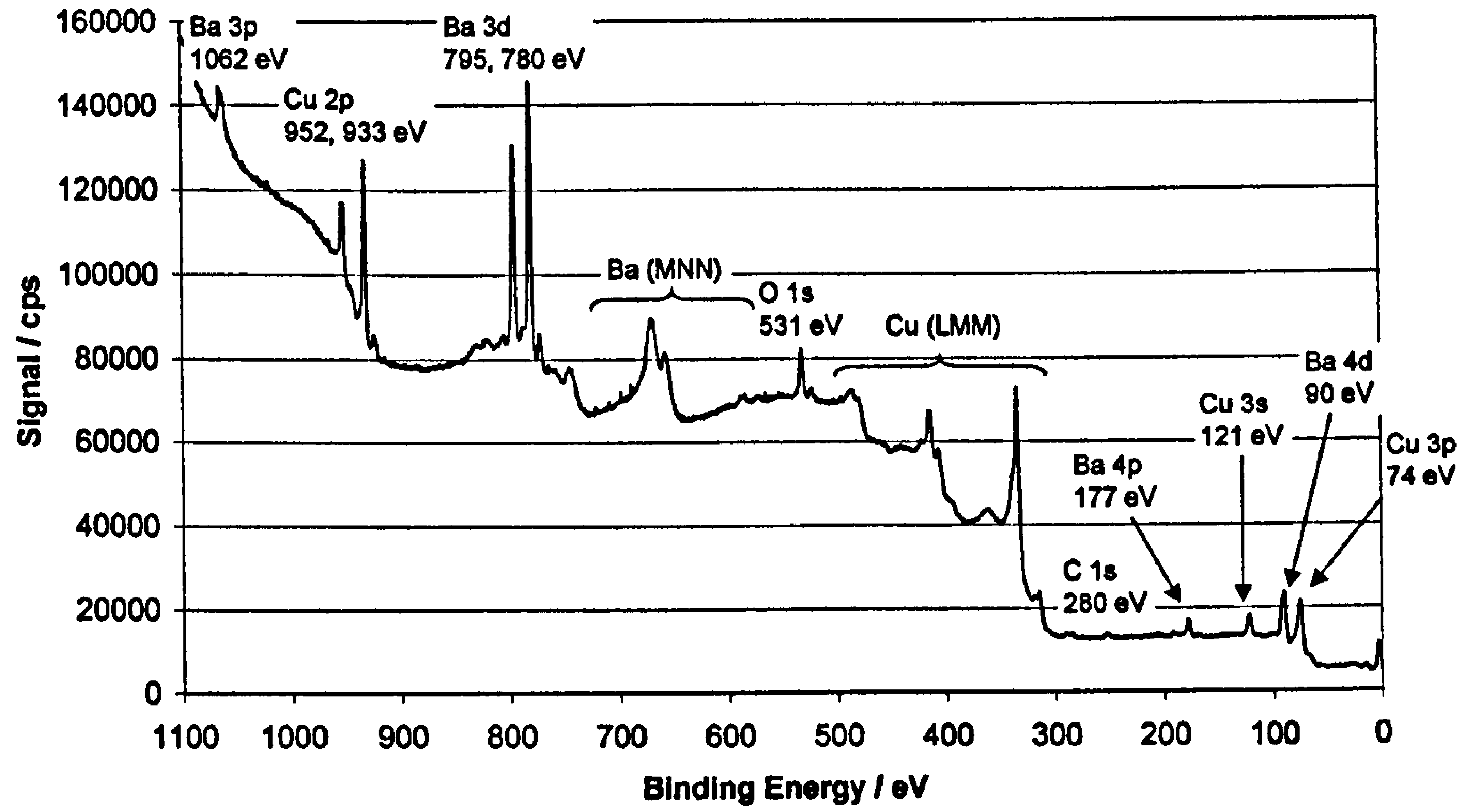

Figure 2.6: Survey spectrum for BaO deposition on a Cu(111) substrate

2.2.3 *Titanium Metal Evaporation Source*

The titanium deposition source consisted of two tantalum/titanium alloy wire filaments (Kemet - 80% Ta /20% Ti, 0.25 mm diameter) coiled and spot welded to the electrical feedthroughs. The source was run by passing current through just one of the Ta/Ti filaments, leaving the second filament as a reserve. The source was outgassed for one minute before each deposition, during which time the sample was facing away from it. Ti deposition was first observed at an operating current of 2.0 A.

During the early stages of operation, XPS analysis of the deposited Ti film showed weak peaks at binding energies of 685 eV, 620 eV and 595 eV, indicative of the presence of F. However after running the source for some time no more F was detected. The deposition current initially used for experiments was 2.25 A, but after time this needed to be increased to 2.5 A to maintain the Ti flux (as measured as the 48 *m/z* peak on the mass spectrometer), which was required for depositions of ~ 1.3 nm Ti per 5 minutes deposition time. Analysis of the XPS survey scan (see Figure 2.7) showed the only impurity to be carbon, as indicated by a small C 1s signal.

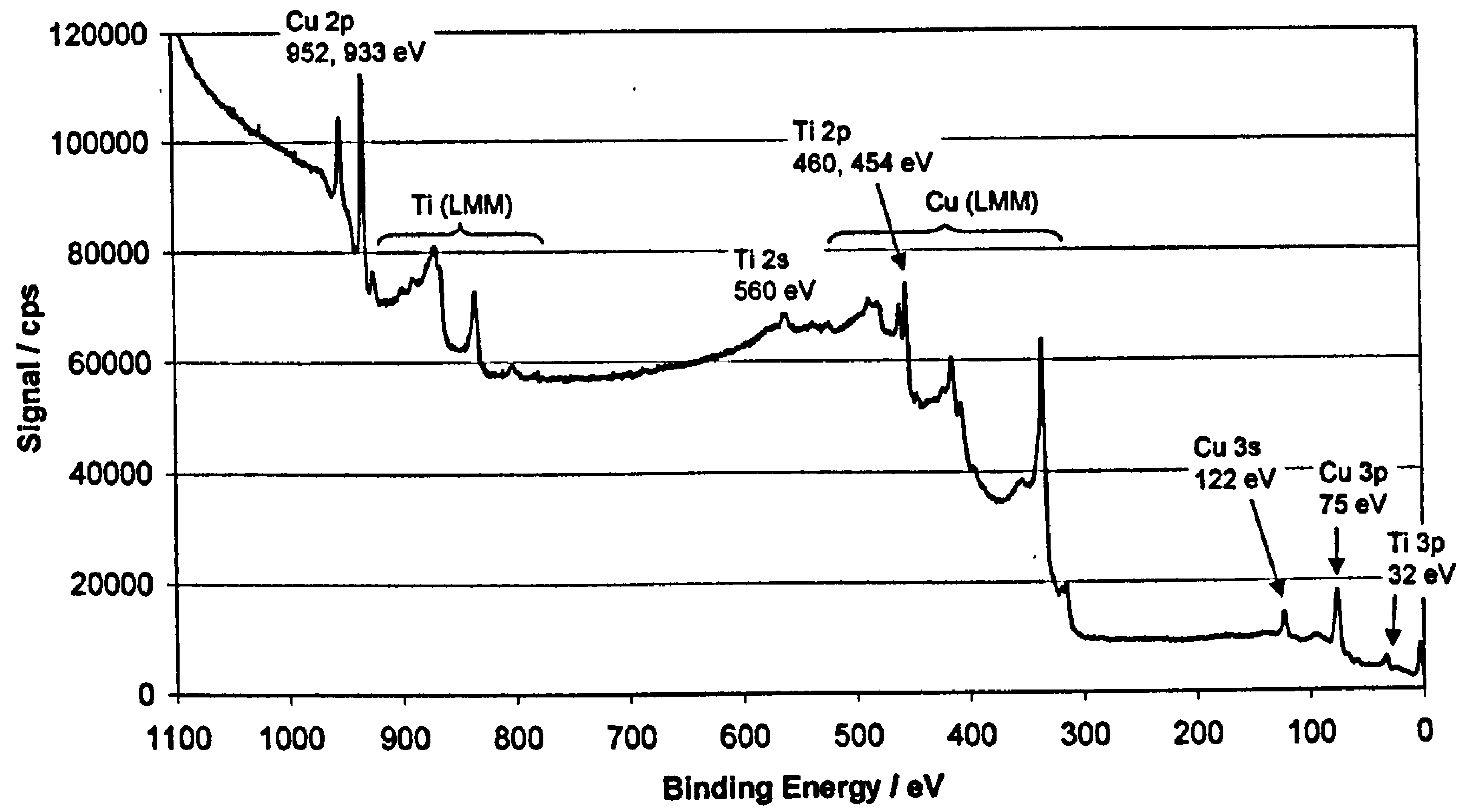

Figure 2.7: Survey spectrum for Ti deposition on a Cu(111) substrate

2.2.4 Iron Metal Evaporation Source

The iron deposition source consisted of two tungsten wire filaments (0.35 mm diameter), with tungsten wire (0.125 mm) and iron wire (Johnson Matthey - 0.25 mm diameter) wound around it and spot welded to the electrical feedthroughs. The intention was to operate just one of the filaments, the other being left as a reserve.

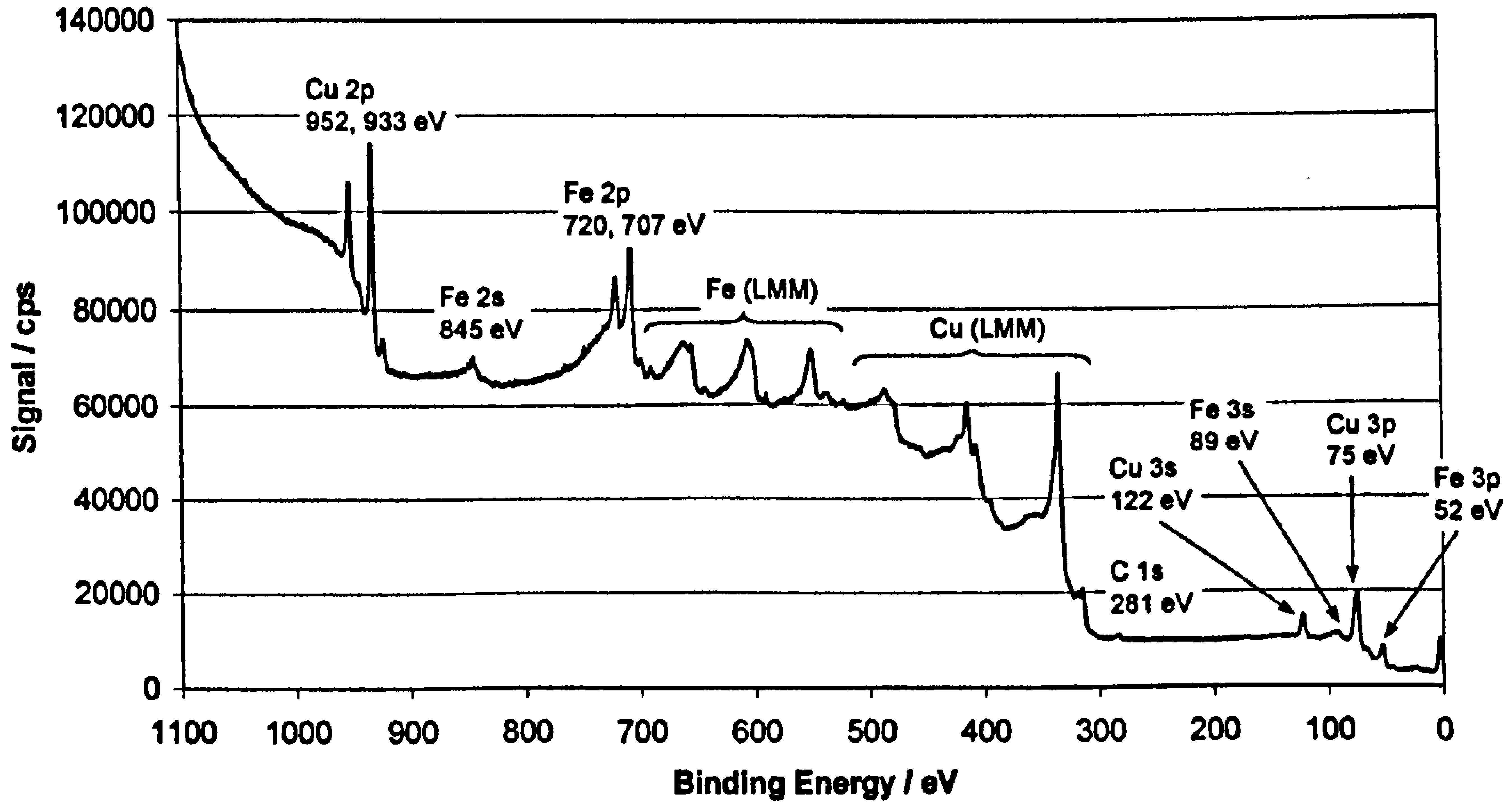

Figure 2.8: Survey spectrum for Fe deposition on a Cu(111) substrate

During initial tests, the Fe deposition source was run at increasing current each time for 1 minute with the Cu(111) substrate facing away from the deposition source followed by 1 minute with the crystal in position for deposition. Slight Fe deposition was first evidenced by XPS for operation at 9.0 A and at 9.5 A there was further deposition. Analysis of the XPS survey scan (see Figure 2.8) showed the only impurity to be carbon, as indicated by a small C 1s signal. During normal operation the source was run at 9.5 A.

2.2.5 Silver Metal Evaporation Source

The silver deposition source was of a similar design to the Fe-source and consisted of two tungsten wire filaments, with tungsten wire (0.125 mm) and silver wire (Advent – 99.99%, 0.125 mm diameter) wound around it and spot welded to the electrical feedthroughs. The source was always run for 1 minute before each deposition, during which time the sample was facing away from it. Evaporation of Ag was observed for filament currents in excess of 10.0 A. Analysis of the XPS survey scan (see Figure 2.9) showed the only impurity to be carbon, as indicated by a small C 1s signal.

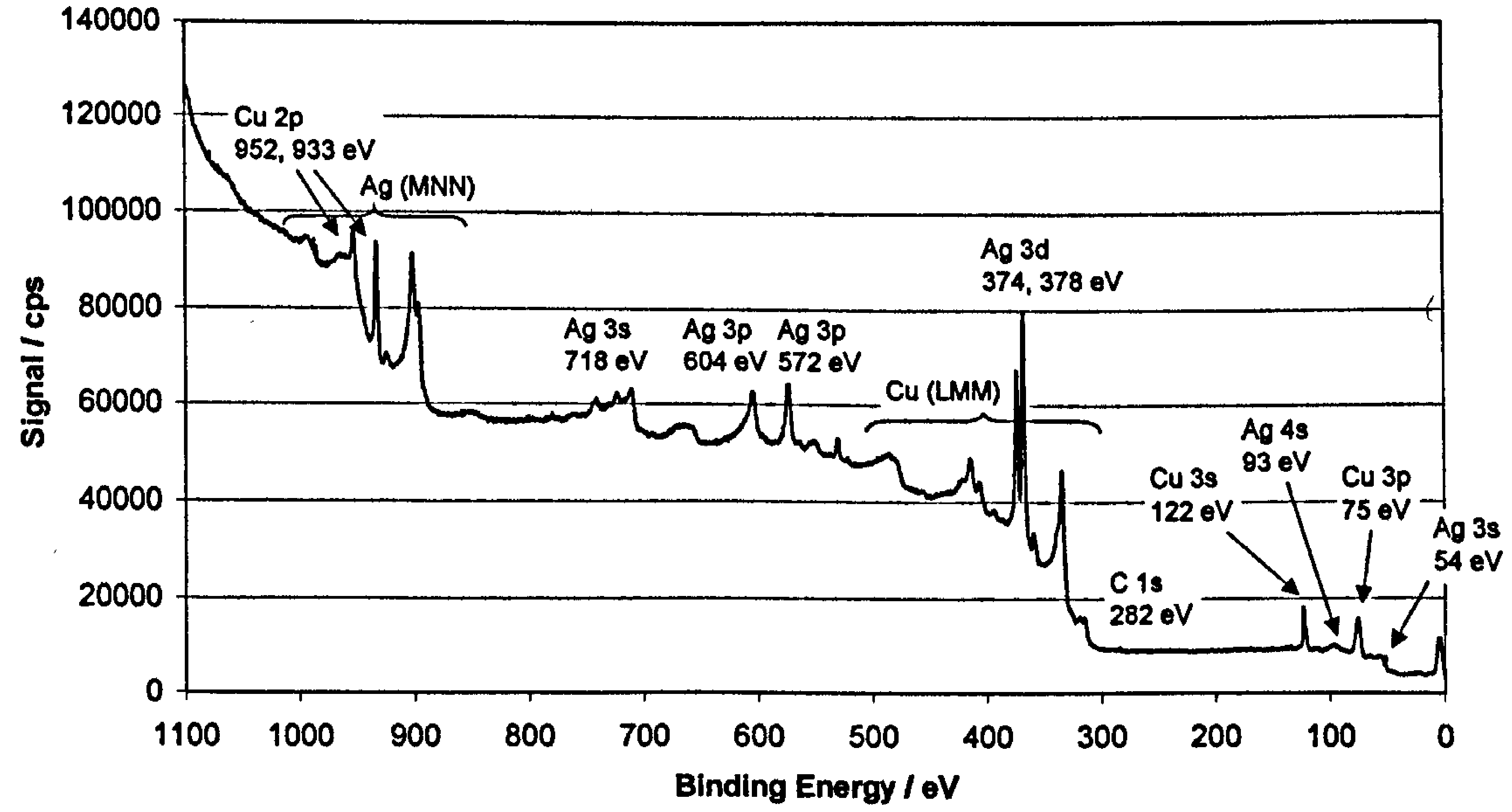

Figure 2.9: Survey spectrum for Ag deposition on an FeO_x covered Cu(111) substrate

2.3 X-ray Photoelectron Spectroscopy (XPS)

In XPS the sample is irradiated with monochromatic x-rays inducing a photoelectric effect, whereby core electrons are emitted.[1-7] An electron energy analyser records the kinetic energy (E_K) of the emitted photoelectrons, which is less than the energy of the photons ($h\nu$), due to the energy needed to remove the electron from its core state to the vacuum level - this includes the binding energy (E_B) of electrons to the atoms and the workfunction (Φ) between the Fermi level and vacuum level. Thus:

$$E_B = h\nu - E_K - \Phi \qquad (2.1)$$

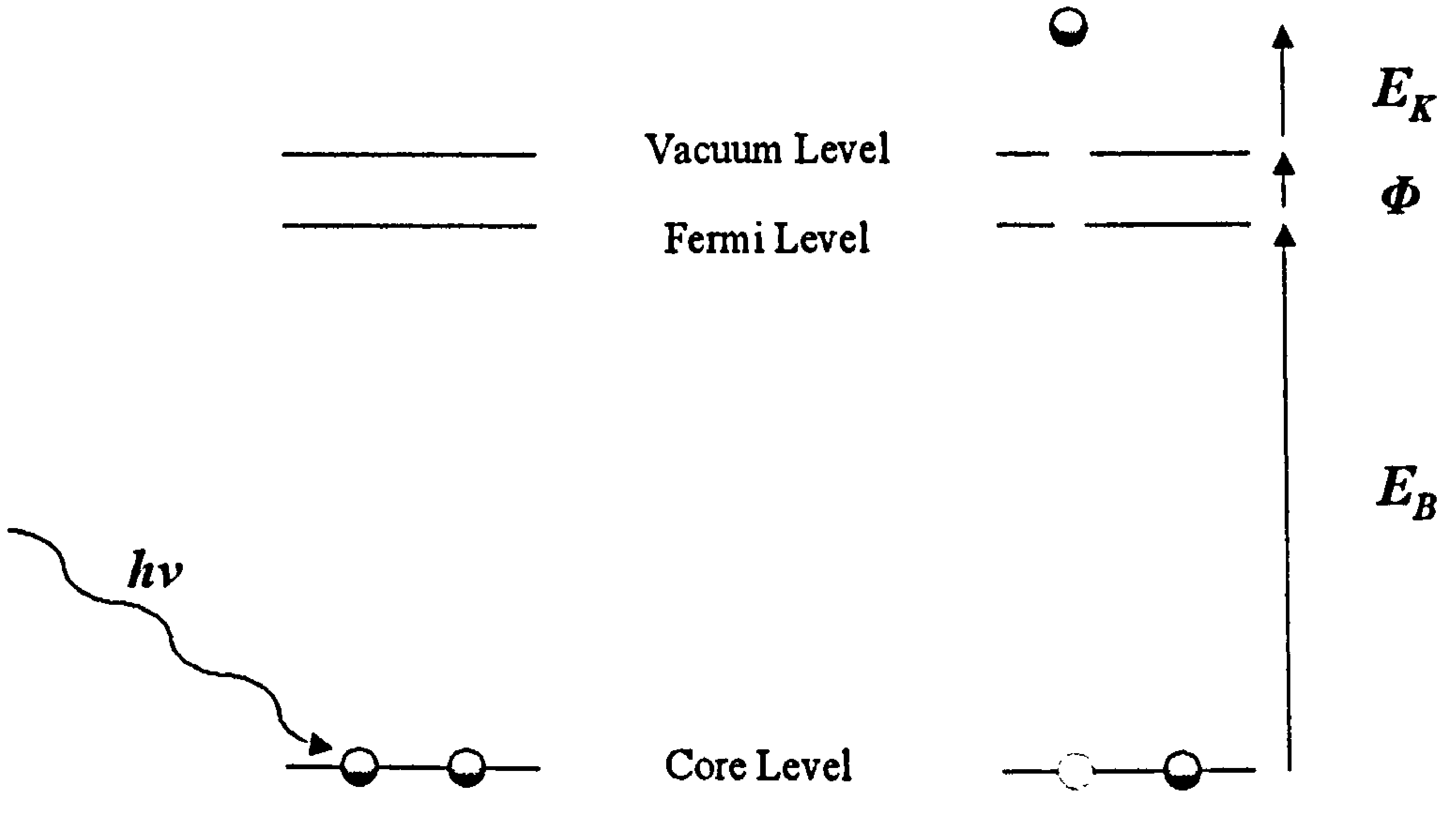

Figure 2.10: Electron energy level diagram for the XPS process

This technique is inherently surface sensitive since the kinetic energies of the emitted photoelectrons are low, thus photoelectrons emitted from nearer the surface have a greater probability of reaching the detector without loss of kinetic energy through inelastic scattering. The inelastic mean free path of a photoelectron, λ, is dependent upon the nature of the solid through which it traverses and the kinetic energy the electron possesses.

Firstly, peaks at particular binding energies relate to the characteristic energy levels in different atoms and XPS thereby provides a qualitative elemental analysis of the sample. Secondly, XPS is quantitative, since the area under the peaks is proportional to the amount of each element present in the surface region. However, in order to compare the concentration of elements it is necessary to know the atomic sensitivity factors and to account for a variety of instrumental factors. Because XPS is a surface sensitive technique, the signal intensity also varies depending on the depth distribution of the element. Finally, the precise binding energy values are subject to "chemical shifts", which arise from (and give information on) the chemical environment of the atom and its oxidation state.

The binding energy of a particular electron is equal to the difference in energy between the initial state (the atom with n electrons) and the final state (the ion with $n - 1$ electrons).

$$E_B = E_f(n - 1) - E_i(n) \qquad (2.2)$$

The binding energy can be influenced by both initial-state and final-state effects. Chemical shifts are generally regarded as being the result of initial state effects caused by chemical bonding influencing the electronic configuration of the atom and its environment. Usually the binding energy increases with increasing oxidation state due to increased electrostatic attraction between the atom or ion and outgoing photoelectron. Electronegative substituents have a similar effect.

Since the energy of a particular electronic state is partly determined by angular momentum coupling, any final state with an unpaired electron with $l > 0$ exhibits spin-orbit splitting, where it is split into two states relating to $j = l \pm \frac{1}{2}$, thus giving rise to a doublet in the spectrum. There are also a number of final state effects that give rise to satellite features. Multiplet splitting is the consequence of spin–spin interactions between an unpaired electron in an ionised orbital and any other unpaired electrons in the outer shells of the atom. Shake-up satellites result from the loss of kinetic energy from the emitted photoelectron as it excites a valence electron to a previously unoccupied state (*e.g.* formation of an electron-hole pair in metals). Therefore a shake-up feature lies to the high binding energy side of the main peak.

The two essential components in XPS are the x-ray source (commonly twin-anode) and the electron energy analyser (commonly a concentric hemispherical analyser). Typically Mg K$\alpha_{1,2}$ x-rays are used which have a photon energy of 1253.6 eV). XPS is normally carried out in a high vacuum, preferably better than 10^{-7} Torr - a significant pressure would cause scattering of the photoelectrons as they travel from surface to the detector and the x-ray source can be damaged by operation at higher pressures.

For the purpose of x-ray photoelectron spectroscopy (XPS) the system used in the experiments detailed in this work was equipped with a VG CLAM-2 concentric hemispherical analyser with single-channeltron detector system. The photoelectron emission was stimulated by Mg $K\alpha$ radiation from a single-anode x-ray source. The XPS control unit was interfaced to a data acquisition program (VGX900) allowing the collection of experimental data under PC control and its subsequent manipulation and interpretation in Microsoft Excel. The core electron binding energies were calibrated with respect to the Cu $2p_{3/2}$ peak and the Cu 3p peak (binding energies 932.66 eV and 75.13 eV respectively)[2] of the clean Cu(111) substrate. The electron emission angle, θ_e, (angle between detector and sample normal) was typically 15° (*i.e* near-normal emission). However, measurements involving the study of adsorbed species were carried out with an emission angle of 75° (grazing emission) to increase the sensitivity for species on the surface. For angle-resolved XPS measurements (AR-XPS) take-off angles of 15°, 75° and sometimes 45° were employed. Since the detector position is fixed, different emission angles were achieved by rotating the sample. The angle between the x-ray source and the detector was 70°.

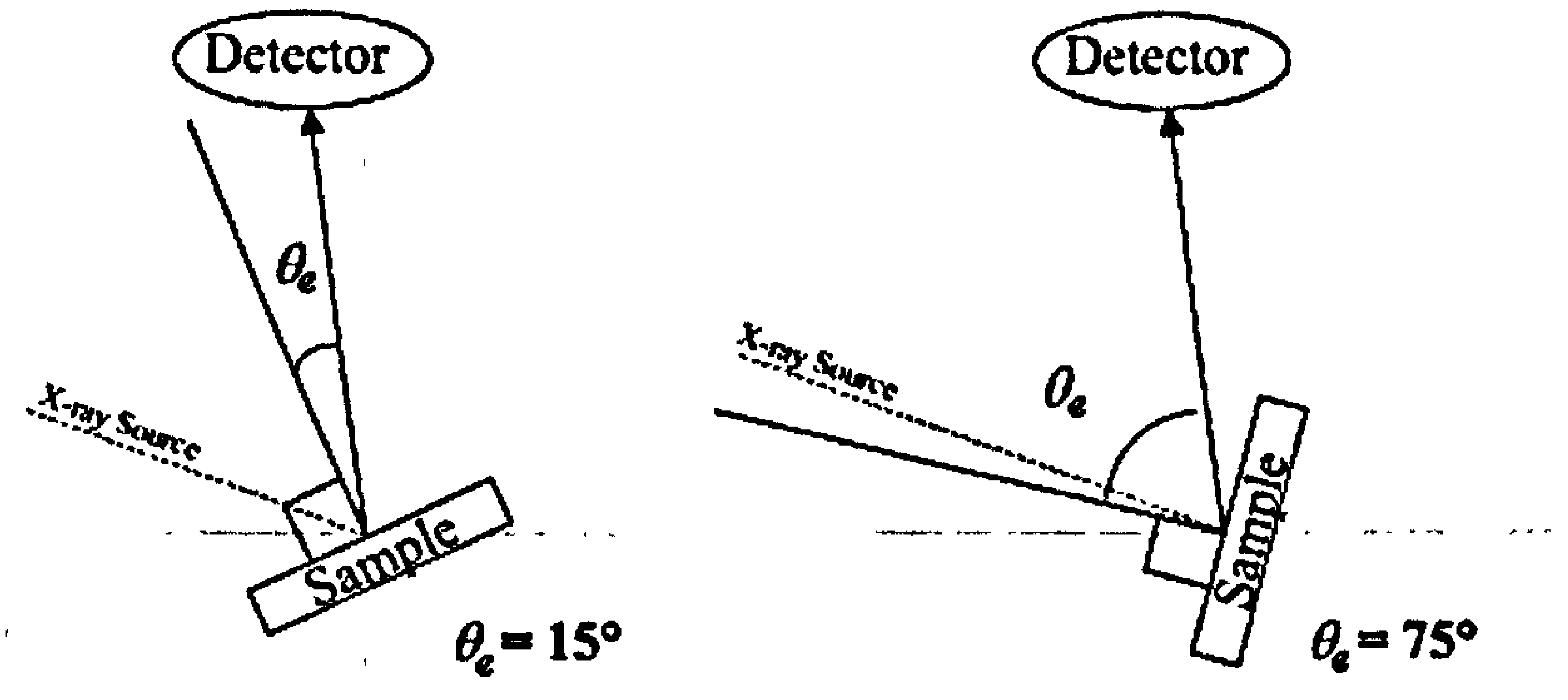

Figure 2.11: The electron emission angles

The factors that affect the relative signal intensity for a particular XPS peak at different emission angles are complicated and include the kinetic energy of the emitted photoelectron and the thickness of the film. A modelling program was used to assess these factors when drawing conclusions as to the relative concentrations of different elements at the surface compared to the sub-surface layers of the film *e.g.* if the film is oxygen-terminated. In addition to a survey scan (0 eV – 1100 eV) it was customary to record at higher resolution the O 1s region, the C 1s region and the strongest peak from the metal system being studied (Cr, Ba, Ti, Fe or Ag). The typical parameters used in XPS measurements are presented in the following tables.

Chapter 3 – Chromium oxide

Region	**Range / eV**	**Steps / eV**	**Scans**	**Dwell Time / s**	**Pass Energy / eV**
O 1s	525-538	0.15	4	0.4	50
Cu 2p	928-938	0.1	4	0.1	20
C 1s	282-297	0.15	8	0.4	50
Cr 2p	567-597	0.15	4	0.2	50
Survey	0-1100	0.5	2	0.1	100

Chapter 4 – Barium oxide

Region	**Range / eV**	**Steps / eV**	**Scans**	**Dwell Time / s**	**Pass energy / eV**
O 1s	527-537	0.15	4	0.8	50
Cu 2p	929-937	0.1	4	0.2	20
C 1s	282-297	0.2	4	0.4	100
Ba 3d	775-790	0.2	4	0.2	50
Survey	0-1100	0.5	2	0.1	100

Chapter 5 – Titanium oxide

Region	**Range / eV**	**Steps / eV**	**Scans**	**Dwell Time / s**	**Pass energy / eV**
O 1s	528-538	0.15	4	0.8	50
Cu 2p	929-937	0.1	4	0.2	20
C 1s	282-297	0.2	4	0.4	100
Ti 2p	448-470	0.2	4	0.8	50
Survey	0-1100	0.5	2	0.1	100

Chapter 6 – Iron oxide and silver nanoparticles

Region	**Range / eV**	**Steps / eV**	**Scans**	**Dwell Time / s**	**Pass energy / eV**
O 1s	528-538	0.15	4	0.4	50
Cu 2p	929-937	0.1	4	0.2	20
C 1s	282-297	0.2	4	0.4	100
Fe 2p	702-732	0.2	4	0.2	50
Ag 3d	365-380	0.1	4	0.4	50
Ag MVV	893-913	0.15	4	1.6	50
Survey	0-1100	0.5	2	0.1	100

2.4 Low Energy Electron Diffraction (LEED)

In LEED a beam of well-defined low energy electrons (20-200 eV) are incident normally-upon the surface.[3,4,6-9] The electrons are back-scattered by regions of high electron density *i.e.* surface atoms and detected on a fluorescent screen. Due to the principles of wave-particle duality, electrons can be considered as waves and furthermore at the energies employed in LEED the corresponding wavelength is comparable to atomic spacing - thus diffraction effects associated with atomic structure can be observed. The electron wavefront is scattered by the surface atoms in all directions. However due to the path difference (*d*) between the scattered waves from adjacent atoms, the electron waves will interfere constructively or destructively at the detector depending on the scattering angle (θ).

$$d = a \sin\theta \tag{2.3}$$

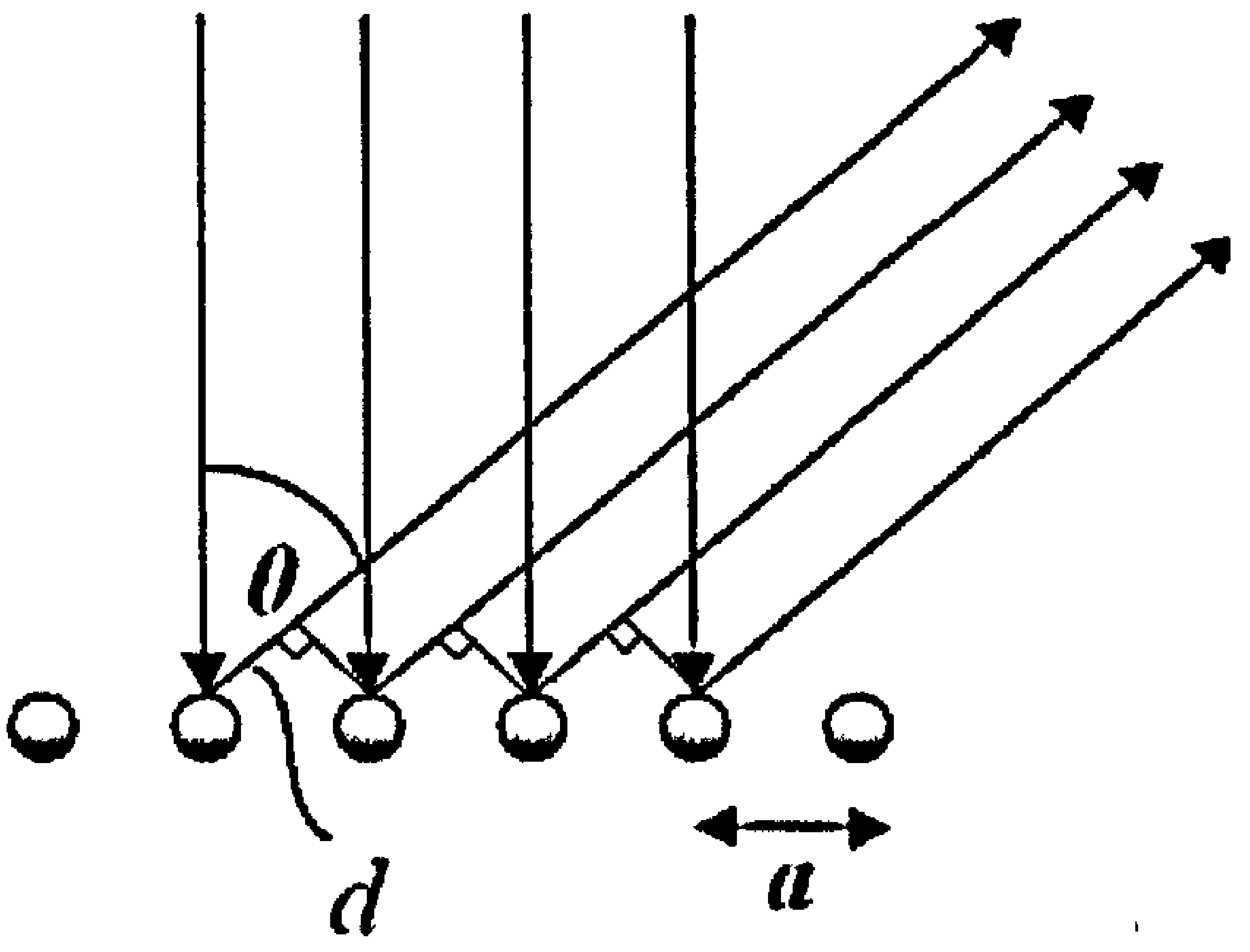

Figure 2.12: Schematic representation of LEED

Constructive interference will occur when the path difference is equal to an integer number of wavelengths (λ) and the intensity will only be significant when the Bragg condition (see equation 2.4) is satisfied exactly.

$$a \sin\theta = n.\lambda \tag{2.4}$$

Providing the sample exhibits long-range ordering a diffraction pattern is created. The diffraction patterns, evident as a series of "spots" on the fluorescent screen, show symmetry relating to the surface structure, are centrally symmetric and distances between the spots are the reciprocal of the spacings in real space. Clearly in the case where the sample is disordered or amorphous, there will be no spots but a diffuse background.

At the centre we observe the so called 00 spot, where n = 0. Outside this we see the first order spot, where n = 1. Whether we can see spots of other order may depend upon the beam energy. At higher beam energy the pattern displayed on the screen appears to contract, because at higher energy the wavelength is less and the angle θ, where n = 1 is smaller. This technique provides qualitative information on the size, symmetry and rotational alignment of an adsorbate unit cell relative to the substrate unit cell. The real space vectors $\mathbf{a}_1$ and $\mathbf{a}_2$ are mathematically related to the reciprocal space $\mathbf{a}_1$* and $\mathbf{a}_2$* (see equations 2.5 – 2.7)[7] where γ is the angle between the vectors $\mathbf{a}_1$ and $\mathbf{a}_2$.

$$\mathbf{a}_1{}^* = \frac{1}{\mathbf{a}_1 \sin\gamma} \tag{2.5}$$

$$\mathbf{a}_2{}^* = \frac{1}{\mathbf{a}_2 \sin\gamma} \tag{2.6}$$

$$\sin\gamma = \sin\gamma^* \tag{2.7}$$

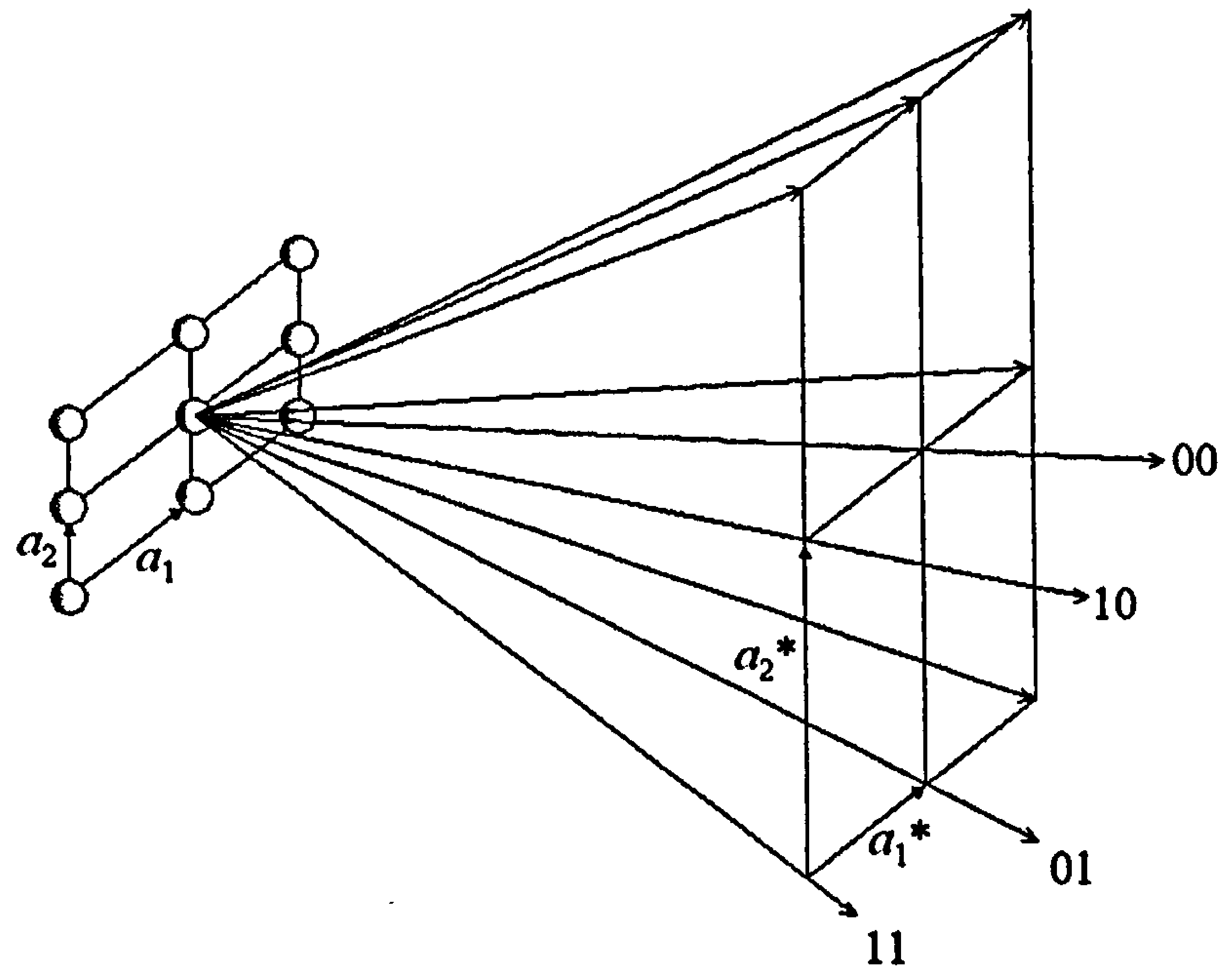

Figure 2.13: Relationship of real space and reciprocal space vectors

Since this technique involves electrons moving between the sample and detector, LEED must be carried out in ultra-high vacuum conditions to avoid scattering of the electrons by molecules in the gas phase (<10^{-7} Torr would actually be satisfactory). The electron gun produces low energy electrons. These electrons may be diffracted (elastically scattered) or may be inelastically scattered. In LEED only the elastically scattered electrons are of interest. The electrons pass through a series of hemispherical grids positioned before the phosphor screen. The sample and first grid are earthed so that the electrons traverse a field-free region after being diffracted from the surface. A negative potential is applied to the second and third grids so as to repel (filter out) the secondary electrons. The remaining electrons are then accelerated towards the phosphor screen, upon which a high voltage (typically 4-5 kV) is applied. When the electrons strike the phosphor, photons are emitted which we see as spots. The image is typically caught on photographically. The instrumentation can be either front-view or rear-view.

The system used in these experiments was equipped with Omicron 3-grid reverse view low energy electron diffraction (LEED) optics with integral electron gun. LEED patterns were recorded using a digital camera. Figure 2.14 shows LEED patterns of the clean Cu(111) substrate at various beam energies.

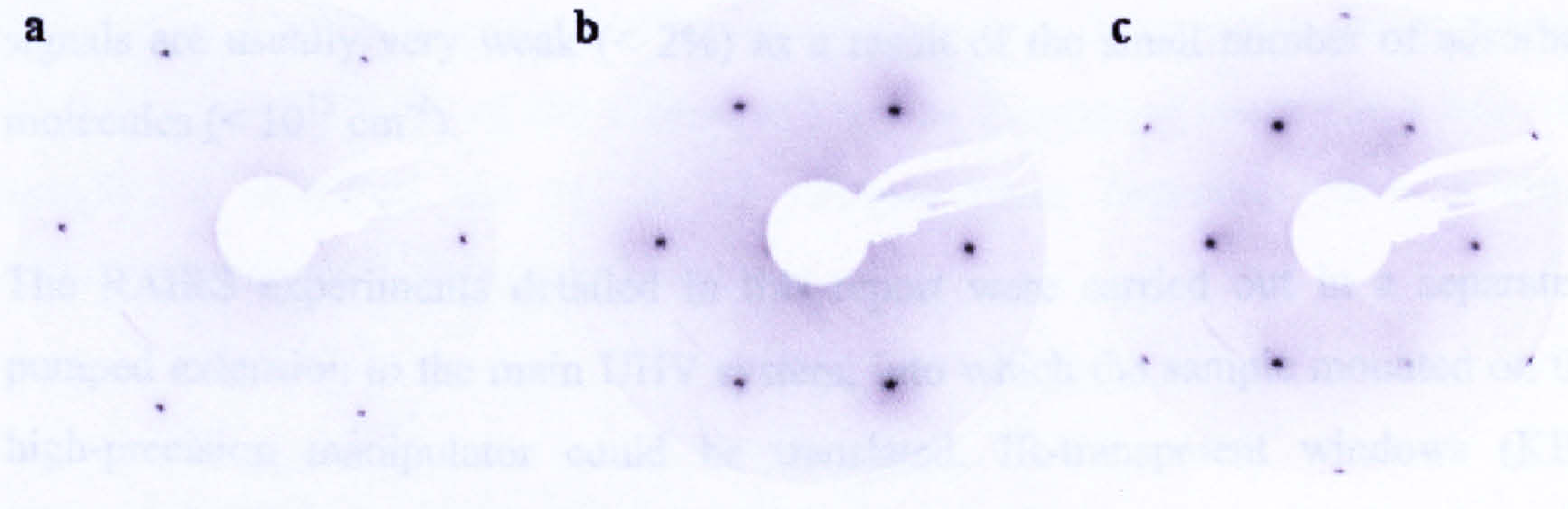

Figure 2.14: LEED patterns for the Cu(111) substrate at beam energy a) 78 eV; b) 135 eV; c) 176 eV

2.5 Reflection Absorption Infrared Spectroscopy (RAIRS)

Vibrational spectroscopy can be implemented in a number of ways for the study of species adsorbed on solid surfaces. Reflection absorption infrared spectroscopy (RAIRS or IRAS as it is sometimes called) is one example in which an infrared beam is specularly reflected off a highly reflective surface at grazing incidence.[3,4,6-8]

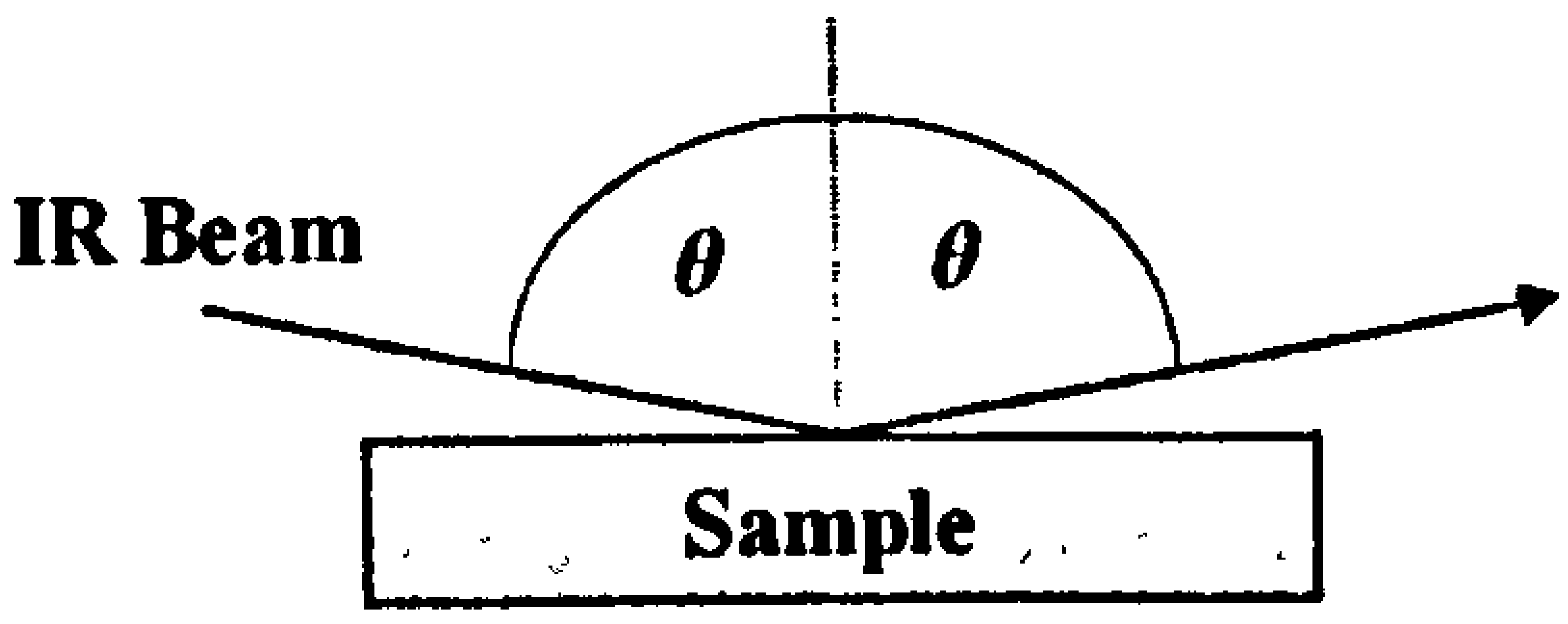

Figure 2.15: Specular reflection of IR light at grazing incidence off a metallic sample

As in other forms of infrared spectroscopy the light reaching the IR detector is found to have reduced intensity at particular frequencies, which relate to modes of vibrational excitation of particular chemical bonds. Typically the instrumentation allows analysis in the 600 cm^{-1} – 3600 cm^{-1} range, where vibrations of the adsorbed molecule, rather than the metal-adsorbate bond are observed. On metal surfaces, only molecular vibrations giving rise to an oscillating dipole with a component that is perpendicular to the surface will be IR active, in accordance with the surface dipole selection rule. This can be explained by the fact that metals can only support an electric field perpendicular to their surfaces due to the image dipole effect. The signals are usually very weak (< 2%) as a result of the small number of adsorbed molecules (< 10^{15} cm^{-2}).

The RAIRS experiments detailed in this report were carried out in a separately pumped extension to the main UHV system, into which the sample mounted on the high-precision manipulator could be translated. IR-transparent windows (KBr) allowed the light to pass from source to detector with grazing reflection from the sample surface. The instrumentation consisted of a Mattison RS2 Fourier-transform IR (FTIR) spectrometer and a narrow-band mercury-telluride detector. In some of the RAIRS experiments it was necessary to cool the sample to sub-ambient temperature in order to study the adsorption of gases. Cooling was achieved by passing a constant flow of liquid nitrogen through the cooling tubes of the sample probe. Temperatures approaching 123 K were obtainable.

2.6 Temperature Programmed Desorption (TPD)

TPD is a technique for studying the adsorption of molecules on surfaces.[3,4,6,8] This involves the adsorption of a particular gas (or gas mixture) on the sample surface and then controlled heating (ideally linearly) of the surface, whilst simultaneously monitoring any gaseous species desorbing from the surface. Typically a quadrupole mass spectrometer is used for detection of evolving species. Effectively this records the intensity of different mass fragments as a function of temperature. The desorption of different species give rise to desorption peaks. There is a wealth of information that can be inferred from this data. The peak area is proportional to the initial surface coverage and the temperature at which desorption occurs is related to the strength of binding to the surface. It is possible to distinguish between molecular and dissociative adsorption, and between different adsorbed states. In some cases where molecules are dissociatively adsorbed, there may be surface reactions such that the species which are evolved differ from those adsorbed. Again this provides important information on the surface chemistry, but this is usually referred to as temperature programmed reaction spectroscopy (TPRS).

In the experiments detailed in this report, gases were dosed from the gas line into the main chamber through a leak valve, whilst monitoring the pressure on the ion gauge. All TPD experiments were typically run with the mass spectrometer (VG Quadrupole Micromass 200D) ion source positioned approximately 5 mm above the sample, to optimise the sensitivity of the technique towards desorption components from the sample. A selection (up to 15) of relevant mass fragments were recorded simultaneously with thermocouple data.

2.7 Data Analysis Procedures

2.7.1 Determination of XPS Peak Intensities

Peak intensities were normally estimated manually as the difference between the top of the peak and a linear baseline projected under the peak (see Figure 2.16).

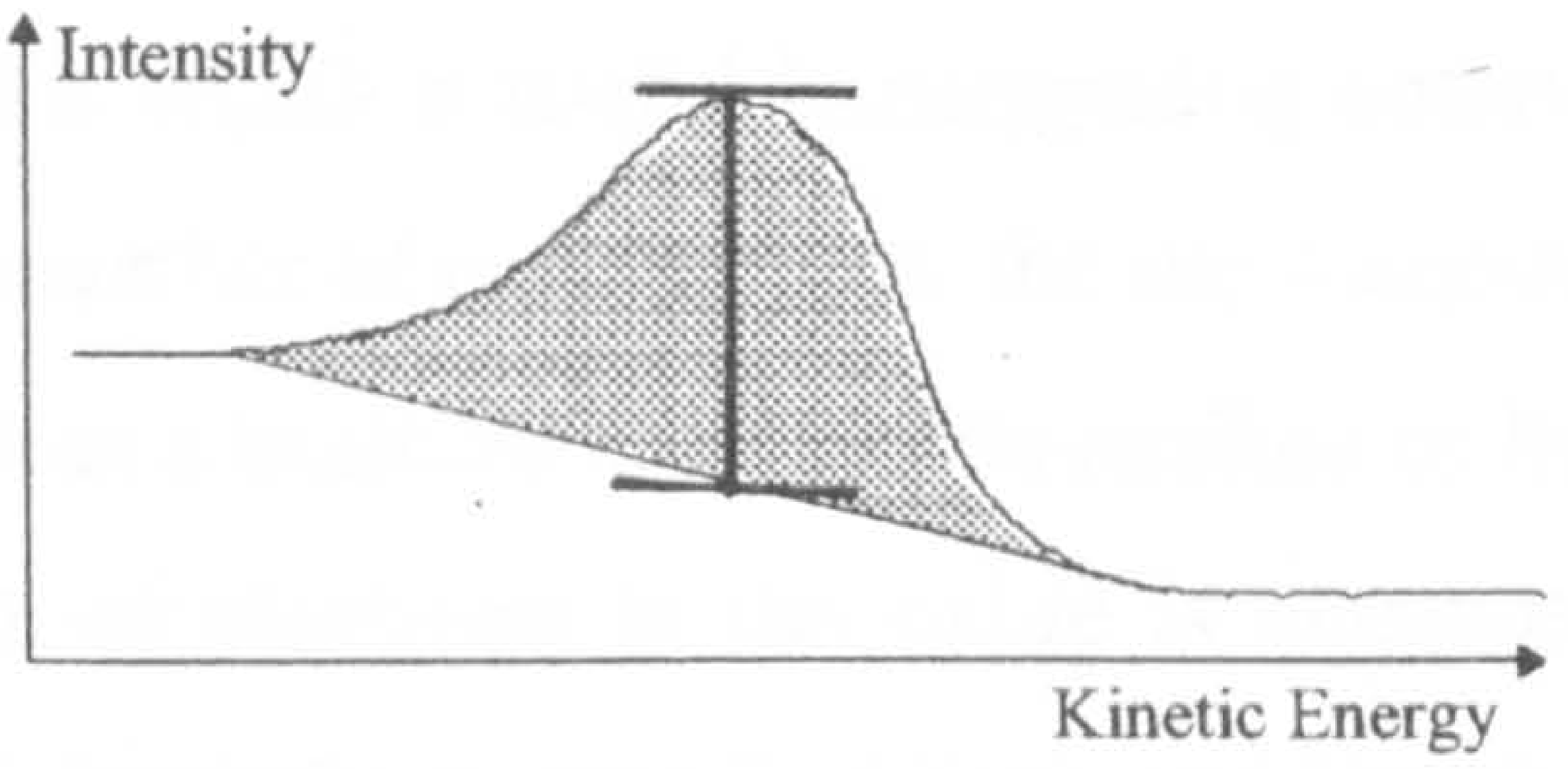

Figure 2.16: Estimation of peak height.

This method provided a satisfactory estimate of the peak intensities for O 1s, Cu 2p, Cr 2p, Ba 3d, Ti 2p, Fe 2p, Ag 3d and C 1s peaks. In cases where more accurate determination was required (*e.g.* for calculating stoichiometries) peak areas were calculated using a fitting program, normalised for experimental parameters (*e.g.* dwell time) and corrected using atomic sensitivity factors.[2] In principle using peak areas provides a more accurate estimation of the peak intensity, particularly for peaks subject to changes in shape due to factors such as chemical environment. The main application of the estimated peak intensities was the use of the Cu 2p peak intensities for oxide film thickness estimation (detailed in section 2.7.2). For this purpose, peak heights were certainly sufficient, as the Cu substrate was not subject to any chemical change and retained the same Cu $2p_{3/2}$ peak shape throughout.

2.7.2 Determination of Film Thickness

The oxide layer thickness, *d*, was estimated from the attenuated Cu $2p_{3/2}$ signal using the following formula:

$$d = -\lambda.\cos\theta.\ln\left(\frac{I}{I_0}\right) \qquad (2.8)$$

Where, λ is the inelastic mean free path of Cu $2p_{3/2}$ electrons in the oxide,
θ is the angle of the detector from the sample normal,
I/I_0 is the ratio of the reduced peak intensity exhibited by the oxide-covered surface to the peak intensity of the clean Cu substrate.

For Cu $2p_{3/2}$ emission stimulated by Mg K_α radiation, the inelastic mean free path (λ) of the photoelectrons in an element is taken to be 0.97 nm and for an oxide around 1.72 nm.[10]

It is important to appreciate that the above calculation is nothing more than an estimate of film thickness which is useful in comparing otherwise similar films. This estimate is subject to a number of assumptions, the most important being:

1. The oxide is present as a uniform layer on the surface of the copper substrate.
2. The mean free path of electrons in the oxide is adequately represented by the value taken from the "universal curve" of Seah and Dench.[10]

Such estimates of film thickness are also very dependent upon the reproducibility of the XPS data collected over quite extended periods.

2.7.3 Determination of Lattice Cell Constants from LEED Data

The LEED pattern dimensions $\mathbf{a}_1^*$, $\mathbf{a}_2^*$ and $\mathbf{b}_1^*$, $\mathbf{b}_2^*$ are the reciprocal of the real space vectors $\mathbf{a}_1$, $\mathbf{a}_2$ and $\mathbf{b}_1$, $\mathbf{b}_2$. It is known that the lattice cell constant of the Cu(111) surface is 2.556 Å. Providing that the Cu substrate spots are observable and identifiable, it is possible to calculate the real space dimensions of the oxide unit cell. A simple example is shown in Figure 2.17 of an oxide with hexagonal symmetry.

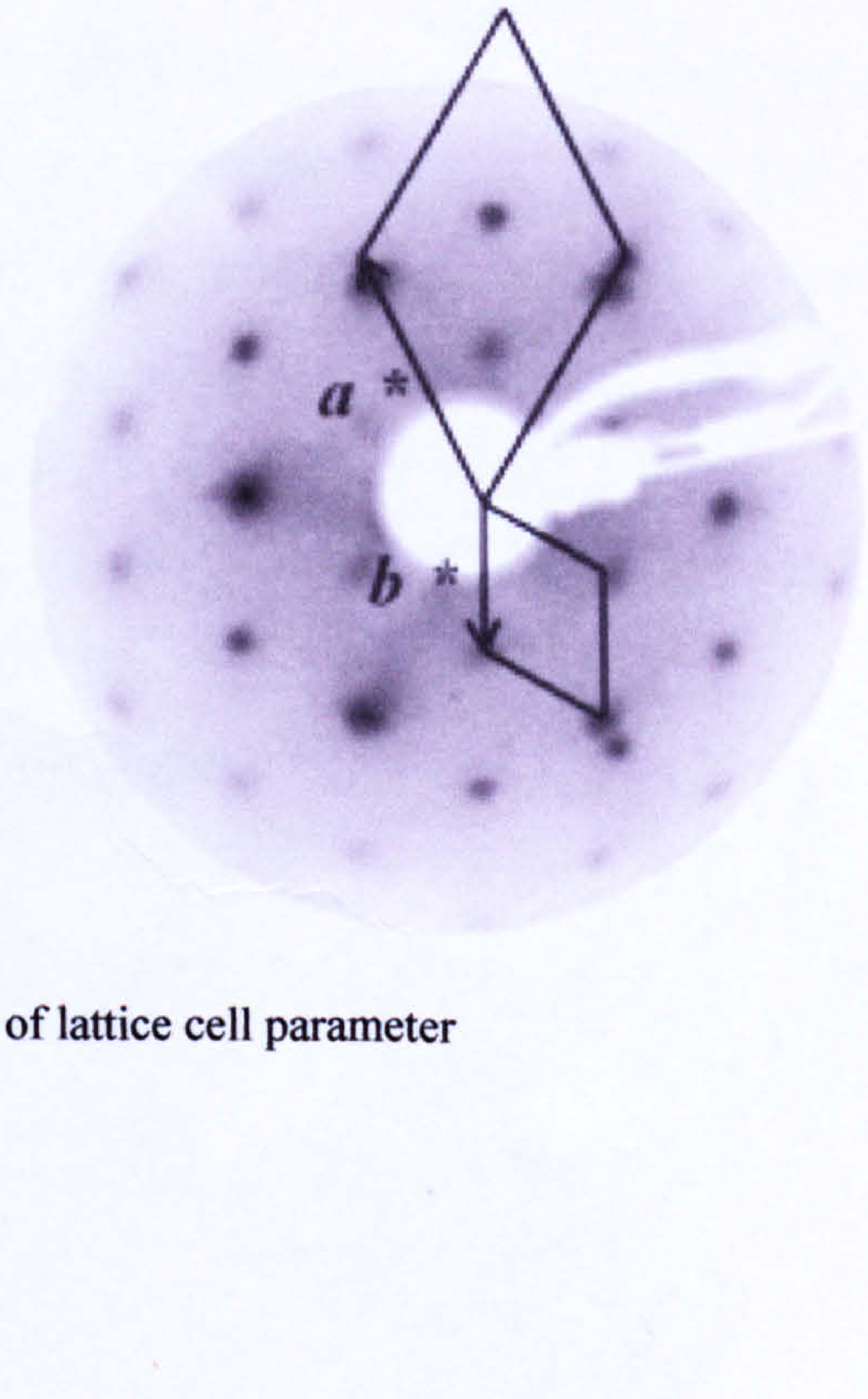

Figure 2.17: Determination of lattice cell parameter

$$\mathbf{b} = \frac{2.556\ \text{Å}}{(\mathbf{a}^*)^{-1}} \times (\mathbf{b}^*)^{-1} \qquad (2.9)$$

References

1 G.E. Mullenberg, *Handbook of X-ray Photoelectron Spectroscopy*, 1979, Perkin-Elmer

2 D. Briggs and M.P. Seah, *Practical Surface Analysis, 2nd Edition, Volume 1 – Auger and X-ray Photoelectron Spectroscopy*, 1990, Wiley

3 J.W. Niemantsverdriet, *Spectroscopy in Catalysis: An Introduction*, 2000, Wiley

4 G. Attard and C. Barnes, *Surfaces (Oxford Chemistry Primer; no. 59)*, 1998, Oxford University Press

5 J.M. Walls, *Methods of Surface Analysis*, 1989, Cambridge University Press

6 D.P. Woodruff and T.A. Delchar, *Modern Techniques of Surface Analysis*, 1986, Cambridge University Press

7 K.W. Kolasinski, *Surface Science Foundations of Catalysis and Nanoscience*, 2002, Wiley

8 E.M. McCash, *Surface Chemistry*, 2001, Oxford University Press

9 G. Ertl and J. Küppers, *Low Energy Electrons and Surface Chemistry*, 1985, Weinheim

10 M.P. Seah and W.A. Dench, *Surf. Interface Anal.* 1979, 1, 2

Chapter 3:

Growth & Characterisation of CrO_x/Cu(111)

3.1 Literature Review of CrO_x Surface Science Studies

There are many important catalytic applications involving the transition metal oxide chromium(III) oxide, Cr_2O_3, (usually modified – either promoted or supported) and this has led to a considerable amount of research.

3.1.1 Motivation for Surface Science Studies

Supported chromium oxide has been found to be active in the **catalytic dehydrogenation** of alkanes to alkenes and this has received a lot of attention from researchers as an alternative to the thermal cracking process which has a number of disadvantages. This subject dominates the literature reflecting the growing demand for alkenes and the recent need for isobutene used in the synthesis of MTBE (methyl tertiary-butyl ether). In industrial applications the catalyst (usually $Cr_2O_3/\gamma\text{-}Al_2O_3$ modified by alkali ions, often potassium) is rapidly deactivated and so must be reactivated in an oxidising atmosphere, which is carried out in cycles.[1] Recently the activity for supported chromium oxide catalysts has been demonstrated in many research articles for dehydrogenation of ethane,[2-4] propane[4-6] and iso-butane.[4,7-9] Issues addressed include deactivation, mechanism of catalysis and obtaining a selective yield (*i.e.* favouring the dehydrogenation product over oxides of carbon). While the industrial catalyst in common use is alumina-supported, research suggests that zirconia-supported catalysts may be superior.[2,5] The higher activity of ZrO_2-supported chromium oxide was rationalised in terms of active Cr^{3+} sites arising from reduction of Cr^{5+} abundant in the chromia-zirconia system. Despite the amount of research on this subject, there is much controversy regarding the active sites for dehydrogenation.[1,5,7-9] Most research agrees that Cr^{3+} sites play an important role.

Chromium oxide based catalysts have also been widely researched for **catalytic oxidation**. Many of these are in relation to elimination of environmentally-unfriendly compounds. Oxidation of carbon monoxide to the less damaging carbon dioxide by chromium oxide based catalysts has been the focus of various research articles commonly using copper-modified chromium oxide.[10,11] Other environmental applications of chromium oxide include the selective oxidation of hydrogen sulphide to elemental sulfur by unsupported amorphous chromium oxide and SiO_2-supported chromium oxide,[12] and the oxidative removal of chlorine-containing organic compounds such as trichloroethylene[13] and polychlorinated aromatics.[14]

There are many **other examples of catalytic application** involving chromium oxide to be found in the literature. Methanol synthesis through catalytic hydrogenation of carbon dioxide, ethylene polymerisation and various isomerisation reactions are just a few. However many of these involve chromium oxide as a modifier of other catalytic systems. NO decomposition has been achieved by redox-treated CuO-Cr_2O_3/Mordenite (an aluminosilicate), where the activity has been attributed to copper chromate sites,[15] however, the selective catalytic reduction of NO by ammonia in excess oxygen using chromium oxide catalysts is more well known. It has been widely found[16] that amorphous Cr_2O_3 is very much more active and selective than crystalline α-Cr_2O_3.

Chromium oxide films have been grown and characterised on Cu(110)[17] and Cu(100),[18] by chromium evaporation onto the substrate and oxidation in increments at 673 K. However, to the author's knowledge, there have not yet been any published studies of CrO_x on Cu(111).

3.1.2 Bulk Structure

Chromium oxide occurs naturally as eskolaite (chromium (III) oxide) with the stoichiometric formula Cr_2O_3 and this is by far the most important and widely researched form. Other forms include the synthetically produced chromium (IV) oxide (CrO_2) and chromium (VI) oxide (CrO_3).[19] Chromium (III) oxide, Cr_2O_3, is isomorphous with corundum (α-Al_2O_3), which has the $R\bar{3}c$ (167) space group. The bulk structure can be envisaged as an approximately hexagonal close packed array of oxygen anions (O^{2-}), which possesses octahedral and tetrahedral holes. Two thirds of the octahedral holes are occupied by the chromium cations (Cr^{3+}), which are six-co-ordinated. An alternative perspective is to consider the structure as comprising pairs of face-sharing CrO_6 octahedra linked by edge sharing, stacked along the *c*-axis (see Figure 3.1).[20]

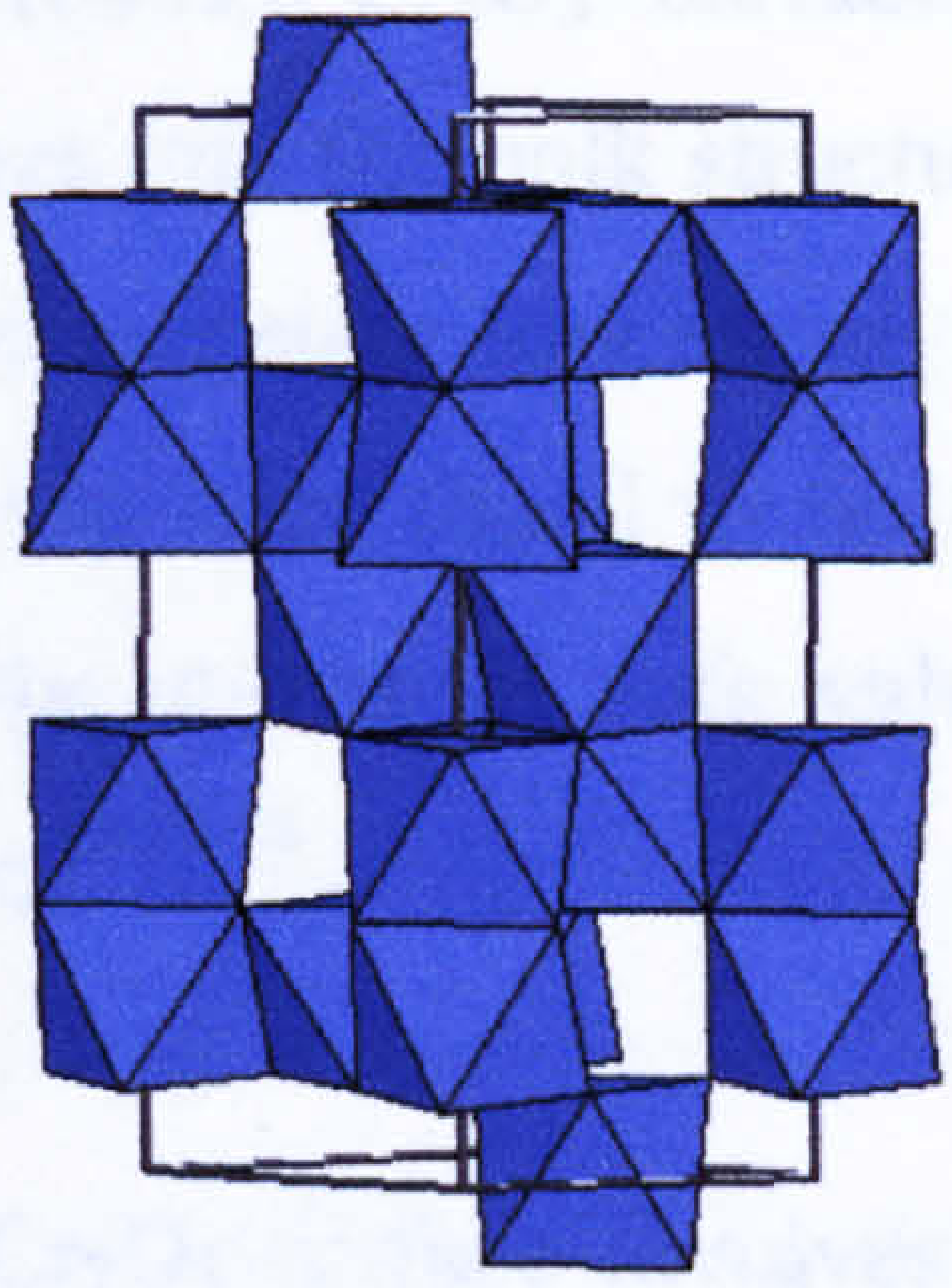

Figure 3.1: Unit cell of chromium (III) oxide[21]

The primitive cell is rhombohedral, but is commonly displayed as the equivalent hexagonal lattice, containing 3 primitive cells. The hexagonal lattice cell parameters have been determined by numerous research groups[22-28] to be $a = b = 4.95$ Å, $c = 13.59$ Å. There is known to be some deviation from ideality in the hexagonally close packed array of oxygen anions[24] and in the chromium sublattice as a result of the filled-filled-unfilled pattern of the Cr^{3+} cations along the *c*-axis.[29]

3.1.3 Surface Structure

The $Cr_2O_3(0001)$ plane is formed by cutting between the buckled Cr layer (see Figure 3.2) effectively giving a half Cr^{3+} layer. This avoids the electrostatically unstable chromium-terminated surface with a full Cr^{3+} layer formed by cutting between the O and Cr layers (to give an oxygen-terminated and a chromium-terminated surface).

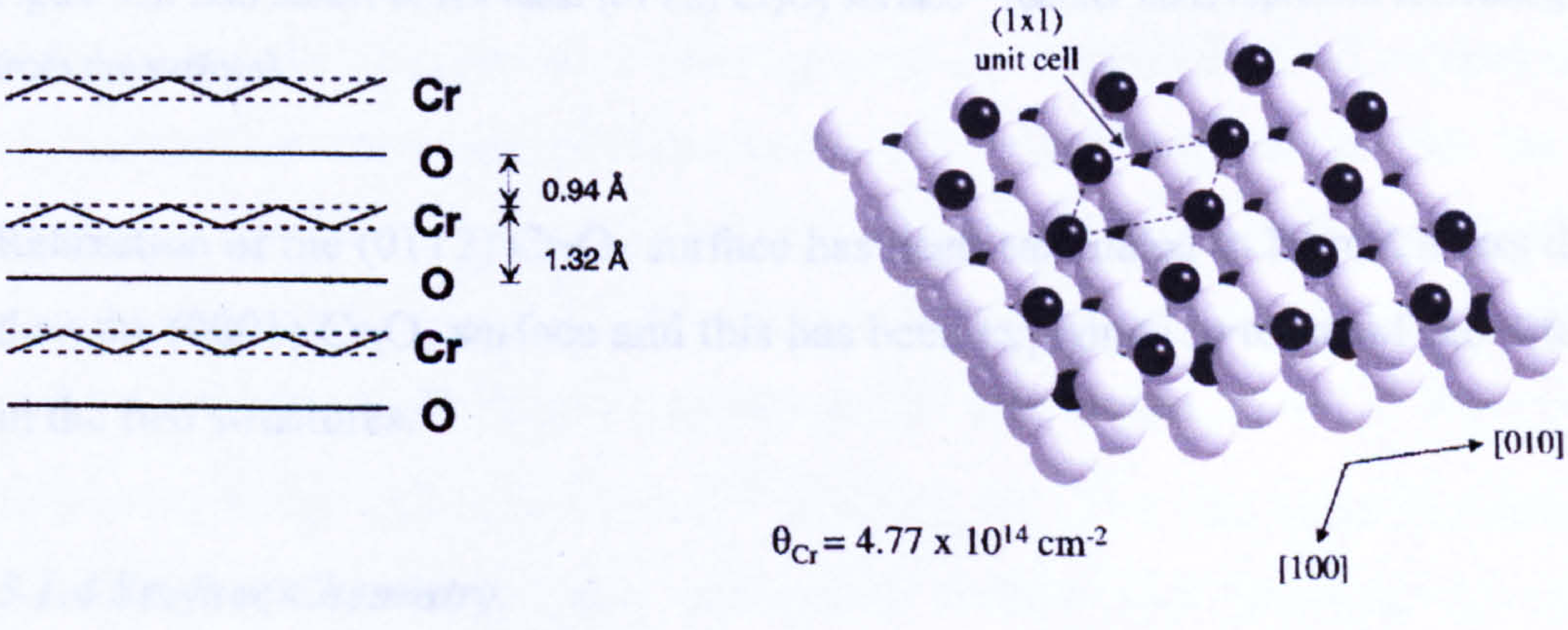

Figure 3.2: Schematic diagram of stacking perpendicular to the (0001) plane[30] (left) and ball model of chromium-terminated (0001) surface viewed from above[31] (right)

In the chromium-terminated (0001) Cr_2O_3 surface, a very pronounced surface relaxation extending a few layers into the bulk structure has been calculated by MD, and this is also supported by quantitative low energy electron diffraction (LEED).[30] The interlayer distances from top were found to be -38%, -21%, +17% and +33%, expressed as a percentage of the unrelaxed bulk values. These general trends have been supported by other studies.[30,32-34]

The formation of the (01$\bar{1}$2) Cr_2O_3 surface involves each Cr^{3+} losing a short Cr-O bond and becoming 5-co-ordinate with two short and three long Cr-O bonds. Although controversial, the (01$\bar{1}$2) Cr_2O_3 surface is believed to be energetically favoured to the (0001) by authors using X-ray diffraction[35], electron microscopy[36] and also theoretical methods.[32] The (01$\bar{1}$2) surface is believed to be the predominantly exposed crystal plane on microcrystalline Cr_2O_3 powders.[36]

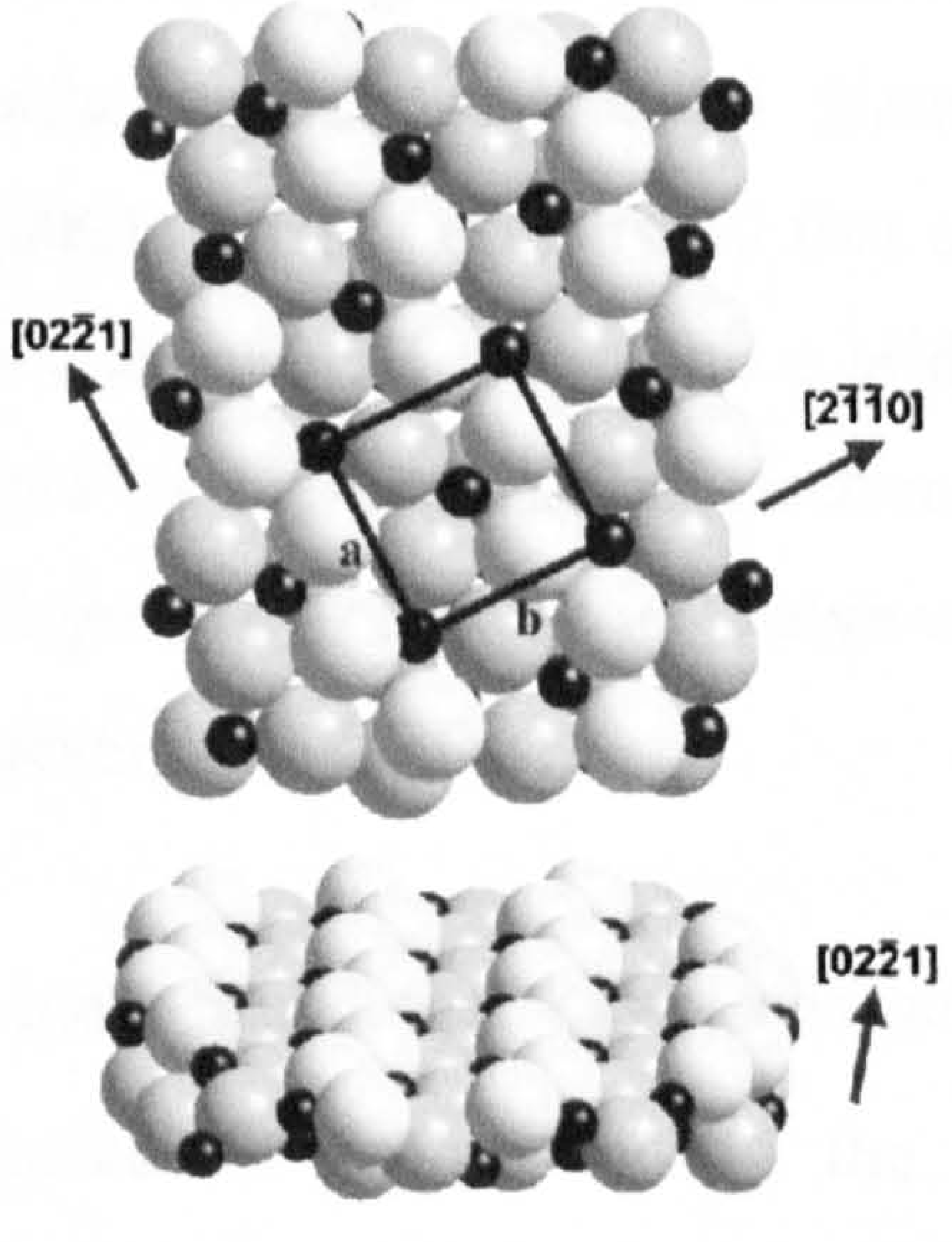

Figure 3.3: Ball model of the ideal (01$\bar{1}$2) Cr_2O_3 surface[37] (darker balls represent increasing distance from the surface)

Relaxation of the (01$\bar{1}$2) Cr_2O_3 surface has been calculated to be much less dramatic than the (0001) Cr_2O_3 surface and this has been explained in terms of the differences in the two structures.[32]

3.1.4 Surface Chemistry

The interaction of **water** with α-Cr_2O_3 is known to result in surface hydroxylation and this has been the subject of a number of research articles, which have addressed various different crystal planes by largely experimental approaches,[31,38-40] but also by theoretical study.[41] In 1971 it was acknowledged that adsorption of water on microcrystalline α-Cr_2O_3 leads to dissociation and hydroxyl groups (evidenced by infra-red spectroscopy).[38] Surface hydroxide groups have been studied on α-$Cr_2O_3(111)$[39] by molecular adsorption of an ice film under ultra-high vacuum (UHV) conditions. Using angle resolved ultraviolet photoelectron spectroscopy (ARUPS) it was found that the OH layer was stable up to 540 K. It was believed that the adsorption occurred only at defect sites. A more recent study[40] looked at hydroxylation by dosing of water on α-$Cr_2O_3(0001)$ films (grown on Cr(110)). Water dissociation resulting in surface hydroxylation was evidenced by XPS. In contrast to the study on $Cr_2O_3(111)$ mentioned above,[39] it was believed from scanning tunnelling microscopy (STM) data that the reaction was not defect specific and that water dissociated on regular sites. Furthermore it was inferred from the resulting disordered surface that there was significant OH-induced surface diffusion and rearrangement of the surface cation and anion planes. Another study[31] also investigating the α-$Cr_2O_3(0001)$ surface established that adsorption results in paired OH groups consisting of a terminal OH group and a bridging OH group which are hydrogen bonded, evidenced by high resolution electron energy loss spectroscopy (HREELS). The paired OH groups recombine to evolve water at 345 K according to temperature programmed desorption (TPD).

A number of IR studies have found that **oxygen** is strongly adsorbed by Cr_2O_3 powders, which are believed to expose mostly the $(01\bar{1}2)$ surface.[42,43] Both dissociative and molecular adsorption of O_2 have been reported in this context. Two states of adsorbed oxygen have been reported - a terminal chromyl oxygen (Cr = O) species and an adsorbate believed to be O^{2-}. It was also shown that the sample pretreatment could influence the type of adsorption (*i.e.* dissociative or molecular). Furthermore it was postulated that dissociative O_2 adsorption occurred at Cr^{2+} sites and that molecular adsorption occurred at Cr^{3+} sites leading to a Cr^{4+}-O_2^- complex[43] In a more recent well-defined study[37] of Cr_2O_3 $(01\bar{1}2)$ it was noted that dissociative adsorption giving an oxygen terminated surface was preferred to molecular adsorption. At 163 K molecular adsorption led to a coverage equivalent to only 2% of the available chromium sites, leading to the belief that adsorption occurred at defect sites. Well-defined Cr_2O_3 (0001) surfaces have also been studied in terms of oxygen adsorption.[44,45] Following O_2 adsorption, molecularly adsorbed O_2 was removed between 110 K and 320 K, and removal of dissociatively adsorbed O_2 did not occur until 800 K.[45]

Adsorption of **CO_2** on a thin $Cr_2O_3(0001)$ film grown on Cr(110) has been investigated utilising IR methods.[46] The researchers have identified four different adsorbed species of which two are strong (believed to be chemisorbed) and two are weak (believed to be physisorbed). The physisorbed species desorbed at 120 K and – 180 K, whereas the chemisorbed species were stable to room temperature. The chemisorbed species were believed to be bent $CO_2^{\delta-}$ species (carboxylates) bound to the surface metal cations. The authors explained the formation of carboxylates as opposed to surface carbonates by the characteristics of the polar $Cr_2O_3(0001)$ surface which is terminated by Cr ions with a reduced charge. A comparison with polycrystalline α-Cr_2O_3 was made and it was found that the IR spectra of the chemisorbates differed; those from the polycrystalline surface were compatible with either a different kind of carboxylate or more likely bidentate surface carbonates formed from CO_2 adsorption on Cr^{3+}-O^{2-} ion pairs. A different earlier study[47] had identified strong chemisorption resulting in bidentate carbonates and bicarbonates and weak chemisorption resulting in organic carbonates, upon CO_2 adsorption on α-Cr_2O_3 with predominately the (0001) face exposed. **CO** adsorption has also been studied.[38] It is believed to chemisorb through formation of weak σ bonds to Cr^{3+} ions.

The surface acidity has been probed by **ammonia** (a Lewis base) by reaction with Lewis acid sites on $Cr_2O_3(0001)$ (grown on Cr(110)).[48] XPS and TPD identified non-dissociated (NH_3) and partially dissociated (NH_2) species. Another study[49] identified NH_3 on Lewis acid sites but also another species involving N-O. **H_2S** adsorption on Cr_2O_3 has been studied with relevance to catalytic poisoning.[50] At 300 K with an exposure of 22 L H_2S, a sulfur coverage of 0.15 ML was realised. At doses of 100 L an XPS peak, believed to be indicative of an SH species, was seen, which disappeared upon annealing at 450 K. Both **NO** and **NO_2** adsorption on a $Cr_2O_3(111)$ film (grown on Cr(110)) were the subject of one study.[51] NO was found to chemisorb, as judged by a desorption maximum of 340 K. NO_2 however adsorbed dissociatively yielding adsorbed NO and oxygen. It was believed that O released in the dissociation process led to oxidation of Cr^{2+} to Cr^{3+} while NO_2 was reduced to NO. An IR study[52] addressed adsorption of **methane** and **hydrogen** on the $(01\bar{1}2)$ and $(11\bar{2}0)$ surfaces of α-Cr_2O_3, finding that both molecules were adsorbed on Cr^{3+} sites.

3.2 Growth in Different Conditions

CrO_x films were grown in a variety of conditions and in particular the technique of XPS was used to characterise the films grown - and thus to assess the effect of the different preparation parameters.

Firstly, film A was grown by Cr metal deposition and then oxidation carried out in small increments, to establish the required O_2 exposure to completely oxidise the base metal. Deposition of chromium was carried out in the manner described in chapter 2 for 5 minutes. The XP spectra of the Cr $2p_{3/2}$, O 1s, Cu $2p_{3/2}$, C 1s regions and a survey scan were recorded before and after deposition. The intensity of the Cu $2p_{3/2}$ peak (see Figure 3.4a) was seen to fall as chromium is deposited and from this a film thickness of 0.34 nm was estimated. Furthermore the appearance of the double Cr 2p XP peaks (see Figure 3.5a) with the $2p_{3/2}$ peak at a binding energy of 574.1 eV were in good agreement with literature values for Cr metal.[53] The oxidation was then carried out in 10 L (200 s at 5×10^{-8} Torr) increments at 673 K and each time the XP spectra recorded until a total exposure of 50 L O_2 had been achieved. The Cu $2p_{3/2}$ peak intensity (see Figure 3.4a) was seen to fall from 0 L to 20 L exposure, but showed no significant variation thereafter. From this an oxide thickness of 1.1 (±0.1) nm was estimated. The film thickness after 10 L O_2 was not calculated, because it was assumed that at this stage the chromium had not been fully oxidised and so there was uncertainty as to the inelastic mean free path (IMFP) of the overlayers. The experimental data suggests that ca. 20 L O_2 is required to oxidise 0.34 nm Cr at 673 K. After the first exposure to 10 L O_2, there was a clear shift in the Cr $2p_{3/2}$ binding energy from 574.1 eV to 576.5 eV (see Figure 3.5a), which was again in excellent agreement with the literature values[53] for oxidised Cr. Furthermore after oxidation there was a change of XP peak shape (the Cr 2p peaks became broader) and the spin-orbit splitting (*i.e.* the gap between the Cr $2p_{3/2}$ and Cr $2p_{1/2}$ components) changed from 9.2 eV to 9.8 eV, which is also in agreement with reference spectra.[53] In the O 1s region there was an increase in the peak area (see Figure 3.4b) which stabilised after about 20 L exposure. With respect to the binding energies (see Figure 3.5b) there was a shift from 530.4 eV after 10 L exposure to 530.1 eV after 20 L, but the peak position was (within experimental error) stable thereafter.

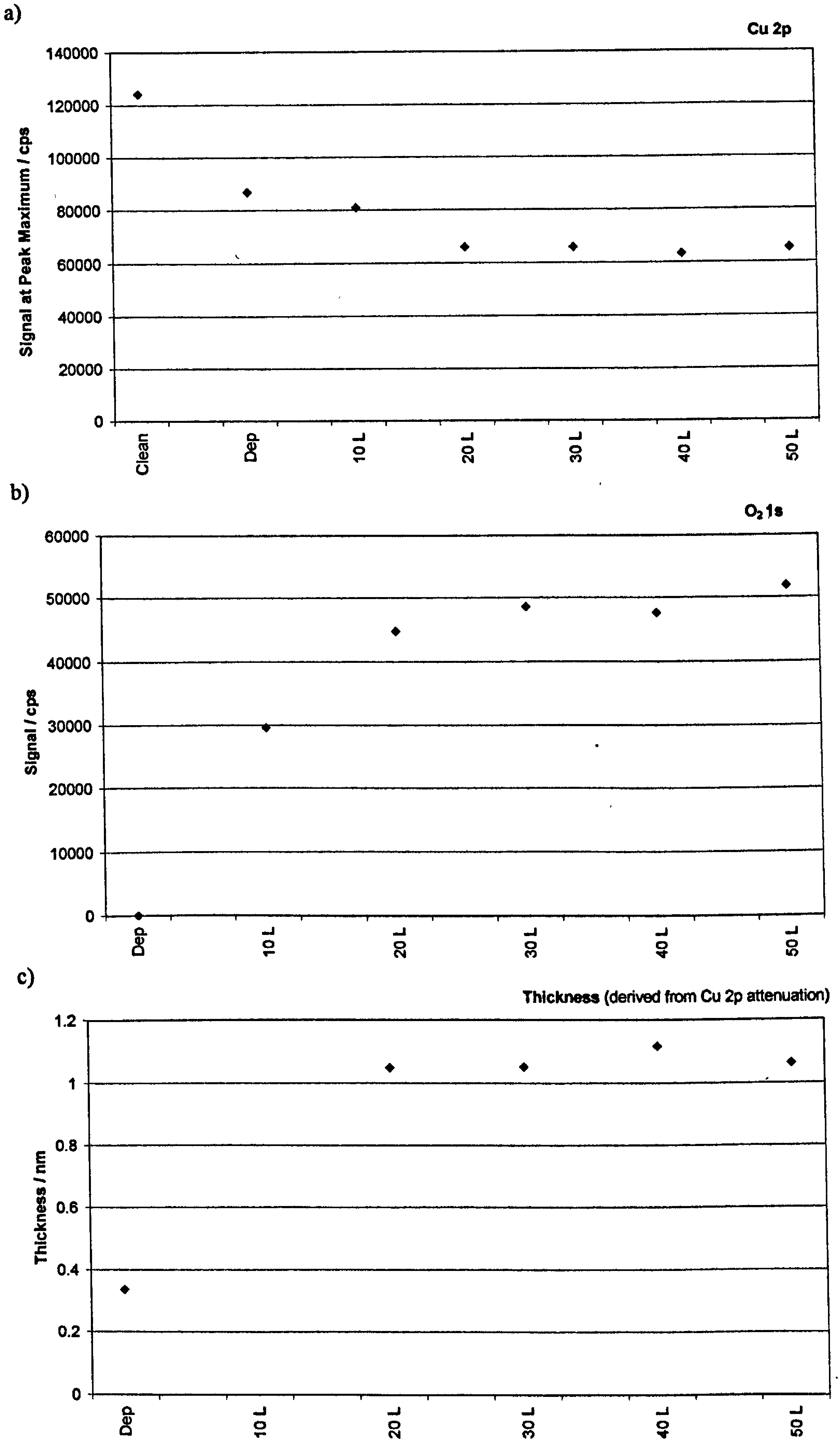

Figure 3.4: XPS data with increasing O_2 exposure a) Peak intensity for Cu $2p_{3/2}$ region; b) Peak area for O 1s region; c) Film thickness; (cps = counts per second; Clean = clean Cu(111) substrate; Dep = after Cr metal deposition)

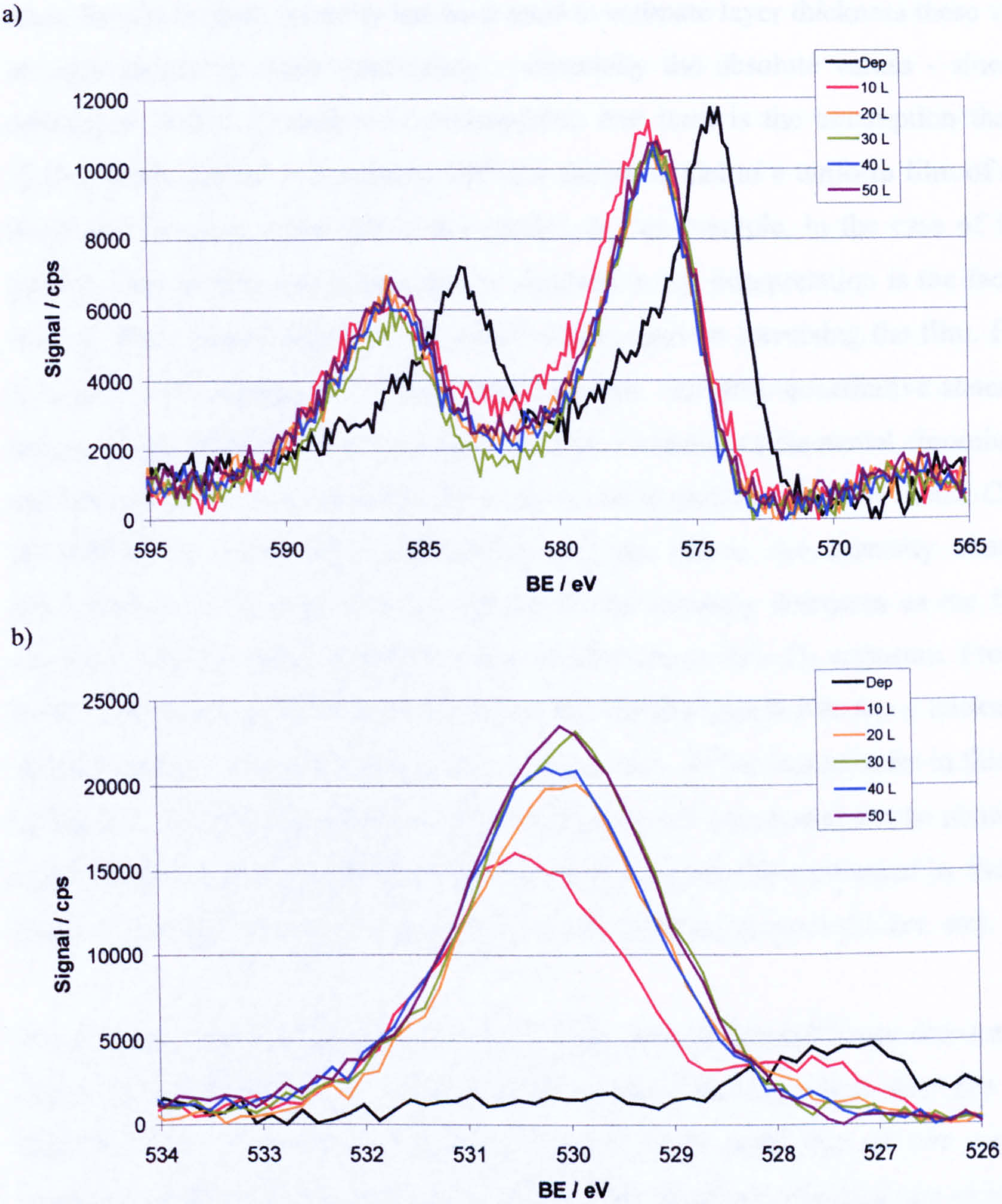

Figure 3.5: XPS data after Cr evaporation and with increasing O_2 exposure a) Cr 2p region; b) O 1s region

A certain amount of caution is required in the interpretation of XPS data. Binding energies are generally well determined by the instrumentation, however peak areas, although well determined by the peak fitting program, have been seen to fluctuate slightly (both from day to day and from measurement to measurement) and this has been attributed to the instrumentation (most likely due to variations in the channeltron sensitivity).

Since the Cu 2p peak intensity has been used to estimate layer thickness these values are also subject to some uncertainty – especially the absolute values - since the calculation makes a number of assumptions. Not least is the assumption that the system being studied is consistent with the simple model of a uniform film of equal thickness. In many cases this is not correct as, for example, in the case of island growth. One further area where care is required in the interpretation is the fact that there is often uncertainty as to the IMFP of the electron traversing the film. Figure 3.4a shows the change in Cu $2p_{3/2}$ peak intensity, but fully-quantitative statements are incorrect, since in one case we have a film consisting of elemental chromium, in another we have the oxide and in between we have partially oxidised metal. Clearly the IMFPs of these films will differ and this effects the intensity observed. Nevertheless the general trend is that the Cu 2p intensity decreases as the film is oxidised, and that this appears to even out after about 20 L O_2 exposure. From the layer thickness estimation it would appear that the final oxide film has a thickness of approximately 1.1 nm. Despite the above discussion on the inaccuracies in thickness estimation, it should be appreciated that whilst precise values may not be obtainable, this method does give sufficient information to compare films prepared by the same method (*e.g.* this film is as thick as that one, those films are much thicker, *etc*).

It has been assumed that since the O 1s peak intensity is relatively constant after about 20 L and the Cu $2p_{3/2}$ peak intensity is also relatively stable after this value, that 20 L O_2 is sufficient for the oxidation of a Cr metal film of this particular thickness. After this point there is no appreciable change in composition observable by XPS. After oxidation there was an observed binding energy shift in the Cr $2p_{3/2}$ spectrum, which was in excellent agreement with the reference data. In order to do this one would ideally need to use references. A binding energy shift was likewise observed in the O 1s spectra. After 10 L O_2 the O 1s binding energy is about 530.4 eV, but after further oxidation the peak shifts before the binding energy attains a relatively constant value at around 530.1 eV. The shift to lower binding energy may be indicative of an increasing electron density associated with oxygen anions (as chromium becomes more oxidised) which would support the theory that after 10 L O_2 the chromium is only partially oxidised.

A second film (film B) was grown to demonstrate growth of a thicker film by cycles of deposition and oxidation. Once again Cr was initially deposited for 5 minutes, although this time a layer thickness of 0.28 nm was estimated (see Figure 3.6). Having established previously that 20 L O_2 at 673 K was required for complete oxidation, the oxidation was this time carried out in one 20 L step (*i.e.* 5×10^{-8} Torr for 400 s) and the XP spectra recorded. From the attenuated Cu $2p_{3/2}$ peak, an oxide thickness of 0.73 nm was estimated (see Figure 3.6). A shift in the Cr 2p binding energy (see Figure 3.7a) from 573.9 eV to 576.1 eV and an increase in the peak width are indicative of oxidation as previously observed with film A. Further chromium was then deposited for 5 minutes onto the oxide film. The film thickness was not calculated from this, because the film may have consisted of elemental and oxide phases and hence there is considerable uncertainty as to the appropriate IMFP value. There was no significant change in the binding energy of the Cr $2p_{3/2}$ peak maximum, but the peak became visibly broader (see Figure 3.7a). There was also an increase in O 1s binding energy from 530.02 eV to 530.9 eV (see Figure 3.7b), and also some attenuation of the O 1s signal intensity. Oxidation was then carried out for a second time (again 20 L O_2 at 673 K). From the final Cu $2p_{3/2}$ signal, an oxide layer thickness of 1.35 nm was estimated (see Figure 3.6).

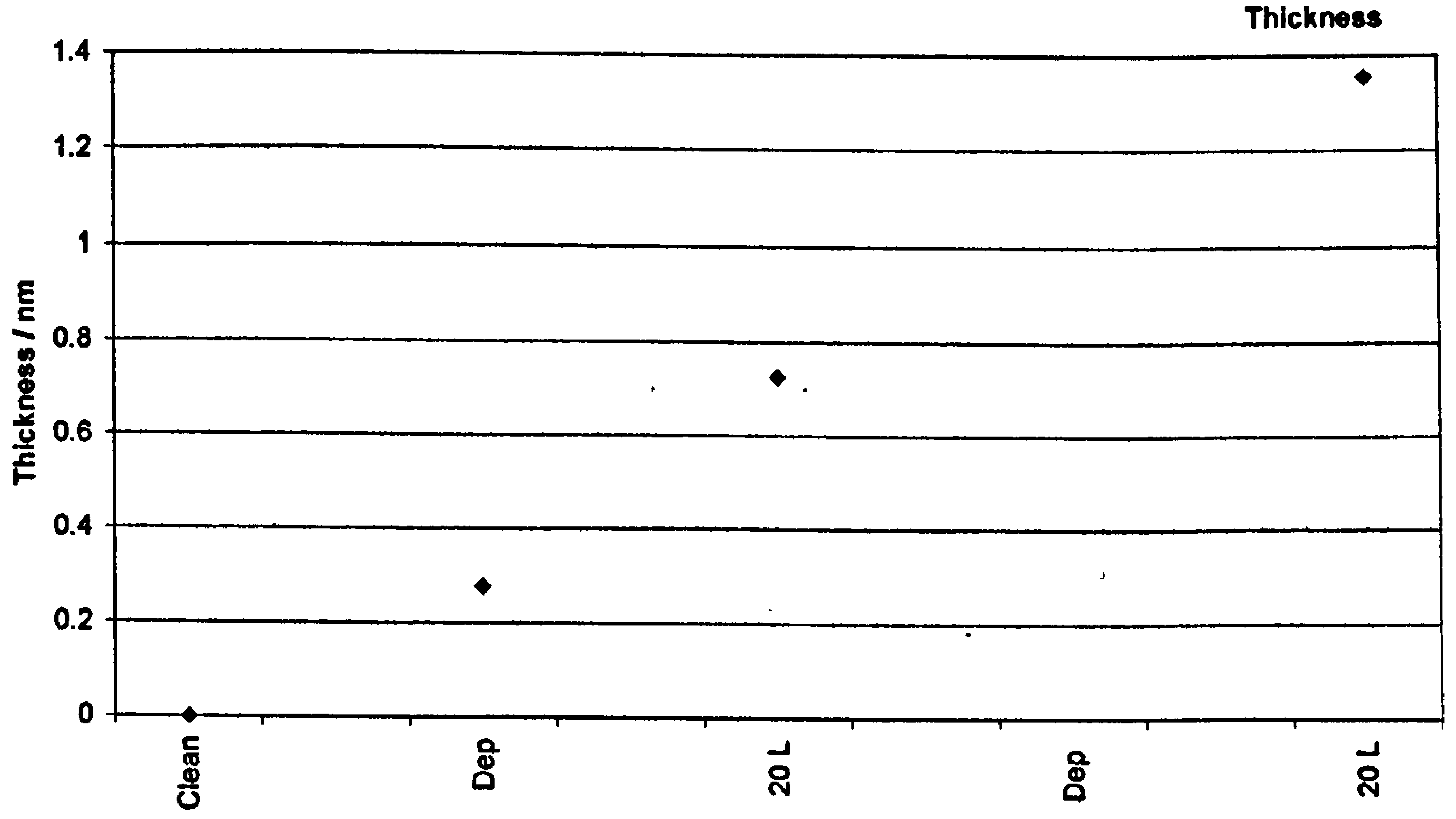

Figure 3.6: Film thickness at different stages of film growth

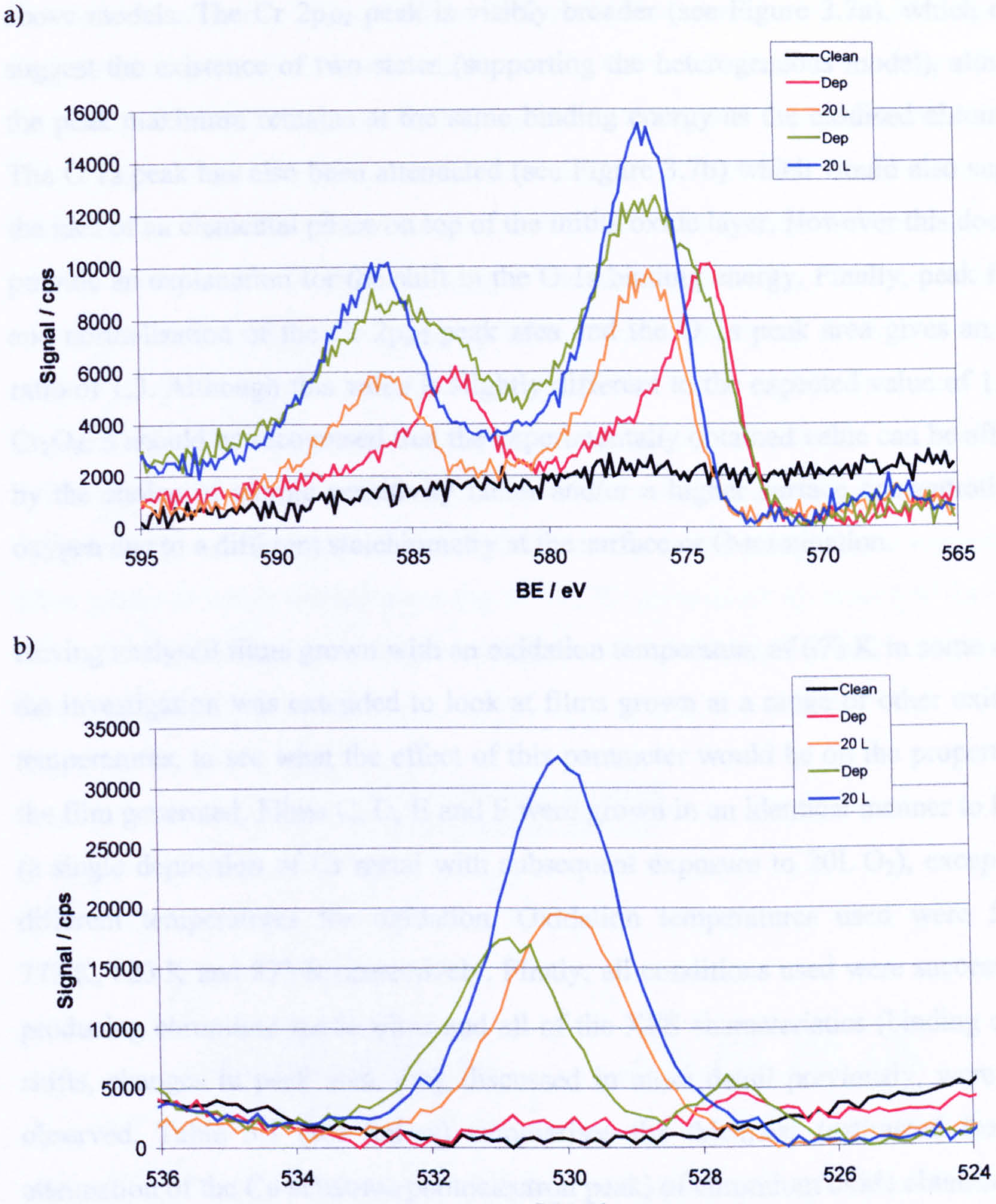

Figure 3.7: XP spectra at different stages of film growth a) Cr 2p region; b) O 1s region

The same general trends were observed in the growth of film B as had been observed with film A. Again there was a shift in the Cr $2p_{3/2}$ binding energy to higher binding energy indicative of oxidation. In the step where chromium was deposited onto the oxide, great caution is needed when interpreting the XPS data, especially the peak areas. The film can be considered to consist of either 1) two phases, metal and oxide, with some extent of inter-diffusion between the phases (heterogeneous), or 2) a fully homogeneous oxygen deficient layer (CrO_{x-y}). In both cases there is great uncertainty as to the IMFP of electrons in such a film, so an estimate cannot be made of the thickness. However it is interesting to look at the data and see if it favours one of the above models. The Cr $2p_{3/2}$ peak is visibly broader (see Figure 3.7a), which could suggest the existence of two states (supporting the heterogeneous model), although the peak maximum remains at the same binding energy as the oxidised chromium. The O 1s peak has also been attenuated (see Figure 3.7b) which would also support the idea of an elemental phase on top of the initial oxide layer. However this does not provide an explanation for the shift in the O 1s binding energy. Finally, peak fitting and normalisation of the Cr $2p_{3/2}$ peak area and the O 1s peak area gives an O:Cr ratio of 1.3. Although this value is slightly different to the expected value of 1.5 for Cr_2O_3, it should be recognised that the experimentally obtained value can be affected by the choice of atomic sensitivity factor and/or a higher surface concentration of oxygen due to a different stoichiometry at the surface or O-termination.

Having analysed films grown with an oxidation temperature of 673 K in some detail, the investigation was extended to look at films grown at a range of other oxidation temperatures, to see what the effect of this parameter would be on the properties of the film generated. Films C, D, E and F were grown in an identical manner to before (a single deposition of Cr metal with subsequent exposure to 20L O_2), except with different temperatures for oxidation. Oxidation temperatures used were 573 K, 773 K, 823 K and 873 K respectively. Firstly, all conditions used were successful in producing chromium oxide films and all of the XPS characteristics (binding energy shifts, changes in peak area, *etc*), discussed in more detail previously, were again observed. Table 3.1 (see below) summarises the thickness (estimated from the attenuation of the Cu substrate photoelectron peak) of chromium oxide obtained from deposited chromium metal for all of the oxidation temperatures investigated in the course of this work.

T_{ox} / K	d_{Cr} / nm	d_{CrOx} / nm	d_{CrOx} / d_{Cr}
573	0.45	1.40	3.1
673	0.34	1.10	3.2
773	0.55	1.75	3.2
823	0.44	1.15	2.6
873	0.48	0.90	1.9

Table 3.1: Thickness of chromium oxide obtained at different oxidation temperatures

As can be clearly seen from the d_{CrOx} / d_{Cr} ratio, the amount of oxide film obtained from oxidising the deposited metal is stable up to 773 K, but decreases rapidly thereafter. This does appear to be a genuine trend and it suggests that higher temperatures have a detrimental effect on the oxide film growth. In these experiments when the correct amount of oxidation time (400 s) had elapsed the heating was switched off and the oxygen dosing simultaneously stopped. Since the crystal cools relatively slowly, this has the effect of exposing the film to vacuum while it is still at a high temperature. This could lead to partial breakdown/decomposition of the film and explain the trend in Table 3.1. Additionally this trend could be indicative of the mode of growth. Figure 3.8 shows different solid-on-solid growth modes. The trend in estimated thickness suggests that films grown at lower temperatures (up to 773 K) grow layer by layer ("a" in Figure 3.8), whereas films grown at higher temperatures exhibit layer plus island growth or island growth ("b" or "c").

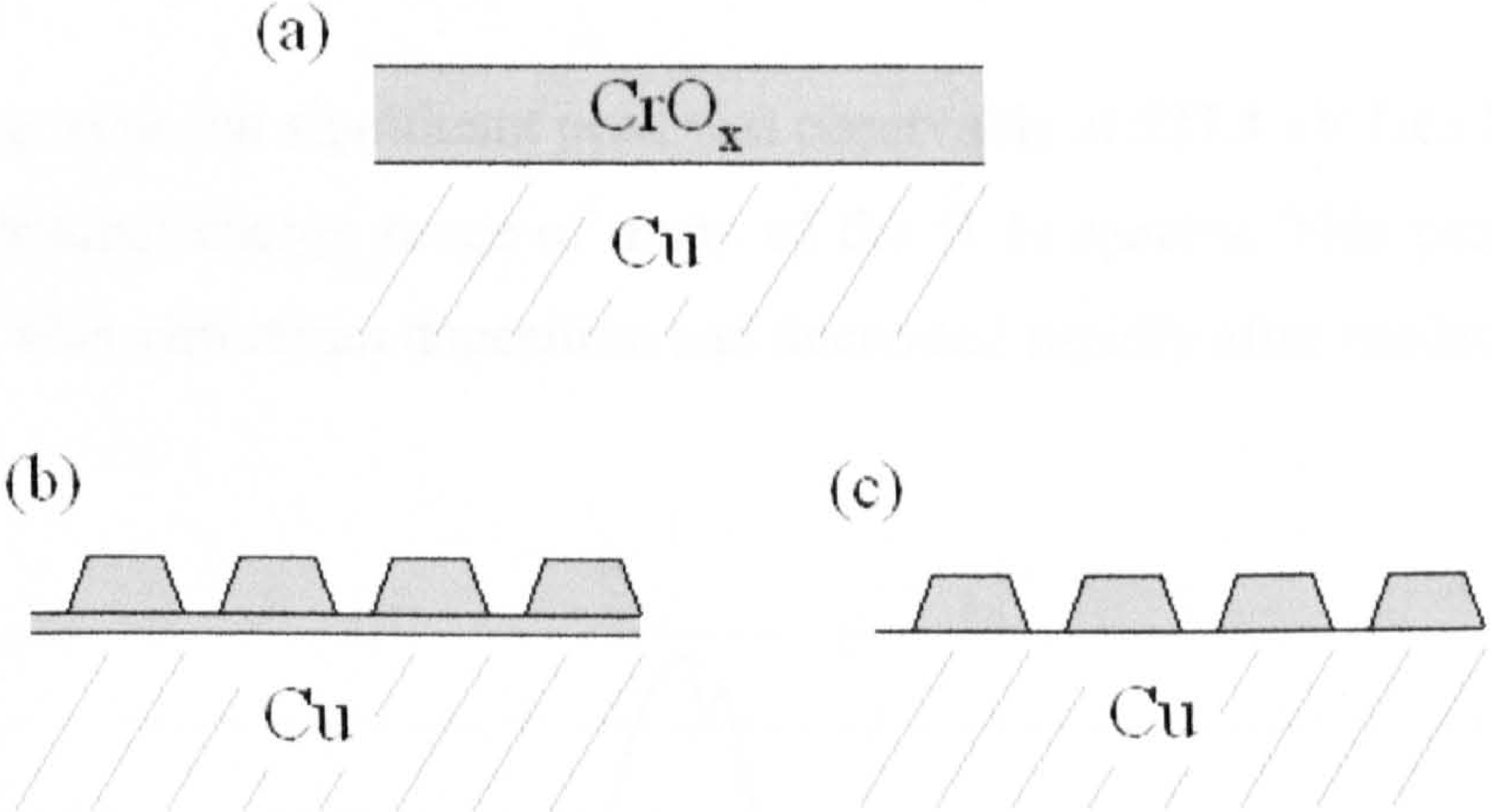

Figure 3.8: Different solid-on-solid growth modes (a) Frank-van der Merwe; (b) Stranski-Krastinov; (c) Volmer-Weber

It is worth mentioning that the absolute values of thickness given in this table are subject to some uncertainty (as discussed previously) and an increase in film thickness of three times upon oxidation (as seen at $T_{ox} \leq 773$ K) is unrealistic.

Throughout the experiments detailed in this report, the presence of metallic and non-metallic impurities was monitored. Carbon is a common impurity in these kind of systems (especially with resistive deposition sources) and for this reason the carbon 1s region was routinely recorded. Although always present (see, for example, Figure

3.9), the intensity of this peak did not vary significantly between experiments. It needs to be remembered that as the atomic sensitivity factor of carbon in XPS is very low, the amount of carbon present is greater than might initially seem to be the case.

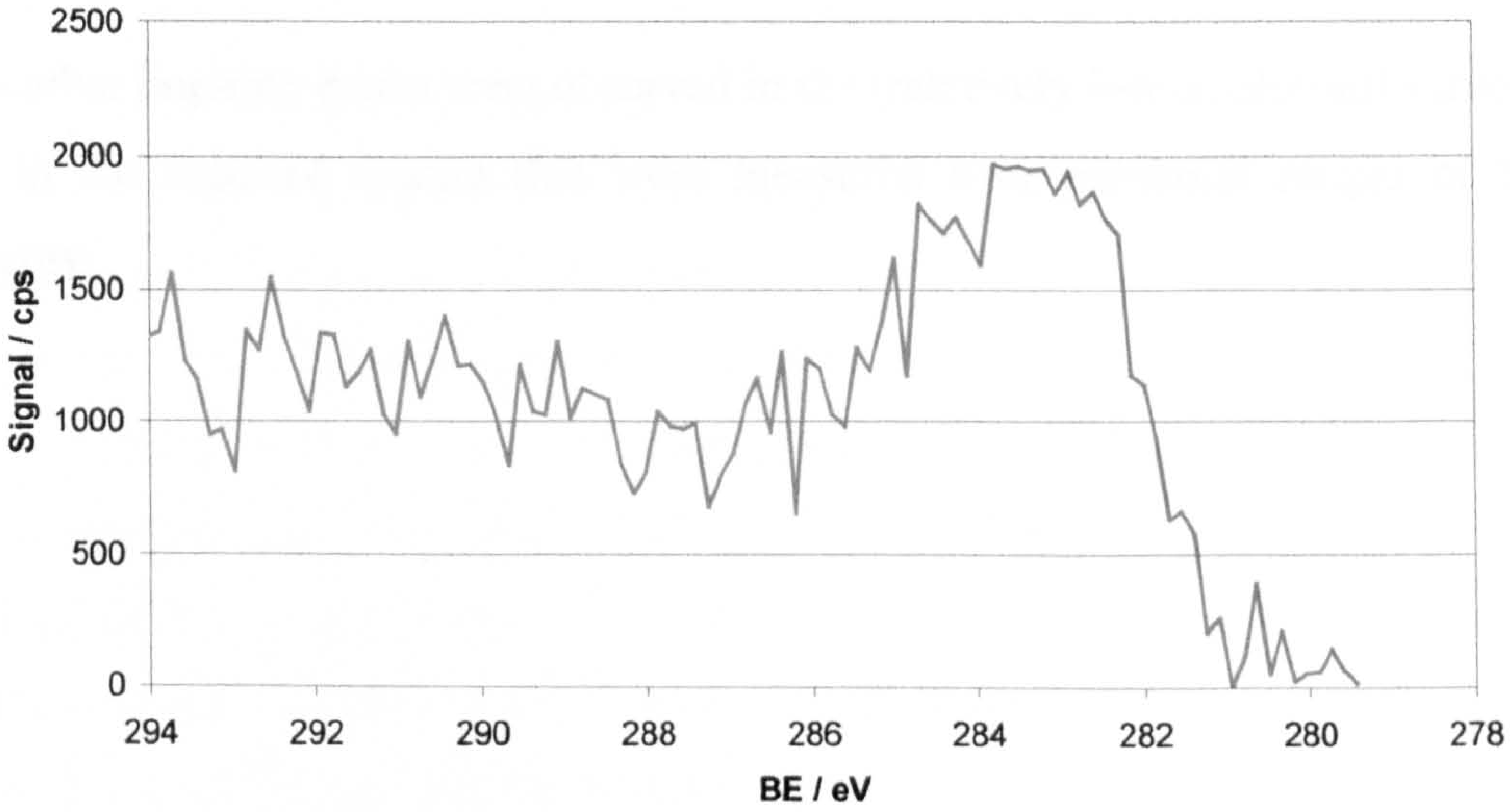

Figure 3.9: Typical C 1s spectrum obtained from a deposited chromium oxide film

In addition, a weak but significant peak was observable at 527.4 eV (see Figure 3.10) in the low binding energy range of many of the O 1s spectra. This peak was most pronounced after chromium deposition and decreased rapidly after oxidation.

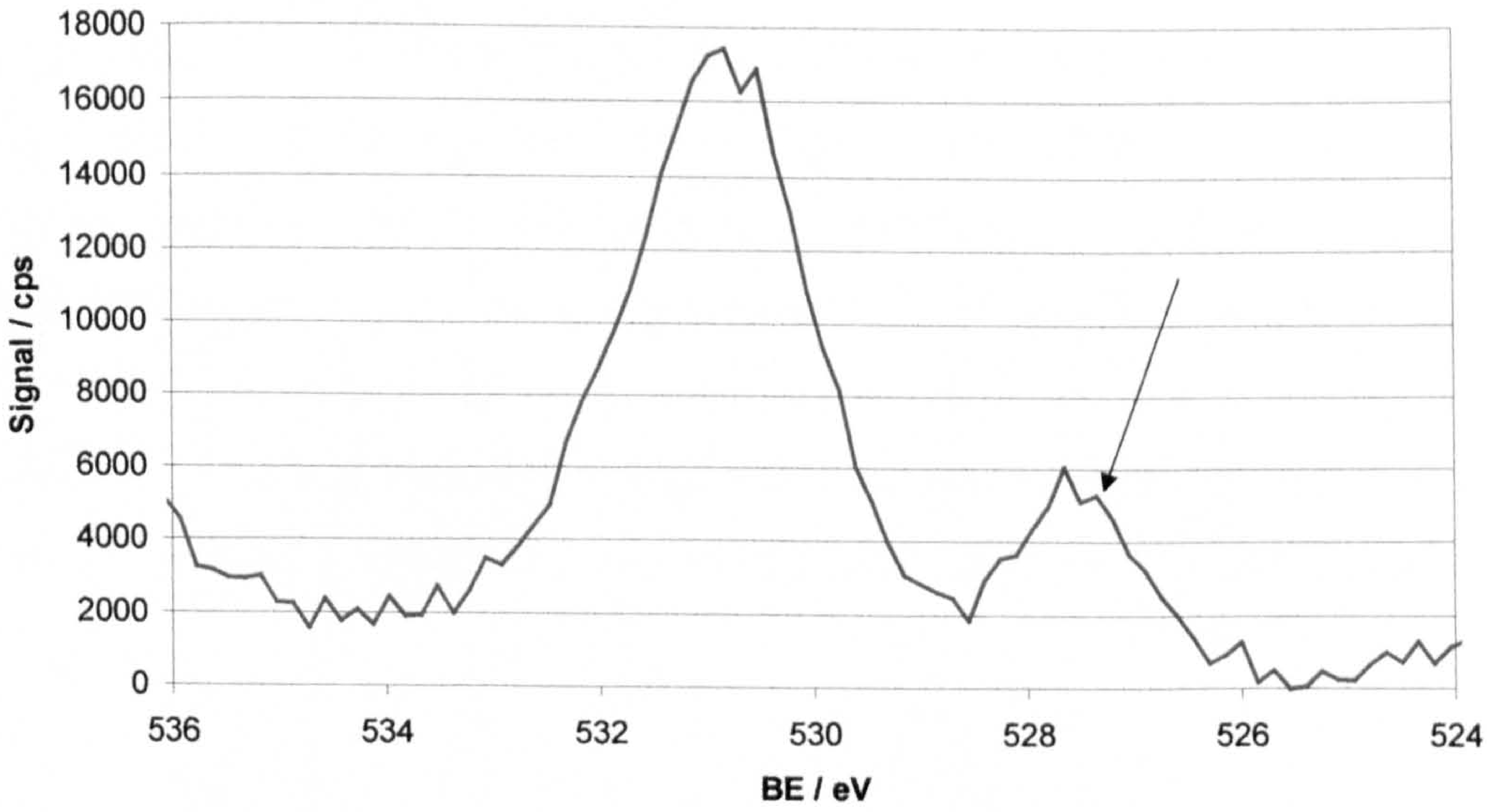

Figure 3.10: Unidentified peak at low binding energy end of O 1s region

This peak is most likely to be a Mg K_β satellite associated with the Cr $2p_{3/2}$ peak. Such a satellite is expected at ~ 48 eV to lower binding energy of the main peak and to have a relative intensity of 0.5%.

No other impurity peaks were observed in the (relatively low resolution) survey scan, or in the regional spectra that were measured over particular ranges of binding energy.

3.3 Post-Deposition Treatments

A freshly deposited oxide film, film G, (which had been prepared by oxidation at 673 K) was further-annealed in vacuum at higher temperatures in order to assess its thermal stability and to investigate the parameters required for generation of ordered CrO_x films. From the attenuated Cu $2p_{3/2}$ signal the thickness of the initial oxide film was estimated to be 1.9 nm. The sample was then heated again to 673 K for five minutes and allowed to cool, after which the Cu 2p, Cr 2p and O 1s regions were recorded. This procedure was repeated with the temperature being raised in 50 K increments up to 973 K. No significant changes in the XP spectra were observed up to and including a temperature of 873 K. At 923 K however some breakdown of the CrO_x film was evident from the XP spectra (see Figure 3.11a and b). An increase in the Cu $2p_{3/2}$ peak intensity and a decrease in the both the Cr 2p and O 1s peak areas was observed. Furthermore there was a shift in the Cr $2p_{3/2}$ peak maximum to higher binding energy (from 576.4 eV to 576.6 eV) and the O 1s binding energy also increased (from 530.3 eV to 530.5 eV). After heating the crystal to a temperature of 973 K, further breakdown of the CrO_x film was evidenced by XPS (see Figure 3.11a and b), with a further shift to higher binding energies for the Cr $2p_{3/2}$ and O 1s peaks (576.6 eV to 576.8 eV and 530.5 eV to 530.7 eV respectively). The O/Cr ratio was seen to decrease significantly (see Figure 3.11c).

The decrease in O/Cr ratio is interesting. There was a general decrease over the course of the experiment, but a much larger decrease from 923 K to 973 K. The observed decrease in O/Cr could arise for several reasons. It could be indicative of different diffusion coefficients (O greater than Cr) in the Cu substrate. Alternatively it is reasonable to expect a change in stoichiometry as oxygen is lost from the chromium oxide to the vacuum at high temperatures. Additionally, the breakdown is probably associated with a change in morphology (3D crystallite nucleation).

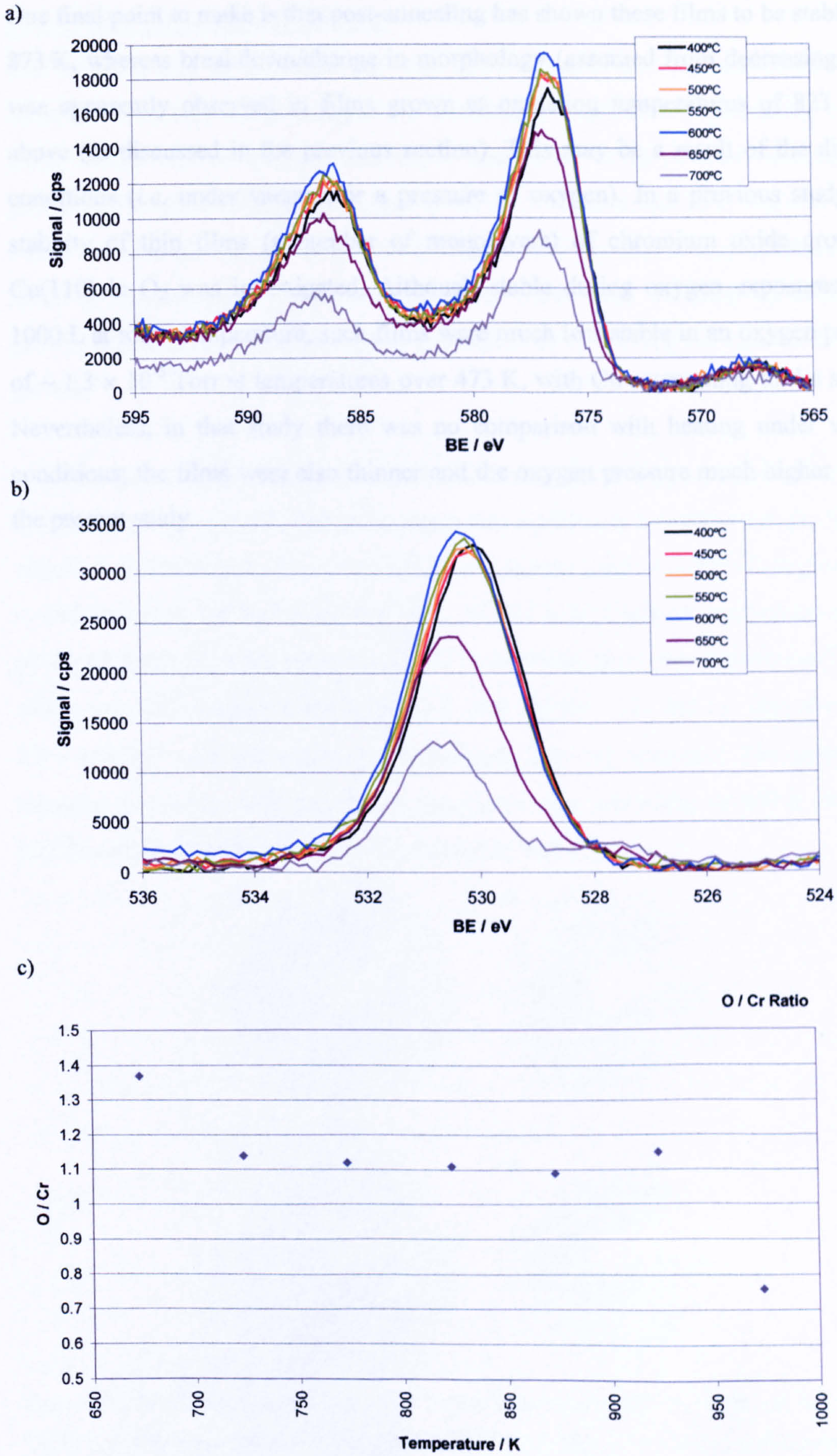

Figure 3.11: XPS data with vacuum annealing at increasing temperature a) Cr 2p region; b) O 1s region; c) O/Cr ratio

One final point to make is that post-annealing has shown these films to be stable over 873 K, whereas breakdown/change in morphology (assumed from decreasing yield) was apparently observed in films grown at oxidation temperatures of 823 K and above (as discussed in the previous section). This may be a result of the different conditions (*i.e.* under vacuum or a pressure of oxygen). In a previous study[17] the stability of thin films (a number of monolayers) of chromium oxide grown on Cu(110) in O_2 was investigated. Although stable during oxygen exposures up to 1000 L at room temperature, such films were much less stable in an oxygen pressure of ~ 1.3×10^{-5} Torr at temperatures over 473 K, with Cu segregating to the surface. Nevertheless, in that study there was no comparison with heating under vacuum conditions; the films were also thinner and the oxygen pressure much higher than in the present study.

3.4 Conditions for Ordering

The ultimate aim of this research was to investigate well-defined films. It was therefore necessary to investigate the conditions required for generating ordered films. LEED was the primary technique used to see if an ordered film had been grown and to assist in the characterisation of the film, although XPS was also carried out to estimate the film thickness and to observe any binding energy shifts, that may relate to any underlying processes. Ordered films were obtained by either post growth-annealing of a film previously disordered or by altering the conditions of film growth.

The post-annealing in vacuum of film G was discussed in the previous section where it was found that at 923 K and above there was significant breakdown of the film and reduction in O/Cr ratio. There was no LEED pattern (only a diffuse background) up to and including the annealing at 873 K. At 923 K however an ordered pattern was observed. Superimposed upon the Cu(111) substrate spots was a hexagonal pattern with a unit cell constant a = 4.8 (±0.1) Å (see Figure 3.12a and b). This structure is 1.9 × 1.9R30° with respect to the underlying Cu(111) substrate. The pattern was recorded at various different beam energies. After annealing at 973 K the same LEED pattern was observed (see Figures 3.12c and d).

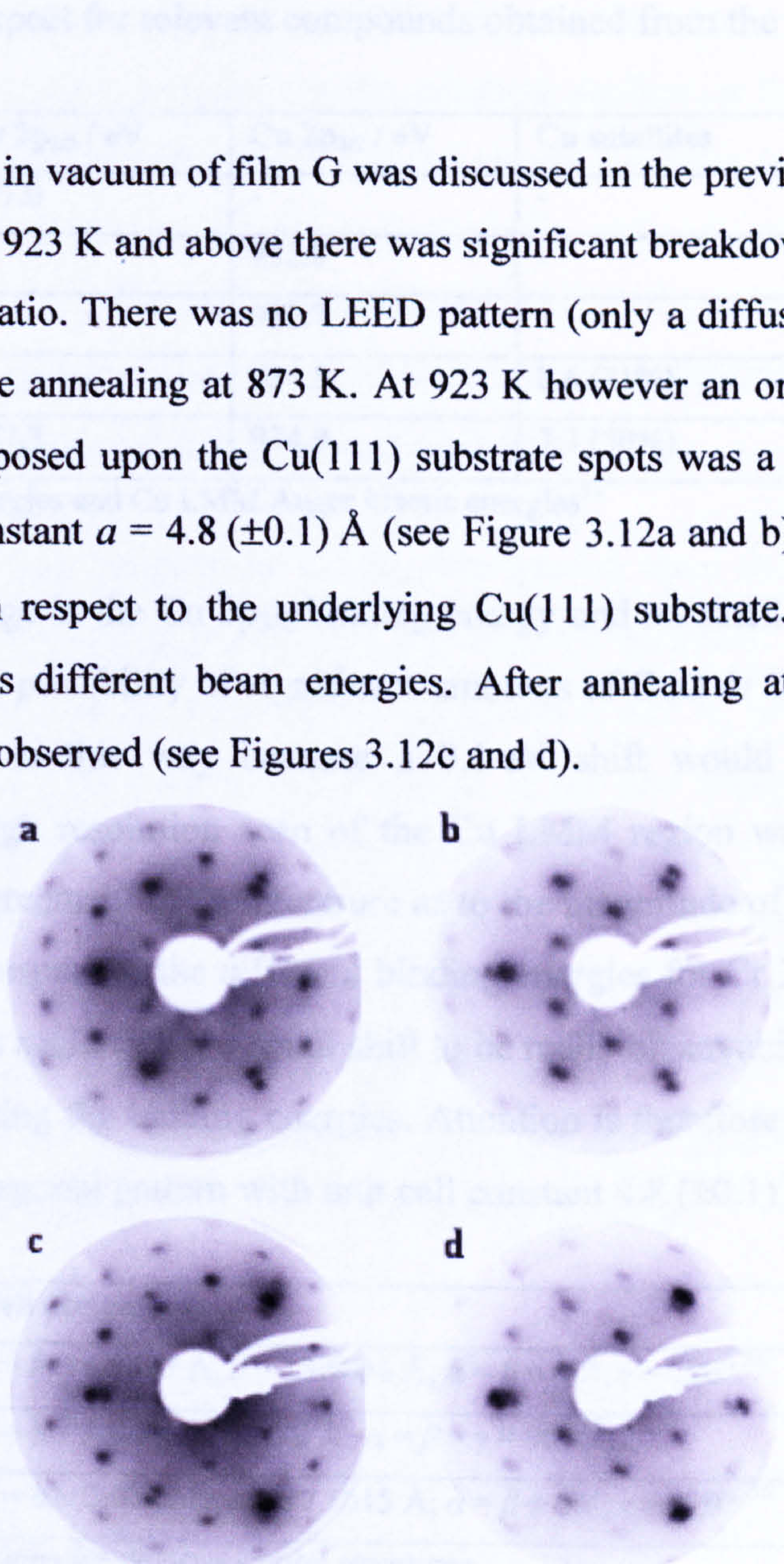

Figure 3.12: LEED patterns after heating a) 923 K, beam energy = 133 eV; b) 923 K, beam energy = 117 e; c) 973 K, beam energy = 133 eV; d) 973 K, beam energy = 117 eV; the Cu(111) substrate spots are the outermost of the pair of spots

Before making the assumption that the observed structure formed after post-heating is chromium oxide, it is first necessary to prove that copper is not in some way involved in the oxide: It is not inconceivable that a copper oxide (Cu_2O or CuO), copper chromate ($CuCrO_2$) or copper dichromium oxide ($CuCr_2O_4$) could be formed under these conditions at the substrate-film interface. Although copper oxidation states are notoriously difficult to deduce from XPS, there are a number of points worthy of discussion. Firstly from the XPS measurements we might expect to see a shift in the Cu $2p_{3/2}$ binding energy if copper were oxidised. Table 3.2 shows the peaks one would expect for relevant compounds obtained from the literature.[54]

Compound	Cr $2p_{3/2}$ / eV	Cu $2p_{3/2}$ / eV	Cu satellites	Cu LMM
Cr_2O_3	577.0	-	-	-
Cu	-	932.8	-	918.3
Cu_2O	-	932.7	-	916.0
CuO	-	934.5	8.6 (31%)	917.3
$CuCr_2O_4$	577.3	934.9	7.3 (50%)	917.8

Table 3.2: Binding energies and Cu LMM Auger kinetic energies[54]

There was no change in the Cu $2p_{3/2}$ binding energy and no satellites were observed which rules out the possibility of significant amounts of CuO or $CuCr_2O_4$. Cu_2O can not be ruled out in this way because a 0.1 eV shift would not be observed. Unfortunately a high resolution scan of the Cu LMM region wasn't recorded and there is some disagreement in the literature as to the magnitude of this shift (c.f. refs. 53 and 54). With respect to the different binding energies for Cr $2p_{3/2}$ for Cr_2O_3 and $CuCr_2O_4$, 0.3 eV is again rather a small shift to be really observable and there may be other factors affecting the binding energies. Attention is therefore turned towards the LEED data. A hexagonal pattern with unit cell constant 4.8 (±0.1) Å was observed.

Compound	Cell dimensions
Cr_2O_3	$a = b = 4.9507$ Å, $c = 13.5656$ Å; $\alpha = \beta = 90°, \gamma = 120°$ [24]
$CuCr_2O_4$	$a = b = 6.04$ Å, $c = 7.78$ Å; $\alpha = \beta = \gamma = 90°$ [55]
$CuCrO_2$	$a = b = 2.9747$ Å, $c = 17.1015$ Å; $\alpha = \beta = 90°, \gamma = 120°$ [56]

Table 3.3: Cell dimensions for relevant crystal structures

This value is in reasonable agreement with that expected for the (0001) surface of Cr_2O_3, which possesses a hexagonal unit cell with a = 4.95 Å (see Table 3.3). The determination of the cell size from LEED may be slightly in error, or the cell dimensions of the surface may indeed vary slightly from the bulk due to relaxation effects or the different energetic environment that a thin film on a metal substrate experiences compared to the topmost layers of a bulk oxide. It is thus reasonable to assume that the observed structure is that of Cr_2O_3. As previously noted, ordering of the oxide film was only evident at temperatures where some breakdown was also apparent. The change in binding energies observed, as the film orders (Cr $2p_{3/2}$ and O 1s binding energies increasing), although slight, may be an indication as to the process occurring. Either the initially-disordered chromium oxide film may restructure into crystalline particles on the substrate surface or there may be some diffusion of the chromium and oxygen into the copper substrate (quite possibly with different diffusion coefficients) leaving just a thin ordered epitaxial oxide film remaining on the surface. Both of these models could lead to an increase in Cr $2p_{3/2}$ and O 1s binding energies. There was no observable asymmetry in the O 1s peak, which would be indicative of different O environments.

The effect of oxidation temperature during film growth upon the ordering of films was investigated. No ordered pattern was observed for oxidation temperatures up to and including 773 K. Film E, which had been grown at 823 K, however, exhibited a faint LEED pattern. This pattern was different to the one observed before in that there were less spots (see Figure 3.13a and b for comparison). Upon closer analysis, however, it seems that the pattern is in fact the same as before, but that the first order spots are not immediately evident (due to the faintness of the pattern). Further stages of deposition and oxidation were carried out on top of this film. The LEED pattern was still observed up to a film thickness of 2 nm, but after that only the increasingly-faint substrate spots were visible upon a diffuse background.

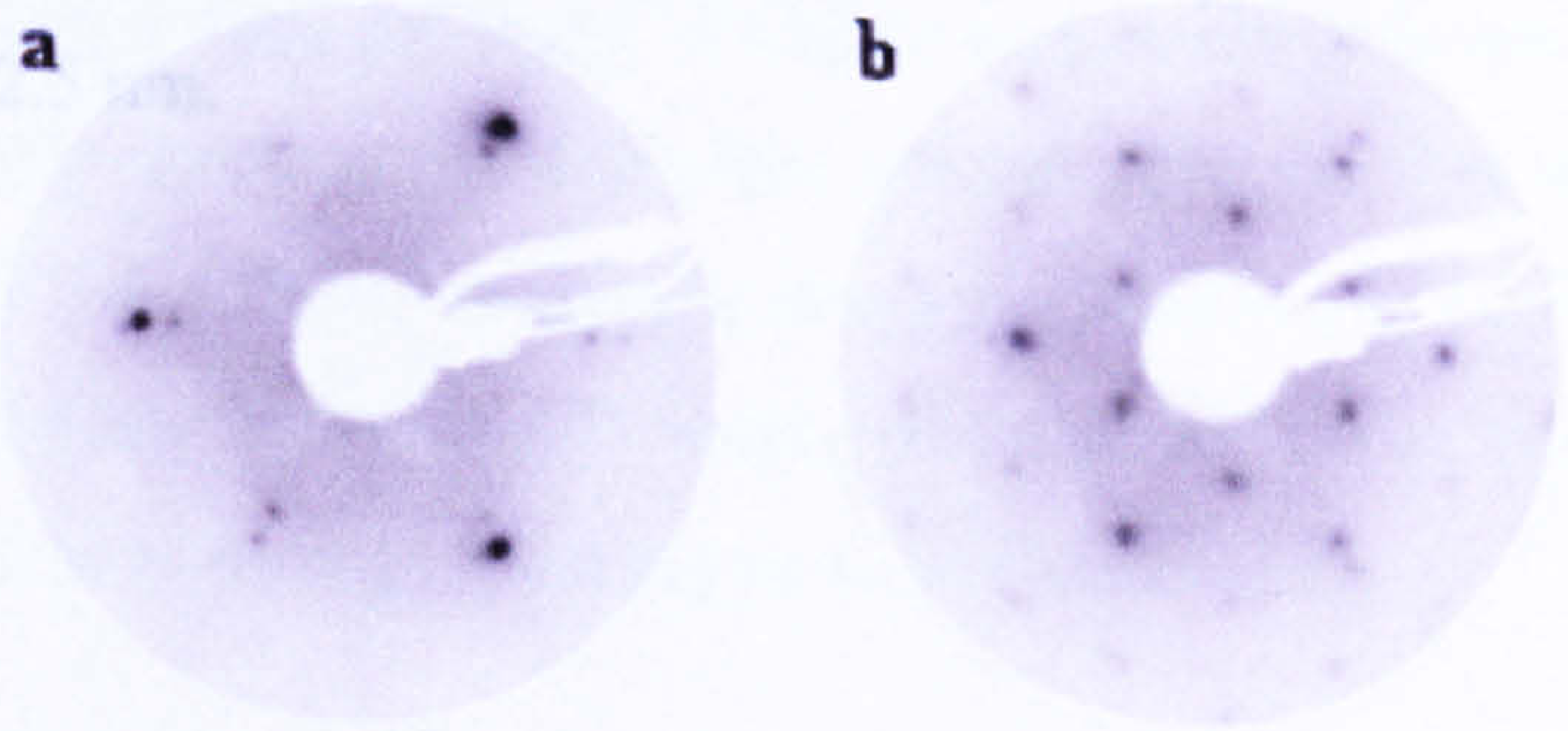

Figure 3.13: LEED patterns of film grown at a) 823 K, beam energy = 123 eV; b) 873 K, beam energy = 122 eV

Film H was grown by multiple cycles of chromium metal deposition followed by oxidation at 873 K under an oxygen pressure of 5×10^{-8} Torr for 16 minutes for the first cycle and an oxygen partial pressure of 1×10^{-7} Torr for 8 minutes for subsequent cycles (approximately 50 L). In addition to ascertaining whether ordered films could be grown under these conditions, the aim of the experiment was also to grow the film to a reasonable thickness. It was found necessary for 10 consecutive Cr depositions/oxidations to be carried out in order to obtain a film of 2.5 nm thickness (as estimated from the Cu 2p peak attenuation). From the first cycle of Cr deposition and oxidation, an ordered film was evidenced by the observed LEED pattern proving that at 873 K an ordered film could be grown. The LEED pattern observed in this experiment had the same appearance as the one obtained from film G (where ordering was induced by heating), with a hexagonal pattern with lattice parameter $a = 4.8$ Å. As the film became thicker, two observations were made. Firstly, the Cu spots become less clear. It is difficult to establish exactly where this occurs, since at certain beam energies the Cu spots are less intense anyway. Secondly above a thickness of 2 nm, an extra pattern was observed albeit a very faint one (see Figure 3.14). From the spacing it is evident that this pattern is associated with the oxide film and seems to relate to a $(4/\sqrt{3} \times 4/\sqrt{3})R30°$ overlayer structure in real space, with respect to the original chromium oxide structure. After 10 cycles of deposition/oxidation a thickness of approximately 2.5 nm was estimated by XPS (see Figure 3.15a). At this stage an ordered pattern was still observed by LEED. With respect to the XPS data gathered, similar binding energy shifts were evident to those seen in previous experiments. The final point to make is that the growth of the film, as measured by the attenuation of the Cu substrate signal, was very slow. The first cycle of deposition/oxidation led to a film of 1 nm in thickness. After that, however 2 nm was not reached until the fifth cycle and by ten cycles the thickness was only just approaching 2.5 nm.

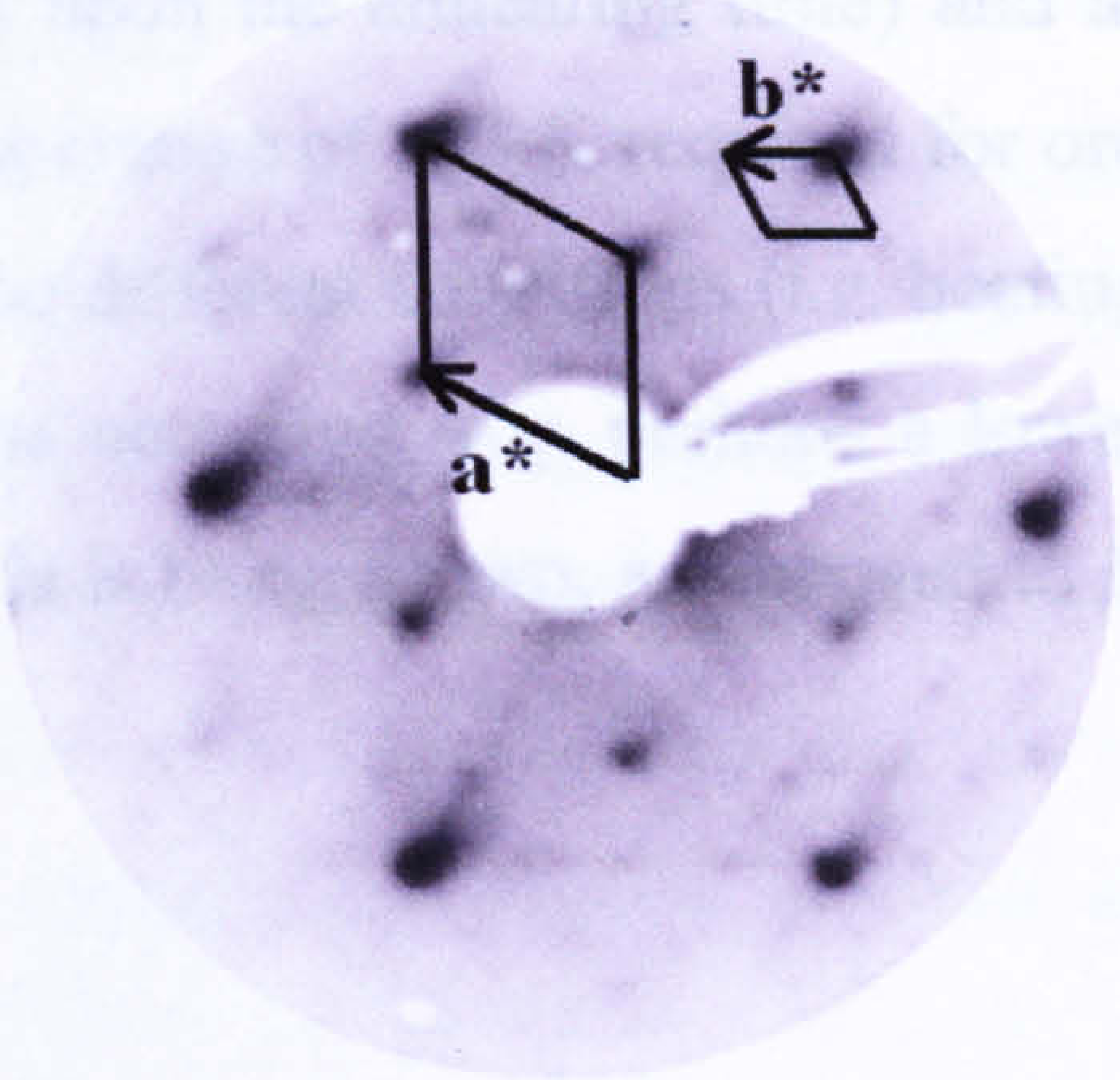

Figure 3.14: LEED pattern showing extra spots, film thickness ~ 2.3 nm, beam energy = 71 eV

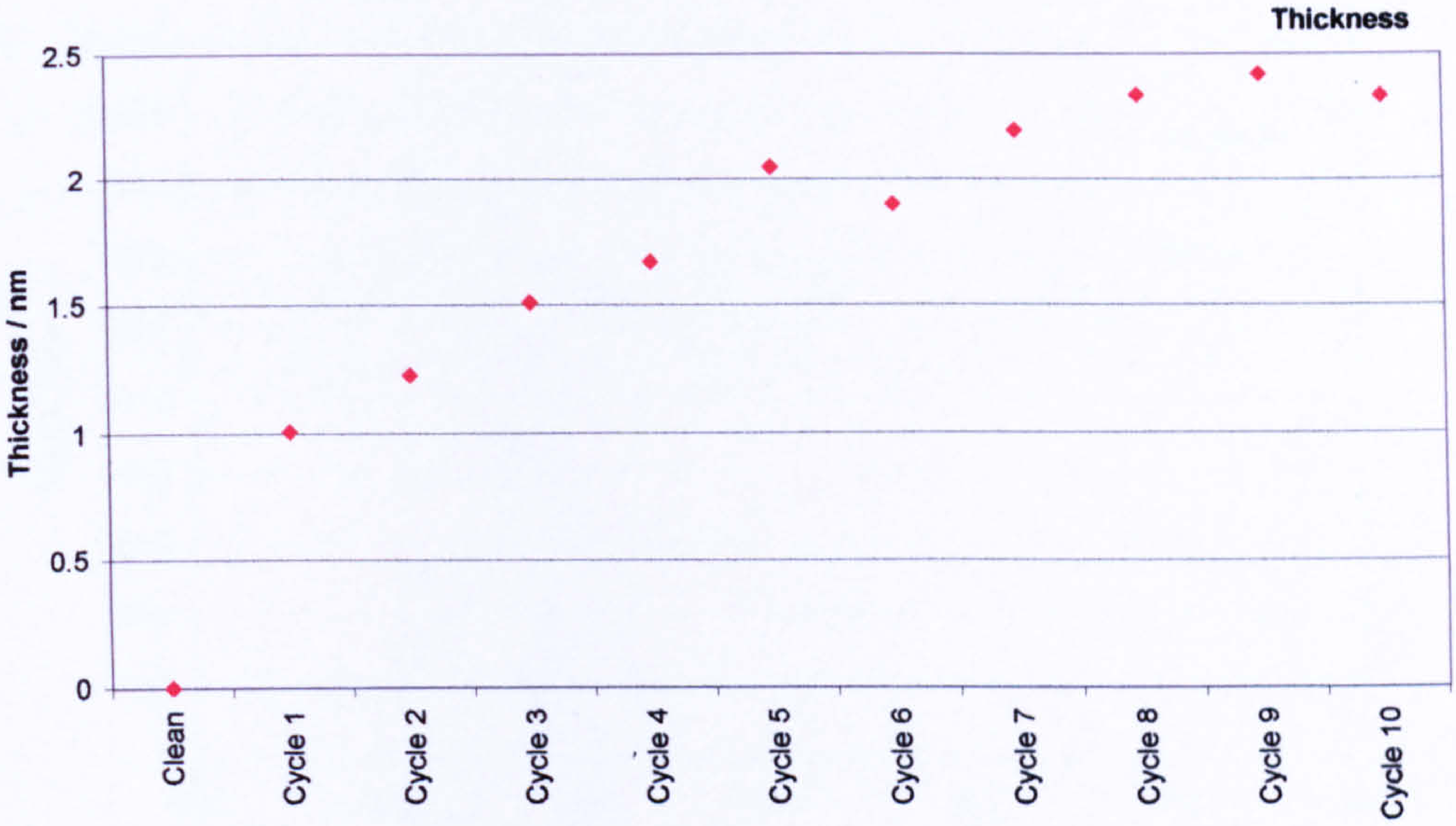

Figure 3.15: Thickness of Film growth at 873 K

The fact that the Cu spots became less clear at greater film thickness is to be expected. In fact for a uniform film with a thickness of over 2 nm one would really not expect to see them at all. Taken together with the previous observations this suggests that the oxide film produced at higher temperatures is not a uniform layer, but instead probably involves 3D crystallite growth after the first layer of oxide has formed. The $(4/\sqrt{3} \times 4/\sqrt{3})R30°$ overlayer structure observed by LEED at greater film thickness is particularly interesting. It would be helpful if it was possible to obtain a clearer pattern, perhaps through growing an even thicker film.

In summary, with the parameters chosen for these experiments, films are disordered up to and including an oxidation temperature of 773 K, are at an intermediate state at

823 K (perhaps dependant upon the annealing time) and are ordered above 873 K. This is different to the temperature of 923 K required for ordering by post-annealing, which may be a result of the different conditions (*i.e.* heating in a vacuum or oxygen) and/or the different process occurring (*e.g.* perhaps a lower temperature is required for ordering while the oxide is being grown, as opposed to ordering a film after it has been grown).

3.5 Angle-Resolved XPS

Angle-resolved XPS provides insight into the depth distribution of detected species by recording spectra at varying emission angles and hence exhibiting different surface sensitivities. AR-XPS was used to study a film (I) which had been grown with an oxidation temperature of 573 K. The thickness of the oxide film generated was estimated to be 1.7 nm. XPS was recorded at a near-normal electron emission angle (15° from sample normal) and grazing electron emission angle (75° from sample normal).

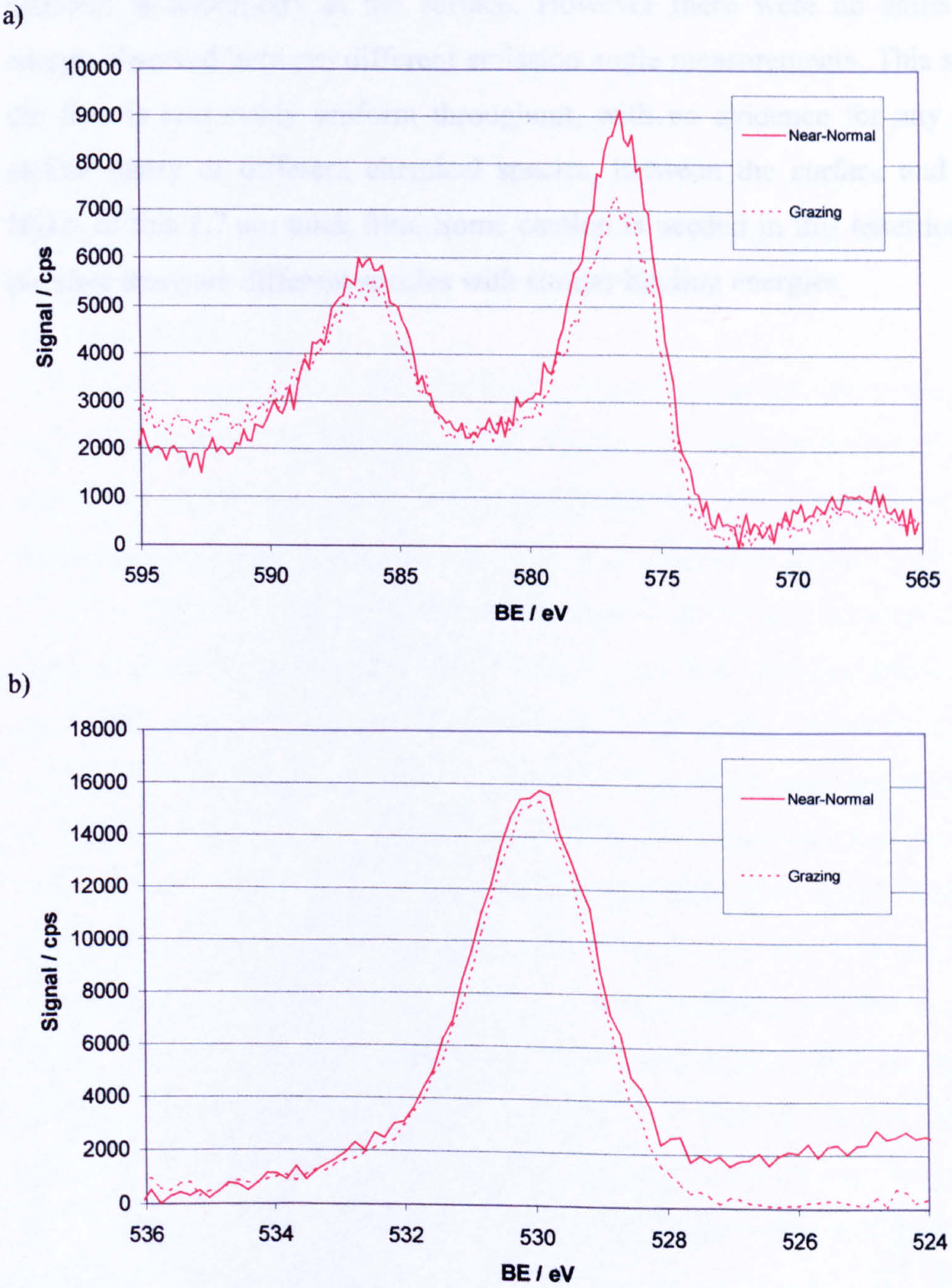

Figure 3.16: XPS data at grazing and near-normal emission angle a) O 1s region; b) Cr 2p region

As mentioned in section 2.3, when comparing XPS data recorded at different electron emission angles, a number factors come into play, which affect the intensities of the XP peaks. It was no surprise that the Cu 2p signal decreased to half its intensity when measured at a grazing angle, since the substrate is covered by the overlying film. The O 1s peak actually appears to be little affected in intensity (see Figure 3.16a), whereas the Cr 2p peak reduces in intensity somewhat (see Figure 3.16b). The Cr 2p/O 1s signal intensity ratio is thus seen to decrease. This proves that the concentration of O is higher at the surface than that of Cr. From this alone it is not possible to say whether this is because the film is O-terminated or there is a different stoichiometry at the surface. However there were no shifts in binding energy observed between different emission angle measurements. This suggests that the film is reasonably uniform throughout, with no evidence for any variation in stoichiometry or different chemical species, between the surface and sub-surface layers of this 1.7 nm thick film. Some caution is needed in this assertion, since it is possible there are different species with similar binding energies.

3.6 Interaction with H_2O, CH_3OH and CO_2

The next phase of work concerned the interaction of small molecules with the surface of the chromium oxide films. The molecules chosen for the investigation were H_2O, CH_3OH and CO_2. Films were grown in the manner previously described. For the purpose of these adsorption studies, two different types of film were considered: low temperature annealed films grown with an oxidation temperature of 573 K, known to be disordered, and high temperature annealed films grown with an oxidation temperature of 873 K, known to be ordered. Typically, XPS measurements used for analysing surface adsorbates were carried out with a grazing electron emission angle of 75° (angle between detector and sample normal). In addition to the O1s, Cr 2p and C1s regions, the Cu $2p_{3/2}$ region was also scanned in order to provide a reference peak so that the intensities could be normalised, thus eliminating experimental inconsistencies with the data. Gases were typically dosed directly onto the sample for 1000 s at a pressure of 5×10^{-8} Torr. TPD was also used in these studies.

3.6.1 Blank Tests

Blank tests were carried out to eliminate a number of factors that could contribute to misinterpretation of the adsorption data. Firstly, CH_3OH was dosed and TPD carried out in the normal way, except that no chromium oxide film was grown. It is known that CH_3OH does not adsorb on a clean Cu(111) substrate at ambient temperatures.[58] This experiment shows the effect of adsorption of the gas on parts of the system which become heated during TPD and give rise to their own desorption peaks, which are not related to the sample being tested. The only peaks evident in this experiment were at very low temperatures (*i.e.* at the beginning of the run), and most likely relate to gas evolution from the heating wires. The second test was to grow a chromium oxide film (in this case a high temperature annealed film) and to carry out a TPD measurement, but without dosing any gas. This experiment gave rise to a peak for $m/z = 28$, with a maximum at 798 K and weak shoulders at 548 K and 673 K (see Figure 3.17). The $m/z = 44$ trace exhibited similar features, but all much weaker in intensity. These peaks relate almost certainly to CO and CO_2 as the features coincide at the same temperatures. The most likely explanation for the source of these peaks is due to carbon (which is present as an impurity in the deposited films) which under heating becomes oxidised to give rise to (predominantly) CO. Crucially, this experiment has shown that these peaks are unequivocally related to the film itself or other parts of the system outgassing, rather than arising from an adsorbed species of interest.

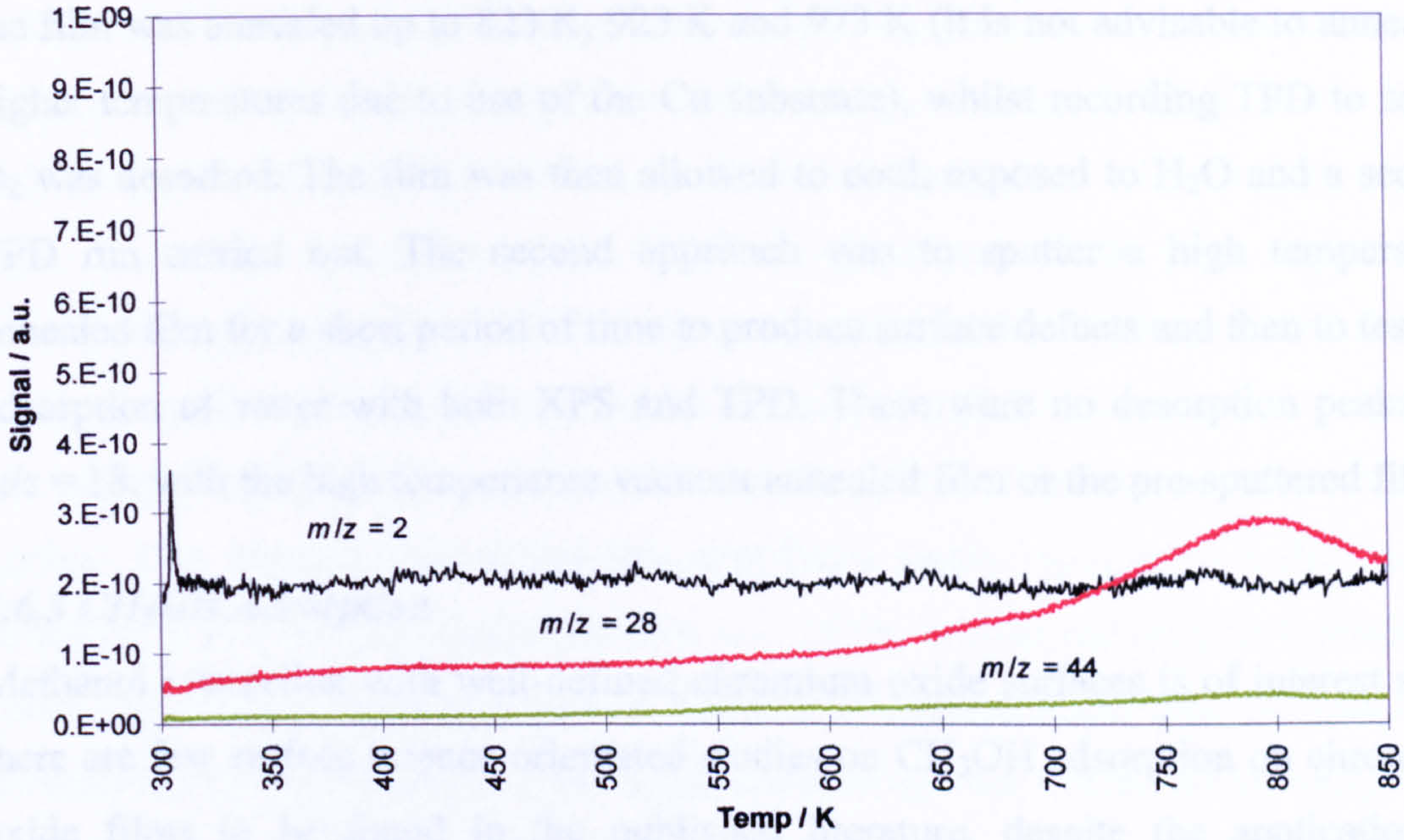

Figure 3.17: TPD spectrum of high temperature annealed film with no exposure to gas (blank test)

3.6.2 H_2O Adsorption

The study of water interaction with chromium oxide surfaces is considered important because water adsorption on chromia catalysts is known to result in reversible surface hydroxylation,[31,39,40,47] which is considered a key factor in determining the catalytic properties. Dissociatively adsorbed H_2O has also been seen by TPD to desorb at 345 K from $Cr_2O_3(0001)$.[31] In the present work, a low temperature annealed film was grown and grazing-emission XPS carried out. Although previous literature[40] reports that the uptake of water leads to slight high binding energy shoulders on the O 1s and Cr 2p peaks, in the current study no conclusive evidence of H_2O adsorption was observed by XPS. A TPD investigation of H_2O adsorption also failed to produce evidence for uptake. The TPD spectrum of the existing low temperature annealed film showed no desorption peak for m/z = 18. There were however weak peaks associated with m/z = 28 and 44 (CO and CO_2), (which are without doubt a result of the phenomenon discussed in 3.6.1). Previous literature has discussed how oxygen interacts strongly with chromium oxide surfaces, generating Cr=O species, essentially producing an oxygen terminated surface.[45] O_2 pre-adsorption is known to block dissociative H_2O adsorption channels.[31] Researches employ a number of methods to obviate this problem including annealing to T > 1000 K [39] and chemical treatment (*e.g.* reduction with CO).[38] It is possible that the procedures used in the current study for growing films produce an O-terminated surface. Therefore two attempts were made to try and activate the surface towards H_2O adsorption. Firstly, the film was annealed up to 823 K, 923 K and 973 K (it is not advisable to anneal at higher temperatures due to use of the Cu substrate), whilst recording TPD to see if O_2 was desorbed. The film was then allowed to cool, exposed to H_2O and a second TPD run carried out. The second approach was to sputter a high temperature annealed film for a short period of time to produce surface defects and then to test for adsorption of water with both XPS and TPD. There were no desorption peaks for $m/z = 18$, with the high temperature vacuum annealed film or the pre-sputtered film.

3.6.3 CH_3OH Adsorption

Methanol interaction with well-defined chromium oxide surfaces is of interest since there are few surface science orientated studies on CH_3OH adsorption on chromium oxide films to be found in the published literature, despite the application of chromium(III) oxide in methanol synthesis discussed in section 3.1.1. In the current work, some of the XPS data pointed in the direction of CH_3OH adsorption. For the high temperature annealed film there was a slight increase in the O 1s peak intensity after exposure to CH_3OH, which returned to the original intensity after annealing. There was no significant change in the C 1s peak. For the low temperature annealed film, however, there was a significant increase in the C 1s peak intensity after CH_3OH dosing, which returned to the original intensity after annealing. However in this latter case the O 1s peak did not increase, in fact it decreased very slightly. Since the data was normalised to the Cu $2p_{3/2}$ peaks, experimental error (*i.e.* variation in intensity from experiment to experiment) can be ruled out. Nonetheless, this data is not particularly conclusive. TPD was carried out on a high temperature annealed film. This was then repeated with a new film (to test reproducibility with different films) and the second film was tested twice more (to test reproducibility on the same film). There was no desorption for m/z values associated with CH_3OH (*i.e.* 31, 29, 15) in any of these experiments, which would have indicated molecular adsorption (or perhaps dissociation and re-association). There were however peaks for $m/z = 28$ and (at a lower level) 44, at a comparable level of intensity to those discussed in section 3.6.1. In some cases there are discrete peaks for $m/z = 28$ at 548 K and 648 K (like the sub-peaks mentioned in section 3.6.1) and in some cases a broader desorption feature at about 723 K. TPD was also carried out on a low temperature annealed film. This resulted in a broad desorption peak for *m/z* = 28 and 44, with a peak maximum at 788 K (CO) and 823 K (CO_2). Since all of these experiments result in CO and CO_2 adsorption at a comparable level and with similar temperatures to the peaks observed in the blank experiment discussed in section 3.6.1, it seems likely that these peaks too are the result of the factors suggested in 3.6.1, *i.e.* they do not arise from any interaction with CH_3OH, which would in part explain the inconsistency in the results. This is further supported by the observation that there is no H_2 desorption observed. Nevertheless it is not completely implausible that these other features are obscuring some peaks associated with CH_3OH interaction with the surface. One possible way to test this hypothesis would be to grow a film and to anneal it at 973 K. This should remove any of the carbon impurity and hence the peaks which were causing confusion. CH_3OH adsorption could then be tested. An alternative explanation is that when a gas is dosed into the system the pressure of all gases increase to some extent, and this could lead to some adsorption from CO and/or CO_2. It is quite possible that dissociative CH_3OH adsorption could be blocked by chemisorbed oxygen, in the same way as was discussed with respect to H_2O adsorption.

3.6.4 CO_2 Adsorption

A number of studies on CO_2 adsorption on chromium oxide films have already been undertaken by other researchers.[46,47,57] In the present work a high temperature annealed film was tested. XPS data was similar to that obtained for CH_3OH adsorption on the low temperature annealed film (*i.e.* an increase in the C 1s peak area but a slight decrease in the O 1s peak area). With respect to the TPD experiment, there was a broad desorption for *m/z* = 28 and (at a lower level) 44, at a comparable level to that seen before, with a sub-peak at 648 K. If there had have been a much more intense desorption then it would have been concluded that the peaks observed for CH_3OH adsorption may have been the result of small amounts of CO/CO_2 in the gas phase. At any rate in previous literature CO and CO_2 were adsorbed at temperatures well below those in the present work (although chemisorbed species were found to be stable up to room temperature.[46,57] It is likely that the peaks observed in the present study are the same as those observed in the blank test.

3.7 Summary

CrO_x films have been grown on Cu(111) in UHV by deposition of Cr metal and oxidation. The effect of different growth conditions and post-growth treatments were investigated, in particular by XPS and LEED. An oxidation temperature of 573 K was adequate to produce fully oxidised films with an estimated thickness of 1-2 nm and there was no significant difference in the XPS peaks for films grown at 673 K or 773 K. For higher oxidation temperatures (823 K and 873 K) there was a reduction in d_{CrOx} / d_{Cr} ratio (*i.e.* the thickness of oxide film obtained from a given thickness of Cr metal). This suggests that films grown below 773 K grow layer-by-layer resulting in a reasonably uniform film, whereas films grown at higher temperatures grow as 3D crystallites. Post annealing in vacuum of a film (grown at 673 K) showed the $CrO_x/Cu(111)$ system to be stable up to and including 873 K, but increasing breakdown occurred after annealing at 923 K and 997 K. Reduction in the O/Cr ratio suggests that the mechanism for film breakdown involves either loss of O_2 into the vacuum or diffusion of O into the Cu substrate. Angle-resolved XPS has revealed the films to be reasonably uniform throughout. Additionally there is reasonable evidence that the films are oxygen-terminated.

Films grown at oxidation temperatures up to and including 773 K were disordered, at 823 K were at an intermediate state and at 873 K were well-ordered. Additionally a disordered film grown at 673 K could be post annealed at 923 K or higher in vacuum to produce an ordered film. In the case of ordered films generated both during oxidation and by post annealing, it appears that the process of ordering coincides with film breakdown or change in morphology. All ordered structures resulted in a hexagonal LEED pattern, from which a surface unit cell constant of ~ 4.8 Å was extracted. This is consistent with chromium(III) oxide, α-Cr_2O_3, orientated with the (0001) plane parallel to the surface. The small difference with the bulk value of 4.95 Å may be evidence of the film structure deviating slightly from that of the bulk oxide. Above a film thickness of 2 nm, an extra pattern was observed that relates to a $(4/\sqrt{3} \times 4/\sqrt{3})R30^\circ$ overlayer structure associated with the oxide film.

The interaction of small molecules with the chromium oxide films were investigated with disordered "low temperature annealed" films and ordered "high temperature-annealed" films. Despite literature reports of dissociative adsorption of H_2O, no XPS or TPD evidence of adsorption were found on the low-T annealed film, even after post annealing to 997 K to induce ordering, or on a pre-sputtered high-T annealed film. There was some inconsistent XPS evidence of CH_3OH adsorption on both the low-T annealed film and high-T annealed film, in the form of an increase in C 1s and O 1s peaks upon adsorption and decrease upon desorption. With regards to TPD data there was no clear observation of desorption peaks associated with CH_3OH. Likewise there was no conclusive XPS or TPD evidence for CO_2 adsorption on a high-T annealed film. The inertness of these surfaces towards the probe molecules tested could be explained by the lack of surface Cr^{3+} sites due to oxygen-termination, as supported by the surface analysis.

References

1 C.H. Marcilly and B. Delmon, *J. Catal.* 1972, **24**, 336

2 D.W. Flick and M.C. Huff, *Appl. Catal. A Gen.* 1999, **187**, 13

3 S. Wang, K. Mutara, T. Hayakawa, S. Hamakawa and K. Suzuli, *Appl. Catal. A Gen.* 2000, **196**, 1

4 B. Grzybowska, J. Sloczyński, R. Grabowski, L. Keromnes, K. Wcislo and T. Bobińska, *Appl. Catal. A Gen.* 2001, **209**, 279

5 S.D. Rossi, G. Ferraris, S. Fremiotti, E. Garrone, G. Ghiotti, M.C. Campa and V. Indovina, *J. Catal.* 1994, **148**, 36

6 I. Takahara, W.C. Chang, N. Mimura and M. Saito, *Catal. Today*, 1998, **45**, 55

7 F. Cavani, M. Koutyrev, F. Trifirò, A. Bartolini, D. Ghisletti, R. Iezzi, A. Santucci and G.D. Piero, *J. Catal.* 1996, **158**, 236

8 B. Grzybowska, J. Sloczyński, R. Grabowski, K. Wcislo, A. Kolowska, J. Stoch and J. Zieliński *J. Catal.* 1998, **178**, 687

9 A. Hakuli, M.E. Harlin, L.B. Backman and A.I.O. Krause, *J. Catal*, 1999, **184**, 349

10 M.I. Zaki, M.A. Hasan and L. Pasupulety, *Appl. Catal. A Gen.* 2000, **198**, 247

11 P.W. Park and J.S. Ledford, *Ind. Eng. Chem. Res.* 1998, **37**, 887

12 JH Uhm, MY Shin, J Zhidong, JS Chung, *Appl. Catal. B Environ.* 1999, **22**, 293

13 M. Kulażyński, J.G.V. Ommen, J. Trawczyński and J. Walendziewski, *Appl. Catal. B Environ.* 2002, **36**, 239

14 S. Krishnamoorthy, J.A. Rivas and M.D. Amiridis, *J. Catal.* 2000, **193**, 264

15 C.Y. Lee, T.H. Jung and B.H. Ha, *Appl. Catal. B Environ.* 1996, **9**, 77

16 H.E. Curry-Hyde, H. Musch, A. Baiker, M. Schraml-Marth and A. Wokaun, *J. Catal.* 1992, **133**, 397

17 A. Maetaki and K. Kishi, *Surf. Sci.* 1998, **411**, 35

18 A. Maetaki, M. Yamamoto, H. Matsumoto and K. Kishi, *Surf. Sci.* 2000, **445**, 80

19 J.E. Macintyre (Ed.), *Dictionary of Inorganic Compounds, Volume 3*, Chapman and Hall, 1992, p.3078, 3079, 3081, 3088, 3092

20 R.B. King, *Encyclopedia of Inorganic Chemistry, Volume 2*, Wiley, 1994, p.668

21 H. Swada, *Mat. Res. Bulletin*, 1994, **29**, 239

22 http://ruby.colorado.edu

23 P.D. Battle, T.C. Gibb, S. Nixon and W.T.A. Harrison, *J. Solid State Chem*, 1988, **75**, 21

24 L.W. Finger and R.M. Hazen, *J. Appl. Phys*, 1980, **51**, 5362

25 H. Saalfeld, *Z. Krystallogr.* 1964, **120**, 342

26 R.E. Newnham and Y.M. de Haan, *Z. Krystallogr.* 1962, **117**, 235

27 J. Graham, *J. Phys. Chem. Solids.* 1960, **17**, 18

28 W.H. Zachariasen, *Skrifter utgitt av det Norske Videnskapelig-Akademi*, 1928, 1

29 M. Wilson, M. Exner, Y. Huang and M.W. Finnis, *Phys. Rev. B*, 1996, **54**, 15683

30 F. Rohr, M. Bäumer, H.J. Freund, J.A. Mejias, V. Staemmler, S. Müller, L. Hammer and K. Heinz, *Surf. Sci.* 1997, **372**, L291

31 M.A. Henderson and S.A. Chambers, *Surf. Sci.* 2000, **449**, 135

32 A.J. Rowley, M. Wilson and P.A. Madden, *J. Phys.: Condens. Matter*, 1999, **11**, 1903

33 C. Rehbein, N.M. Harrison and A. Wande, *Phys. Rev. B*, 1996, **54**, 14066

34 P.J. Lawrence, S.C. Parker and P.W. Tasker, *Commun. Am. Ceram. Soc.* 1988, **71**, 389

35 S.L.M. Schröder, G.D. Moggridge, T. Rayment and R.M. Lambert, *J. Physique*, 1997, **7**, 923

36 D. Scarano, A. Zecchina, S. Bordiga, G. Ricchiardi and G. Spoto, *Chem. Phys.* 1993, **177**, 547

37 S.C. York, M.W. Abee and D.F. Cox, *Surf. Sci.* 1999, **437**, 386

38 A. Zecchina, S. Coluccia, E. Guglielminotti and G. Ghiotti, *J. Phys. Chem.* 1971, **75**, 2774

39 D. Cappus, C. Xu, D. Ehrlich, B. Dillmann, C.A. Ventrice, K.A. Shamery, H. Kuhlenbeck and H.J. Freund, *Chem. Phys.* 1993, **177**, 533

40 V. Maurice, S. Cadot and P. Marcus, *Surf. Sci.* 2001, **471**, 43

41 T. Bredow, *Surf. Sci.* 1998, **401**, 82

42 A. Zecchina, S. Coluccia, L. Cerruti, E. Borello, *J. Phys. Chem.* 1971, **75**, 2783

43 D. Klissurski, K. Hadjiivanoy and A. Davydov, *J. Catal.* 1988, **111**, 421

44 J.S. Foord and R.M. Lambert, *Surf. Sci.* 1986, **169**, 327

45 B. Dillman, F. Rohr, O. Seiferth, G. Klivenyi, M. Bender, K. Homann, I.N. Yakovkin, D. Ehrlich, M. Bäumer, H. Kuhlenbeck and H.J. Freund, *Faraday Discuss. Chem. Soc.* 1996, **105**, 295

46 O. Seiferth, K. Wolter, B. Dillman, G. Klivenyi, H.J. Freund, D. Scarano and A. Zecchina, *Surf. Sci.* 1999, **421**, 176

47 A. Zecchina, S. Coluccia, E. Guglielminotti and G. Ghiotti, *J. Phys. Chem.* 1971, **75**, 2790

48 H. Ma, Y. Berthier and P. Marcus, *Appl. Surf. Sci.* 1999, **153**, 40

49 Y.V. Belokopytov, V.A. Kuzenetsov, K.M. Kholyavenko and S.V. Gerei, *J. Cat.* 1976, **44**, 1

50 J.A. Rodriguez, S. Chaturvedi, M. Kuhn, J.V. Ek, U. Diebold, P.S. Robbert, H. Geisler and C.A. Ventrice, *J. Chem. Phys.* 1997, **107**, 9146

51 C. Xu, M. Hassel, H. Kuhlenbeck and H.J. Freund, *Surf. Sci.* 1991, **258**, 23

52 D. Scarano, S. Bordiga, S. Bertarione, G. Ricchiardi and A. Zecchina, *Catal. Lett.* 2000, **68**, 185

53 G.E. Mullenberg, *Handbook of X-ray Photoelectron Spectroscopy*, Perkin-Elmer, 1979, p.72, 82

54 F.M. Capece, V. Di Castro, C. Furlani, G. Mattogno, C. Fragale, M. Gargano and M. Rossi, *J. Electron Spectrosc. Related Phenom,* 1982, **27**, 119

55 O. Crottaz, F. Kubel, H. Schmid, *J. Mat. Chem*, 1997, **7**, 143

56 W. Dannhauser and P.A. Vaughan, *J. Ammer. chem. soc*, 1955, **77**, 896

57 M. Pykavy, V. Staemmler, O. Seiferth, and H.J. Freund, *Surf. Sci.* 2001, **479**, 11

58 S.M. Johnston, A. Mulligan, V. Dhanak and M. Kadodwala, *Surf. Sci.* 2003, **530**, 111

Chapter 4:

Growth & Characterisation of $BaO_x/Cu(111)$

4.1 Literature Review of BaO_x Surface Science Studies

The alkaline earth metal oxide barium oxide is used in a number of applications and there has been some research interest into its surface chemistry.

4.1.1 Motivation for Surface Science Studies

Recently, BaO has been applied as a **NO_x storage/reduction catalyst** (in combination with Pt or similar noble metals), which has led to a large number of papers on this topic[1-11]. TWC's (three-way catalysts) are reasonably effective at oxidising CO and hydrocarbons - however in modern lean-burn (oxygen rich) engines, which are more economical, reduction of NO_x is difficult. In the early 1990's Toyota developed the NO_x storage concept, which makes use of (usually) Al_2O_3-supported BaO with a dispersed noble metal (*e.g.* Pt). The engine operates in lean-burn conditions, during which NO is oxidised to NO_2 on the Pt and becomes stored (as nitrate) on the BaO. At fixed intervals, the engine switches (for a much shorter period of time) to fuel rich operation, during which the stored NO_x is released and reduced to N_2 on the Pt. Although BaO acts as a storage medium, and it is the noble metal that clearly plays the important role in the actual catalytic reduction of NO_x, it is important to understand the interactions between NO_x and BaO as well as to study how the Pt interaction with BaO also affects the process. There is some debate as to the source of oxygen required to raise the state of nitrogen from +4 (as in NO_2) to +5 (as in NO_3^-). Possible sources include excess O_2 in the exhaust gas, or from reduction of another NO_x molecule.[4] There are also a number of catalytic studies of the effect of sulfur poisoning on model NO_x trap catalysts.[12-17] Asides from NO_x storage reduction catalysts there is some evidence that BaO may be of relevance to hydrocarbon oxidation,[18] although this appears to be as a thermal and morphological modifier (to Al_2O_3-supported Pd).

There are some **other applications** of BaO, many of which inspired the early surface science work on BaO surfaces. For example, a BaO monolayer adsorbed on tungsten is used in dispenser cathodes, since it reduces the work function.[19] As a consequence there have been a number of surface science studies of BaO on W.[19,20] Additionally, BaO has been used for electron emission applications[21,22] and a BaO thin film has been grown on a glass substrate in high vacuum (and then Cu deposited).[23] In terms of growth and characterisation of BaO thin films, there has been no published work on BaO grown on a copper substrate of any orientation.

4.1.2 Bulk Structure

Barium oxide, BaO, possesses the rock salt structure, which has the $Fm\bar{3}m$ (225) space group. This bulk structure can be envisaged as a face-centred cubic array of oxygen anions (O^{2-}), in which all the octahedral sites are occupied by the barium cations (Ba^{2+}), which are six-co-ordinated (see Figure 4.1). The cubic lattice cell parameters have been determined to be $a = b = c = 5.54$ Å.[24]

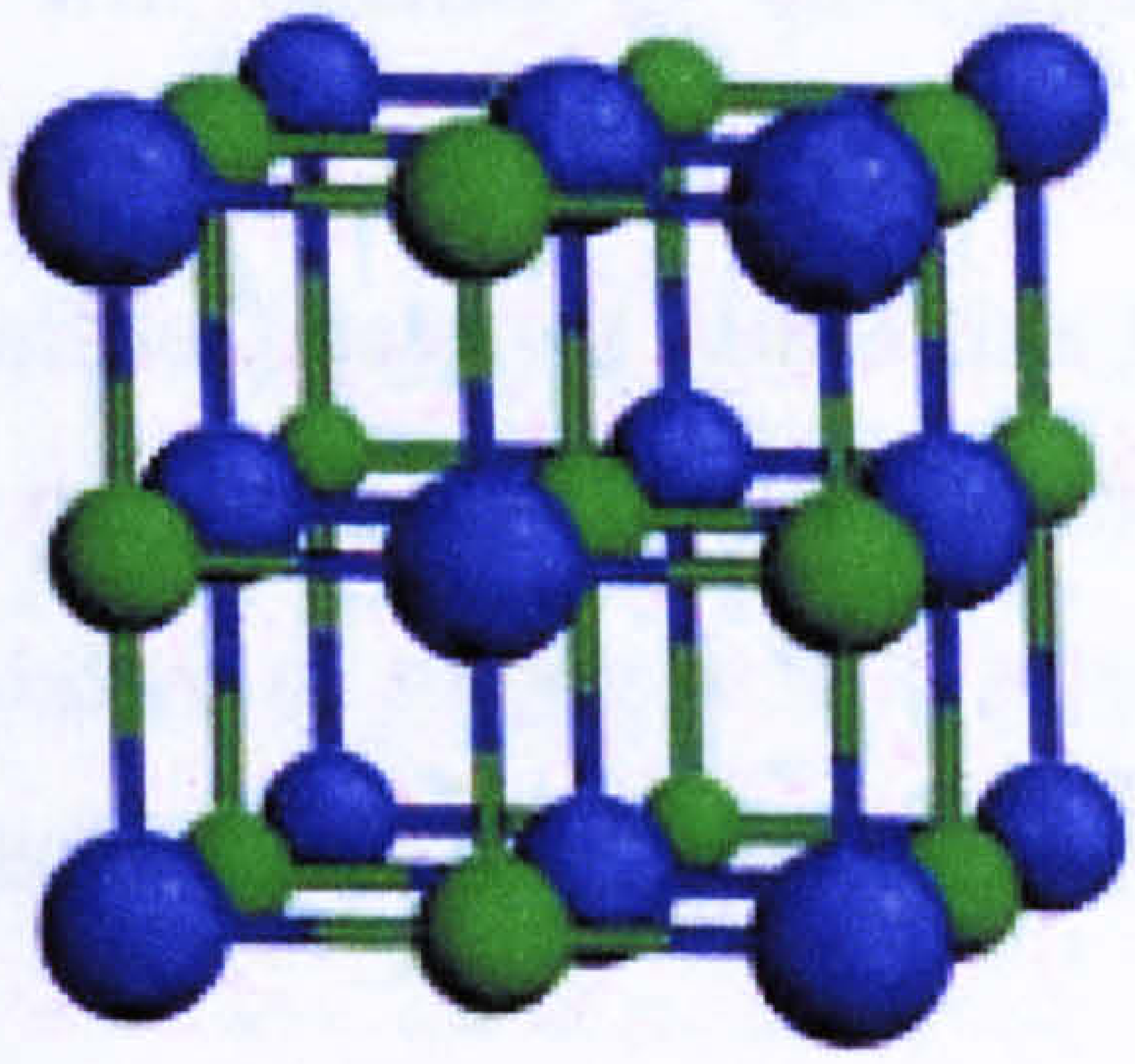

Figure 4.1: Bulk structure of BaO[25]

4.1.3 Surface Structure

The surfaces of BaO are not as well studied experimentally as other metal oxides, but there are also a handful of computational studies.[26,27] The BaO(100) surface consists of 5-fold co-ordinated Ba^{2+} cations and 5-fold co-ordinated O^{2-} anions. The BaO(100) surface is believed to be more stable than the BaO(110) surface – although the difference is less than in the case of Mg.[26] Relaxation and the occurrence of surface rumpling have been suggested by theoretical methods for both the (100) and (110) surfaces.

4.1.4 Surface Chemistry

As a result of the application of BaO to NO_x storage catalysis, there have been a significant number of studies of the interaction of BaO with **NO** and **NO_2**. Of these studies the majority are studies of prepared catalysts in flow reactors[1,3,4,6,8,9-11] making use of a variety of techniques including IR spectroscopy, surface characterisation techniques, XRD and BET. It has been widely found that the stored NO_x is in the form of surface nitrate and this has been proved by XRD and FTIR.[1,11]

In one study[1] on BaO/Al_2O_3 and noble metal/BaO/Al_2O_3 model catalysts, FTIR spectra showed characteristic nitrate peaks when NO_x was stored, but isocyanate peaks during catalyst regeneration by hydrocarbons. Another study[28] utilising IR and TPD on a model BaO/γ-Al_2O_3 catalyst identified bridging and chelating bidentate nitrates and monodentate nitrate resulting from NO/O_2 coadsorption. According to a Raman spectroscopy study[6] of BaO/MgO, nitrate ions are formed via a nitro (Ba^{2+} - NO_2^-) species. Presence of molecular O_2 suppresses the formation of the nitro species and increases the rate of nitrate formation. Above 673 K crystalline BaO_2 was detected, which can also transform nitro species into nitrate ions. Obviously in real applications these catalysts will operate in environments with other gas phase molecules present. An investigation[3] into the effect of different gas components on NO_x storage on a noble metal/BaO catalyst found that CO_2 increases the release of NO_x and this was explained by carbonates being thermodynamically favoured over nitrates. In contrast O_2 was shown to suppress NO_x release, which was explained by the thermodynamic O_2 stabilisation of the nitrate phase.

There is one UHV study of NO and NO_2 adsorption on a BaO thin film deposited on an Al substrate.[5] At high exposures of NO surface nitrates formed via molecular adsorption were evidenced by XPS, whereas for NO_2, surface nitrates were favoured, appearing to form via a nitrite intermediate. Additionally, there is a theoretical study of NO_x storage on a modelled BaO(100) surface,[7] which found the BaO(100) surface to be highly reactive towards NO_2. The reaction was initiated by NO_2 adsorption to form a nitrite over a Ba^{2+} site. A second NO_2 can either form a surface nitrite-peroxide pair or bind to an O^- surface site to generate a nitrate.

To the authors knowledge there are no further adsorption studies of molecules with well-defined BaO films in UHV. Due to application in dispenser cathodes, BaO overlayers on W(110) have been studied with respect to their interaction with H_2O, CO_2 and O_2.[19] This research found UPS evidence of surface OH and CO_3 species on W(110)-c(5 × 1)-BaO, W(110)-c(7 × 1)-BaO and W(110)-c(2 × 4)-BaO. It should however be recognised that interaction with the exposed W surface is also probable and that such overlayer structures do not necessarily relate very closely to an actual bulk-truncated BaO surface.

4.2 Growth in different Conditions

To investigate the effect of different conditions of growth on the structure of the BaO_x films generated, films were grown varying the deposition time and oxygen partial pressure. Table 4.1 shows the different films produced in the initial phase of this work and the conditions under which they were grown.

Film	Deposition Time	Deposition Current	Deposition Temperature	Partial Pressure O_2 (exposure)
A	5 min	14 A	Ambient	Vacuum
B	5 min	14 A	Ambient	Vacuum
C	5 min	14 A	Ambient	5×10^{-8} Torr (15 L)
D	5 min	14 A	Ambient	5×10^{-8} Torr (15 L)
E	2.5 min	14 A	Ambient	2×10^{-8} Torr (3 L)
F	5 min	14 A	Ambient	2×10^{-8} Torr (6 L)
G	1 min	14 A	Ambient	5×10^{-8} Torr (3 L)
H	1 min	14 A	723 K	5×10^{-8} Torr (3 L)

Table 4.1: BaO_x films grown and the conditions under which they were grown

In each case XPS was recorded prior to deposition to check that the Cu(111) substrate was suitably clean, following cleaning by argon ion sputtering, and to provide a substrate photoelectron peak intensity value used for estimating the thickness of the subsequently grown film. XPS was then recorded after deposition had taken place to characterise the film. Table 4.2 summarises the findings of the XPS data and Figures 4.2a and 4.2b show the O 1s and Ba $3d_{5/2}$ regions of films A-H.

From the attenuation of the Cu $2p_{3/2}$ photoelectron peak, the thickness of each film was estimated as discussed in chapter 2. The estimated values for films A-H are displayed in Table 4.3. Values of the estimated growth rate in nm per minute are also given, which permits comparison of the thickness of different films regardless of the deposition time.

Film A	Binding Energy (intensity)
O 1s (peak 1)	-
O 1s (peak 2)	531.4 eV (90000)
C 1s	285.3 eV (9100)
C 1s (carbonate)	290.1 eV (9600)
Ba $3d_{3/2}$	795.7 eV (113000)
Ba $3d_{5/2}$	780.5 eV (151000)

Film B	Binding Energy (intensity)
O 1s (peak 1)	528.3 eV (36000)
O 1s (peak 2)	531.7 eV (44000)
C 1s	284.5 eV (6300)
C 1s (carbonate)	290.1 eV (7400)
Ba $3d_{3/2}$	795.1 eV (110000)
Ba $3d_{5/2}$	779.9 eV (150000)

Film C	Binding Energy (intensity)
O 1s (peak 1)	528.4 eV (44000)
O 1s (peak 2)	531.1 eV (32000)
C 1s	284.5 eV (7000)
C 1s (carbonate)	290.1 eV (4000)
Ba $3d_{3/2}$	794.7 eV (118000)
Ba $3d_{5/2}$	779.3 eV (160000)

Film D	Binding Energy (intensity)
O 1s (peak 1)	528.6 eV (48000)
O 1s (peak 2)	531.0 eV (28000)
C 1s	284.5 eV (4200)
C 1s (carbonate)	-
Ba $3d_{5/2}$	779.3 eV (153000)

Film E	Binding Energy (intensity)
O 1s (peak 1)	528.8 eV (33000)
O 1s (peak 2)	530.9 eV (18000)
C 1s	284.5 eV (3900)
C 1s (carbonate)	-
Ba $3d_{5/2}$	779.4 eV (95000)

Film F	Binding Energy (intensity)
O 1s (peak 1)	529.6 eV (43000)
O 1s (peak 2)	530.9 eV (29000)
C 1s	284.5 eV (2900)
C 1s (carbonate)	-
Ba $3d_{5/2}$	779.5 eV (140000)

Film G	Binding Energy (intensity)
O 1s (peak 1)	528.9 eV (23000)
O 1s (peak 2)	531.3 eV (14000)
C 1s	285.5 eV (4800)
C 1s (carbonate)	-
Ba $3d_{5/2}$	779.3 eV (41000)

Film H	Binding Energy (intensity)
O 1s (peak 1)	529.4 eV (19000)
O 1s (peak 2)	-
C 1s	284.3 eV (4000)
C 1s (carbonate)	-
Ba $3d_{5/2}$	779.5 eV (25000)

Table 4.2: XPS data obtained from BaO_x films grown using the parameters specified in Table 4.1
A dash (-) means that no peak was distinguishable from the noise

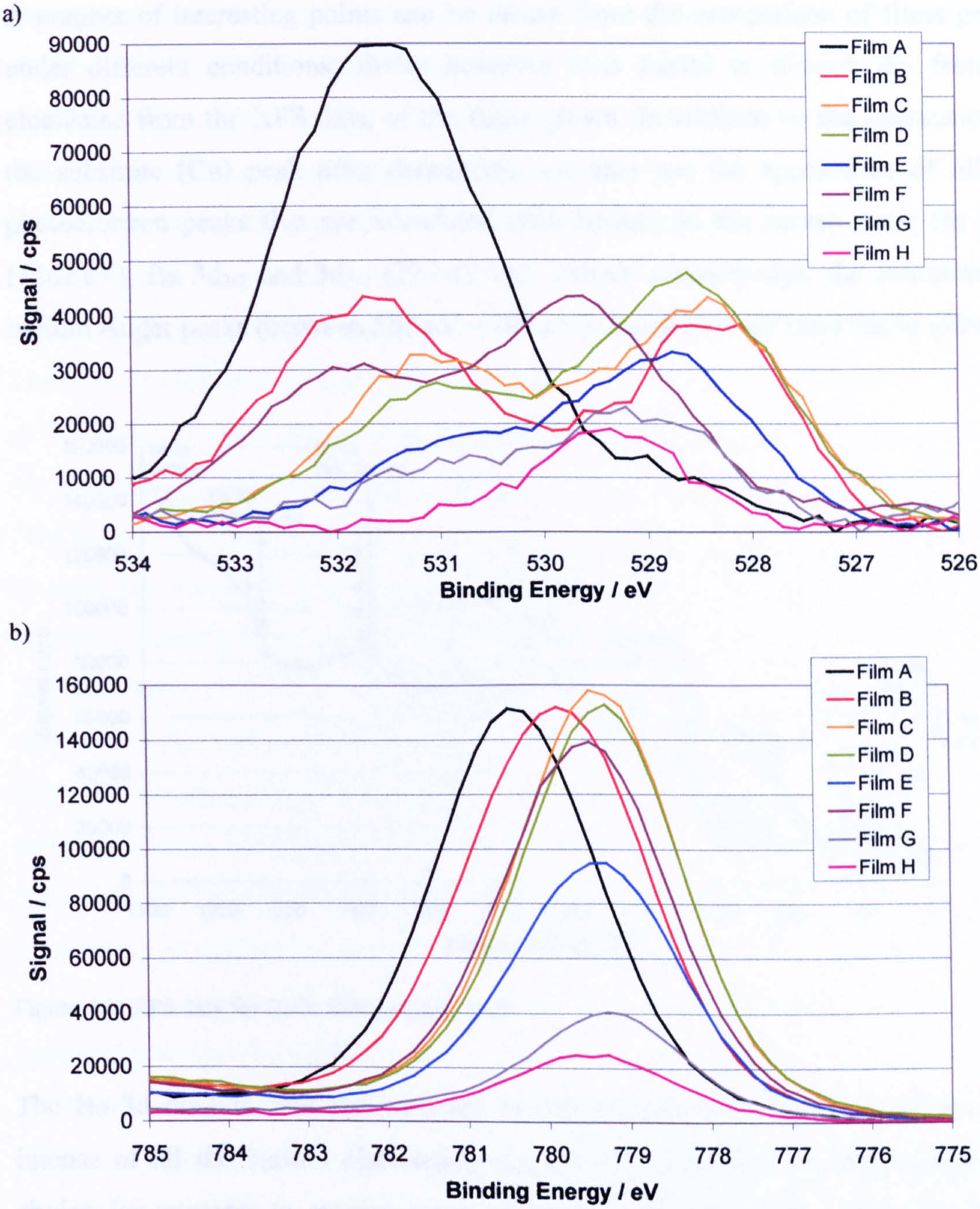

Figure 4.2: XPS data for films A-H a) O 1s region; b) Ba $3d_{5/2}$ region

Film	d_{BaO} / nm	d_{BaO} / nm.min^{-1}
A	2.2	0.44
B	2.0	0.40
C	2.1	0.42
D	2.2	0.44
E	0.9	0.36
F	2.3	0.46
G	0.6	0.6
H	0.4	0.4

Table 4.3: Estimated thickness of BaO_x films and growth rate

A number of interesting points can be drawn from the comparison of films grown under different conditions; firstly however it is useful to discuss the features, elucidated from the XPS data, of the films grown. In addition to the attenuation of the substrate (Cu) peak after deposition, we also see the appearance of all the photoelectron peaks that are associated with barium in the survey scan: Ba $3p_{3/2}$ (1062 eV), Ba $3d_{3/2}$ and $3d_{5/2}$ (795 eV and 780 eV respectively), the characteristic barium Auger peaks (between 550 eV – 700 eV), Ba 4p (177 eV) and Ba 4d (90 eV).

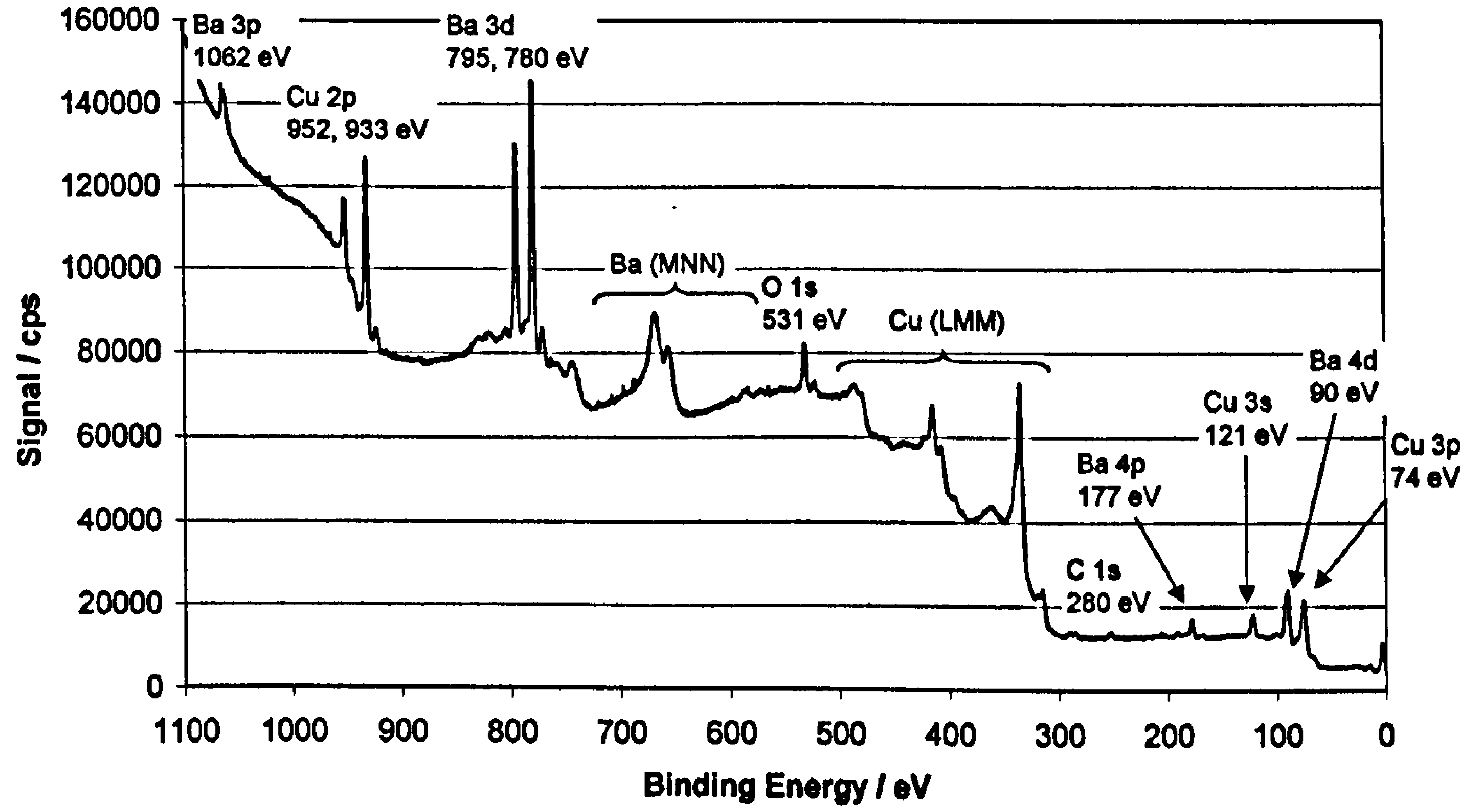

Figure 4.3: XPS data for BaO_x film (survey scan)

The Ba 3d doublet was also scanned at higher resolution because it is the most intense of all the barium photoelectron peaks and therefore the most appropriate choice for attempts to extract some chemical state information. From the higher resolution scan the Ba $3d_{3/2}$ and $3d_{5/2}$ peaks are found to have maxima at 794.7 eV – 795.7 eV and 779.3 eV - 780.5 eV respectively with a spin-orbit splitting of approximately 15.2 eV. The exact values seem to depend upon the conditions of preparation, as shall be discussed later. These values are in good agreement with those in the literature[29], which gives values of 795.05 eV and 779.65 eV with a 15.4 eV splitting for BaO. An alternative comparison is with the work of Koenig and Grant[30] who quote a value of 779.9 eV for the Ba $3d_{5/2}$ peak of oxidised Ba. At this point it is also worth mentioning that there is reason to believe that there may be some surface charging effects in this current work. These would result in small shifts in the binding energy values obtained.

The appearance of an O 1s peak at 530.9 eV – 531.7 eV (again depending on preparation conditions) after the deposition also shows that the film is at least partially oxidised. It should be borne in mind that XPS is more sensitive to barium $3d_{5/2}$ photoelectrons than the oxygen 1s photoelectrons by a factor of approximately 10 (with atomic sensitivity factors of 6.1 and 0.63 respectively[29]).

The XPS data can also be used for assessing the purity of the films generated. Carbon is a common impurity of films grown in ultra-high vacuum conditions and although a C 1s peak was not clearly evident in survey scans, the C 1s region was also recorded as a separate region using longer dwell-times and more scans (since XPS is not very sensitive to carbon, ASF for C 1s 0.205).[29] In the regional scans a C 1s peak can clearly be seen at around 284.4 eV. In addition, some of the films also exhibit a second peak at around 290.1 eV. Comparing the peak area of C 1s before and after BaO_x deposition we find a great deal of variation - it sometimes doubles (approximately) and sometimes decreases slightly. The second C 1s peak at about 290.1 eV binding energy is most likely to be as a result of the formation of some barium carbonate ($BaCO_3$) on the surface. A piece of information we can potentially draw from the O 1s region is whether the surface is hydroxylated. This could occur as a result of adsorption from the low level of background water vapour in the analytical chamber. If it was hydroxylated then one might expect to see some asymmetry in the O 1s peak or even a distinct shoulder. Unfortunately no previous literature could be found to support this. As shall be discussed later, the oxygen chemistry appears to be rather complicated. There are a number of oxygen species evident from the O 1s region and it may be that one of these is associated with hydroxide. Apart from carbon there was no XPS evidence for any other impurities. Particular attention was paid to the possible presence of peaks associated with platinum or rhodium (as the sample holder was made from Pt/Rh foil) or chlorine or iron (as the BaO lumps contain 0.1% Cl^- and 0.05% Fe), but none were found in the survey spectra obtained.

The film growth rate data of Table 4.3 will now be considered. In doing so it should be noted that the inelastic mean free path of the film is assumed to be that for an oxide system (1.72 nm). If, for example there were portions of unoxidised barium metal in the film, then the thickness may be underestimated. Secondly we are assuming here a rather simplistic model of an evenly dispersed oxide on the surface. In reality there may be variation in thickness on a macroscopic level or indeed at a nanoscale-level (*e.g.* islands of oxide, patches of uncovered substrate, and surface defects affecting film thickness). With one exception the variation in the values obtained for the different films is quite small - the smallest value being 0.36 nm/min for film E and the greatest 0.46 nm/min for film F. There are various possible reasons for the differences. Firstly it may be that there are differences in the metal/oxide flux, *i.e.* the deposition source is unstable. However, this would most likely manifest itself as a gradual decrease in flux, which is clearly not the case across the results presented. Secondly the difference may relate to the actual growth rate of the film, which may very well be affected by the conditions – in particular the gas-phase concentration of O_2. There are however no clear trends when one cross-references the growth rate with the preparation conditions. A third possibility for variation is that in dividing the thickness of the film by the deposition time to obtain a meaningful comparison we have overlooked the possibility that the rate of growth may vary over time, or that the estimated thickness may change over time due to changes in morphology with thickness (consider, for example, how a change from uniform coverage to island growth would affect the thickness estimation and hence how a film grown for one minute might be estimated to have a higher growth rate than one grown for 5 minutes). Finally of course, these thickness and growth rate estimations are all dependent upon the reproducibility of the XPS intensity data collected and this alone could lead to a significant variation in the estimated growth rate.

In conclusion, there appears little evidence for the growth rate being strongly dependent upon the variations in growth conditions, and the apparent variations that are seen are most likely to arise from variations in the time to establish the steady-state operation of the dosing source (most evident in the data for short deposition times) and changes in the composition of the film (discussed further below).

It is evident from the O 1s region of different films that the oxygen chemistry of these films is somewhat complicated. There are several peaks present, although not always at the same time. There is usually (except for film A) a peak at 528.3 eV – 529.6 eV which is named in the results (Table 4.2) as O 1s peak 1. From a review of the current literature concerning XPS studies of BaO (see Table 4.4) we can conclude that peak 1 is associated with lattice oxygen. All previous literature[30-34] refers to this peak at 528.4 eV. From the results of the current study there is clearly some variation in this value, which shall be discussed later.

Ba $3d_{5/2}$		**O 1s**	**C 1s**	**Reference**
Ba	**BaO**			
780.6 eV	779.9 eV	528.4 eV (lattice) 530.0 eV (adsorbed)		[30]
780.4 eV	779.2 eV	530.0 eV		[31]
		528.4 eV (lattice) 530.8 eV (O-containing adsorbates) 532.0 eV (carbonate)	290.6 eV (carbonate)	[32]
779.1 eV 781.0 eV	778.9 eV 779.4 eV	528.4 eV		[33]
		528.5 eV (lattice) 530.6 eV (O^-) 532.1 eV (OH^-)		[34]

Table 4.4: Previous XPS studies of BaO

In the results of the current study there is usually an additional peak at higher binding energy, which is referred to in Table 4.2 as O 1s peak 2. In actual fact this may arise from a number of different species which give rise to peaks with binding energies ranging from 530.9 eV – 531.7 eV. Such interpretation is only possible from analysis of other data (*e.g.* comparison with C 1s region to see if there is a correlation to surface carbonate, angle-resolved XPS, *etc.*) which will be dealt with in due course.

Films A and B were actually prepared using identical conditions, but the 0.6 eV difference in Ba $3d_{5/2}$ binding energy is indicative of inconsistencies in these early growth experiments. This is even more evident in a comparison of the O 1s region which is quite different for films A and B. In the case of film A there is no O 1s peak 1 (assigned to lattice O), but an intense peak at 531.4 eV, whereas film B has two peaks at 528.3 eV and 531.7 eV. There is clearly something fundamentally different about these two films, despite them being prepared in the same way. It may be that small partial pressures of background gases have a particularly profound effect on the films grown, especially in the absence of gas-phase oxygen. Comparison of the O 1s regions of all the films grown does clearly indicate that the oxygen-chemistry of these films is extremely variable which would be consistent with a high sensitivity to contamination by background gases. The O 1s peak of film A at 531.4 eV is clearly associated with a different oxygen/oxygen-containing species from the O^{2-} of the lattice which gives rise to the peak at around 528.4 eV in other films. This 531.4 eV peak of film A may be associated with O_2^{2-} (peroxide), OH^- (hydroxide) or CO_3^{2-} (carbonate). The higher C 1s signals for films A and B suggest that carbonate is the most likely possibility. Peak fitting and normalisation of the C 1s peak area at 290.1 eV and the O 1s peak area at 531.4 eV, reveals a stoichiometric ratio of 4.5. This value is very close to the value of 4.4 obtained for film D after exposure to CO_2 (discussed in section 4.6). The difference between these values and the expected value of 3 for carbonate could be due to the choice of atomic sensitivity factors. It should be noted, however, that the binding energy for the C 1s peak (believed to be carbonate) is 290.1 eV for film A and 289.5 eV for film D after CO_2 exposure.

Putting films A and B aside, all other films (prepared in more oxidising conditions) have Ba $3d_{5/2}$ peaks with similar binding energies (about 779.4 eV). Nonetheless, the O 1s regions are significantly different across all of the films grown. Films C and D were prepared in identical conditions. They both have two O 1s peaks at about 528.5 eV and 531.0 eV and film have similar overall O 1s intensities, but there is a small difference in intensity ratio between the O 1s peak 1 and 2. Overall this shows an acceptable reproducibility. The O 1s peak at approximately 531.0 eV is seen with films C, D, E, F and G. This is clearly a different O species from the O^{2-} in the lattice. This may or may not be the same species as that giving the peak at 531.4 eV for film A, but could be attributed to O_2^{2-} (peroxide), OH^- (hydroxide) or some similar species. Films F and H have an O 1s peak maximum at about 529.5 eV, rather than around 528.4 eV. This could again be indicative of a different oxygen species, but in the absence of further data it is difficult to reach any firm conclusion.

One of the main conclusions of the work discussed above is that there was a reproducibility problem, possibly caused by instability of the deposition source or adsorption of background gases. A number of experiments were therefore carried out to obtain a more reproducible method of film generation, using deposition in an oxygen atmosphere at elevated temperature. The refined method consisted of BaO_x deposition (5 min × 14 A, 15 L O_2) with a substrate temperature of 573 K. This was successful in producing films I, J and K with a single O 1s peak with a maximum at

529.2 eV and Ba $3d_{5/2}$ with a maximum at 779.3 eV. The XPS data is presented in Figures 4.4a and 4.4b.

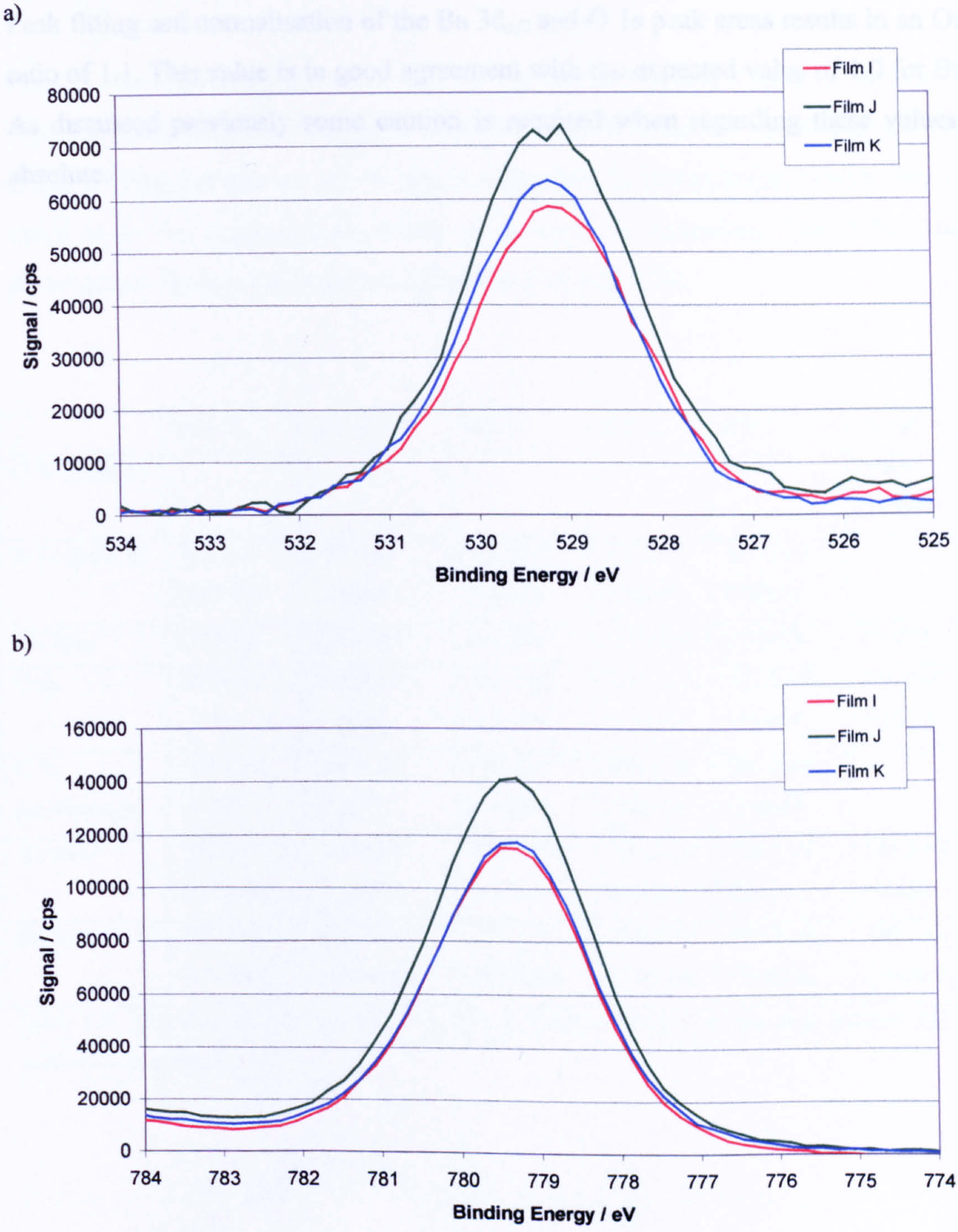

Figure 4.4: XPS data for films I, J and K a) O 1s region; b) Ba $3d_{5/2}$ region

A binding energy value of 529.2 eV for the O 1s peak associated with lattice O^{2-} is a little higher than the expected value of 528.4 eV from a variety of literature sources.[30-34] This cannot be the result of surface charging because the Ba $3d_{5/2}$ peak (at 779.3 eV) does not exhibit the same shift.

Peak fitting and normalisation of the Ba $3d_{5/2}$ and O 1s peak areas results in an O:Ba ratio of 1.1. This value is in good agreement with the expected value of 1.0 for BaO. As discussed previously some caution is required when regarding these values as absolute.

4.3 Post-Deposition Treatments

Some of the films described in section 4.2 were subsequently subjected to various treatments, including annealing at different temperatures and exposure to oxygen.

Film A was annealed at 373 K, 473 K, 573 K, 673 K and 773 K in vacuum for 5 minutes each time and allowed to cool so that XPS could be recorded to assess the extent of film breakdown and to observe changes in composition, which may give clues as to the processes occurring as a result of annealing. The XPS data is presented in Table 4.5 and shown in Figures 4.5a and 4.5b.

	Film A	**373 K**	**473 K**	**573 K**	**673 K**	**773 K**
O 1s (peak 1)	-	-	-	-	-	528.6 (24000)
O 1s (peak 2)	531.4 eV (90000)	531.6 eV (68000)	532.0 eV (74000)	532.2 eV (72000)	532.5 eV (70000)	-
Cu $2p_{3/2}$	(39000)	(27000)	(34000)	(350000)	(39000)	(59000)
C 1s	285.3 eV (9100)	285.5 eV (11000)	285.5 eV (11000)	285.1 eV (12000)	285.3 eV (10000)	285.3 eV (10000)
C 1s (carbonate)	290.1 eV (9600)	289.7 eV (8600)	289.0 eV (11000)	290.1 eV (12000)	290.3 eV (11000)	-
Ba $3d_{3/2}$	795.7 eV (113000)	795.9 eV (89000)	795.9 eV (95000)	795.9 eV (94000)	796.1 eV (92000)	795.3 eV (85000)
Ba $3d_{5/2}$	780.5 eV (151000)	780.5 eV (119000)	780.5 eV (128000)	780.7 eV (126000)	780.9 eV (123000)	780.1 eV (114000)

Table 4.5: XPS data for post annealing of film A: binding energies of the peak maxima and peak intensities (in parentheses).

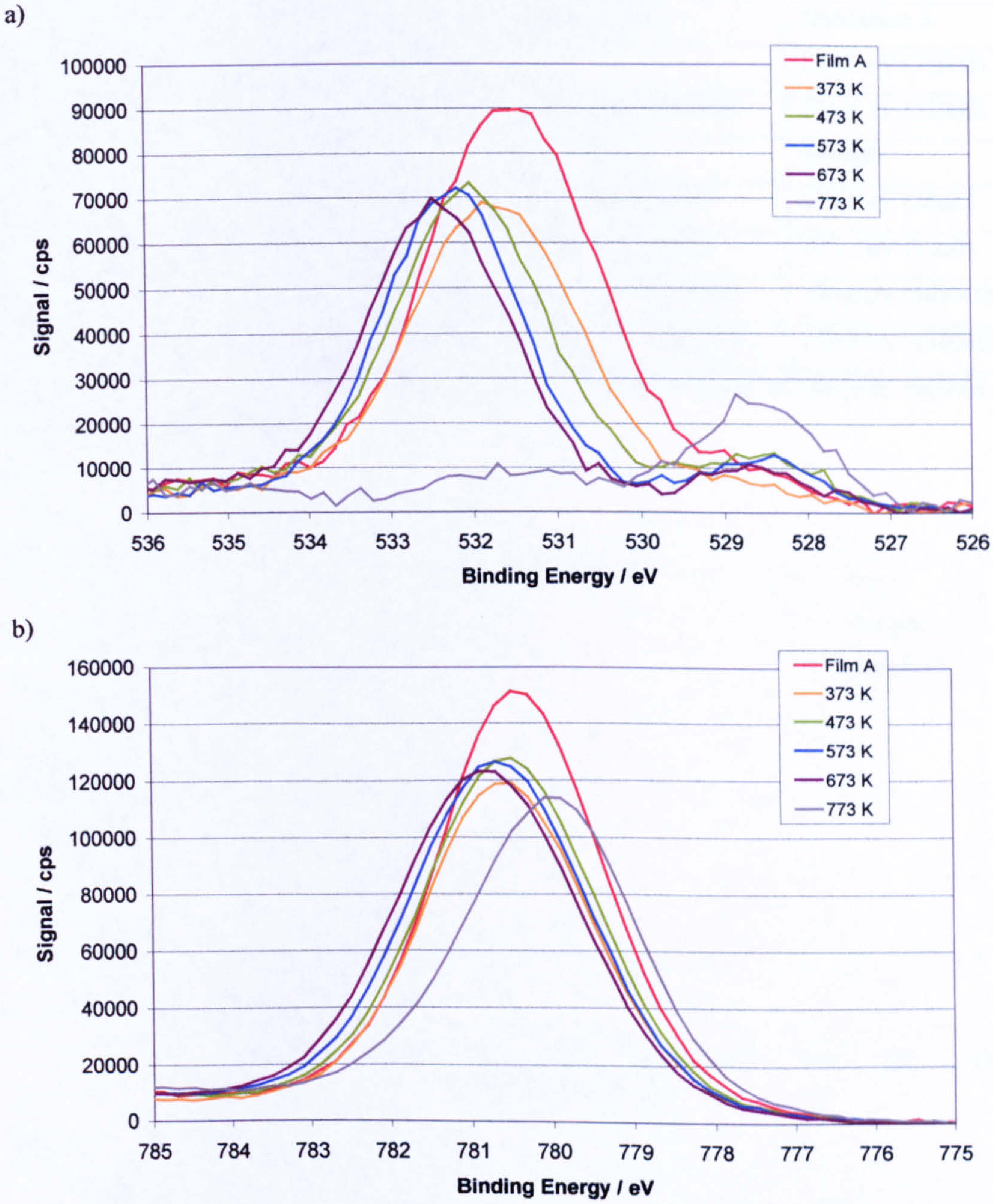

Figure 4.5: XPS data for the post annealing of film A for 5 min at each of the indicated temperatures (a) O 1s region; (b) Ba $3d_{5/2}$ region

Film B was exposed to 50 L (500 s at 10^{-7} Torr) O_2 at ambient temperature. The film was then heated up to 673 K during which it was exposed to 25 L (250 s at 10^{-7} Torr) O_2. Once at 673 K the film was exposed to a further 50 L (500 s at 10^{-7} Torr) O_2, before being allowed to cool. At each stage XPS was recorded to analyse the effect of the oxidation treatments. The XPS data is presented in Table 4.6 and shown in Figures 4.6a and 4.6b.

	Film B	Oxidation 1	Oxidation 2
O 1s (peak 1)	528.3 eV (36000)	-	528.3 eV (36000)
O 1s (peak 2)	531.7 eV (44000)	531.1 eV (106000)	531.7 eV (52000)
Cu $2p_{3/2}$	(38000)	(35000)	(40000)
C 1s	284.5 eV (6300)	284.5 eV (5000)	284.5 eV (4500)
C 1s (carbonate)	290.1 eV (7400)	290.1 eV (5800)	290.1 eV (7300)
Ba $3d_{3/2}$	795.1 eV (110000)	795.5 eV (130000)	795.0 eV (100000)
Ba $3d_{5/2}$	779.9 eV (150000)	780.3 eV (180000)	779.5 eV (130000)

Table 4.6: XPS data for post oxidation of film B: binding energies of the peak maxima and peak intensities (in parentheses).

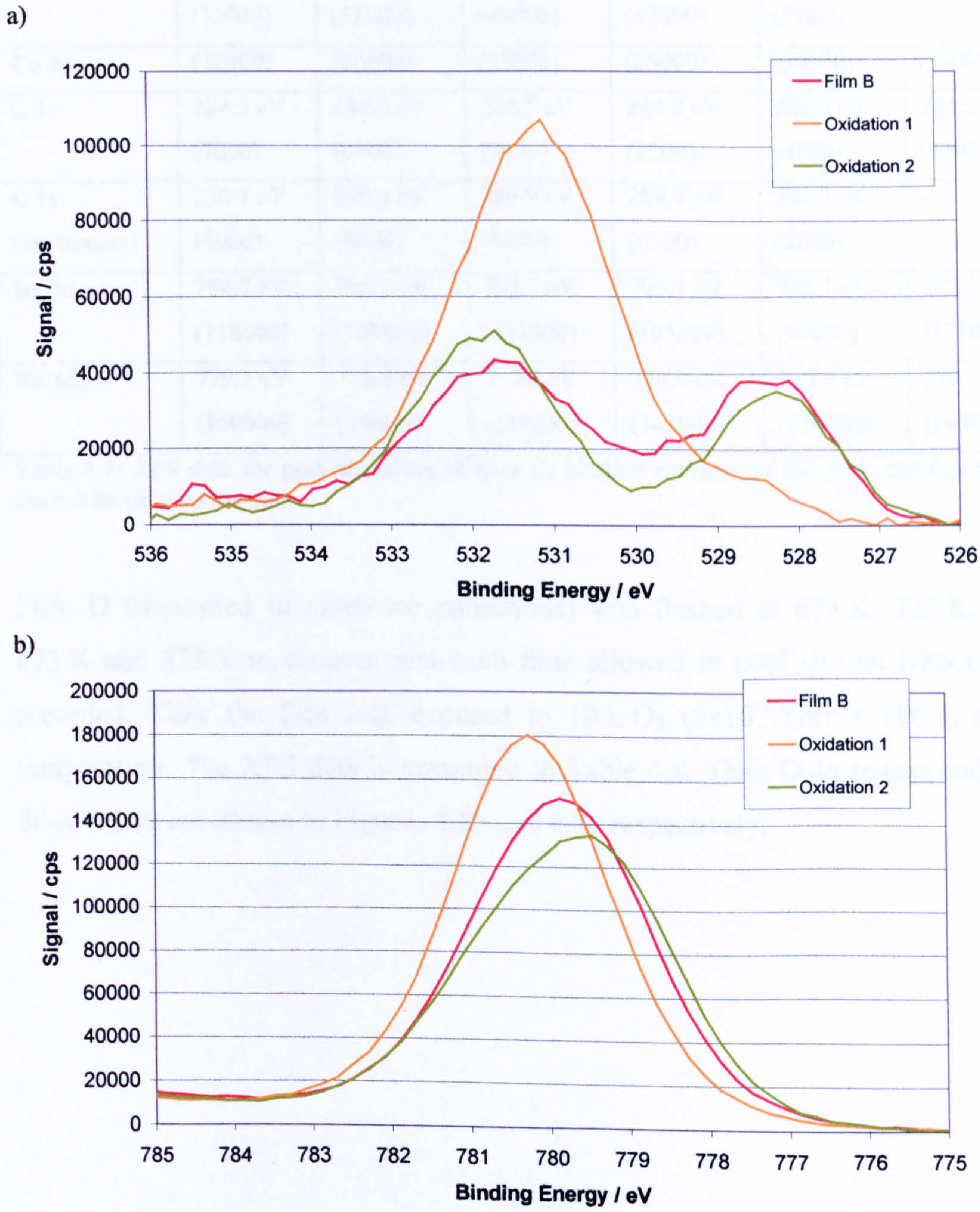

Figure 4.6: XPS data for the oxidation of film B (a) O 1s region; b) Ba $3d_{5/2}$ region; (Oxidation 1 = After exposure to 50 L O_2 at room temperature; Oxidation 2 = After exposure to 50 L O_2 at 673 K)

The film C (grown in oxidative conditions) was subsequently annealed at 373 K, 473 K, 573 K, 673 K and 773 K in vacuum for 5 minutes each time and allowed to cool so that XPS could be recorded. This data was compared with particular interest to the post-annealing of film A (which had not been grown in oxidative conditions). The XPS data is presented in Table 4.7 and in Figures 4.7a and 4.7b.

	Film C	**373 K**	**473 K**	**573 K**	**673 K**	**773 K**
O 1s (peak 1)	528.4 eV (44000)	529.2 eV (34000)	528.9 eV (40000)	528.7 eV (34000)	528.3 eV (34000)	528.7 eV (44000)
O 1s (peak 2)	531.1 eV (32000)	531.1 eV (51000)	531.4 eV (40000)	531.7 eV (42000)	532.0 eV (51000)	-
Cu $2p_{3/2}$	(32000)	(26000)	(30000)	(28000)	(30000)	(39000)
C 1s	284.5 eV (7000)	284.5 eV (6400)	284.5 eV (7000)	284.7 eV (6200)	284.7 eV (4700)	284.5 eV (5300)
C 1s (carbonate)	290.1 eV (4000)	290.1 eV (4400)	289.9 eV (5100)	289.7 eV (6300)	290.3 eV (8000)	-
Ba $3d_{3/2}$	794.7 eV (118000)	795.1 eV (109000)	795.1 eV (111000)	795.1 eV (105000)	795.1 eV (94000)	795.1 eV (111000)
Ba $3d_{5/2}$	779.3 eV (160000)	779.9 eV (146000)	779.7 eV (149000)	779.9 eV (141000)	779.9 eV (126000)	779.7 eV (149000)

Table 4.7: XPS data for post annealing of film C: binding energies of the peak maxima and peak intensities (in parentheses).

Film D (deposited in oxidative conditions) was flashed at 673 K, 723 K, 773 K, 823 K and 873 K in vacuum and each time allowed to cool so that XPS could be recorded. Then the film was exposed to 10 L O_2 (5×10^{-8} Torr × 200 s) at room temperature. The XPS data is presented in Table 4.8. Then O 1s region and the Ba $3d_{5/2}$ region are shown in Figures 4.8a and 4.8b respectively.

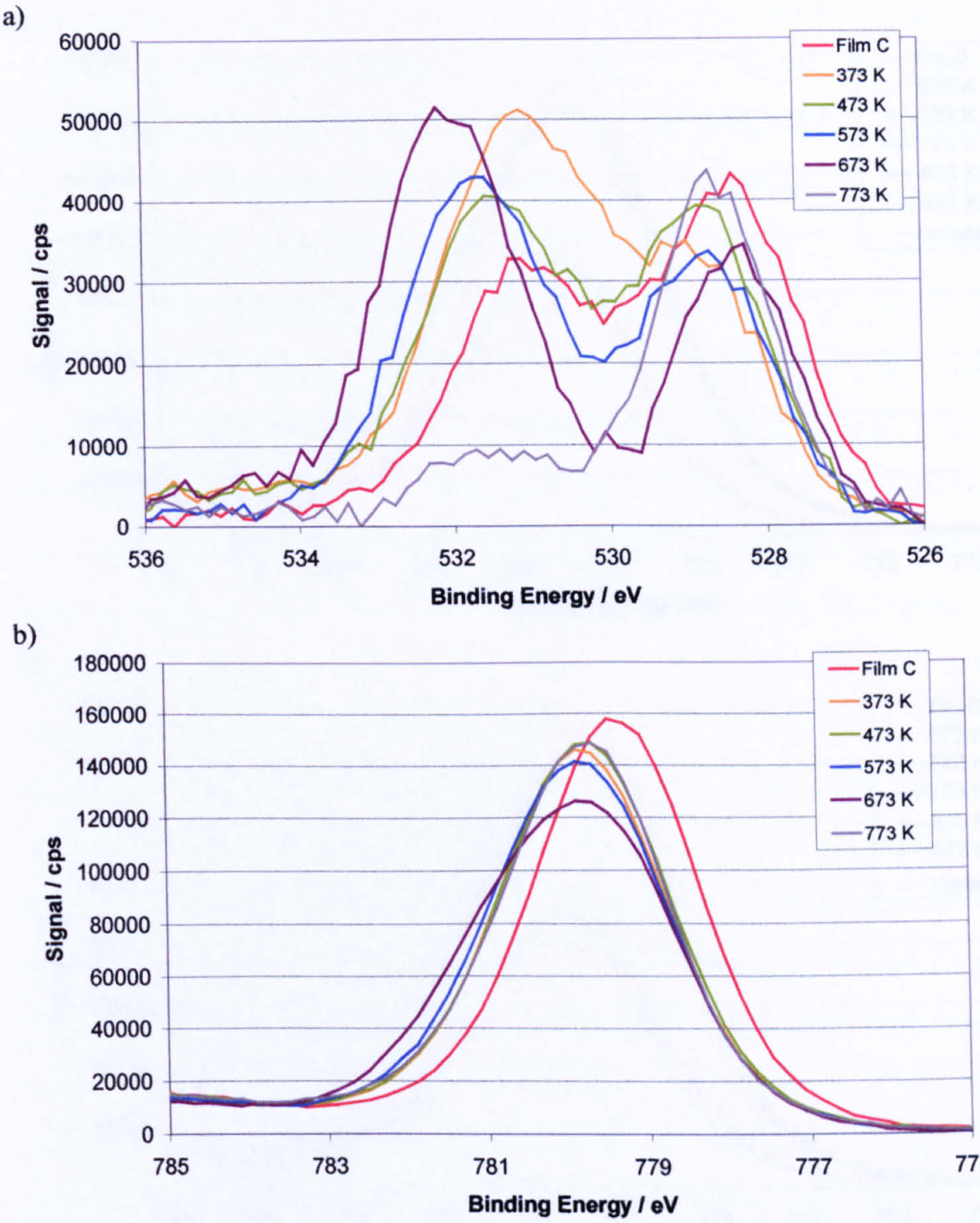

Figure 4.7: XPS data for the post annealing of film C for 5 min at each of the indicated temperatures a) O 1s region; b) Ba $3d_{5/2}$ region (grey trace is behind green)

	Film D	**673 K**	**723 K**	**773 K**	**823 K**	**873 K**	**10 L O_2**
O 1s (peak 1)	528.6 eV (48000)	528.6 eV (42000)	528.6 eV (40000)	528.2 eV (41000)	528.6 eV (27000)	528.6 eV (28000)	528.6 eV (21000)
O 1s (peak 2)	531.0 eV (28000)	531.6 eV (34000)	531.6 eV (42000)	531.6 eV (40000)	-	-	530.7 eV (27000)
Cu $2p_{3/2}$	(29000)	(30000)	(32000)	(34000)	(77000)	(77000)	(64000)
C 1s	284.5 eV (4200)	284.5 eV (25000)	284.5 eV (17000)	284.5 eV (22000)	284.5 eV (31000)	284.5 eV (27000)	284.5 eV (25000)
C 1s (carbonate)	-	289.7 eV (5700)	289.7 eV (6600)	289.7 eV (6800)	-	-	-
Ba $3d_{5/2}$	779.3 eV (153000)	779.5 eV (139000)	779.4 eV (131000)	779.4 eV (142000)	779.5 eV (91000)	779.6 eV (89000)	779.5 eV (78000)

Table 4.8: XPS data for post flashing of film D

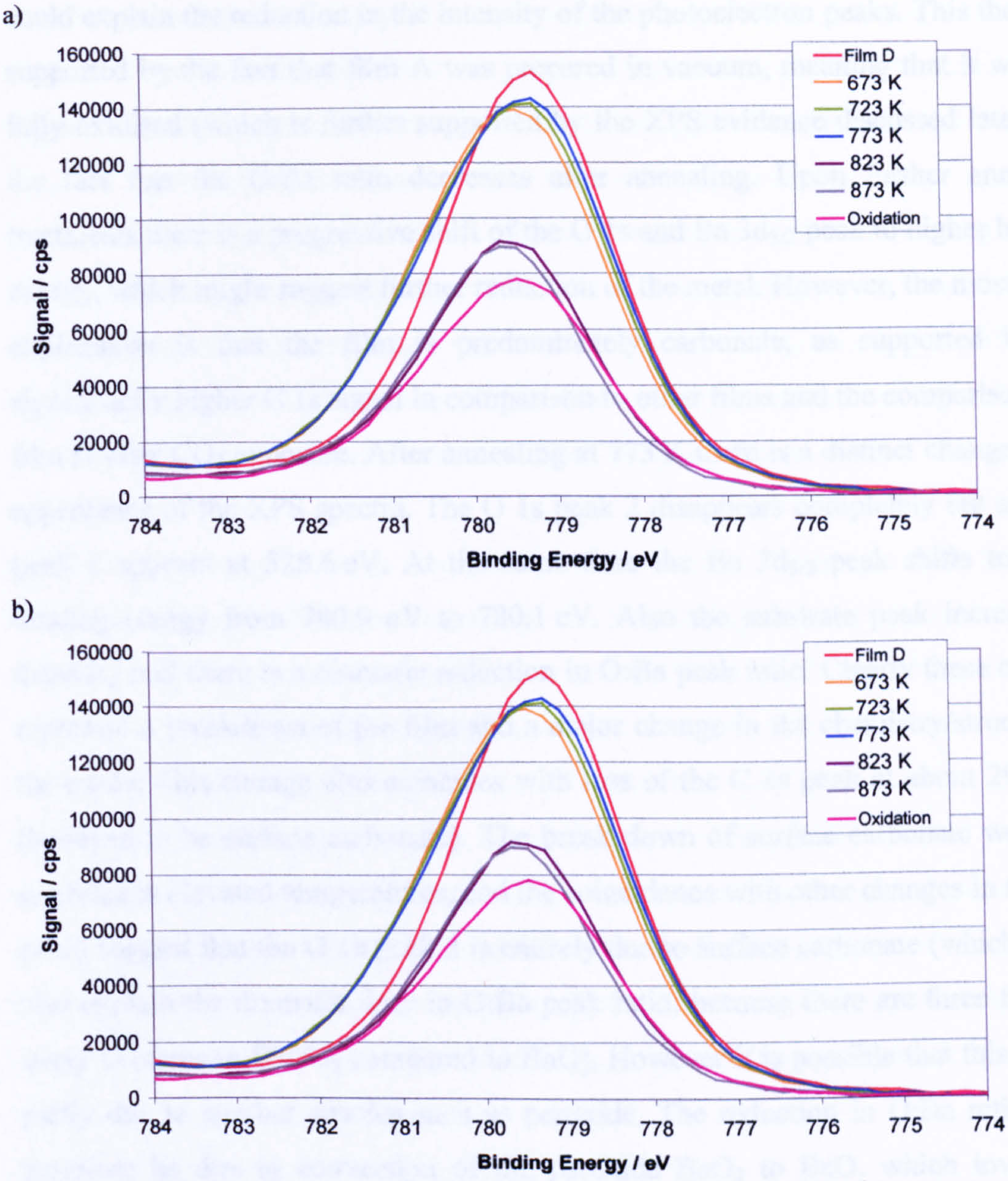

Figure 4.8: XPS data for the post flashing of film D at each of the indicated temperatures a) O 1s region; b) Ba $3d_{5/2}$ region; (Oxidation = After exposure to 10 L O_2 at room temperature)

The post deposition treatments used here can be divided into 2 types: heating (annealing or flashing) or oxidation. Film A (grown in vacuum conditions) was annealed in 373 K increments from 373 K up to 773 K for 5 minutes each time. Even upon annealing to 373 K there is a reduction in O 1s and Ba $3d_{5/2}$ peak intensity. The substrate peak (Cu $2p_{3/2}$) also decreases in intensity. This might be due to experimental error (occasionally the intensities vary from experiment to experiment) or, if real, an indication that the barium layer is changing in both composition and morphology. One possibility is that as the film is heated oxygen is lost, either to the vacuum or by diffusion into the substrate, leaving behind portions of unoxidised barium metal. The inelastic mean free path of electrons is lower in a metal which could explain the reduction in the intensity of the photoelectron peaks. This theory is supported by the fact that film A was prepared in vacuum, meaning that it was not fully oxidised (which is further supported by the XPS evidence discussed later) and the fact that the O:Ba ratio decreases after annealing. Upon further annealing treatments there is a progressive shift of the O 1s and Ba $3d_{5/2}$ peak to higher binding energy, which might suggest further reduction of the metal. However, the most likely explanation is that the film is predominately carbonate, as supported by the significantly higher C 1s signal in comparison to other films and the comparison with film D after CO_2 exposure. After annealing at 773 K there is a distinct change in the appearance of the XPS spectra. The O 1s peak 2 disappears completely but an O 1s peak 1 appears at 528.6 eV. At the same time the Ba $3d_{5/2}$ peak shifts to lower binding energy from 780.9 eV to 780.1 eV. Also the substrate peak increases in intensity and there is a dramatic reduction in O:Ba peak ratio. Clearly these changes represent a breakdown of the film and a major change in the chemistry/structure of the oxide. This change also coincides with loss of the C 1s peak at about 290.1 eV (believed to be surface carbonate). The break down of surface carbonate would be expected at elevated temperatures, and the coincidence with other changes in the film could suggest that the O 1s peak 2 is entirely due to surface carbonate (which would also explain the dramatic drop in O:Ba peak ratio, because there are three times as many O atoms in $BaCO_3$ compared to BaO). However it is possible that this peak is partly due to another species such as peroxide. The reduction in O:Ba ratio could therefore be due to conversion of the peroxide BaO_2 to BaO, which involves a reduction in O:Ba stoichiometry. It is known that BaO_2 melts around 723 K and loses oxygen at around 1073 K,[35] but in vacuum or near the surface this may be different. Some possible reactions are shown below.

$BaO_2 \rightarrow BaO + \frac{1}{2}O_2$

$BaCO_3 \rightarrow BaO + CO_2$

$Ba(OH)_2 \rightarrow BaO + H_2O$

Unlike film A, film C was prepared in more oxidising conditions. Film C was annealed in the same way as film A. After annealing to 373 K O 1s peak 1 decreased and O 1s peak 2 increased (a peak swap-over) and the Ba $3d_{5/2}$ peak shifted to higher binding energy (779.3 eV to 779.9 eV). It seems that O 1s peak 2 is associated with a higher binding energy state of Ba. This is discussed again in section 4.6 where angle-resolved XPS data is presented. With further incremental annealing, there is a gradual shift of O 1s peak 2 to higher binding energies, but no corresponding shift of the Ba $3d_{5/2}$ peak. After annealing at 773 K there is again an apparent breakdown and transformation of the film. Again the O 1s peak 2 disappears, leaving just the O 1s peak 1 at 528.7 eV. As in the case of film A it appears the breakdown coincides with loss of the C 1s peak believed to be associated with carbonate.

Film D was prepared in an identical manner to film C, but the post treatment involved flashing (rather than annealing) the film and greater attention was paid to the temperatures near breakdown (50 K increments from 673 K to 873 K). The same swap-over was observed upon initial heating, as was seen with film C, but to a lesser extent. Film breakdown again occurred, but not until 823 K. The different temperature can be explained by the difference in heating duration (a period of seconds rather than 5 minutes at each temperature). In the O 1s region the breakdown and transformation is characterised by an increase of peak 1 intensity and a decrease of peak 2 intensity. On this occasion peak 2 does not disappear completely. Interestingly re-exposing the film to 10 L O_2 swaps the O 1s peaks back again. This could suggest the following process:

$BaO + \frac{1}{2}O_2 \rightarrow BaO_2$

This does not necessarily mean that film breakdown is the reverse of this process.

Film B was grown in vacuum conditions, but then exposed to oxygen at ambient temperature and then at 673 K. After the first oxidation the O 1s peak 1 (at 528.3 eV) and O 1s peak 2 (at 531.7 eV) transformed to just one peak at 531.1 eV (which was slightly more intense than the sum of the previous two peaks). At the same time the Ba $3d_{5/2}$ peak shifted from 779.9 eV to 780.3 eV. It is not clear if the original peak at 531.7 eV is the same species as the resulting 531.1 eV peak and that the shift is due to the change in environment. The second oxidation at elevated temperature appeared to convert the oxide back to its pre-oxidation form. One explanation is that the film is initially a mixture of BaO and $BaCO_3$ and that the oxidation at room temperature converts the BaO to BaO_2. The heating then breaks down the BaO_2 but not the $BaCO_3$ (as evidenced by the C 1s peak still remaining).

4.4 Conditions for Ordering

Various attempts were made to prepare ordered films. Much thinner films were grown than before to assist the ordering process. Films were grown in one minute steps each time subjecting the film to various heat treatments and at each stage the film was allowed to cool and LEED used to assess which conditions are required for ordering. This was carried out in conjunction with XPS to correlate surface compositional changes with any observed ordering of the sample, so as to increase our understanding of the ordering process.

A film (previously described as film G) was grown (with a deposition source current of 14 A for 1 minute at an O_2 partial pressure of 5×10^{-8} Torr – 3 L) and subsequently flashed at 723 K and then 823 K (in vacuum). After this point what had been a diffuse background in LEED (associated with lack of order) transformed into an extra pattern with spots superimposed upon the Cu(111) substrate pattern. This pattern was however somewhat unclear. After a further deposition, in an identical manner to the first, the film was again flashed this time at 723 K, 773 K and 823 K. The extra pattern was still visible at this stage, but still hard to discern. A third and final deposition was followed by flashing at 723 K and 823 K. The film was then annealed at 723 K and 823 K each time for 5 minutes, flashed to 873 K and finally annealed for 5 minutes at 873 K. Throughout these steps there was no improvement in the clarity of the LEED pattern. The XPS data is presented in Table 4.9.

A second film (previously described as film H) was grown in an identical manner to the previous film (G) (with a deposition source current of 14 A for 1 minute at an O_2 partial pressure of 5×10^{-8} Torr – 3 L) except that the substrate was at a temperature of 723 K during this period. (Prior to this the Cu(111) substrate had been exposed to an O_2 partial pressure of 5×10^{-8} Torr (3 L) to confirm that it would not be oxidised by this treatment – no substrate oxidation was evidenced). The resulting film was then flashed to 773 K and 873 K in vacuum and then annealed at 773 K for 5 minutes. A further 1 minute deposition was carried out, as before, and finally the film was annealed at 773 K for 5 minutes in vacuum. Even after the first deposition, the image observed by LEED was clearer in comparison to the previous experiment (with film G). After the annealing step at 773 K the LEED patterns shown in Figure

4.9a and 4.9b were recorded. After the second deposition the image was again diffuse, but clearer after the annealing at 773 K. The XPS data is presented in Table 4.10.

	Film G	**723 K**	**823 K**	**Deposition**	**723 K**	**773 K**	**823 K**
O 1s (peak 1)	528.9 eV (23000)	529.2 eV (20000)	529.1 eV (17000)	529.1 eV (25000)	528.9 eV (25000)	528.9 eV (24000)	528.9 eV (25000)
O 1s (peak 2)	531.3 eV (14000)	-	-	531.3 eV (16000)	-	-	-
Cu $2p_{3/2}$	(73000)	(78000)	(79000)	(52000)	(57000)	(55000)	(63000)
C 1s	-	-	-	-	-	-	-
Ba $3d_{5/2}$	779.3 eV (41000)	779.5 eV (34000)	779.5 eV (37000)	779.4 eV (58000)	779.3 eV (55000)	779.3 eV (55000)	779.3 eV (59000)

	Deposition	**723 K**	**823 K**	**823 K Anneal**	**823 K Anneal**	**873 K**	**873 K Anneal**
O 1s (peak 1)	528.8 eV (24000)	528.8 eV (25000)	528.7 eV (28000)	528.8 eV (26000)	528.8 eV (26000)	528.6 eV (21000)	528.6 eV (16000)
O 1s (peak 2)	531.3 eV (18000)	531.5 eV (19000)	-	-	-	-	-
Cu $2p_{3/2}$	(42000)	(48000)	(56000)	(59000)	(60000)	(59000)	(60000)
C 1s	-	-	-	-	-	-	-
Ba $3d_{5/2}$	779.5 eV (79000)	779.5 eV (80000)	779.3 eV (74000)	779.3 eV (70000)	779.3 eV (72000)	779.4 eV (63000)	779.5 eV (49000)

Table 4.9: XPS data for the ordering of film G

	Film H	**773 K**	**873 K**	**773 K Anneal**	**Deposition**	**773 K Anneal**
O 1s (peak 1)	529.4 eV (19000)	529.4 eV (19000)	529.4 eV (18000)	529.4 eV (16000)	529.2 eV (25000)	529.4 eV (22000)
O 1s (peak 2)	-	-	-	-	-	-
Cu $2p_{3/2}$	(80000)	(81000)	(88000)	(87000)	(63000)	(73000)
C 1s	-	-	-	-	-	-
Ba $3d_{5/2}$	779.5 eV (25000)	779.5 eV (25000)	779.7 eV (22000)	779.7 eV (22000)	779.3 eV (35000)	779.5 eV (30000)

Table 4.10: XPS data for ordering of film H

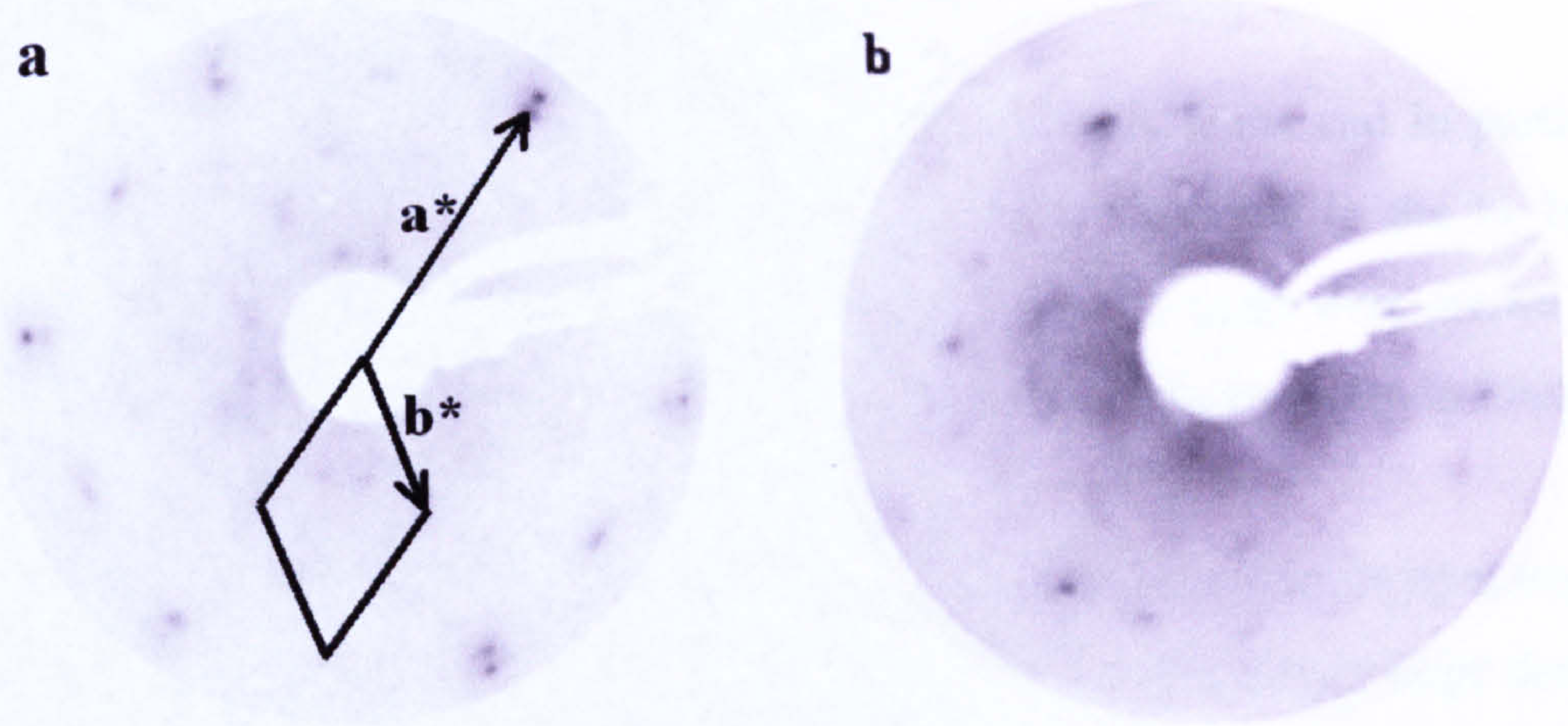

Figure 4.9: LEED pattern observed from film H a) with beam energy 65 eV; b) with beam energy 115 eV; the Cu(111) substrate spots are the outermost of the pair of spots near the edge of the screen

Although still rather unclear, the LEED pattern appears to consist of more than one domain. There seems to be a hexagonal structure with a lattice cell constant of 5.4 (±0.1) Å. This structure is 2.1 × 2.1 with respect to the underlying Cu(111) substrate. Additionally there are other spots present that must relate to some other structure. With the lack of clarity, however it is not possible to make any firm assertions as to this structure. The hexagonal structure does not relate to a possible termination of the bulk structure of rock-salt-type BaO. It therefore appears as if the oxide adopts a structure dictated by the substrate at this thickness.

The importance of growing ordered films is not just to investigate the conditions required for ordering, and thus to increase the understanding of the ordering process and the BaO_x films themselves, but also because the production of ordered films would be very useful for studying the interaction of small molecules with these surfaces. After all it is the study of well-defined systems that allows us to better understand surface chemistry at a fundamental level. Clearly from the results obtained in this study, there was some success in generating ordered BaO_x films; nevertheless this success was somewhat limited. The LEED patterns obtained show spots that are not associated with the substrate, but the image was not very clear. This probably means that the film was not uniformly ordered, but that there were some ordered domains. Some post-deposition annealing treatment was also required to obtain the LEED pattern. Some breakdown of the film (evidenced by an increase in the substrate photoelectron peak intensity) was observed with heating and the onset of such changes often coincides with the ordering of the oxide.

4.5 Angle-Resolved XPS

In order to understand further the structure of the BaO_x films and in particular the oxygen chemistry (*i.e.* the different oxygen species observed in the O 1s region) angle-resolved XPS measurements were carried out. Two films were grown for these experiments which differed in deposition time and consequently also in thickness.

Film E was grown with a deposition time of 2.5 minutes and an oxygen exposure of just 2×10^{-8} Torr (3 L). The film was then exposed to increasingly large doses of O_2: 5 L (5×10^{-8} Torr for 100 s), 10 L (5×10^{-8} Torr for 200 s) and 20 L (5×10^{-8} Torr for 400 s). XPS data from these post-oxidation treatments was recorded at the normal electron detection emission angle of 15° to the surface normal) and is presented in Table 4.11.

	Film E	5 L O_2	10 L O_2	20 L O_2
O 1s (peak 1)	528.8 eV (33000)	528.9 eV (32000)	528.9 eV (31000)	528.9 eV (29000)
O 1s (peak 2)	530.9 eV (18000)	530.6 eV (39000)	530.6 eV (40000)	530.6 eV (40000)
Cu $2p_{3/2}$	(55000)	(54000)	(54000)	(53000)
C 1s	-	-	-	-
Ba $3d_{5/2}$	779.4 eV (95000)	779.5 eV (99000)	779.5 eV (99000)	779.5 eV (100000)

Table 4.11: XPS data for the post oxidation of film E

The film was then flashed in vacuum at progressively higher temperatures: 723 K, 773 K, 823 K, and 873 K. After each treatment, XPS was recorded with the usual emission angle of 15° from the sample normal. However after the flash at 723 K where two well-defined peaks were observable in the O 1s region, the XPS spectrum of all regions was additionally recorded using emission angles of 45° and 75° (*i.e.* grazing emission). After the final flash at 873 K the O 1s region was also recorded with an emission angle of 75°. All of this XPS data is summarised in Table 4.12. The O 1s, C1s and Ba$3d_{5/2}$ regions are presented in Figures 4.10a, 4.10b and 4.10c respectively.

	723 K $\theta = 15°$	723 K $\theta = 45°$	723 OK $\theta = 75°$	773 K	823 K	873 K $\theta = 15°$	873 K $\theta = 75°$
O 1s (peak 1)	528.8 eV (27000)	528.8 eV (33000)	528.8 eV (28000)	528.6 eV (24000)	528.6 eV (19000)	528.8 eV (19000)	528.9 eV (24000)
O 1s (peak 2)	531.5 eV (21000)	531.5 eV (34000)	531.6 eV (64000)	531.5 eV (22000)	531.3 eV (13000)	531.3 eV (10000)	531.2 eV (35000)
Cu $2p_{3/2}$	(57000)	(41000)	(15000)	(62000)	(76000)	(78000)	
C 1s	(3500)	(4300)	(6000)	(3000)	-	-	
Ba $3d_{5/2}$	779.4 eV (92000)	779.5 eV (107000)	780.1 eV (101000)	779.5 eV (90000)	779.5 eV (69000)	779.6 eV (65000)	

Table 4.12: XPS data of angle-resolved investigation on the post flashing of film E (greyed-out boxes mean that no such measurement was recorded)

Film F was grown with a deposition time of 5 minutes (with an O_2 partial pressure of 2×10^{-8} Torr resulting in an oxygen exposure of 6 L). The subsequent oxygen exposures and flashing treatments were identical to the experiment with Film E. XPS spectra were again recorded with emission angles of 15°, 45° and 75° after the flash at 723 K. Furthermore the O 1s region was recorded at grazing emission (75° off sample normal) after the initial deposition, after the 5 L O_2 exposure and after the 873 K flash at the end. Table 4.13 summarises the XPS data and the O 1s, C 1s and Ba $3d_{5/2}$ regions are shown in Figures 4.11a, 4.11b, 4.12a and 4.12b.

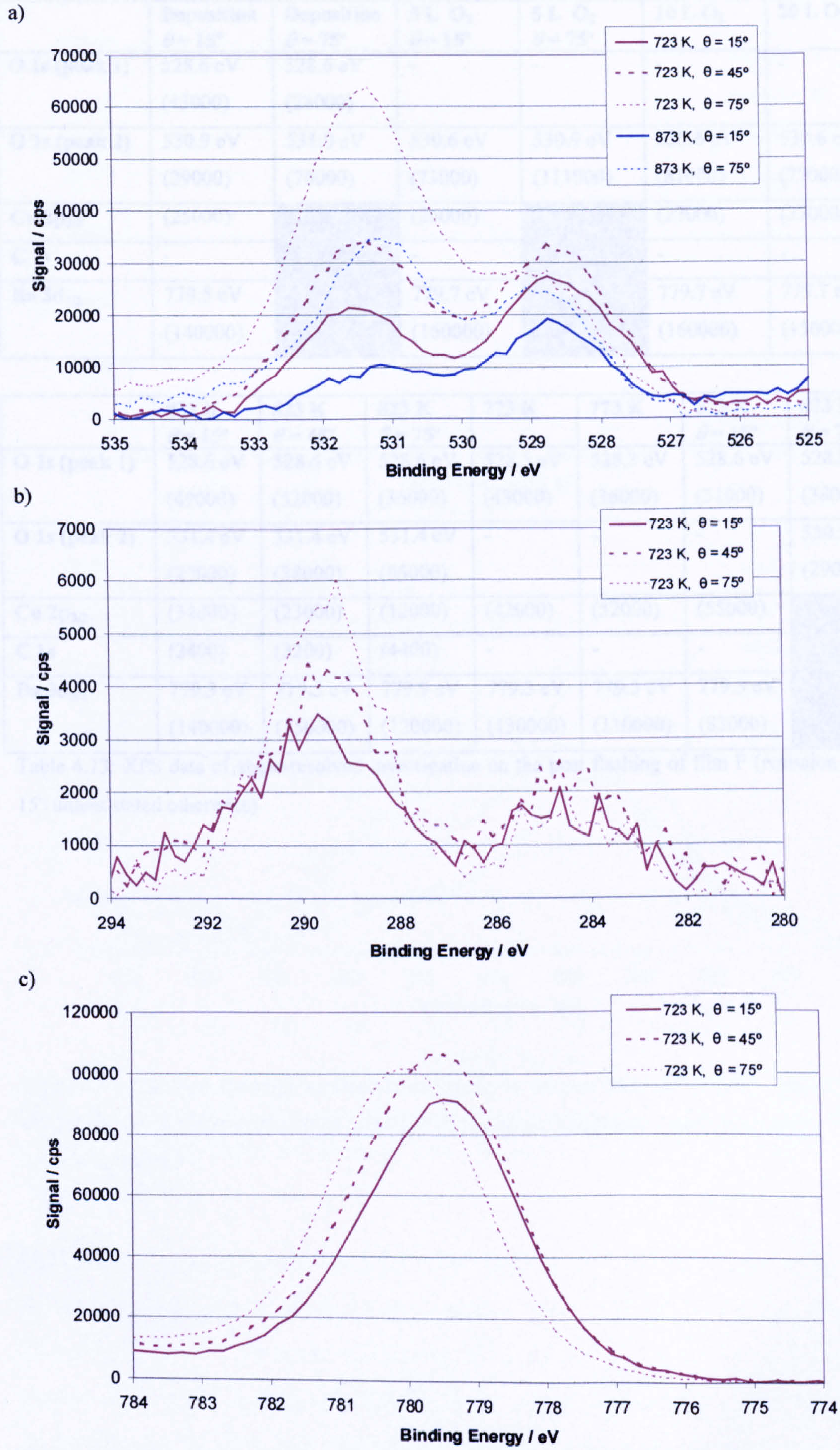

Figure 4.10: XPS data for angle-resolved investigation on the post flashing of film E at each of the indicated temperatures a) O 1s region; b) C 1s region; c) Ba $3d_{5/2}$ region

	Deposition $\theta = 15°$	Deposition $\theta = 75°$	5 L O_2 $\theta = 15°$	5 L O_2 $\theta = 75°$	10 L O_2	20 L O_2
O 1s (peak 1)	528.6 eV (43000)	528.6 eV (28000)	-	-	-	-
O 1s (peak 2)	530.9 eV (29000)	531.0 eV (76000)	530.6 eV (73000)	530.9 eV (111000)	530.6 eV (81000)	530.6 eV (77000)
Cu $2p_{3/2}$	(25000)		(26000)		(27000)	(27000)
C 1s	-		-		-	-
Ba $3d_{5/2}$	779.5 eV (140000)		779.7 eV (160000)		779.7 eV (160000)	779.7 eV (150000)

	823 K $\theta = 15°$	823 K $\theta = 45°$	823 K $\theta = 75°$	773 K	773 K	873 K $\theta = 15°$	873 K $\theta = 75°$
O 1s (peak 1)	528.6 eV (49000)	528.6 eV (52000)	528.6 eV (36000)	528.5 eV (43000)	528.3 eV (36000)	528.6 eV (31000)	528.8 eV (38000)
O 1s (peak 2)	531.4 eV (25000)	531.4 eV (38000)	531.4 eV (65000)	-	-	-	530.9 eV (29000)
Cu $2p_{3/2}$	(34000)	(23000)	(12000)	(42000)	(52000)	(55000)	
C 1s	(2400)	(3200)	(4400)	-	-	-	
Ba $3d_{5/2}$	779.3 eV (140000)	779.5 eV (150000)	779.9 eV (120000)	779.3 eV (130000)	779.3 eV (110000)	779.3 eV (83000)	

Table 4.13: XPS data of angle-resolved investigation on the post flashing of film F (emission angles 15° unless stated otherwise)

a)

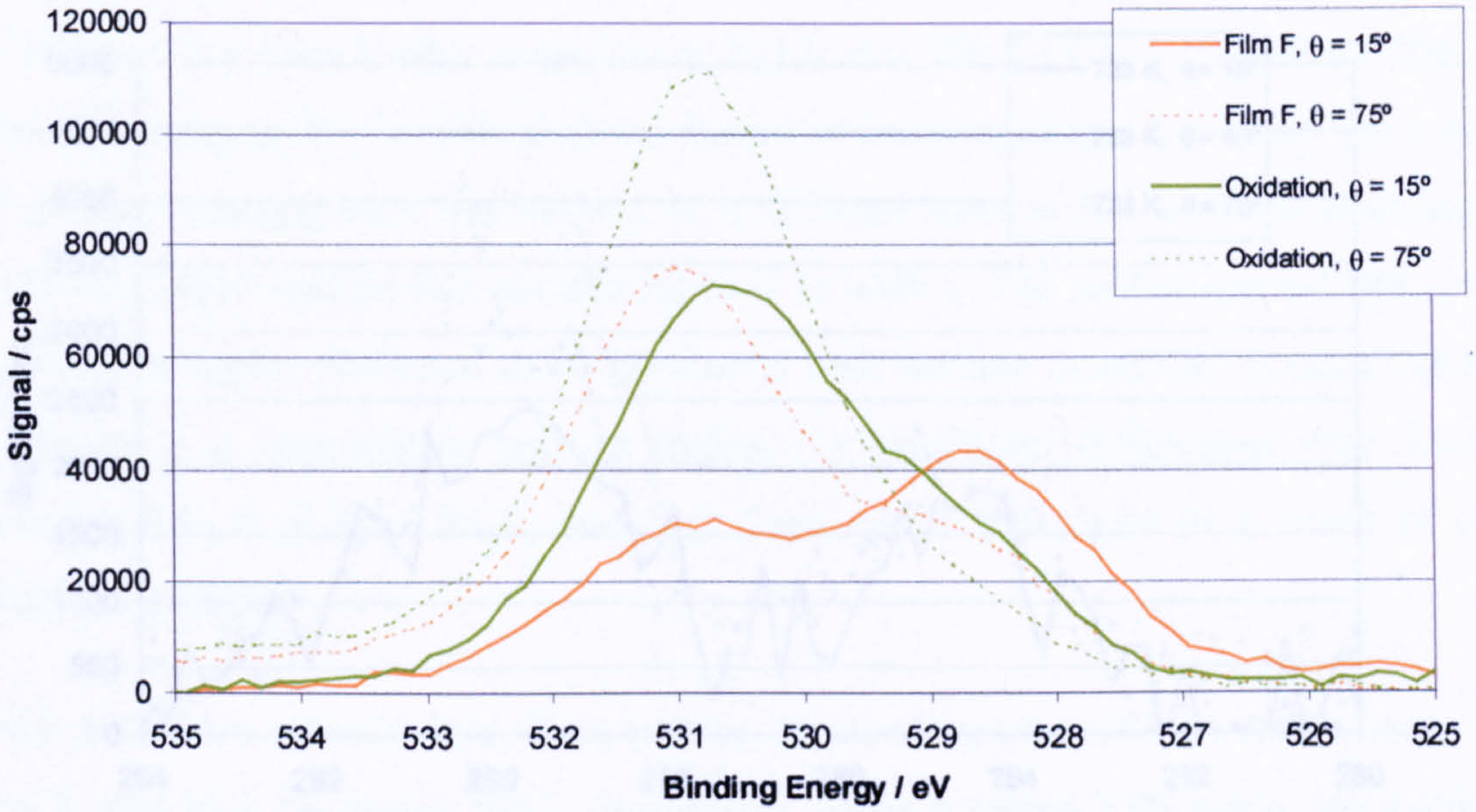

b)

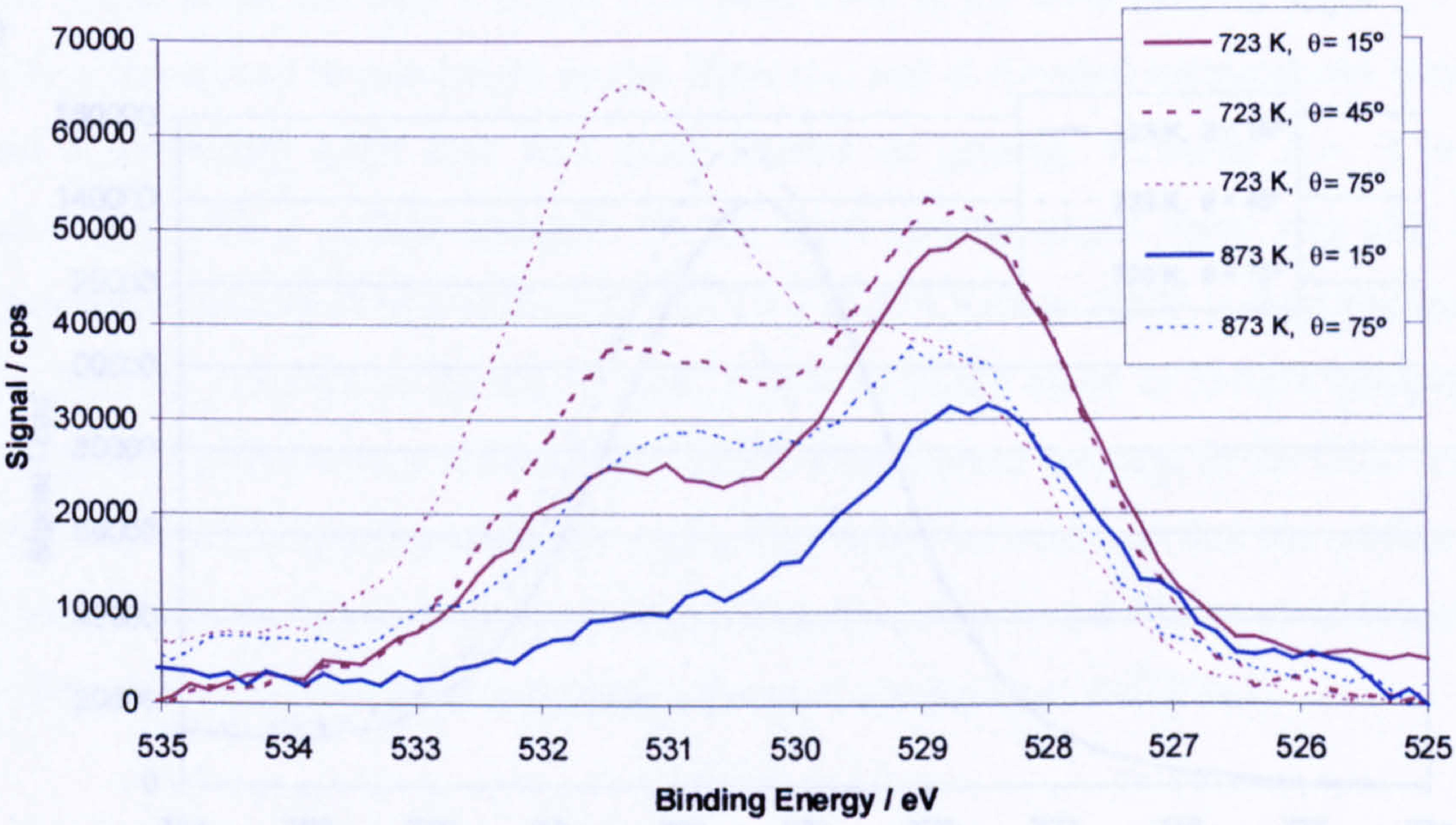

Figure 4.11: XPS data for angle-resolved investigation on the post treatment of film F flashed at each of the indicated temperatures a) O 1s region; b) O 1s region; (Oxidation = After exposure to 5 L O_2 at room temperature)

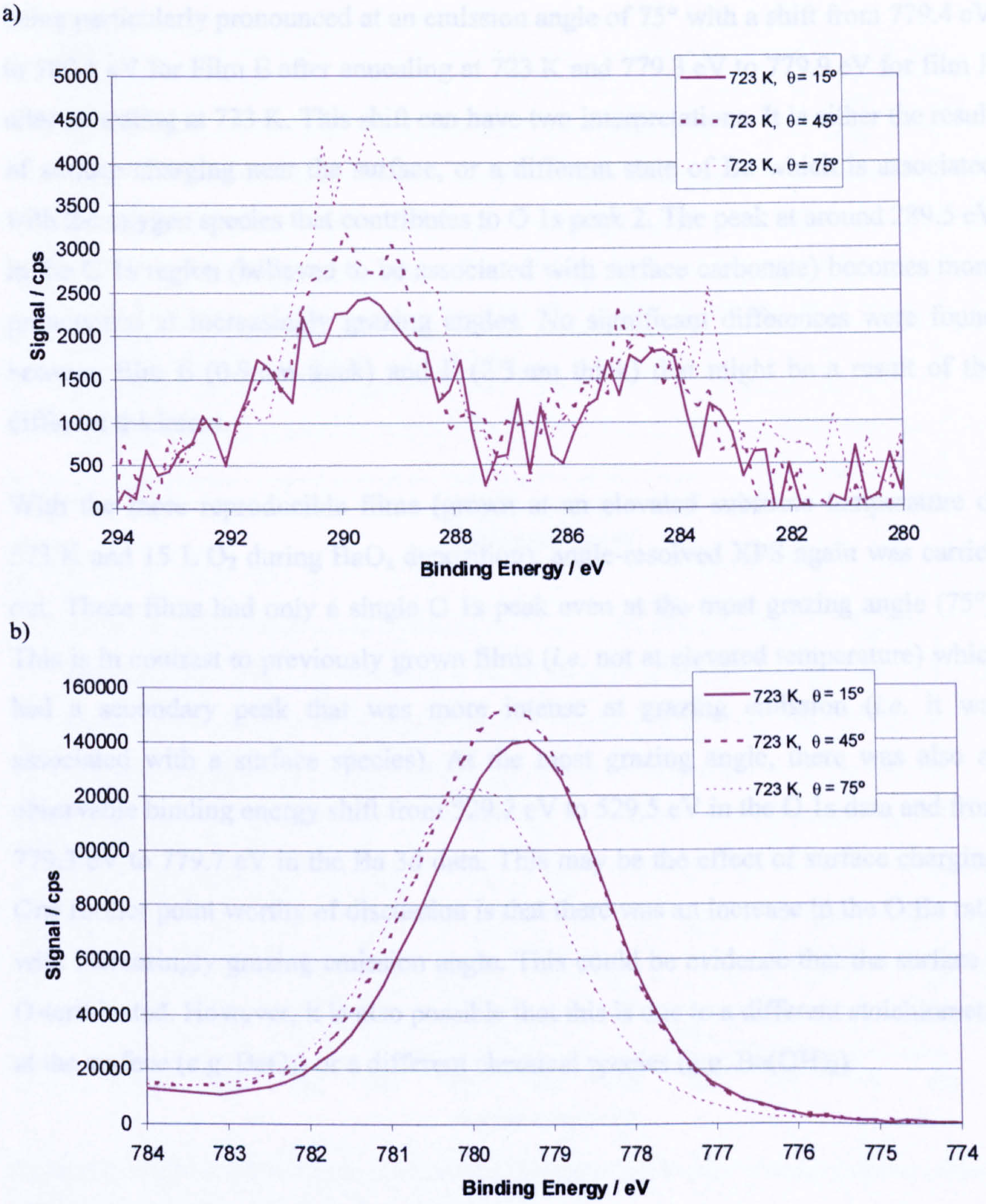

Figure 4.12: XPS data for angle-resolved investigation on the post treatment of film F flashed at each of the indicated temperatures a) C 1s region; b) Ba $3d_{5/2}$ region; (Oxidation = After exposure to 5 L O_2 at room temperature)

In the O 1s region is that the intensity of the peak around 531.5 eV (peak 2) increases as the emission angle becomes more grazing. What is more significant is that the intensity of peak 2 increases relative to the peak around 528.4 eV (peak 1). This means that peak 2 (around 531.5 eV) is associated with an oxygen/oxygen-containing species which is localised nearer to the surface. Furthermore the Ba $3d_{5/2}$ peak is seen to shift to higher binding energy at more grazing emission angles, this being particularly pronounced at an emission angle of 75° with a shift from 779.4 eV to 780.1 eV for Film E after annealing at 723 K and 779.3 eV to 779.9 eV for film F after annealing at 723 K. This shift can have two interpretations. It is either the result of surface charging near the surface, or a different state of Ba which is associated with the oxygen species that contributes to O 1s peak 2. The peak at around 289.5 eV in the C 1s region (believed to be associated with surface carbonate) becomes more pronounced at increasingly grazing angles. No significant differences were found between film E (0.9 nm thick) and F (2.3 nm thick) that might be a result of the different thickness.

With the more reproducible films (grown at an elevated substrate temperature of 573 K and 15 L O_2 during BaO_x deposition), angle-resolved XPS again was carried out. These films had only a single O 1s peak even at the most grazing angle (75°). This is in contrast to previously grown films (*i.e.* not at elevated temperature) which had a secondary peak that was more intense at grazing emission (*i.e.* it was associated with a surface species). At the most grazing angle, there was also an observable binding energy shift from 529.2 eV to 529.5 eV in the O 1s data and from 779.3 eV to 779.7 eV in the Ba 3d data. This may be the effect of surface charging. One further point worthy of discussion is that there was an increase in the O:Ba ratio with increasingly grazing emission angle. This could be evidence that the surface is O-terminated. However, it is also possible that this is due to a different stoichiometry at the surface (*e.g.* BaO_2) or a different chemical species (*e.g.* $Ba(OH)_2$).

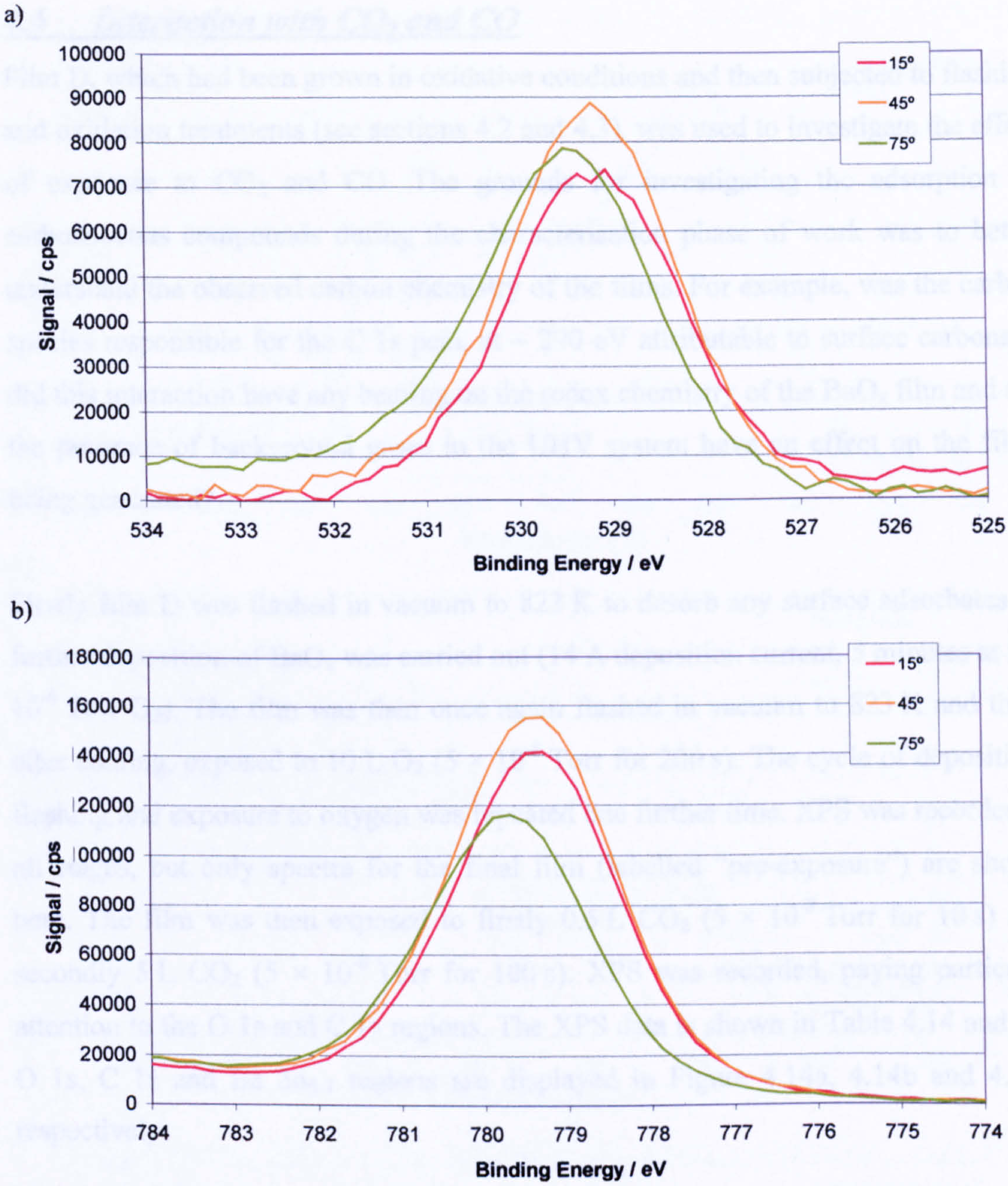

Figure 4.13: XPS data for the angle-resolved investigation of film J at the indicated emission angles a) O 1s region; b) Ba $3d_{5/2}$ region

4.6 Interaction with CO_2 and CO

Film D, which had been grown in oxidative conditions and then subjected to flashing and oxidation treatments (see sections 4.2 and 4.3), was used to investigate the effect of exposure to CO_2 and CO. The grounds for investigating the adsorption of carbonaceous compounds during the characterisation phase of work was to better understand the observed carbon chemistry of the films. For example, was the carbon species responsible for the C 1s peak at ~ 290 eV attributable to surface carbonate, did this interaction have any bearing on the redox chemistry of the BaO_x film and did the presence of background gases in the UHV system have an effect on the films being generated?

Firstly film D was flashed in vacuum to 823 K to desorb any surface adsorbates. A further deposition of BaO_x was carried out (14 A deposition current, 5 minutes at 5×10^{-8} Torr O_2). The film was then once again flashed in vacuum to 823 K and then, after cooling, exposed to 10 L O_2 (5×10^{-8} Torr for 200 s). The cycle of deposition, flashing and exposure to oxygen was repeated one further time. XPS was recorded at all stages, but only spectra for the final film (labelled "pre-exposure") are shown here. The film was then exposed to firstly 0.5 L CO_2 (5×10^{-8} Torr for 10 s) and secondly 5 L CO_2 (5×10^{-8} Torr for 100 s). XPS was recorded, paying particular attention to the O 1s and C 1s regions. The XPS data is shown in Table 4.14 and the O 1s, C 1s and Ba $3d_{5/2}$ regions are displayed in Figure 4.14a, 4.14b and 4.14c respectively.

	Pre-exposure	**0.5 L CO_2**	**5 L CO_2**
O 1s (peak 1)	528.2 eV (57000)	528.3 eV (53000)	528.3 eV (49000)
O 1s (peak 2)	-	531.0 eV (32000)	531.2 eV (45000)
Cu $2p_{3/2}$	(45000)	(43000)	(39000)
C 1s	284.3 eV (3000)	284.5 eV (2500)	284.5 eV (2500)
C 1s (carbonate)	-	289.5 eV (4300)	289.5 eV (6200)
Ba $3d_{5/2}$	778.9 eV (160000)	779.1 eV (147000)	779.3 eV (147000)

Table 4.14: XPS data for the adsorption of CO_2 at room temperature

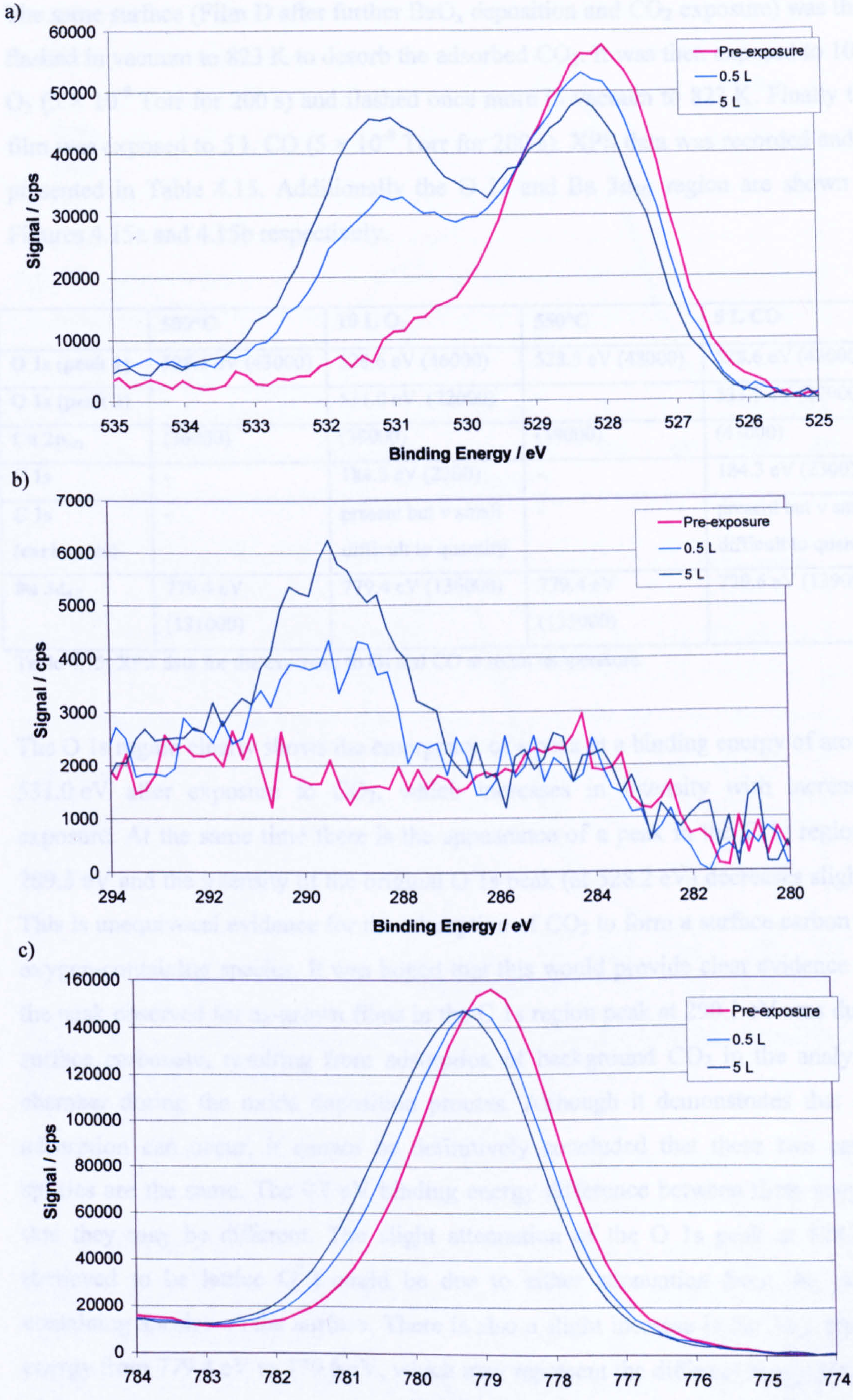

Figure 4.14: XPS data showing the effects of CO_2 exposure at room temperature a) O 1s region; b) C 1s region; c) Ba $3d_{5/2}$ region

The same surface (Film D after further BaO_x deposition and CO_2 exposure) was then flashed in vacuum to 823 K to desorb the adsorbed CO_2. It was then exposed to 10 L O_2 (5×10^{-8} Torr for 200 s) and flashed once more in vacuum to 823 K. Finally the film was exposed to 5 L CO (5×10^{-8} Torr for 200 s). XPS data was recorded and is presented in Table 4.15. Additionally the O 1s and Ba $3d_{5/2}$ region are shown in Figures 4.15a and 4.15b respectively.

	500°C	10 L O_2	550°C	5 L CO
O 1s (peak 1)	528.6 eV (43000)	528.6 eV (46000)	528.5 eV (48000)	528.6 eV (48000)
O 1s (peak 2)	-	531.0 eV (22000)	-	531.0 eV (22000)
Cu $2p_{3/2}$	(36000)	(39000)	(39000)	(41000)
C 1s	-	184.3 eV (2300)	-	184.3 eV (2300)
C 1s (carbonate)	-	present but v small difficult to quantify	-	present but v small difficult to quantify
Ba $3d_{5/2}$	779.4 eV (131000)	779.4 eV (136000)	779.4 eV (133000)	779.6 eV (139000)

Table 4.15: XPS data for the exposure to O_2 and CO at room temperature

The O 1s region clearly shows the emergence of a peak at a binding energy of around 531.0 eV after exposure to CO_2, which increases in intensity with increasing exposure. At the same time there is the appearance of a peak in the C 1s region at 289.5 eV and the intensity of the original O 1s peak (at 528.2 eV) decreases slightly. This is unequivocal evidence for the adsorption of CO_2 to form a surface carbon and oxygen-containing species. It was hoped that this would provide clear evidence that the peak observed for as-grown films in the C 1s region peak at 290.1 eV was due to surface carbonate, resulting from adsorption of background CO_2 in the analytical chamber during the oxide deposition process. Although it demonstrates that CO_2 adsorption can occur, it cannot be definitively concluded that these two carbon species are the same. The 0.6 eV binding energy difference between them suggests that they may be different. The slight attenuation of the O 1s peak at 528.2 eV (believed to be lattice O^{2-}) could be due to either attenuation from the carbon containing species on the surface. There is also a slight increase in Ba $3d_{5/2}$ binding energy from 779.4 eV to 779.6 eV, which may represent the different binding energy of Ba in $BaCO_3$. The binding energy values for O 1s and C 1s are ~ 1 eV lower than literature values for $BaCO_3$.[32]

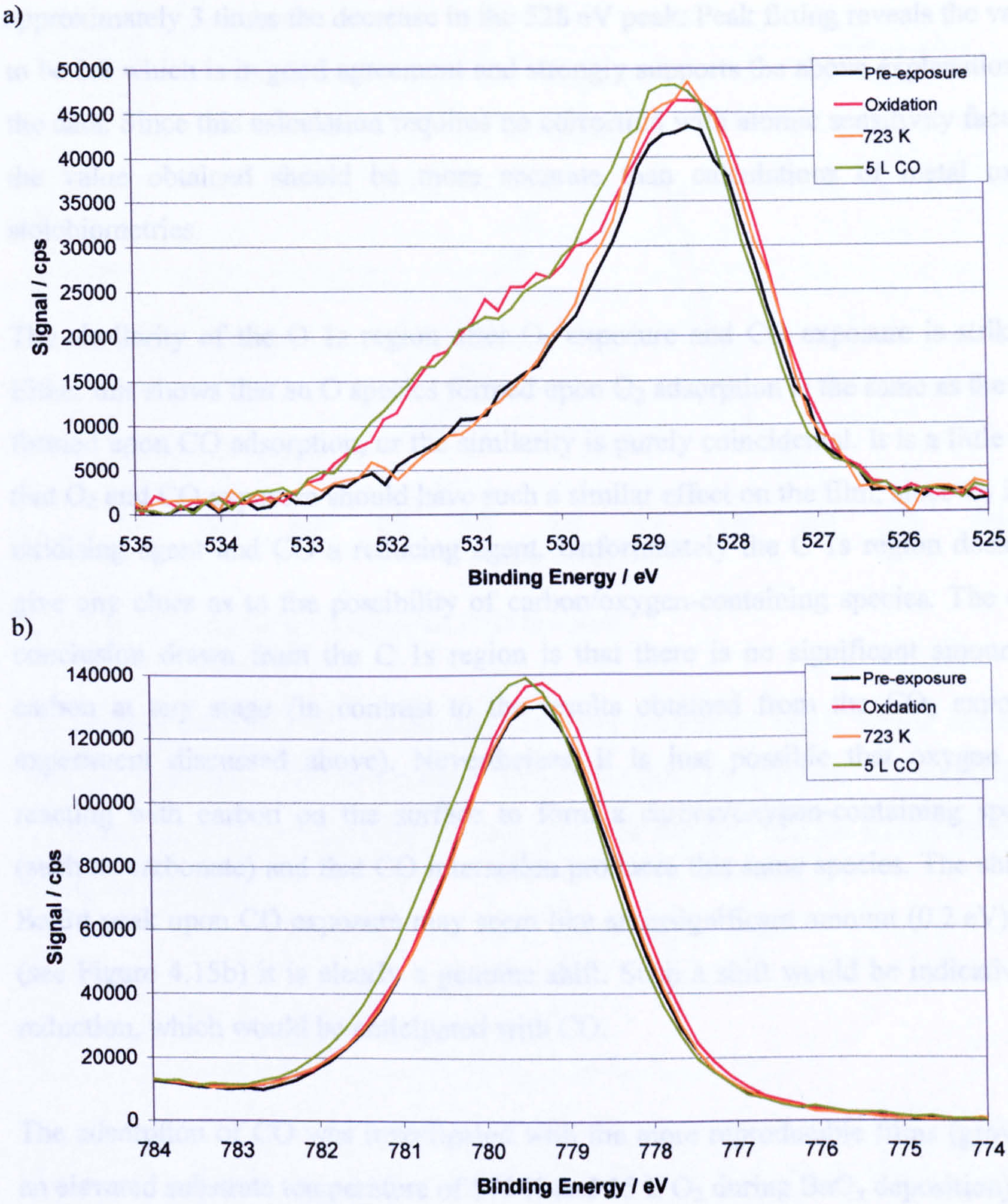

Figure 4.15: XPS data for the exposure of film D to CO a) O 1s region; b) Ba $3d_{5/2}$ region; (Oxidation = after exposure to 10 L O_2 at room temperature)

Peak fitting and normalisation of the C 1s peak at 289.5 eV and the O 1s peak at 531.2 eV, both believed to be attributed to carbonate, reveals a stoichiometric ratio of 4.4. This value is very close to value obtained for film A, which was believed to consist mostly of $BaCO_3$. This strongly suggests that the difference between these values and the expected value of 3 for carbonate is largely due to the choice of atomic sensitivity factors. Furthermore if the reaction is $CO_2 + BaO \rightarrow BaCO_3$, and the O 1s peaks at 528 eV and 531 eV are associated with lattice oxygen and carbonate respectively, then one would expect the increase in the 531 eV peak to be approximately 3 times the decrease in the 528 eV peak. Peak fitting reveals the value to be 2.8 which is in good agreement and strongly supports the above explanation of the data. Since this calculation requires no correction with atomic sensitivity factors, the value obtained should be more accurate than calculations of metal oxide stoichiometries.

The similarity of the O 1s region after O_2 exposure and CO exposure is striking. Either this shows that an O species formed upon O_2 adsorption is the same as the one formed upon CO adsorption, or the similarity is purely coincidental. It is a little odd that O_2 and CO exposure should have such a similar effect on the film, since O_2 is an oxidising agent and CO a reducing agent. Unfortunately the C 1s region does not give any clues as to the possibility of carbon/oxygen-containing species. The only conclusion drawn from the C 1s region is that there is no significant amount of carbon at any stage (in contrast to the results obtained from the CO_2 exposure experiment discussed above). Nevertheless, it is just possible that oxygen was reacting with carbon on the surface to form a carbon/oxygen-containing species (such as carbonate) and that CO interaction produces this same species. The shift in Ba 3d peak upon CO exposure may seem like an insignificant amount (0.2 eV), but (see Figure 4.15b) it is clearly a genuine shift. Such a shift would be indicative of reduction, which would be anticipated with CO.

The adsorption of CO was investigated with the more reproducible films (grown at an elevated substrate temperature of 573 K and 15 L O_2 during BaO_x deposition). CO was dosed in increments of 0.5 L, 5 L and 20 L, each time recording XPS at an emission angle of 75° (*i.e.* grazing). Upon adsorption of CO there is a slight increase in electron emission to the higher binding energy end of the O 1s peak with increasing exposure to CO, probably due to the emergence of a secondary XP peak (associated with adsorbed CO, or some induced change in the oxygen chemistry on the BaO_x surface. Coinciding with the secondary peak increase is attenuation of the primary O 1s peak (perhaps due to attenuation due to the overlayer (increasing elastic collisions), or transfer between species – attenuation of Ba and Cu peaks seems to suggest the former. There is however no evidence in the C 1s region, with no appreciable change in binding energy of the C 1s peak with CO dosing.

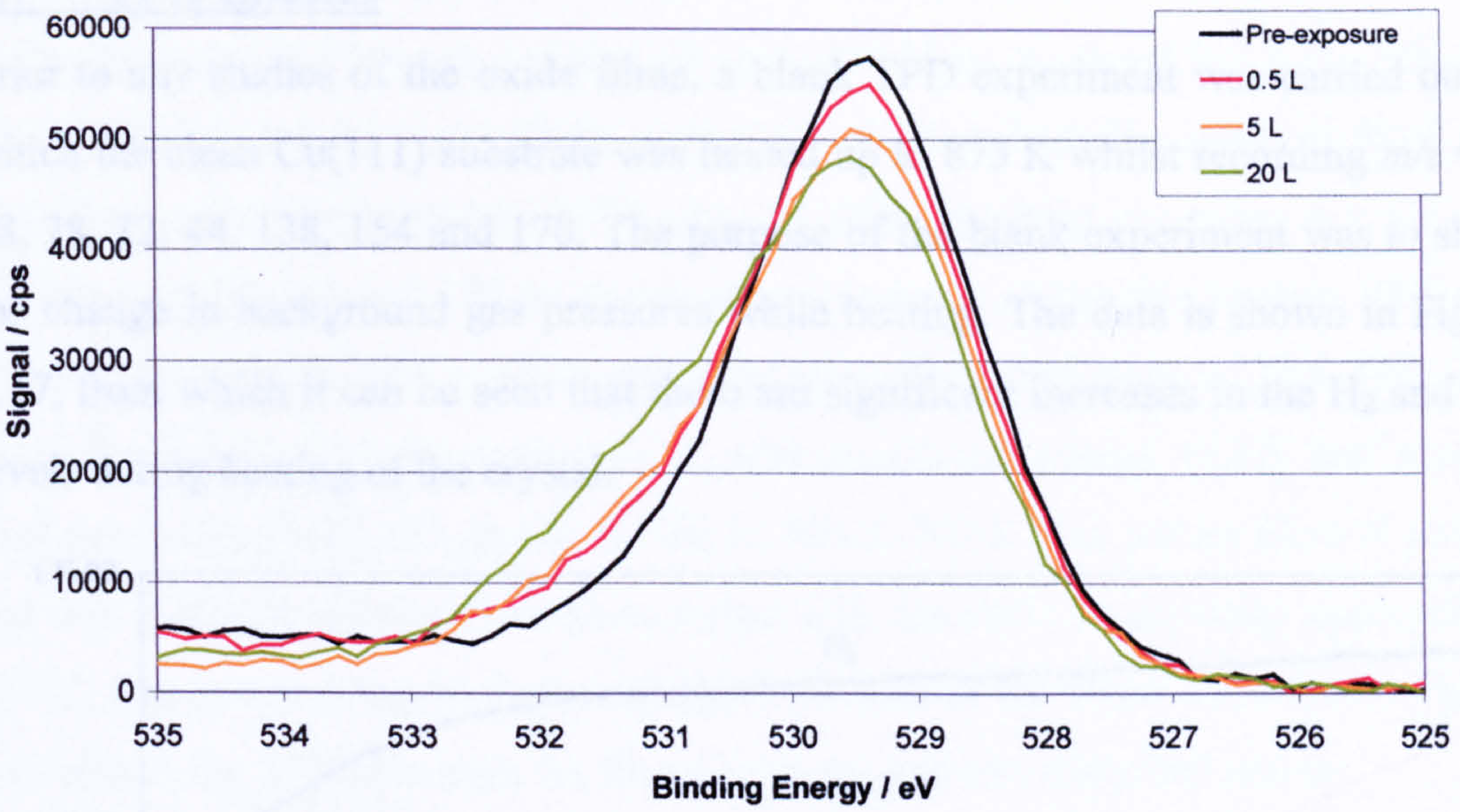

Figure 4.16: XPS data for the exposure to CO (O 1s region)

Immediately after CO adsorption, the film was flashed to 723 K whilst recording TPD, but there is no TPD evidence to support the desorption below 723 K and the C 1s region data was confused by the adsorption of further CO/CO_2 from outgassing during the heating.

4.7 TPD Studies

Prior to any studies of the oxide films, a blank TPD experiment was carried out in which the clean Cu(111) substrate was heated up to 873 K whilst recording $m/z = 2$, 18, 28, 32, 44, 138, 154 and 170. The purpose of the blank experiment was to show the change in background gas pressures while heating. The data is shown in Figure 4.17, from which it can be seen that there are significant increases in the H_2 and CO levels during heating of the crystal.

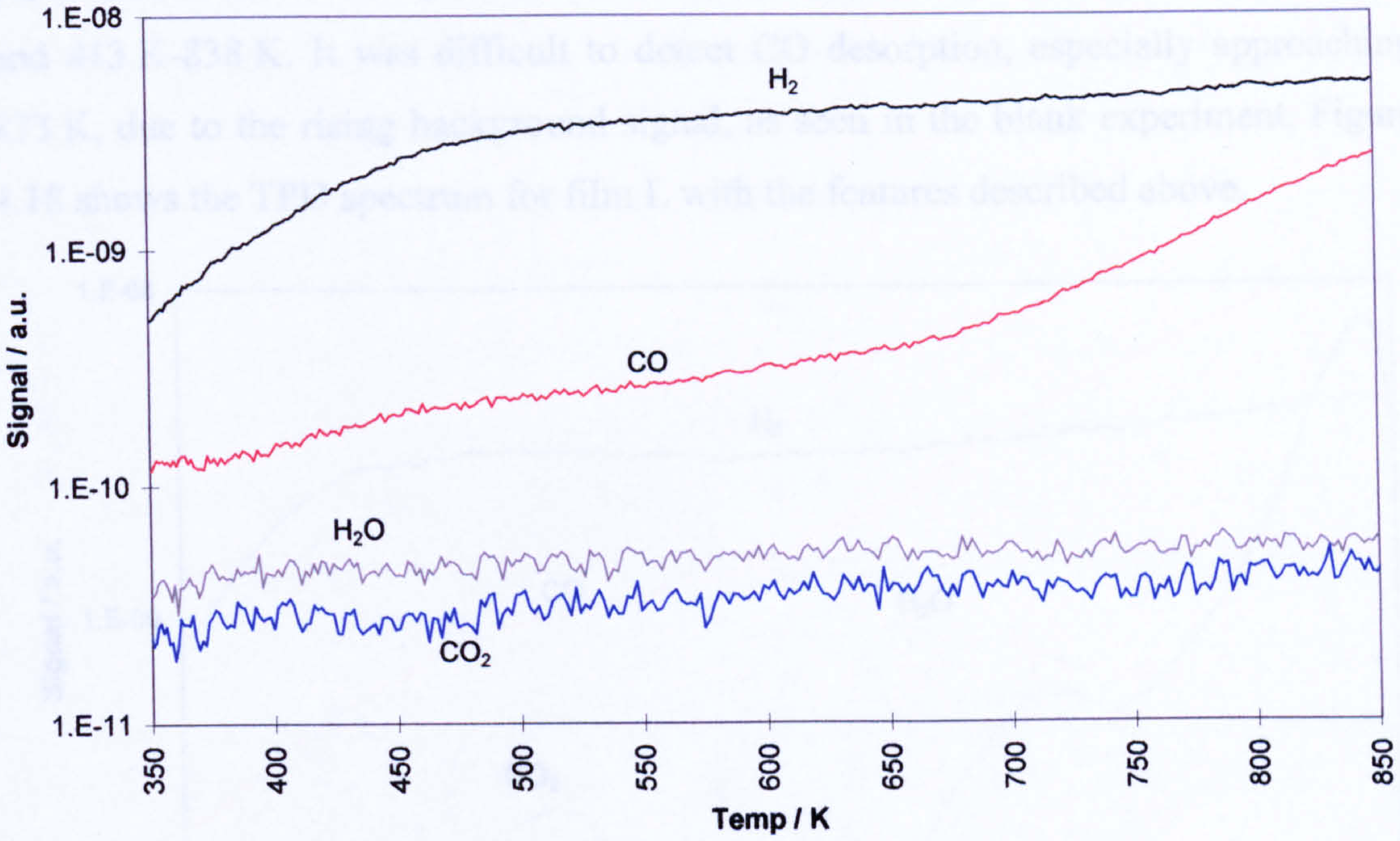

Figure 4.17: TPD spectrum for blank test (heating of the clean substrate)

An increase in these partial pressures can be expected since parts of the system (in the proximity of the sample being heated) outgas as they become heated. It is essential to know what these profiles look like so that they can be disregarded when analysing results from desorption experiments with a film. It must however be recognised that these profiles can depend upon the state of the system, *e.g.* if the crystal is being heated for the first time after an extended period at ambient temperature then one might expect to see more outgassing than if it has recently been heated.

It was hoped that TPD studies of species desorbing from the oxide surfaces would shed some light on the nature of the films. BaO_x films were generated by deposition onto the Cu(111) substrate for 5 minutes at ambient temperature using a deposition current of 14 A producing films of 1.5 nm - 2.3 nm estimated thickness. Films L and M had their main O 1s peak at 530.6 eV with shoulders at around 528.6 eV, whereas films N and O had the major O 1s peak at 528.5 eV and smaller peaks at 531.2 eV. The films were then heated to 873 K (except film O) whilst recording *m/z* = 2, 18, 28, 32, 44, 138, 154 and 170 on the mass spectrometer. After this heating XPS data showed breakdown of the films and loss of oxygen and carbon. The TPD data showed a broad H_2O desorption peak with maximum around 473 K and smaller peaks associated with CO_2 at 503 K-518 K, 683 K-703 K (but not for films N and O) and 813 K-838 K. It was difficult to detect CO desorption, especially approaching 873 K, due to the rising background signal, as seen in the blank experiment. Figure 4.18 shows the TPD spectrum for film L with the features described above.

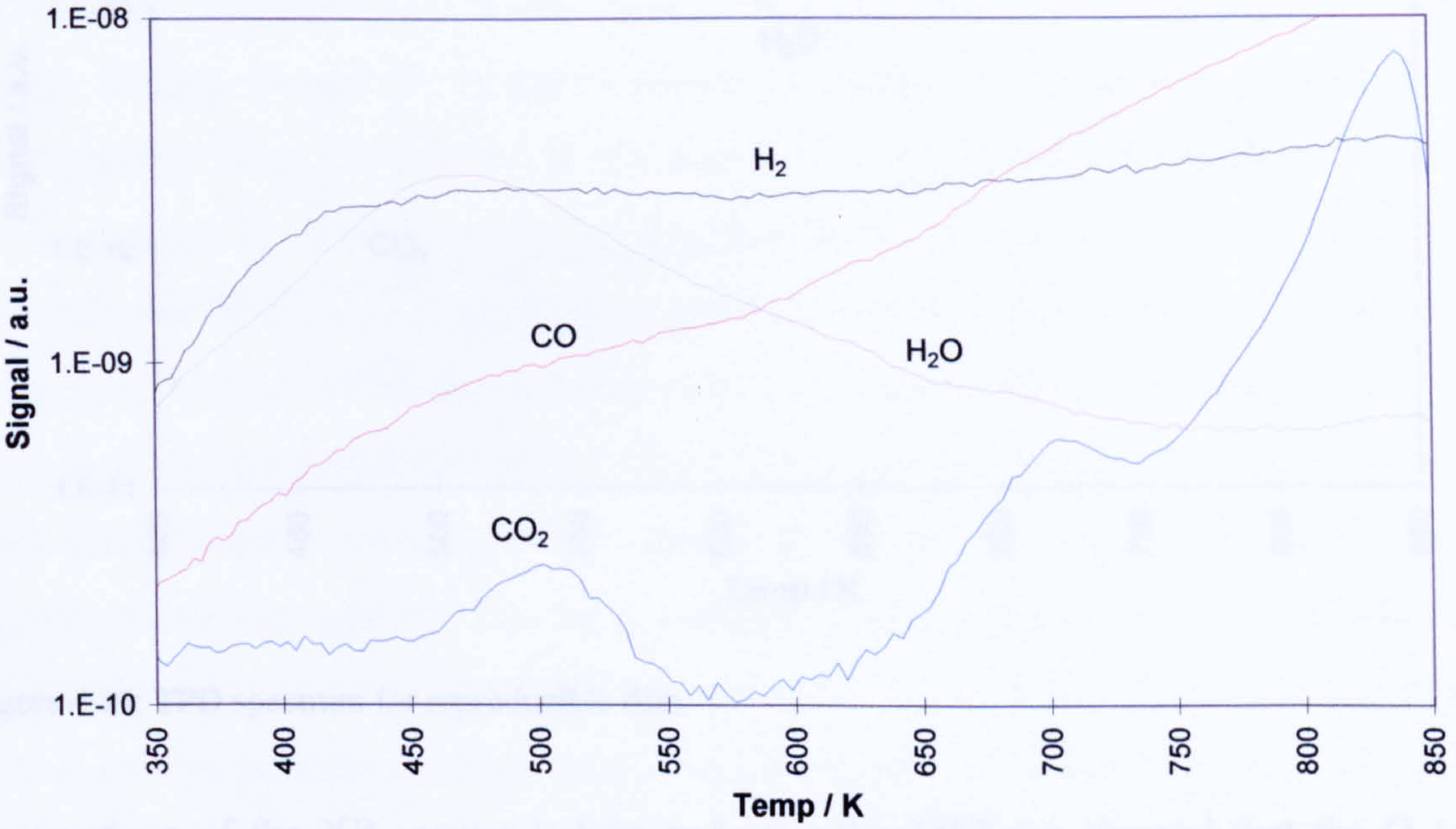

Figure 4.18: TPD spectrum for film L

The H_2O desorption could be due to dehydration of the surface of the oxide, or possibly to the decomposition of some hydroxide present in the film. After heating the O 1s region of films L and M transformed to two peaks at 528.8 eV and 531.2 eV with a reduction in intensity. There was also a reduction in the intensity of the O1s region for films N and O upon heating, but no binding energy shifts. Film O was heated only to 723 K during TPD and interestingly only the O 1s peak at 531.2 eV reduced in intensity. This suggests that the desorption of H_2O at around 473 K is related to the reduction of the O 1s peak at 531.2 eV. Only small shifts in the Ba $3d_{5/2}$

peak were observed, but reductions in intensity were observed, more so for those films heated to 873 K.

TPD on the more reproducible films (grown at an elevated substrate temperature of 573 K and 15 L O_2 during BaO_x deposition), revealed that the H_2O desorption (*m/z* = 17, 18) was much reduced (as anticipated). There was a CO_2 (*m/z* = 44) desorption peak at around 763 K and there was a broad CO (*m/z* = 28) desorption as seen in the blank test, but which included a defined peak at around 603 K.

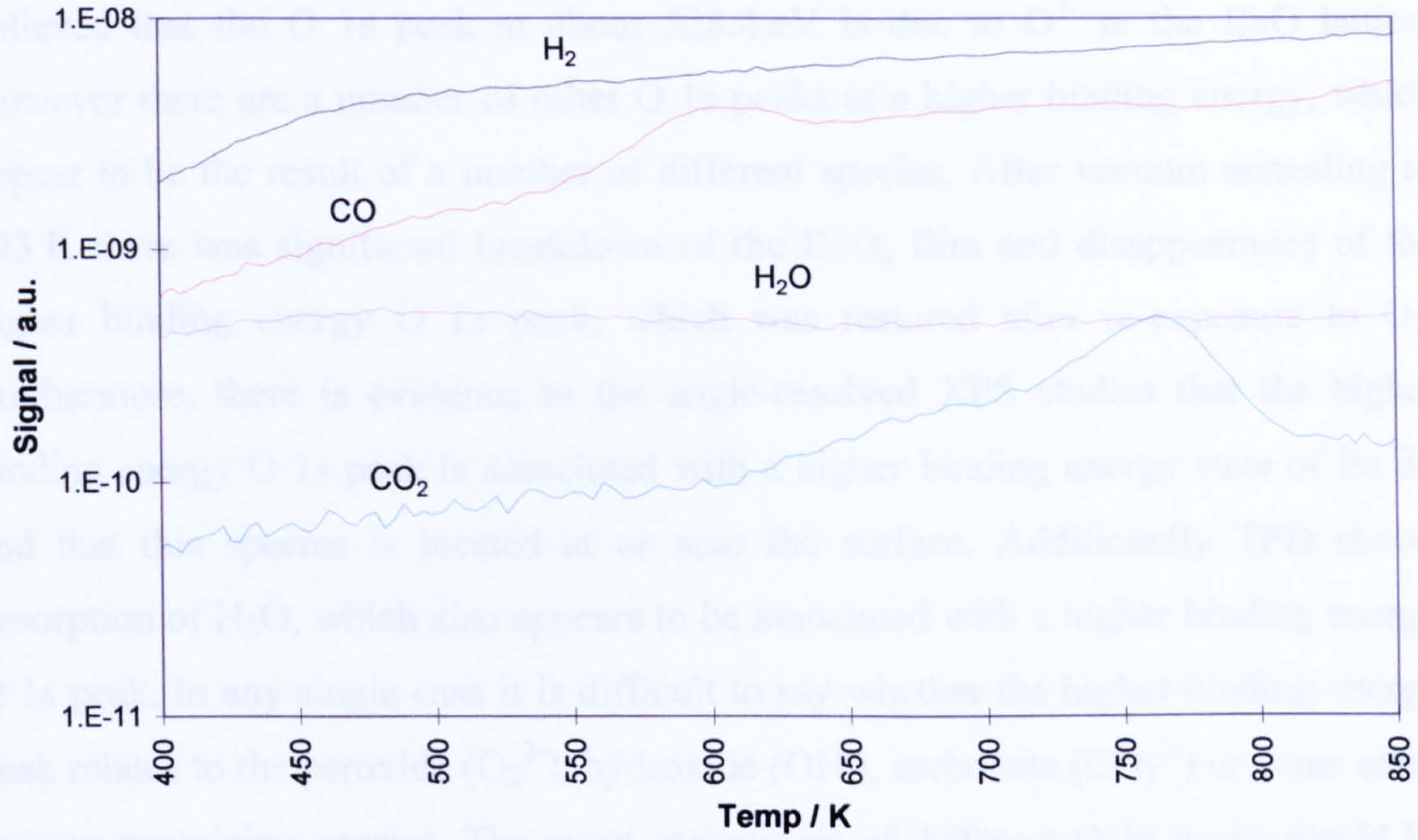

Figure 4.19: TPD spectrum for reproducible film

Comparison of the XP spectra before and after the TPD run showed that the O 1s peak shifted from 529.2 eV to 528.9 eV and reduced to about half its original intensity. The Ba $3d_{5/2}$ peak did not shift, but did reduce in intensity, although not as much as the O 1s peak. Clearly this data represents breakdown of the film, with a reduction in O:Ba ratio.

4.8 Summary

BaO_x films on Cu(111) have been grown in UHV by direct deposition of BaO_x. The effect of different growth conditions and post-growth treatments were investigated by XPS. These films exhibited a complicated oxygen chemistry with transformation between different forms being brought about by different preparation conditions and post-deposition treatments. It is possible that small concentrations of background gases in the UHV analytical chamber and instability of the deposition source may have affected the films grown. In agreement with previous XPS studies of BaO, it is believed that the O 1s peak at about 528.4 eV is due to O^{2-} in the BaO lattice. However there are a number of other O 1s peaks at a higher binding energy, which appear to be the result of a number of different species. After vacuum annealing to 773 K there was significant breakdown of the BaO_x film and disappearance of the higher binding energy O 1s peak, which was restored after re-exposure to O_2. Furthermore, there is evidence in the angle-resolved XPS studies that the higher binding energy O 1s peak is associated with a higher binding energy state of Ba 3d and that this species is located at or near the surface. Additionally TPD shows desorption of H_2O, which also appears to be associated with a higher binding energy O 1s peak. In any single case it is difficult to say whether the higher binding energy peak relates to the peroxide (O_2^{2-}), hydroxide (OH^-), carbonate (CO_3^{2-}) or some other oxygen-containing species. The exact assignment of different O 1s peaks would be speculative from the data obtained. By depositing BaO_x at an elevated temperature (573 K) it was possible to obtain much more consistent films with just one O 1s peak at 529.2 eV. LEED data suggested some long-range ordering of the oxide films, probably with multiple domains. Rapid CO_2 adsorption at room temperature has been evidenced from the emergence of an additional O 1s XP peak to higher binding energy, additional C 1s peak to higher binding energy and a shift to higher binding energy of the Ba 3d peak. It is believed the CO_2 adsorption results in the formation of a surface carbonate. XPS data also shows some interaction of the BaO_x film with CO, resulting in the appearance of an additional O 1s XP peak to higher binding energy, which is evidence of either CO adsorption or a CO-induced change in the BaO_x film chemistry, such as reduction.

References

1 E. Fridell, M. Skoglundh, B. Westerberg, S. Johansson and G. Smedler, *J. Catal.* 1999, **183**, 196

2 Y. Chi and S.S.C. Chuang, *J. Phys. Chem.* 2000, **104**, 4673

3 A. Amberntsson, H. Persson, P. Engström and B. Kasemo, *Appl. Catal. B*, 2001, **31**, 27

4 N.W. Cant and M.J. Patterson, *Catal. Today*, 2002, **73**, 271

5 P.J. Schmitz and R.J. Baird, *J. Phys. Chem.* 2002, **106**, 4172

6 C. Hess and J.H. Lunsford, *J. Phys. Chem.* 2002, **106**, 6358

7 P. Broqvist, I. Panas, E. Fridell and H. Persson, *J. Phys. Chem. B*, 2002, **106**, 137

8 H. Mahzoul, J.F. Brilhac and P. Gilot, *Appl. Catal. B*, 1999, **20**, 47

9 Y. Chi, S. Chuang, *J. Phys. Chem. B*, 2000, **104**, 4673

10 F. Pinetto, G. Ghiotti, I. Nova, L. Lietti, E. Tronconi and P. Forzatti, *J. Phys. Chem.* 2001, **105**, 12732

11 F. Rodrigues, L. Juste, C. Potvin, J.F. Tempere, G. Blanchard and G. Djega-Mariadassou, *Catal. Lett.* **72**, (2001), 59

12 A. Amberntsson, B. Westerberg, P. Engström, E. Fridell and M. Skoglundh, *Stud. Surf. Sci. Catal.* 1999, **126**, 317

13 P. Engstrom, A. Amberntsson, M. Skoglundh, E. Fridell and G. Smedler, *Appl. Catal. B*, 1999, **22**, L241

14 C. Courson, A. Khalfi, H. Mahzoul, S. Hodjati, N. Moral, A. Kiennemann and P. Gilot, *Catal. Commun.* 2002, **3**, 471

15 J.P. Breen, M. Marella, C. Pistarino and JRH Ross, *Catal. Lett.* 2002, **80**, 123

16 A. Amberntsson, M. Skoglundh, M. Jonsson and E. Fridell, *Catal. Today*, 2002, **73**, 279

17 H. Mahzoul, L. Limousy, J.F. Brilhac and P. Gillot, *J. Anal. Appl. Pyrol.* 2000, **56**, 179

18 L.F. Liotta, G. Deganello, D. Sannino, M.C. Gaudino , P. Ciambelli and S. Gialanella, *Appl. Catal. A*, 2002, **229**, 217

19 D.R. Mueller, R.L. Kurz, R.L. Stockbauer, T.E. Madey and A. Shih, *Surf. Sci.* 1990, **237**, 72

20 G.A. Haas, R.E. Thomas, A. Shih and C.R.K. Marrian, *Appl. Surf. Sci.* 1989, **40**, 265

21 G.A. Haas, A. Shih and R.E. Thomas, *Appl. Surf. Sci.* 1977, **1**, 59

22 T. Ikeuchi, R. Souda and S. Yamamoto, *Appl. Surf. Sci.* 2002, **191**, 261

23 J.L. Wu, Q.F. Zhang, C.M. Wang and Y.H. Zou, *Appl. Surf. Sci.* 2001, **183**, 80

24 W.G. Burgers, *Z. Phys.* 1933, **80**, 352

25 http://cst-www.nrl.navy.mil

26 P. Broqvist, H. Grönbeck and I. Panas, *Surf. Sci.* **554**, 2004, 262

27 J. Goniakovski and C. Noguera, *Surf. Sci.* **323**, 1995, 129

28 Y. Chi and S. Chuang, *J. Phys. Chem. B*, 2000, **104**, 4673

29 G.E. Mullenberg, *Handbook of x-ray photoelectron spectroscopy*, Perkin-Elmer, 1979, p130-131, 188

30 M.F. Koenig and J.T. Grant, *Appl. Surf. Sci.* 1985, **20**, 481

31 R.P. Vasquez, *J. Electron. Spec. Rel. Phenomena.* 1991, **56**, 217

32 J.A.T. Verhoeven and H.V. Doveren, *Surf. Sci.* 1982, **123**, 369

33 J.A.T. Verhoeven and H.V. Doveren, *J. Electron. Spec. Rel. Phenomena.* 1980, **21**, 265

34 J. Inoue and I. Yasumori, *Bull. Chem. Soc. Jpn.* 1981, **54**, 1505

35 R.C. Weast, *Handbook of chemistry and physics, Ed.55*, CRC Press, 1974, p 71

Chapter 5:

Growth & Characterisation of $TiO_x/Cu(111)$

5.1 Literature Review of TiO_x Surface Science Studies

Titanium dioxide single crystal surfaces are the most researched oxide surfaces in fundamental surface science. This in part reflects the importance of understanding TiO_2 surface chemistry, but also the availability of single crystals of this material and their suitability for study by UHV surface analysis techniques.

5.1.1 Motivation for Surface Science Studies

One of the main applications of TiO_2 is in **heterogeneous catalysis** where it usually finds a role as support material. This has led to much research activity in the growth of metals on well-defined titanium dioxide surfaces.[1-3] Recently there has been particular interest in the Au/TiO_2 system. This is as a result of the finding that finely dispersed Au on reducible oxide supports (*e.g.* TiO_2) has extra-ordinary activity for a range of low temperature catalytic reactions, including partial oxidation of hydrocarbons, reduction of nitrogen oxides and notably for CO oxidation.[4-6] This discovery has led to a number of studies on the morphology of Au particles dispersed on rutile $TiO_2(110)$.[7-9] However, there are presently no studies of Au nanoparticles on anatase surfaces (which is the form of titania found in the majority of commercial catalysts). The findings of those studies on the Au/$TiO_2(110)$ system reveal that the size of Au particle must be very small (*e.g.* diameter < 5 nm) if high catalytic activity is to be observed, and that the role of support material (*i.e.* the interactions between Au and support material) is very important – perhaps not surprising as neither Au nor TiO_2 on their own have much activity for CO oxidation.

TiO_2 also has some interesting photochemical properties and the **photocatalytic degradation** of organic molecules to CO_2 and H_2O has led to applications in water purification, bacterial disinfectants and development of self-cleaning coatings – to name but a few.[10] Similarly TiO_2 can also remove common air pollutants, such as SO_2 and nitrogen oxides.[11] TiO_2 has also been known for some time to be active in the photolysis of H_2O, where it is believed that surface defects play an important role.[12]

Asides from catalysis and photocatalysis there are many **other applications** of TiO_2, in which understanding of the surface chemistry is important. In particular TiO_2 has been researched as a gas sensor for O_2.[13] Additionally TiO_2 is used as a paint pigment,[14] in optical coatings[14] and in electrical devices.[16]

In previous research TiO_x films have been grown on Cu(100) substrates by oxidation of deposited Ti metal[17,18] and CVD[19] and investigated by AES, XPS and LEED. There appears to be no research on the growth of TiO_x on Cu(111).

5.1.2 Bulk Structure

Titatium dioxide (TiO_2) is by far the most important oxide of titanium. Other well-defined stoichiometries include titanium (III) oxide (Ti_2O_3) and titanium pentoxide (Ti_3O_5). Titanium dioxide crystallises in a number of different structures, the most important being rutile and anatase. These bulk structures differ in the packing of the array of O^{2-} anions, which is hexagonal in rutile (with half the octahedral sites occupied by Ti^{2+}) and cubic in anatase. Rutile has the $P4_2/mnm$ (136) space group and comprises a body-centred cubic arrangement of the Ti^{4+} cations each of which is surrounded by an octahedra of O^{2-} anions (the Ti-O bonds being elongated along one axis). The distorted TiO_6 octahedra run parallel along the *c*-axis and the centre octahedra are rotated 90° with respect to the corner octahedra so that they are corner sharing (see Figure 5.1). The lattice cell parameters have been determined to be $a = b = 4.59$ Å, $c = 2.95$ Å.[20,21] Anatase has the $I4_1/amd$ (141) space group and comprises TiO_6 octahedra connected through the edges of neighbouring units (see Figure 5.1). There is significant deviation from 90° in the O-Ti-O bond angles. The lattice cell parameters have been determined to be $a = b = 3.78$ Å, $c = 9.50$ Å.[20,22]

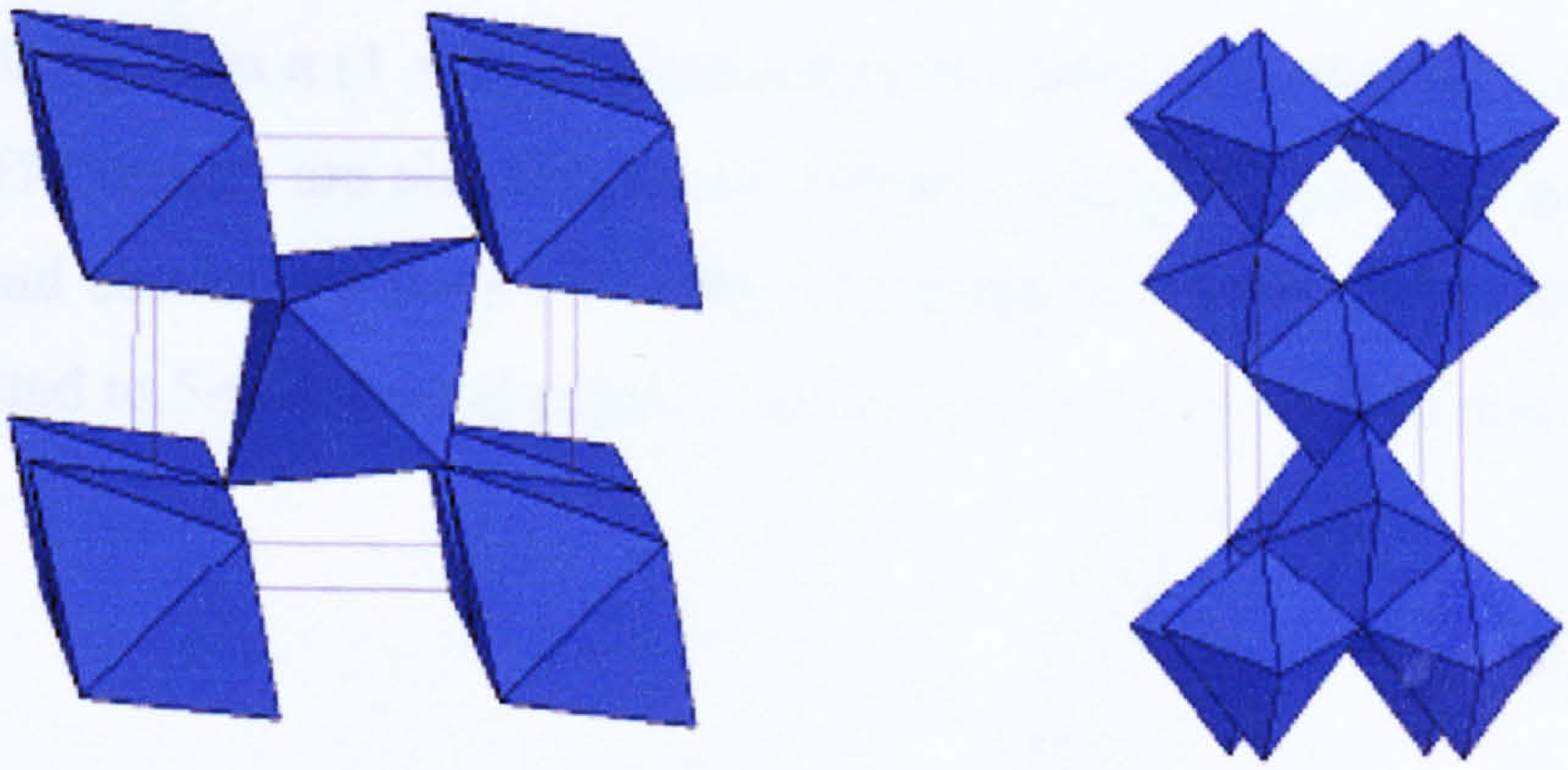

Figure 5.1: Unit Cells of Rutile (left) and Anatase (right)[23]

5.1.3 Surface Structure

The low index surfaces (110), (001) and (100) of rutile have all been studied. The $TiO_2(110)$ surface has the lowest surface energy of the low index surfaces[24] and has been found to be the most stable. Formation of the $TiO_2(110)$- (1 × 1) surface results in 6-fold co-ordinated Ti atoms, alternating with 5-fold co-ordinated Ti atoms with a dangling bond. 3-fold O atoms and 2-fold bridging O atoms are also created.

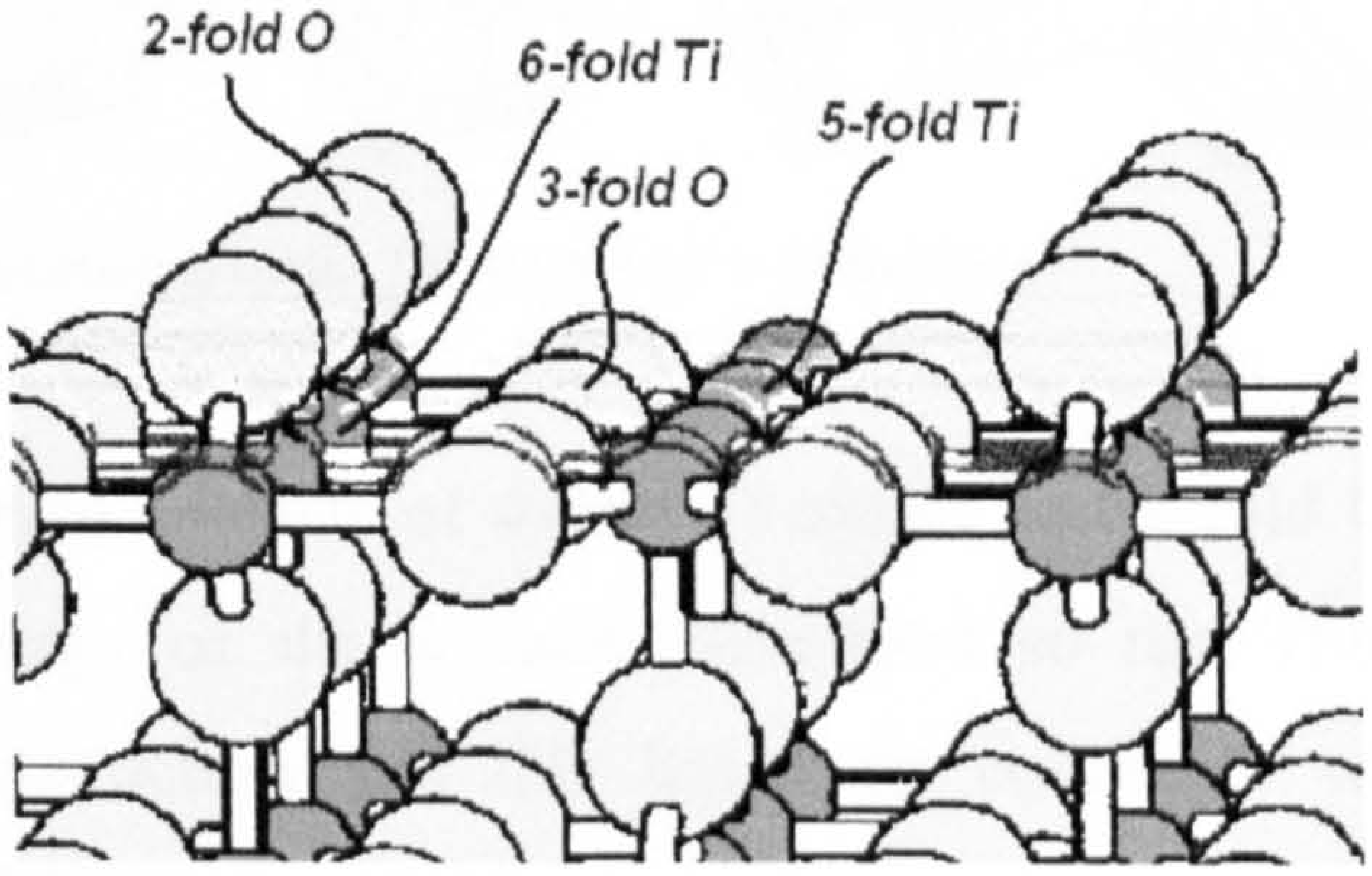

Figure 5.2: The Rutile $TiO_2(110)$-(1 × 1) Surface[10]

Despite the stability of this surface reconstruction and restructuring occurs at high temperatures under oxidising or reducing conditions. Annealing in UHV leads to a flat (1 × 1) reconstruction. Reducing conditions have been found to render a variety of reconstructions, including (1 × 2) formed, it is believed, by adding a row of Ti_2O_3[25] or missing a unit.[26] Relaxations have been found to extend far into the bulk structure by both theoretical[27,24] and empirical studies.[28] Surface defects play an important role in the properties of the $TiO_2(110)$ surface, the most common defect being oxygen vacancies.[29]

On $TiO_2(100)$ surfaces a (1 × 1) reconstruction has been observed with LEED, and STM and AFM images are also consistent with this surface.[30] This surface is highly corrugated and consists of rows of 2-fold co-ordinated O atoms at the end of each ridge connected to 5-fold co-ordinated Ti atoms, connected to 3-fold co-ordinated O atoms.

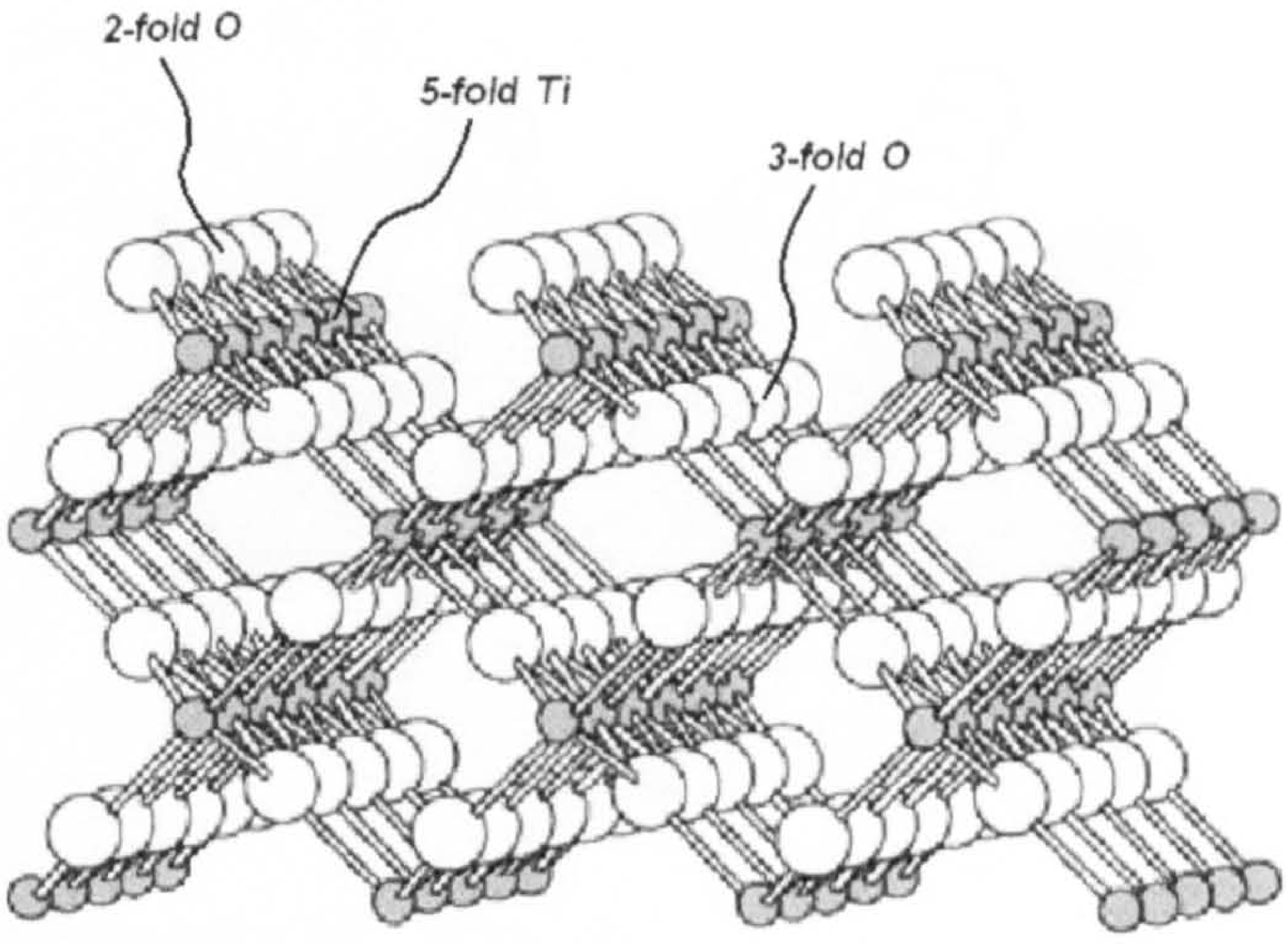

Figure 5.3: The unreconstructed rutile $TiO_2(100)$-(1 × 1) Surface[10]

The $TiO_2(001)$ surface consists of 4-fold Ti atoms and 2-fold O-atoms and has the highest surface energy of the surfaces described so far. Thus there is a strong tendency for reconstruction and this has been consistent with observations by LEED[31,32] and STM.[33]

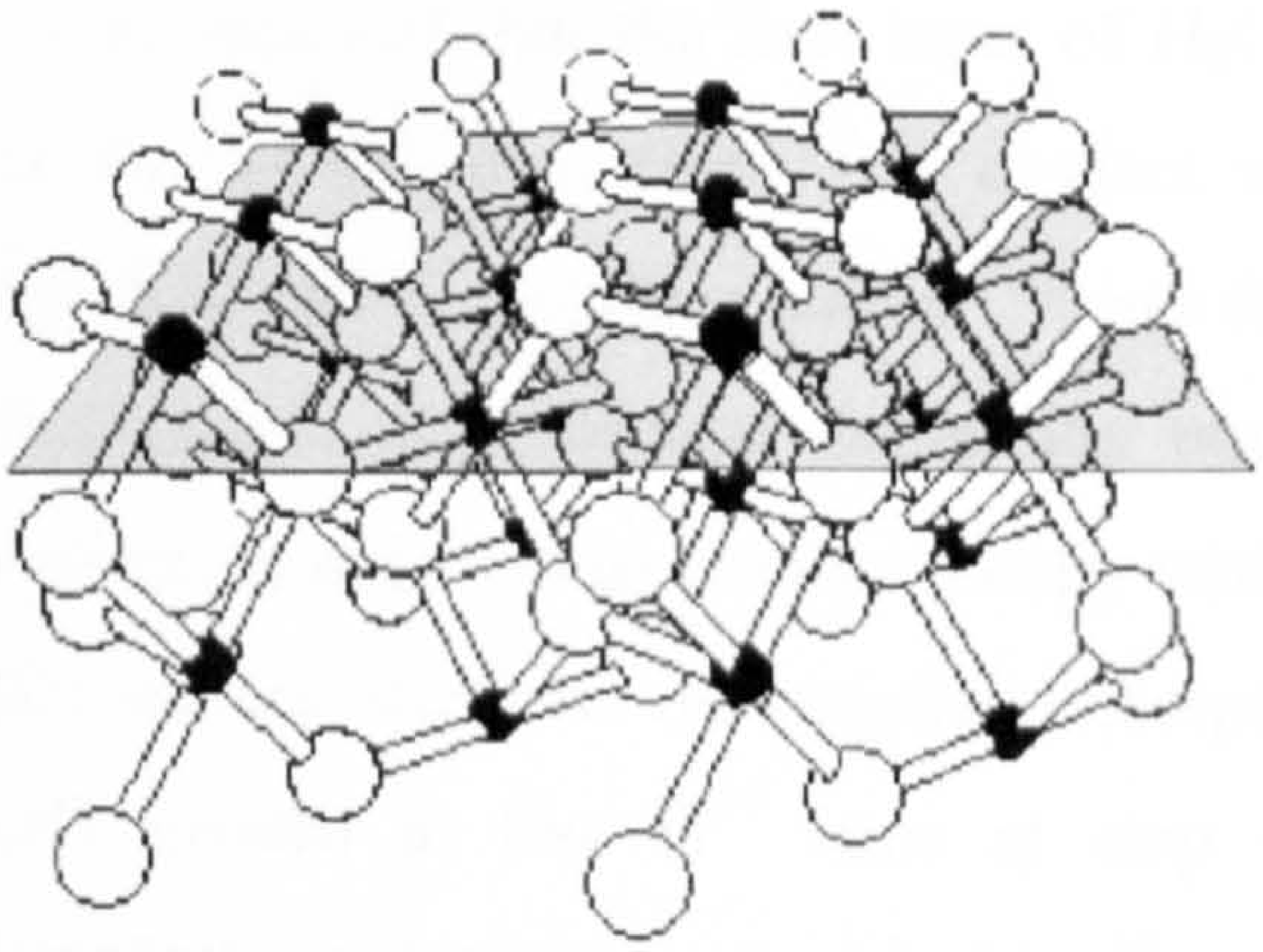

Figure 5.4: The unreconstructed rutile $TiO_2(001)$ Surface[10]

Although rutile, especially the (110) surface, is the most widely researched, industrial catalysts actually contain more anatase[34] and it is believed that in many cases this is the more active form of TiO_2. The (101) surface is the most thermodynamically stable of the common anatase truncations.[35,36] Although there have been only a handful of well-defined surface studies, it is believed[37] that the (101) surface exhibits a saw tooth-like structure consisting of Ti atoms at terraces with 5-fold and 6-fold co-ordination and Ti atoms at step edges with 4-fold co-ordination. In addition to 3-fold co-ordinated O atoms, the O atoms at the ridges of the saw tooth-like structure are 2-fold co-ordinated.

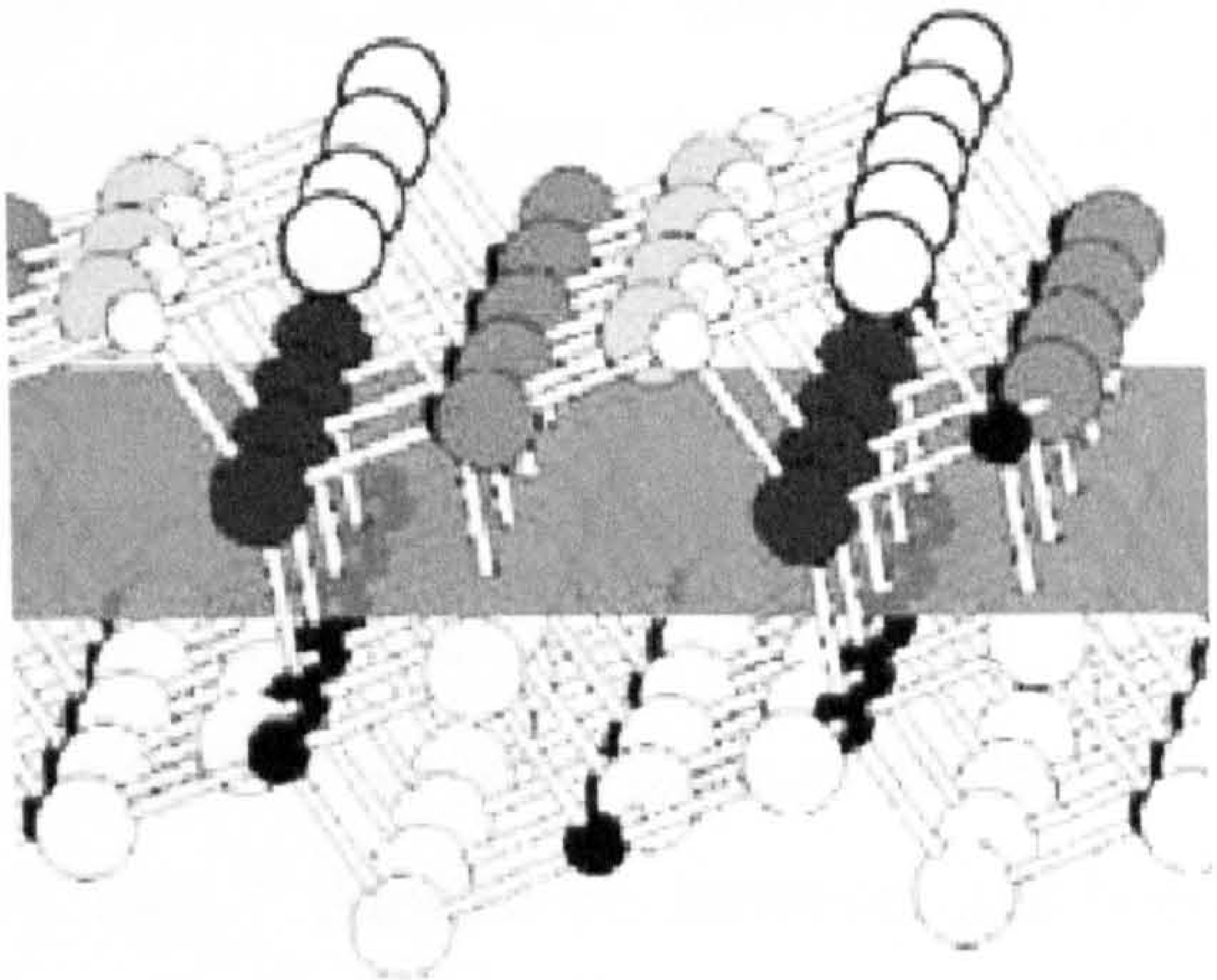

Figure 5.5: Proposed structure of the Anatase $TiO_2(101)$ Surface[10]

5.1.4 Surface Chemistry

The interactions of molecules with all kinds of TiO_2 surfaces, in particular rutile (110), have been extensively researched and are reviewed quite comprehensively.[10,38] All surfaces discussed here are rutile unless stated otherwise. The adsorption of **water** has received considerable attention, with empirical studies[39-42] and many theoretical studies.[43,44] It is believed that the first layer of H_2O molecules adsorb at the 5-fold Ti^{4+} sites of the $TiO_2(110)$ surface.[39] A distinct second state has been observed by TPD to desorb at 180 K. Another author[40,41] has found water adsorption on $TiO_2(110)$ to be dissociative or molecular depending upon the exposure. The second water layer, however, is believed to interact mostly with the bridging O sites. An STM study[42] on this surface supports dissociative adsorption and suggests that there are terminal –OH groups at the Ti^{4+} sites at step edges. Despite some disagreements in the literature, on the whole empirical studies, including STM, agree that dissociative adsorption occurs at defect sites, but that H_2O molecules are adsorbed molecularly on flat terraces.[10] There does however seem to be a general disagreement between the empirical findings that H_2O dissociates only at defect sites and the many theoretical studies that predict dissociative adsorption on the main surface. On the anatase (101) surface, water adsorption has been found by a TPD and XPS study, to be entirely molecular,[10,45] which is in agreement with theoretical studies of this system.[46]

Oxygen is well known to interact strongly with partially-reduced TiO_2 surfaces, filling up O-vacancies. It has been suggested by a study encompassing temperature-programmed desorption (TPD), isotopic labelling studies, sticking probability measurements, and electron energy loss spectroscopy (ELS),[47] that at 120 K, a surface with 8% vacancies has a saturation coverage of O_2 which is three times the concentration of vacancies. This has been explained in terms of adsorption of O^{2-} species, near the vacancies. **Hydrogen, carbon monoxide** and **carbon dioxide** are found to interact weakly with the clean TiO_2(110) surface. High pressures / exposures (10^5 L) were required for adsorption of molecular H_2 to cause additional emission peaks in UPS data.[48] Atomic H, however has been found to stick to the TiO_2(110) surfaces at room temperature.[49] Other research[50,51] has found O-vacancies on the TiO_2(110) surface to act as adsorption sites for H_2 and CO.

Due to the use of TiO_2 in some environmental catalytic applications, the interaction of TiO_2(110) with **nitrogen oxides** has received some interest. Upon interaction of NO with O-vacancies on the TiO_2(110) surface, N_2O is produced according to TPD studies.[52] In other research[53,54] involving SHG, XPS and UPS, it has been found that N_2O "heals" defects on the TiO_2(110) surface, but that no N remains on the surface. A modelling study has suggested that NO_2 adsorbs on the TiO_2(110) surface predominantly through formation of surface NO_3 as a result of disproportionation on Ti sites.[55] **Ammonia** is known to adsorb molecularly on TiO_2(110) at room temperature and bonds with the N-end down on the 5-fold co-ordinated Ti sites.[10,56] **Sulfur-containing compounds** have also received some research interest. Although SO_2 has been found to interact only very weakly with stoichiometric TiO_2(110),[57] there was a strong interaction with sputter-induced defects, which leads to them being oxidised completely at room temperature. Furthermore, no XPS evidence of S-O bonds were found, so it is believed the S atom binds to Ti sites forming TiS_2-like structures. Likewise, interaction of TiO_2(110) surfaces with H_2S is weak, but adsorption has been observed on sputtered surfaces.[57]

Many organic molecules have also been studied in terms of their interaction with TiO_2 surfaces. In particular, **formic acid** and other carboxylic acids have received much attention. Formic acid is well-known to interact strongly with rutile surfaces[58] and to dissociate resulting in formation of a surface formate species and surface hydroxyl group. The formate ion bonds to two 5-fold co-ordinated Ti atoms in a bi-dendate manner.[59,60] Additionally it is has been shown by RAIRS, that formate ions can bond to oxygen vacancies,[61] but this is considered a minority species. On the TiO_2(110)-(1 × 1) surface, one formate ion per every 2 unit cells (or exposed 5-fold co-ordinated Ti atom) was found at saturation coverage below 350 K, thus forming a regular p(2 × 1) structure. At cryogenic temperatures both formate ions and molecularly adsorbed formic acid molecules have been observed, the molecularly adsorbed multilayers desorbing at 164 K.[62] **Acetic acid** interacts with rutile surfaces in a similar manner to formic acid, forming a surface acetate species and a hydroxyl group.[58]

Adsorption of methanol has been investigated on a variety of rutile surfaces. A study[63] utilising XPS, UPS, LEED and TPD found that molecular adsorption of CH_3OH occurs at 289 K on TiO_2(110). Another study[64] on TiO_2(110) with 8% vacancies gave rise to a TPD peak at 480 K, believed to be recombinative desorption of dissociatively adsorbed CH_3OH. Theoretical studies also support both molecular and dissociative adsorption.[65] Dissociative adsorption is believed to occur by breaking of the O-H bond of CH_3OH, resulting in formation of a surface methoxy species and a surface hydroxyl group (probably on a bridging O atom).

5.2 Growth in Different Conditions

During the initial studies, Ti metal was deposited and then oxidised in small increments to establish the required O_2 exposure to completely oxidise the base metal. Film A was generated by depositing Ti onto the clean Cu(111) substrate at room temperature for 5 minutes at a deposition source current of 2.25 A. From the attenuation of the substrate photoelectron peak, the thickness of Ti was estimated to be 1.2 nm. Oxidation was then carried out in four 10 L O_2 increments at 673 K. After each exposure the O 1s, Cu 2p, C 1s, Ti 2p regions and a survey scan were recorded in XPS. After oxidation the Ti 2p peak (see Figure 5.6a) was seen to shift to higher binding energy, as expected, but was not very well defined, suggesting that lower oxidation states were present in addition to Ti^{4+}. The O 1s peak (see Figure 5.6b) increased in intensity and shifted to lower binding energy upon increasing exposure to O_2. The thickness of the final oxide film was estimated to be 2.8 nm. The binding energy of the Ti $2p_{3/2}$ peak is around 458.7 eV. Literature values for the Ti 2p peak attributed to Ti^{4+} ions varies widely due to the effect of surface defects,[10] however 458.5 eV is commonly used as the standard.[66] In carefully calibrated spectra 459.3 eV has been found for formal Ti^{4+}.[10] The values for reduced states of Ti also vary somewhat, however one author gives values of 457.2 eV and 455.3 eV for Ti^{3+} and Ti^{2+} respectively.[67]

To test the effect of different preparation conditions on the structure and properties of the TiO_x films generated, a number of films were grown with different parameters and these films characterised at different stages by XPS. Films B, C and D were grown by deposition of Ti metal for 1 minute, which was then exposed to 10 L (200 s at 5×10^{-8} Torr) O_2 at ambient temperature and then 20 L (400 s at 5×10^{-8} Torr) O_2 at an elevated temperature (623 K, 823 K and 773 K for B, C and D respectively). The reason for ambient temperature oxidation was to oxidise the deposited metal to some extent before annealing, as otherwise the heating might lead to migration of the Ti metal into the Cu substrate before oxidation occurs.

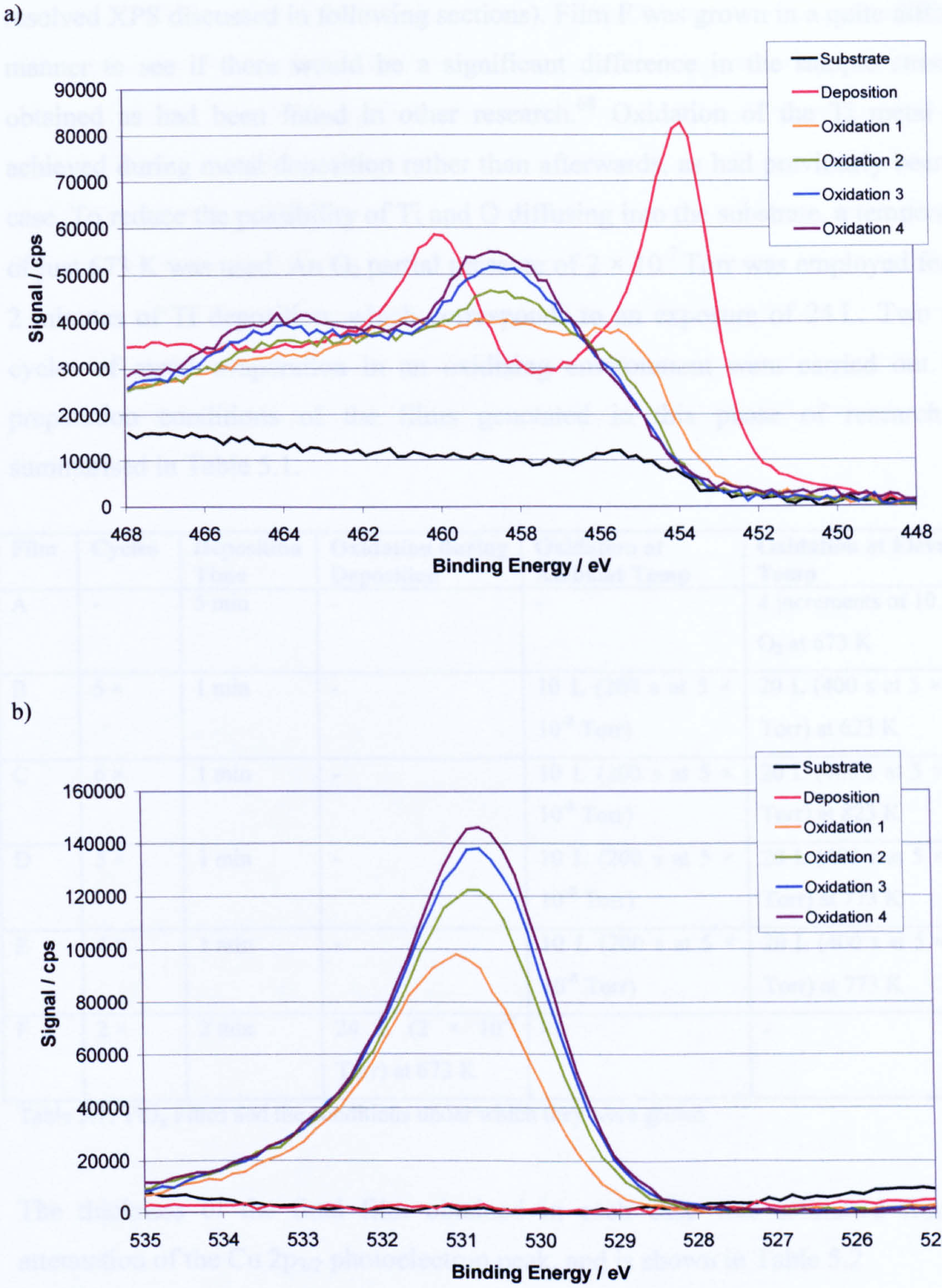

Figure 5.6: XPS data for stages of film A growth a) Ti 2p region; b) O 1s region; (Substrate = clean Cu(111) substrate; Deposition = after deposition of Ti metal for 5 mins at 2.25 A; Oxidation = after exposure to 10 L O_2 at 673 K)

The process of metal deposition, ambient temperature oxidation and elevated-temperature oxidation was repeated a number of times to generate thicker titania films. A further film, film E, was generated in the same way as film D; partly to test reproducibility and partly to focus on other measurements (*e.g.* LEED and angle-resolved XPS discussed in following sections). Film F was grown in a quite different manner to see if there would be a significant difference in the sample structure obtained as had been found in other research.[68] Oxidation of the Ti metal was achieved during metal deposition rather than afterwards, as had previously been the case. To reduce the possibility of Ti and O diffusing into the substrate, a temperature of just 673 K was used. An O_2 partial pressure of 2×10^{-7} Torr was employed for the 2 minutes of Ti deposition, which corresponds to an exposure of 24 L. Two such cycles of metal evaporation in an oxidising environment were carried out. The preparation conditions of the films generated in this phase of research are summarised in Table 5.1.

Film	**Cycles**	**Deposition Time**	**Oxidation during Deposition**	**Oxidation at Ambient Temp**	**Oxidation at Elevated Temp**
A	-	5 min	-	-	4 increments of 10 L O_2 at 673 K
B	5 ×	1 min	-	10 L (200 s at 5×10^{-8} Torr)	20 L (400 s at 5×10^{-8} Torr) at 623 K
C	6 ×	1 min	-	10 L (200 s at 5×10^{-8} Torr)	20 L (400 s at 5×10^{-8} Torr) at 823 K
D	5 ×	1 min	-	10 L (200 s at 5×10^{-8} Torr)	20 L (400 s at 5×10^{-8} Torr) at 773 K
E	4 ×	1 min	-	10 L (200 s at 5×10^{-8} Torr)	20 L (400 s at 5×10^{-8} Torr) at 773 K
F	2 ×	2 min	24 L (2×10^{-7} Torr) at 673 K	-	-

Table 5.1: TiO_x Films and the conditions under which they were grown

The thickness of the final film obtained in each case was estimated from the attenuation of the Cu $2p_{3/2}$ photoelectron peak, and is shown in Table 5.2

Film	d_{TiO_x} **/ nm**
A	2.8
B	2.9
C	1.9
D	1.4
E	1.8
F	1.8

Table 5.2: Estimated thickness of TiO_x films

In the case of films B, C and D (where the deposited Ti metal was oxidised at both ambient temperature and elevated temperature), it was apparent from the binding energy of the Ti $2p_{3/2}$ peak that oxidation of the base metal had occurred even after exposure to O_2 at ambient temperature on the first cycle (see Figure 5.7a and 5.7b). In fact the following exposure to 20 L of O_2 seemed to have relatively little effect on the spectra, other than leading to a slight increase in O 1s intensity. Incidentally, the feature at 455 eV in the substrate spectrum shown in Figure 5.7a is due to the Cu Auger transition seen for the substrate only scan and not a reduced state of Ti, since this feature is present on all the Ti 2p regional spectra from films of comparable thickness.

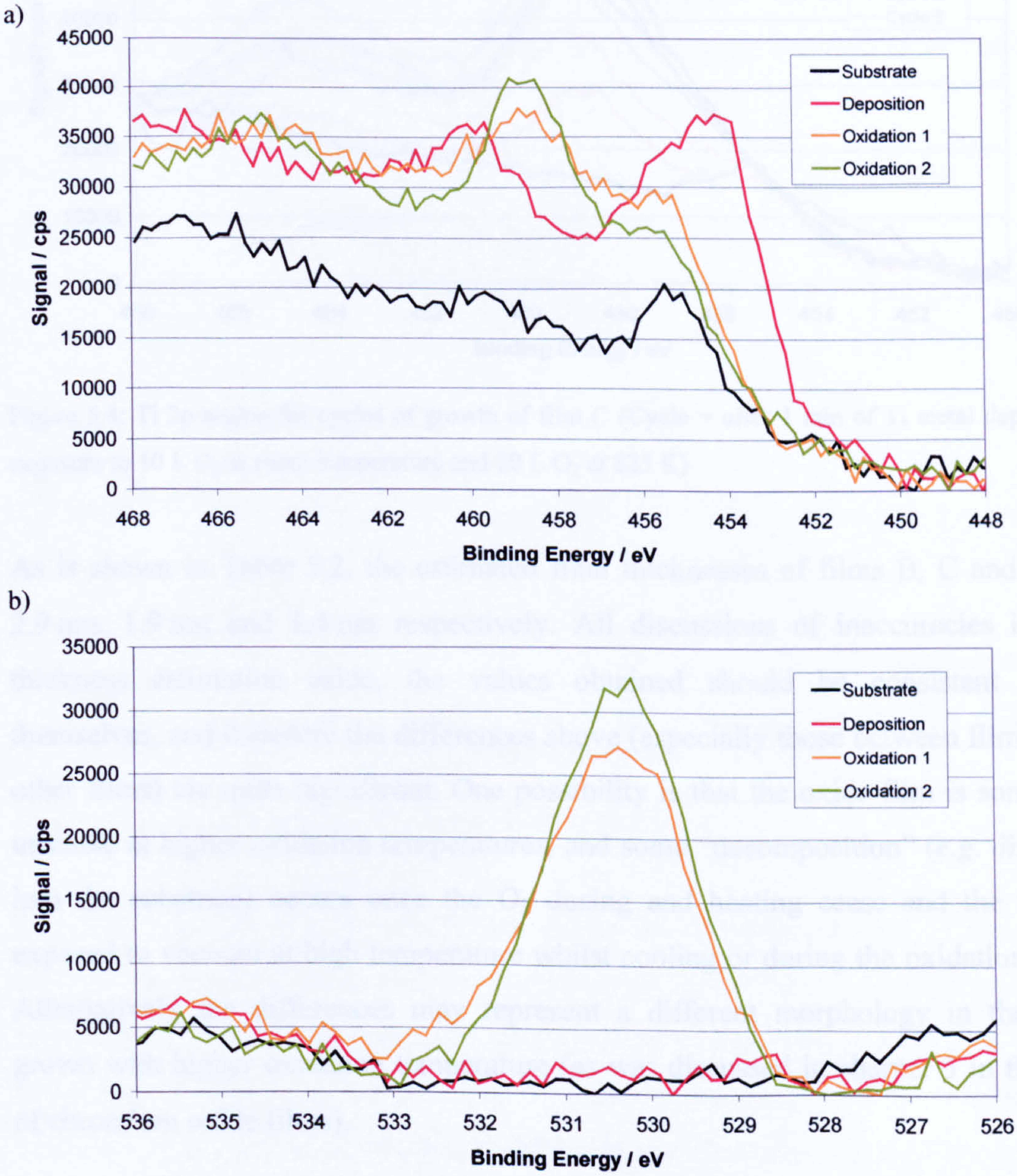

Figure 5.7: XPS data for cycle 1 of film B growth a) Ti 2p region; b) O 1s region; (Oxidation 1 = after exposure to 10 L O_2 at room temperature; Oxidation 2 = after exposure to 20 L O_2 at 623 K)

At this stage in the preparation the Ti 2p region was still poorly defined suggesting either the presence of multiple oxidation states, or at least a very inhomogenous film. With subsequent cycles of deposition and oxidation (see Figure 5.8), the peaks in the Ti 2p and O 1s regions show a steady increase in intensity, whilst the Cu 2p peak shows a steady decrease in intensity, reflecting the growth and increasing thickness of the titania films.

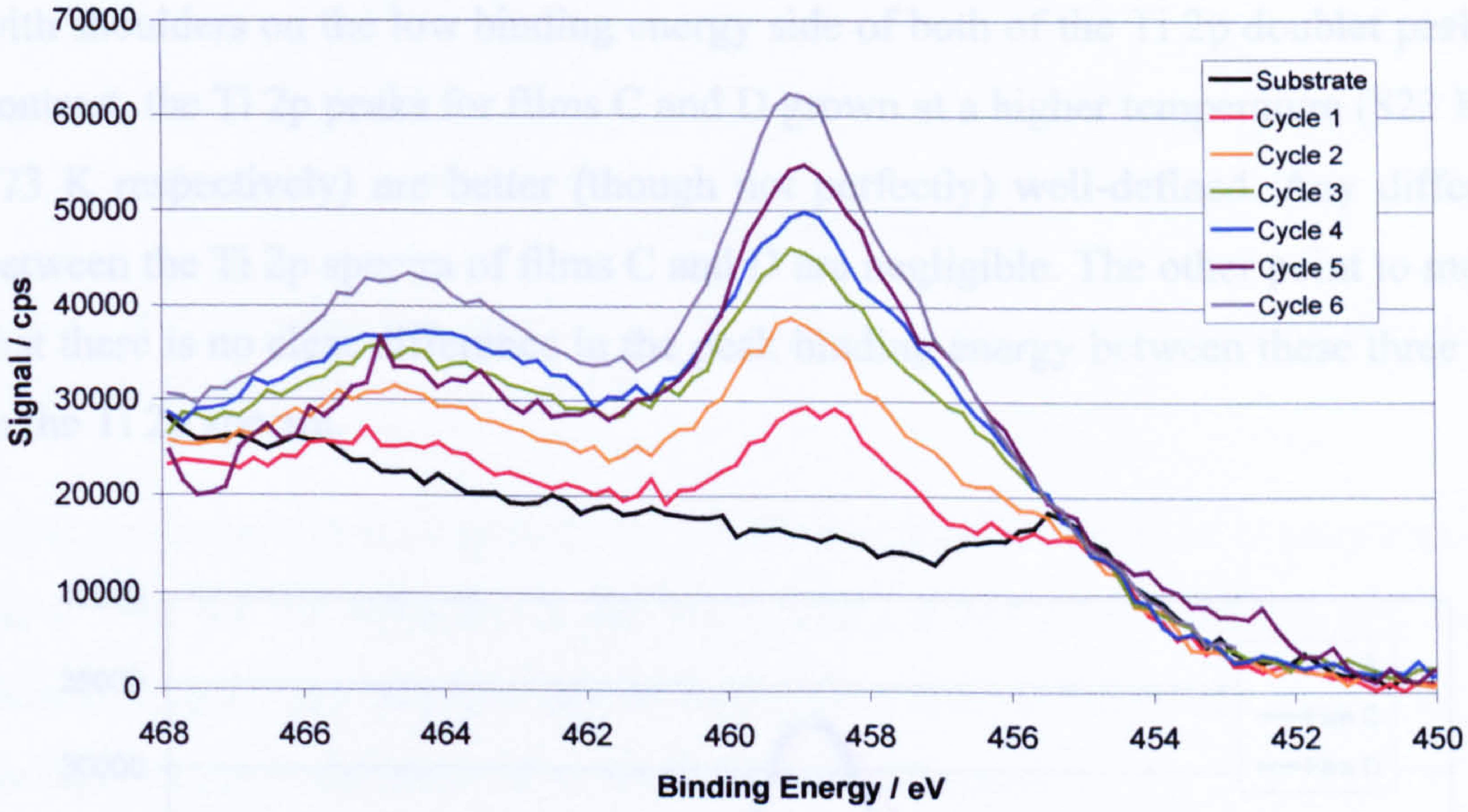

Figure 5.8: Ti 2p region for cycles of growth of film C (Cycle = after 1 min of Ti metal deposition, exposure to 10 L O_2 at room temperature and 20 L O_2 at 823 K)

As is shown in Table 5.2, the estimated final thicknesses of films B, C and D are 2.9 nm, 1.9 nm and 1.4 nm respectively. All discussions of inaccuracies in film thickness estimation aside, the values obtained should be consistent within themselves, and therefore the differences above (especially those between film B and other films) are quite significant. One possibility is that the oxide film is somewhat unstable at higher oxidation temperatures, and some "decomposition" (*e.g.* diffusion into the substrate) occurs once the O_2 dosing and heating cease and the film is exposed to vacuum at high temperature whilst cooling or during the oxidation itself. Alternatively the differences may represent a different morphology in the films grown with higher oxidation temperature (as was discussed in chapter 3 in the case of chromium oxide films).

It is interesting to compare how well-defined the Ti 2p peaks are for films B, C and D after completion of growth, to see what effect the temperature of oxidation has. Due to the difference in thickness of these three films, however, the data in Figure 5.9 has been normalised by dividing the electron counts by the estimated thickness of the film. As expected, this manipulation makes all three spectra appear to have the same Ti 2p intensity. It is now however much easier to compare the spectra and we see that the peak profile for film B, grown at just 623 K, is clearly less well-defined with shoulders on the low binding energy side of both of the Ti 2p doublet peaks. In contrast, the Ti 2p peaks for films C and D grown at a higher temperature (823 K and 773 K respectively) are better (though not perfectly) well-defined. Any difference between the Ti 2p spectra of films C and D are negligible. The other point to make is that there is no clear difference in the peak binding energy between these three films in the Ti 2p spectra.

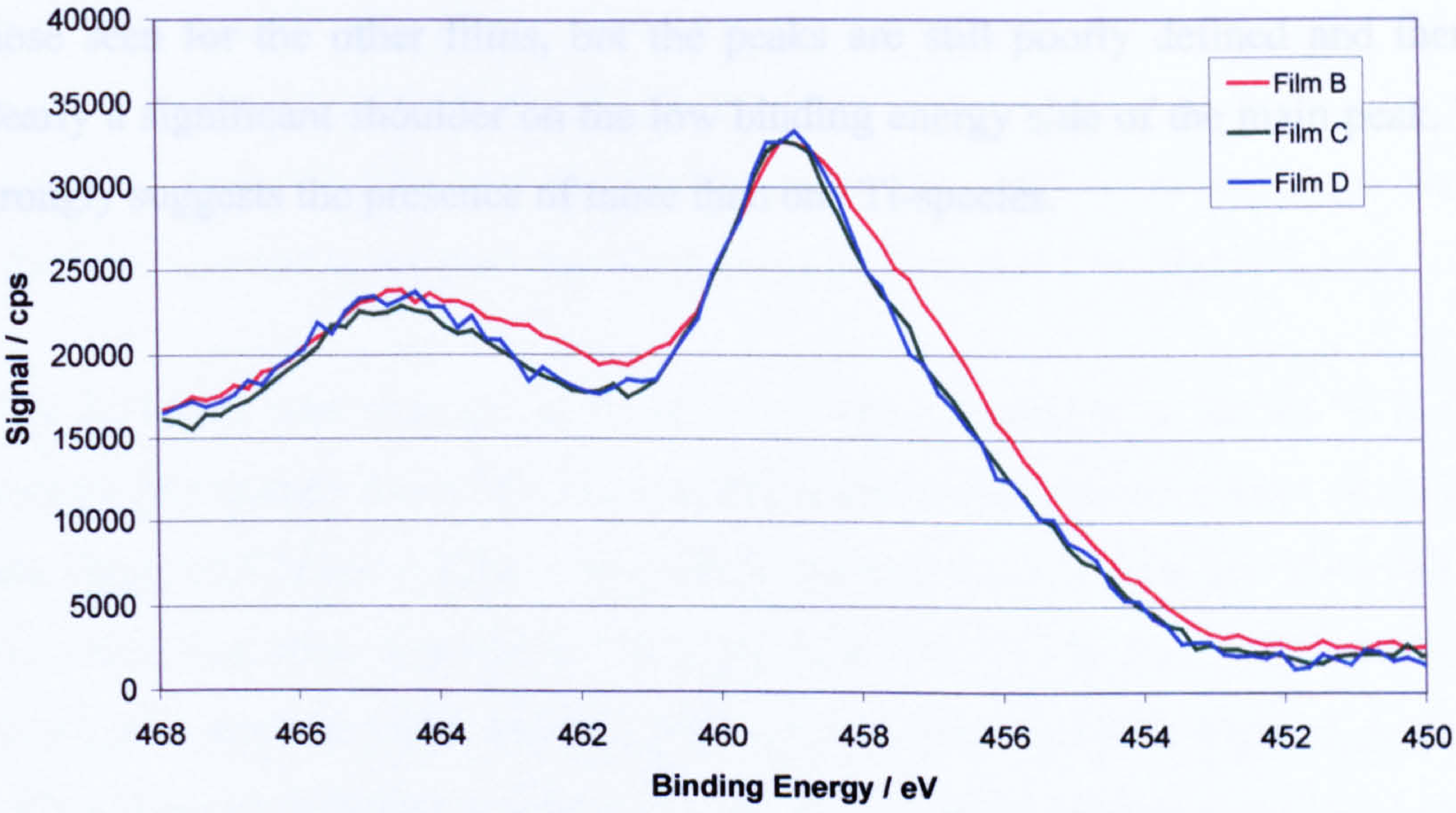

Figure 5.9: A comparison of the Ti 2p region for films B, C and D

The XPS data for film F, which was grown by oxidation during Ti deposition, showed the expected attenuation of the Cu $2p_{3/2}$ signal, from which an oxide film thickness of 1.8 nm was estimated after the two cycles. The O 1s region seemed reasonably well-defined, but the Ti 2p peak profile was very poor (see Figure 5.10). This raises the question of whether Ti diffusion was occurring into the Cu substrate.

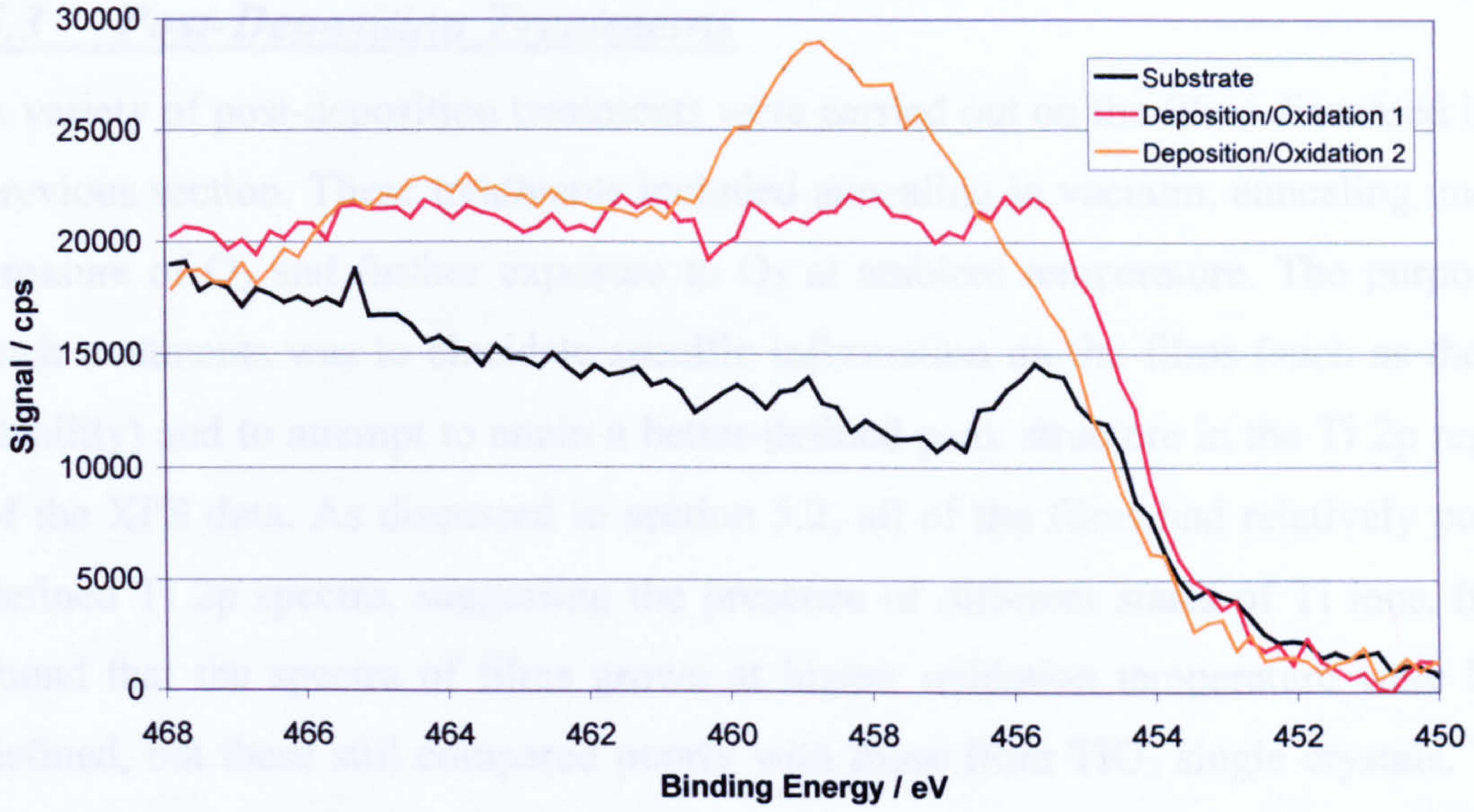

Figure 5.10: Ti 2p region for growth of film F (Deposition/Oxidation = after deposition of Ti metal for 2 mins whist exposing to 24 L O_2 at 673 K)

After the second step of growth, the Ti 2p spectrum much more closely resembles those seen for the other films, but the peaks are still poorly defined and there is clearly a significant shoulder on the low binding energy side of the main peak. This strongly suggests the presence of more than one Ti-species.

5.3 Post-Deposition Treatments

A variety of post-deposition treatments were carried out on the films discussed in the previous section. These treatments included annealing in vacuum, annealing under a pressure of O_2 and further exposure to O_2 at ambient temperature. The purpose of such treatments was to elucidate specific information on the films (such as thermal stability) and to attempt to attain a better-defined peak structure in the Ti 2p regions of the XPS data. As discussed in section 5.2, all of the films had relatively poorly-defined Ti 2p spectra, suggesting the presence of different states of Ti ions. It was found that the spectra of films grown at higher oxidation temperature were better defined, but these still compared poorly with those from TiO_2 single crystals. What would be the effect of post annealing?

Film A, which was oxidised in increments at 673 K, was annealed to 873 K for 5 minutes in vacuum to test the thermal stability and to see if this treatment would improve the uniformity of the film. After this treatment there was only a small decrease in the intensity of the Ti 2p and O 1s peaks relative to the Cu 2p peak, suggesting that this film was reasonably thermally stable. However there was no clear improvement to the peak structure in the Ti 2p region (see Figure 5.11a).

Film B, which was oxidised at 623 K, was then exposed to a further 20 L O_2 at ambient temperature to see if it had lost any oxygen whilst cooling down from 623 K (see Figures 5.12a and 5.12b). A very slight increase in O 1s peak was observed. The TiO_x film was then exposed to 20 L O_2 at 723 K, 773 K and 823 K, each time allowing to cool in UHV before XPS data was recorded (see Figures 5.12a and 5.12b). After each further heating in O_2 the Ti 2p doublet became significantly better defined. This trend was accompanied by a slight decrease in O 1s peak intensity and a smaller decrease in Ti $2p_{3/2}$ peak intensity. This seems to suggest that a higher temperature is required to generate well-defined TiO_2 films. Some "breakdown" of the film (*e.g.* oxide aggregation/sintering) is evident from the reduction in O and Ti peak intensities. The binding energy of the Ti $2p_{3/2}$ peak is 458.9 eV and this slowly increased to 459.1 eV with increasing temperature of oxidation.

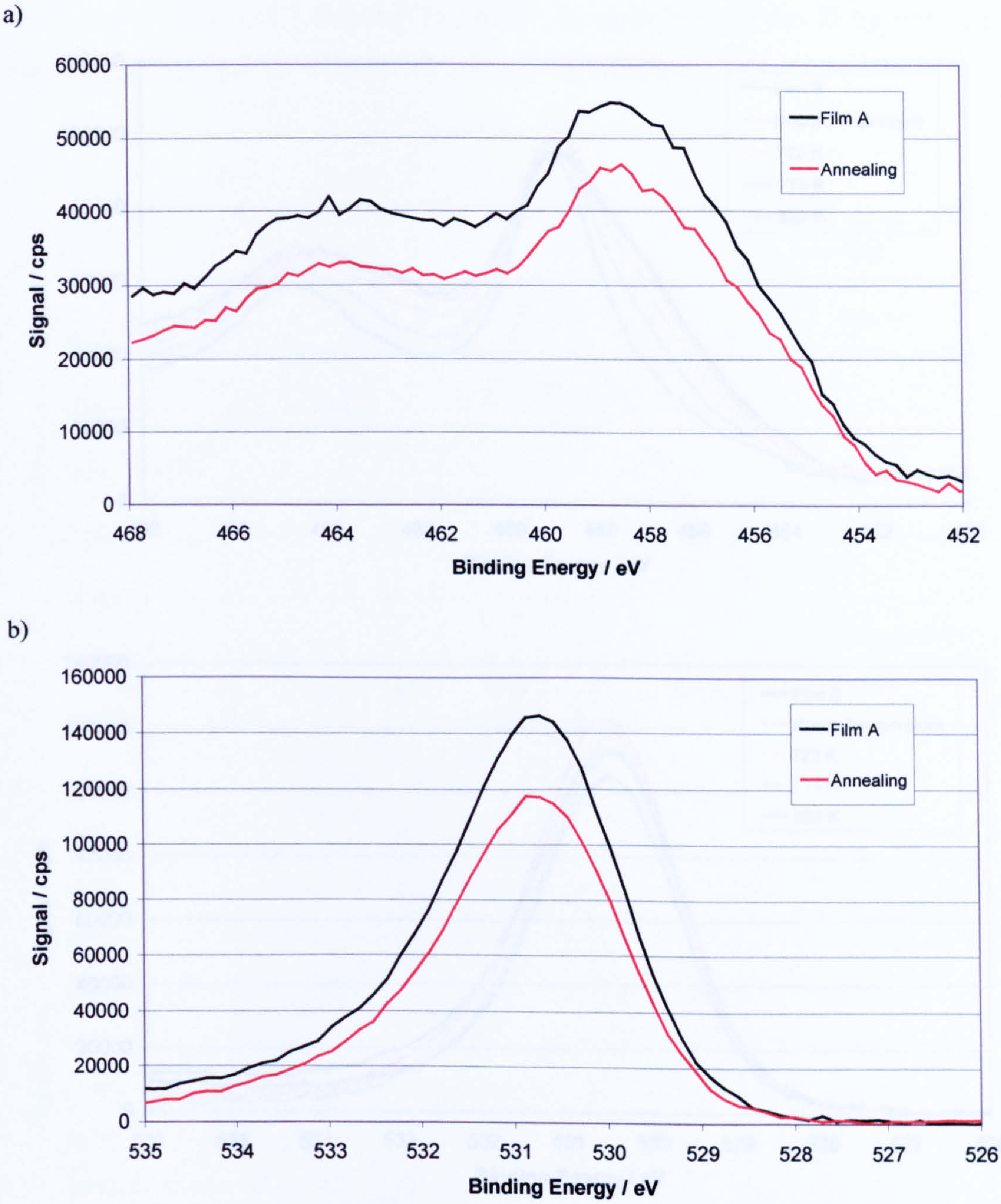

Figure 5.11: XPS data for film A before and after annealing at 873 K for 5 mins in vacuum a) Ti 2p region; b) O 1s region

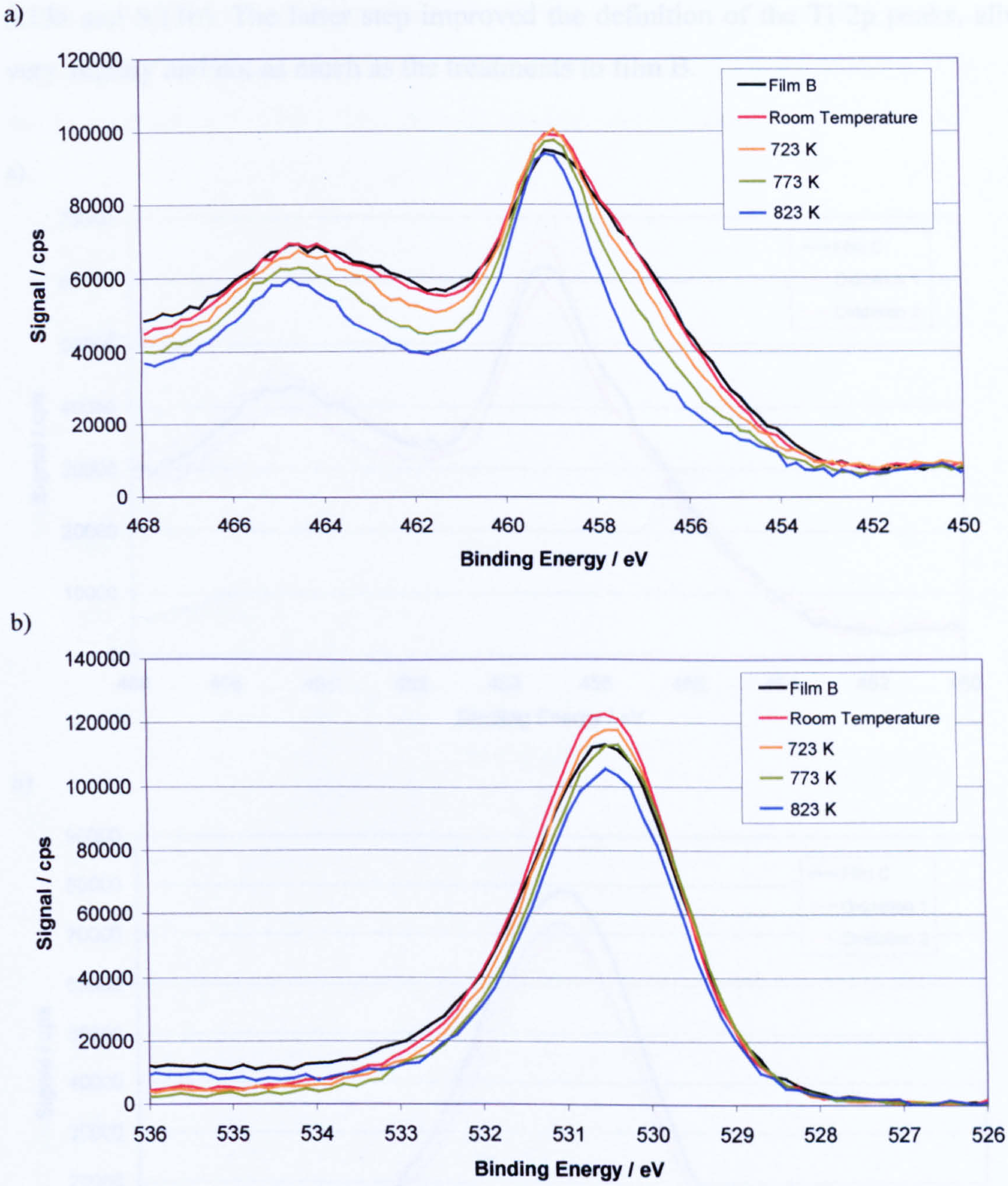

Figure 5.12: XPS data for film B before and after exposure to 20 L O_2 at each of the indicated temperatures a) Ti 2p region; b) O 1s region

Peak fitting and normalisation of the data obtained after annealing at 823 K (*i.e.* when the Ti 2p region is better-defined) gives an O:Ti ratio of 1.6. This is nearest to Ti_2O_3 stoichiometry, but as previously mentioned some caution is required when regarding these values as absolute.

Film C, which was grown at 823 K, was subsequently exposed to 10 L O_2 at ambient temperature, and then exposed to 20 L O_2 at a temperature of 823 K (see Figures

5.13a and 5.13b). The latter step improved the definition of the Ti 2p peaks, albeit very slightly and not as much as the treatments to film B.

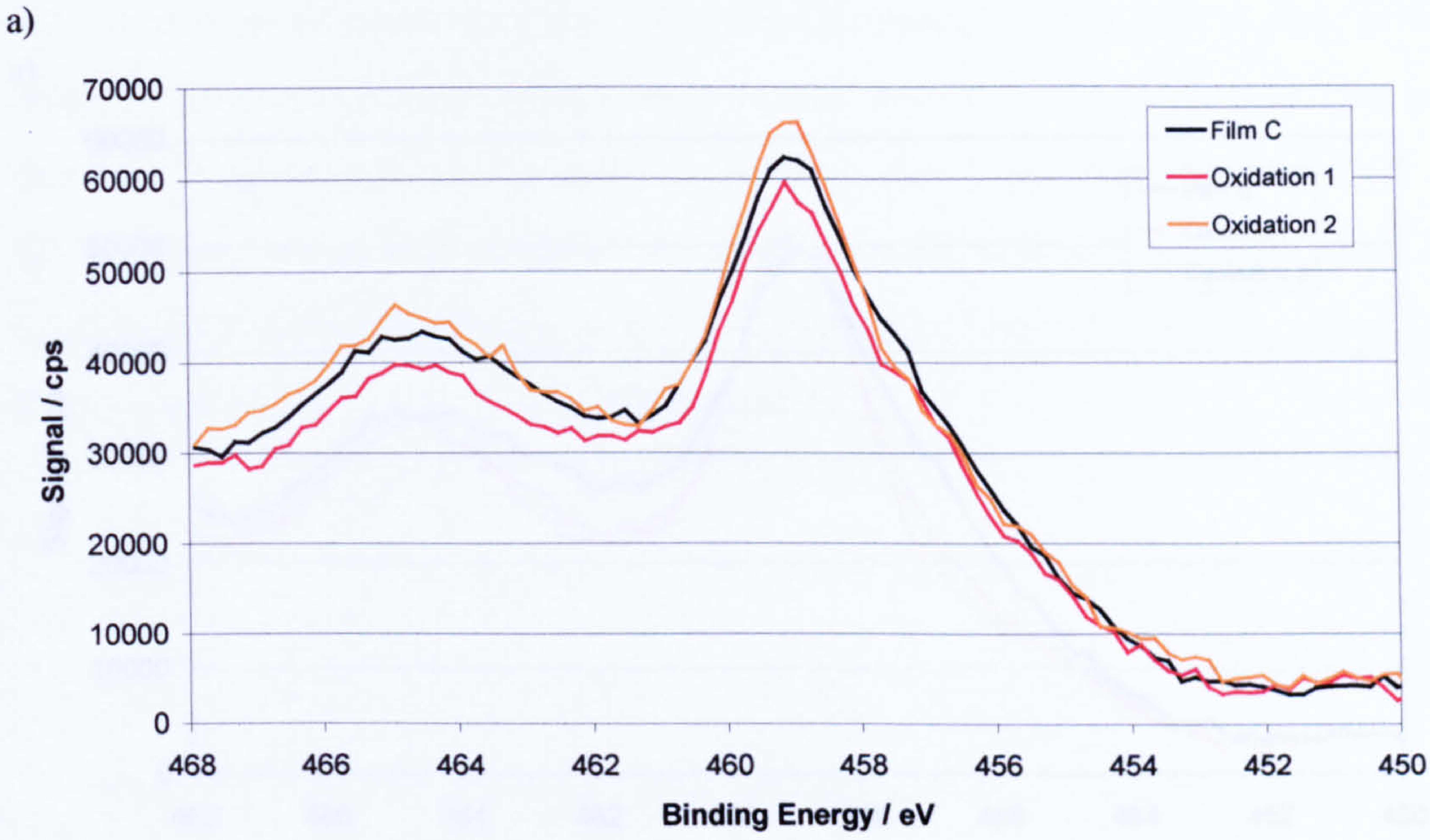

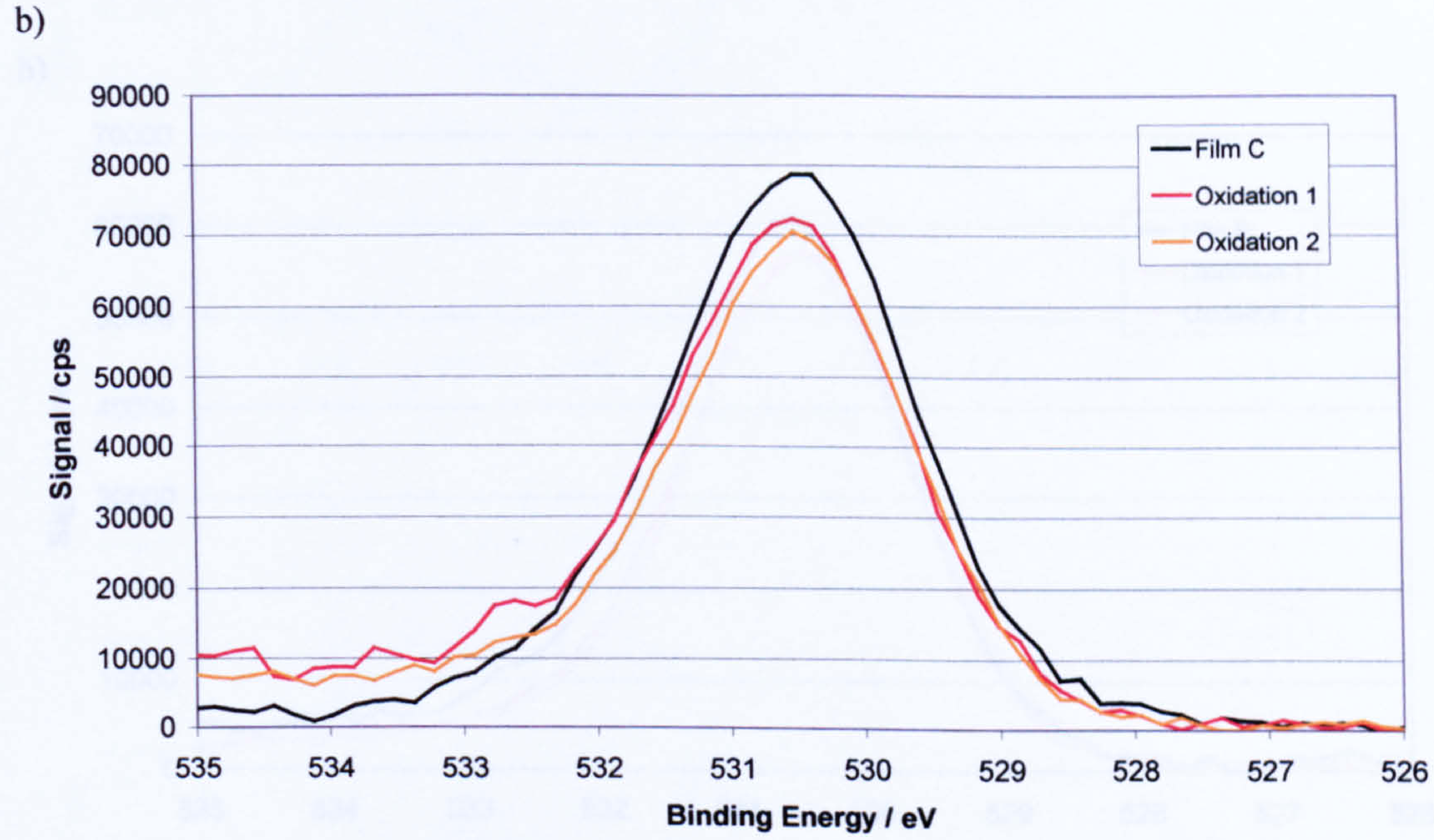

Figure 5.13: XPS data for film C before and after oxidation treatments a) Ti 2p region; b) O 1s region; (Oxidation 1 = 10 L O_2 at room temperature; Oxidation 2 = 20 L O_2 at 823 K)

Film E, which was grown at 773 K, was then exposed to 40 L O_2 at 773 K and this was carried out twice (see Figures 5.14a and 5.14b). With this further oxidation the O 1s peak was seen to increase very slightly in intensity, and shift very slightly to lower binding energy consistent with an increase in oxidation state of the Ti. The Ti $2p_{3/2}$

peak became better-defined, which shows that the additional oxidation treatments successfully shifted the Ti to its 4+ oxidation state and TiO_2 stoichiometry. The O:Ti ratio was estimated to be 1.7 by peak fitting and normalisation.

a)

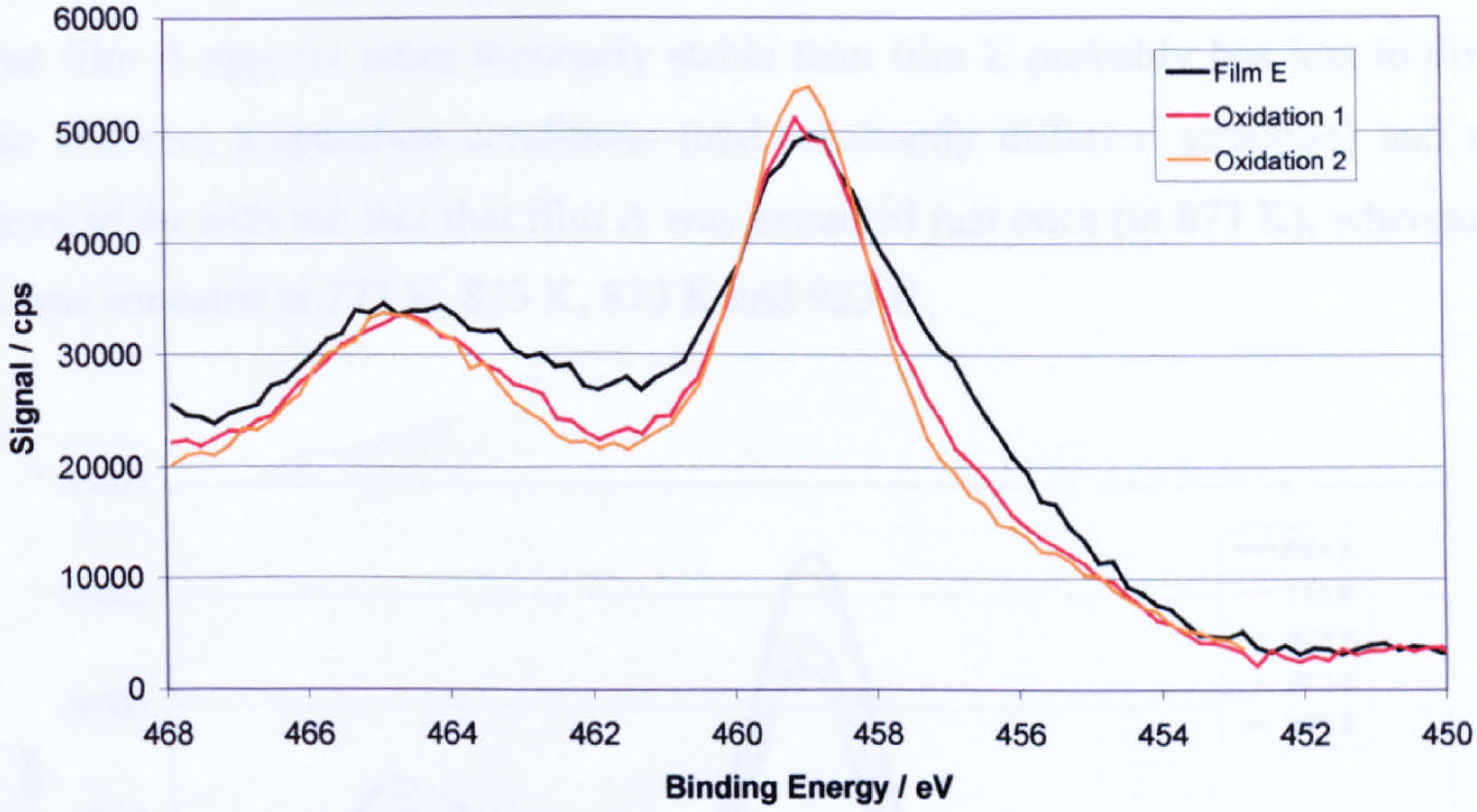

b)

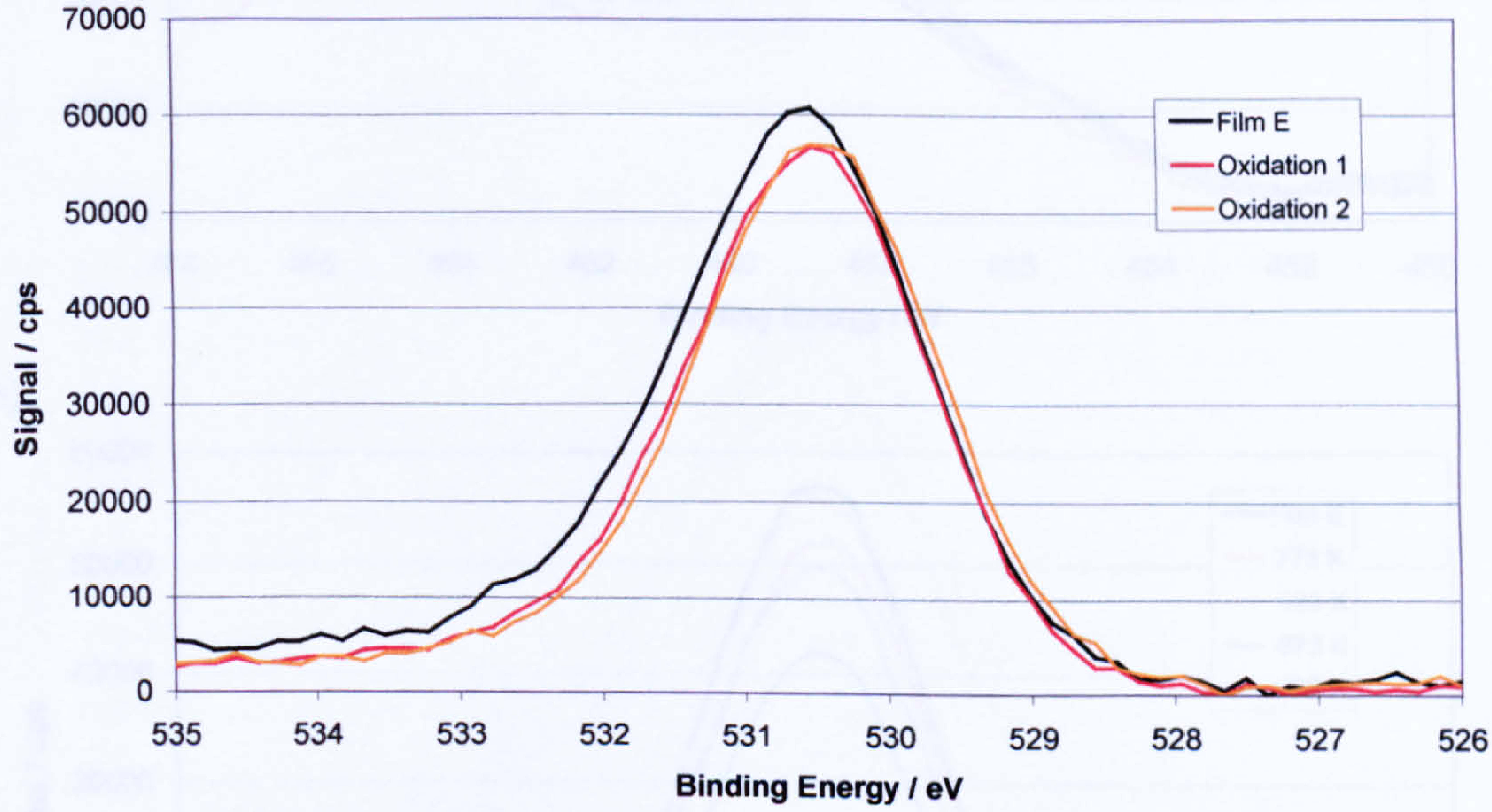

Figure 5.14: XPS data for film E before and after oxidation treatments a) Ti 2p region; b) O 1s region; (Oxidation = after exposure to 40 L O_2 at 773 K)

Film E was then annealed at 773 K, 823 K, 873 K and 923 K each time for 5 minutes in vacuum (see Figures 5.15a and 5.15b). It appears that this treatment did not lead to a significant improvement in the Ti 2p region. Additionally the annealing led to significant breakdown of the film as evidenced by decreases in the intensities of the

Ti 2p and O 1s peaks relative to Cu 2p. The estimated film thickness decreased from 1.8 nm to 1.0 nm as a result of these high temperature treatments. One might ask whether the changes to the film are associated with loss of oxygen by desorption into the vacuum or diffusion into the substrate. Examination of the XPS data, however, does not support this theory, since there is no decrease in the O:Ti ratio. The reason that film A appears more thermally stable than film E probably has less to do with the different preparation conditions (and resultantly different structure) and rather more to do with the fact that film A was annealed just once (at 873 K), whereas film E was annealed at 773 K, 823 K, 873 K and 923 K.

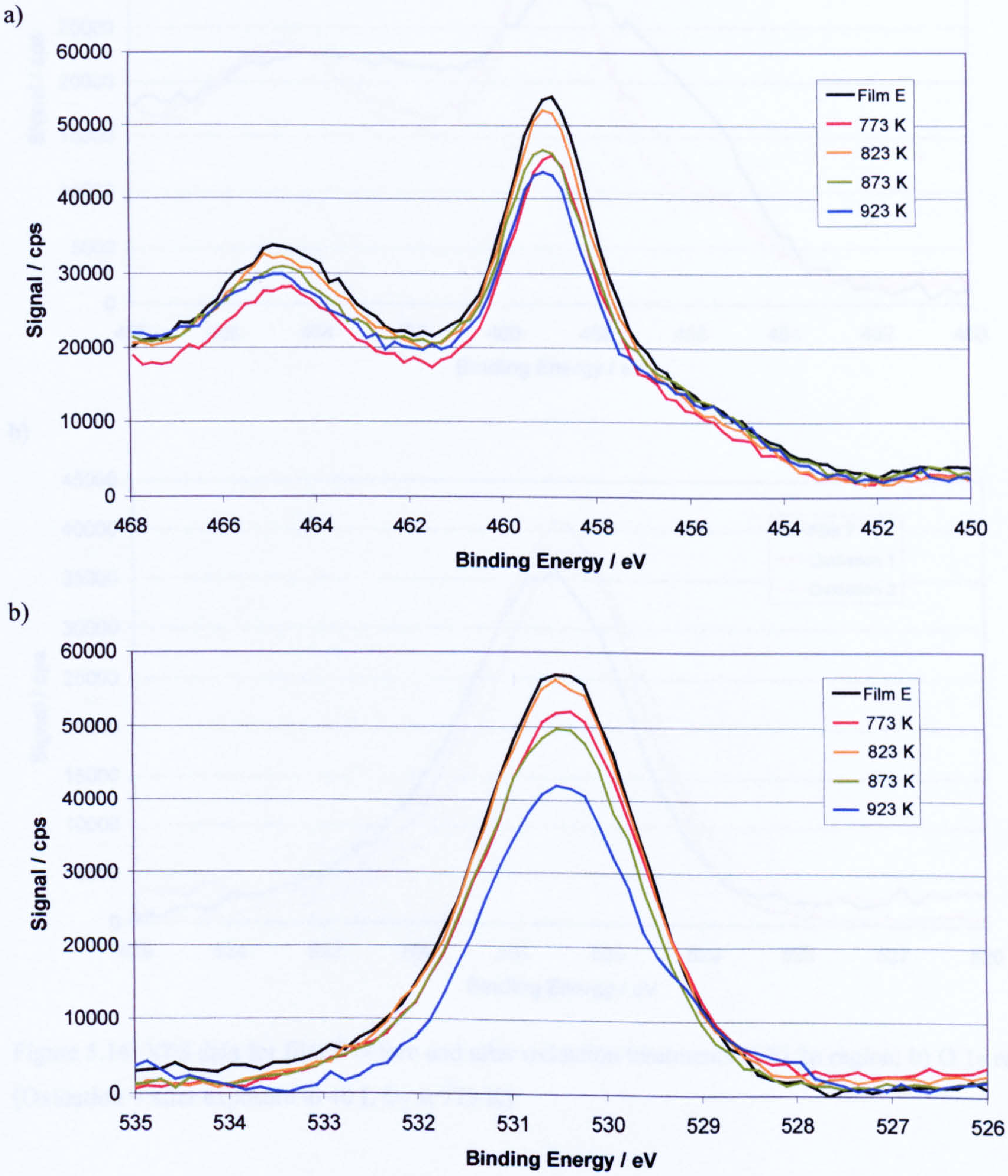

Figure 5.15: XPS data for film E before and after annealing in vacuum at each of the indicated temperatures a) Ti 2p region; b) O 1s region

Film F, which was grown by oxidation during deposition at 673 K was subsequently exposed to 40 L O_2 at 773 K (see Figures 5.16a and 5.16b). The XPS data supported a shift towards TiO_2 stoichiometry, as the Ti $2p_{3/2}$ region became very much better-defined with a peak maximum at 458.9 eV. There was also a slight increase in O 1s peak intensity and a slight shift of the O 1s peak to lower binding energy.

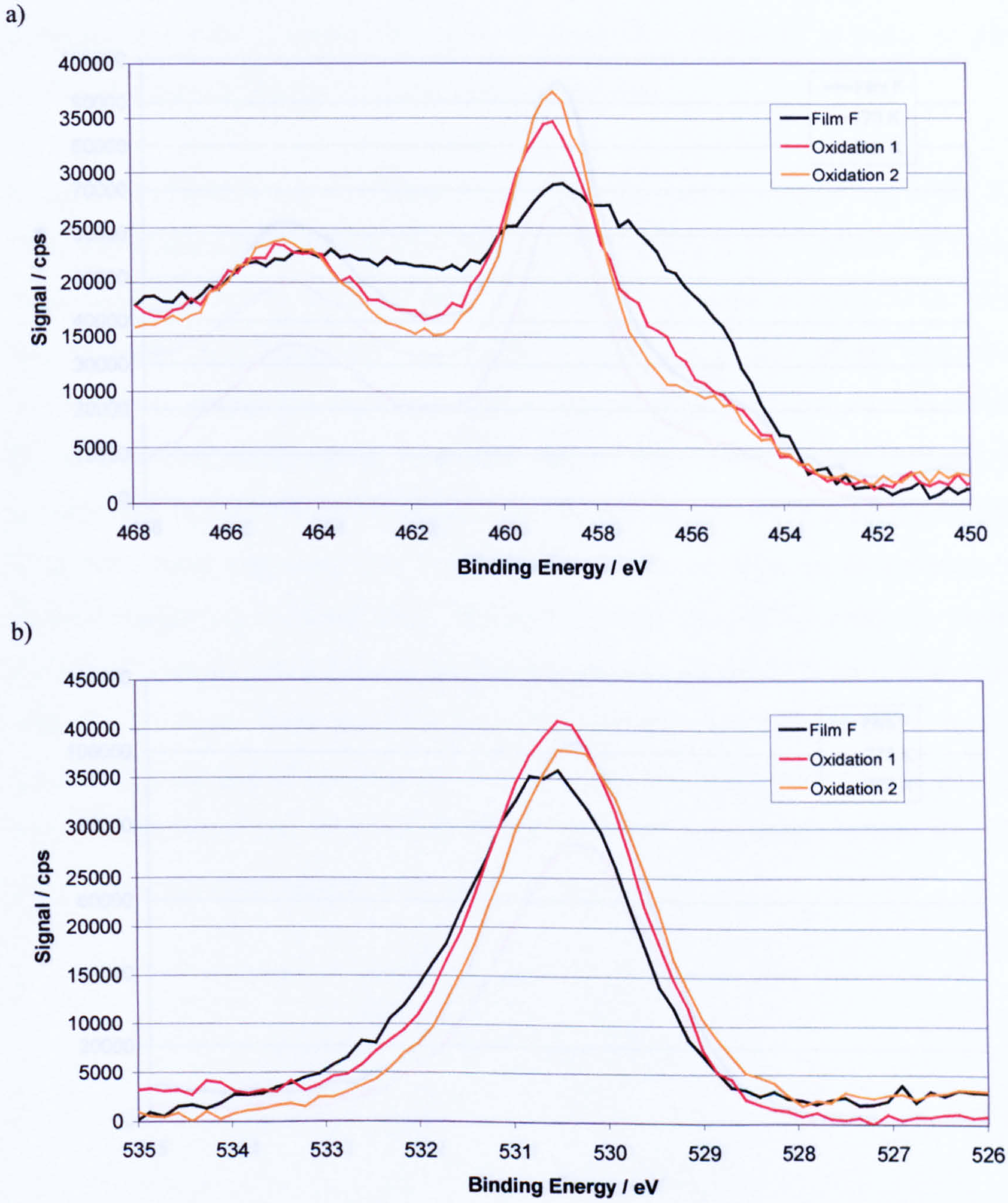

Figure 5.16: XPS data for film F before and after oxidation treatments a) Ti 2p region; b) O 1s region; (Oxidation = after exposure to 40 L O_2 at 773 K)

Film F was then exposed to a further 40 L O_2 at 773 K, after which the Ti 2p region was even better-defined (see Figures 5.16a and 5.16b).

The resulting film was then annealed in vacuum at 773 K and 823 K each time for 5 minutes in vacuum (see Figures 5.17a and 5.17b). There was no improvement in the Ti 2p peak definition with these treatments however and there was also evidence of some film breakdown, as previously observed when annealing at such temperatures in vacuum.

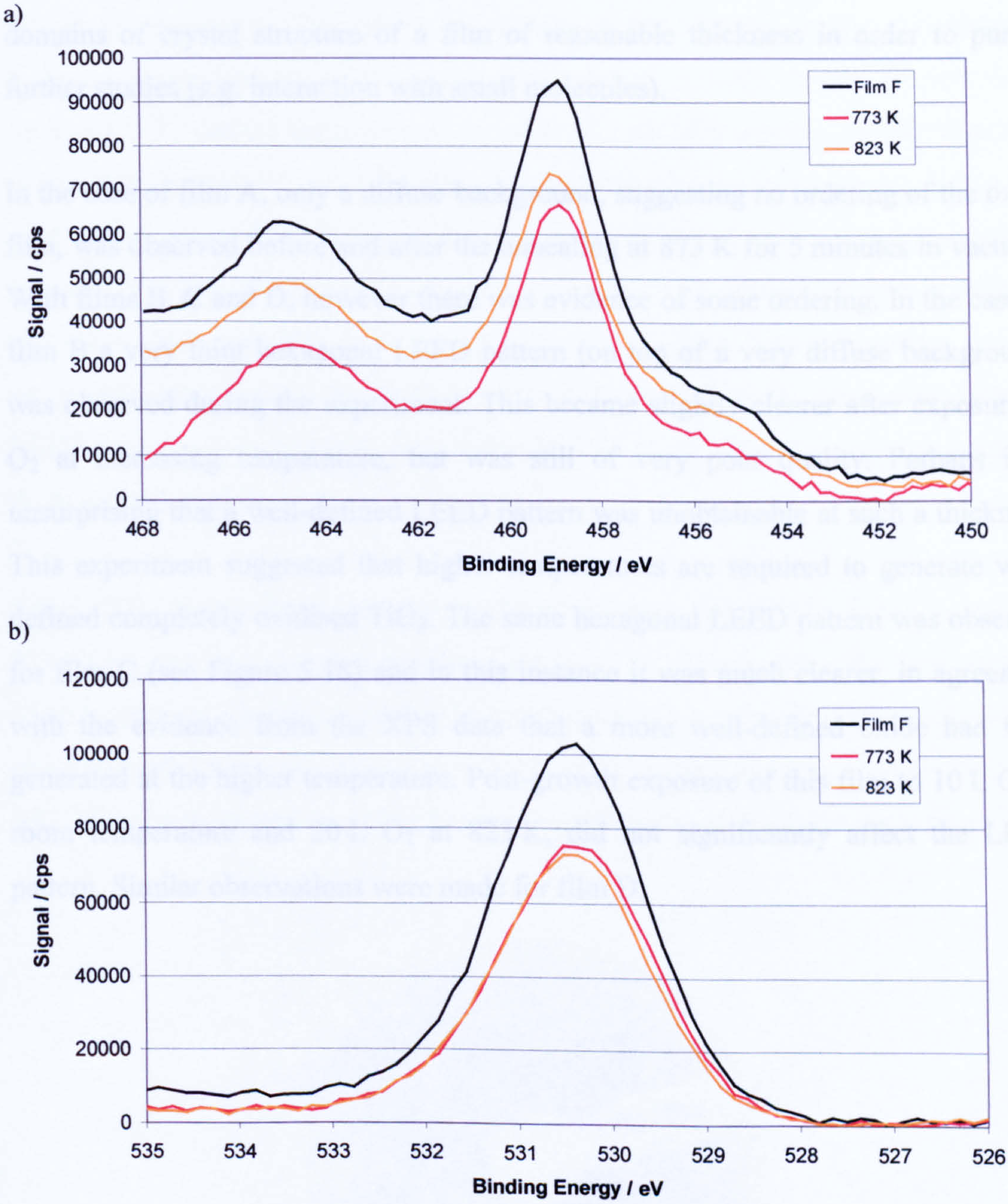

Figure 5.17: XPS data of film F before and after annealing in vacuum for 5 minutes at the indicated temperature a) Ti 2p region; b) O 1s region

5.4 Conditions for Ordering

The aim of this research is to generate well-defined films. One feature which needs to be well-defined is the stoichiometry, which has been tested to some extent by the attempt to produce films with a well-defined Ti 2p region in the XPS data, as discussed in section 5.3. The other key feature is the degree of ordering. The ultimate aim is to obtain a clear LEED pattern indicating the presence of well-ordered domains of crystal structure of a film of reasonable thickness in order to pursue further studies (*e.g.* interaction with small molecules).

In the case of film A, only a diffuse background, suggesting no ordering of the oxide film, was observed before and after the annealing at 873 K for 5 minutes in vacuum. With films B, C and D, however there was evidence of some ordering. In the case of film B a very faint hexagonal LEED pattern (on top of a very diffuse background) was observed during the experiment. This became slightly clearer after exposure to O_2 at increasing temperature, but was still of very poor quality. Perhaps it is unsurprising that a well-defined LEED pattern was unobtainable at such a thickness. This experiment suggested that higher temperatures are required to generate well-defined completely oxidised TiO_2. The same hexagonal LEED pattern was observed for film C (see Figure 5.18) and in this instance it was much clearer, in agreement with the evidence from the XPS data that a more well-defined oxide had been generated at the higher temperature. Post-growth exposure of this film to 10 L O_2 at room temperature and 20 L O_2 at 823 K, did not significantly affect the LEED pattern. Similar observations were made for film D.

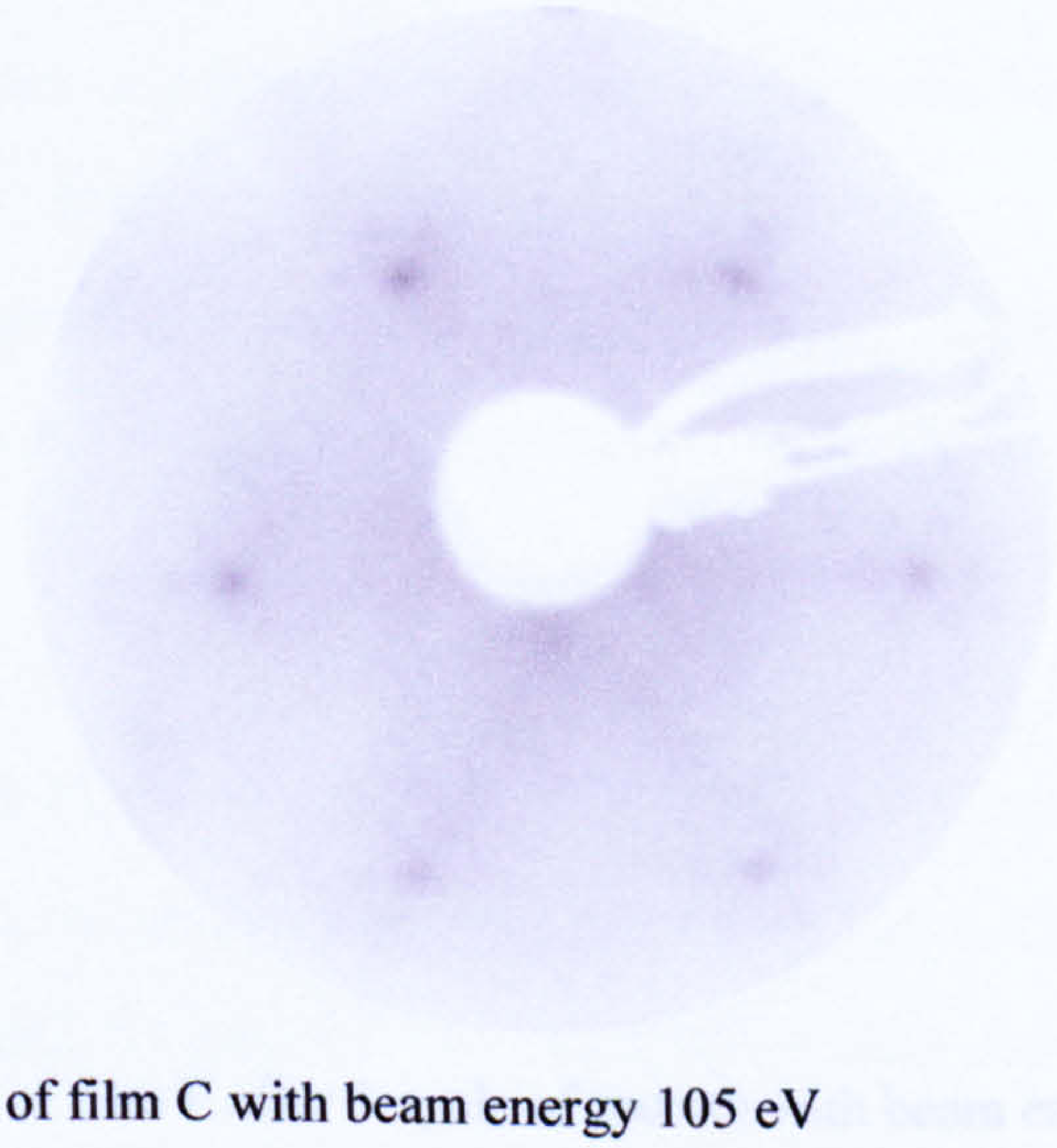

Figure 5.18: LEED pattern of film C with beam energy 105 eV

The clear trend evident from this early work is that a higher temperature of growth is required for obtaining better (yet far from perfect) LEED patterns, as demonstrated by the differences described above between film B grown at 623 K and films C and D grown at 823 K and 773 K. The post-growth treatments seem to have had little or no effect on the LEED pattern clarity in these cases. It is interesting to look at correlations between the clarity of the LEED patterns obtained and how well-defined the Ti 2p region is, throughout the series of experiments. Some consideration however is required as to what such a correlation actually means. A clear well-defined LEED pattern suggests that domains of a specific crystal structure dominate the sample. A well-defined XP peak suggests that only one stoichiometry of (in this case) Ti is present. We might expect a strong correlation between these two results, although it is possible to have a crystal structure with an element present in different oxidation states and just because we have a well-defined stoichiometry, doesn't necessarily mean that the film will be ordered. Nevertheless, the correlation between LEED pattern clarity and how well-defined the Ti 2p XP region is seems to hold true throughout this work.

The LEED pattern formation was examined in more detail with film E, grown at 773 K, by checking the pattern after each cycle of growth. After the first cycle of growth (thickness estimated to be 0.4 nm) a pattern was observed (see Figure 5.19) consisting of a hexagon of rosettes. The Cu(111) substrate spots are the outermost spot of each rosette and the middle spot of each rosette relates to the TiO_x film.

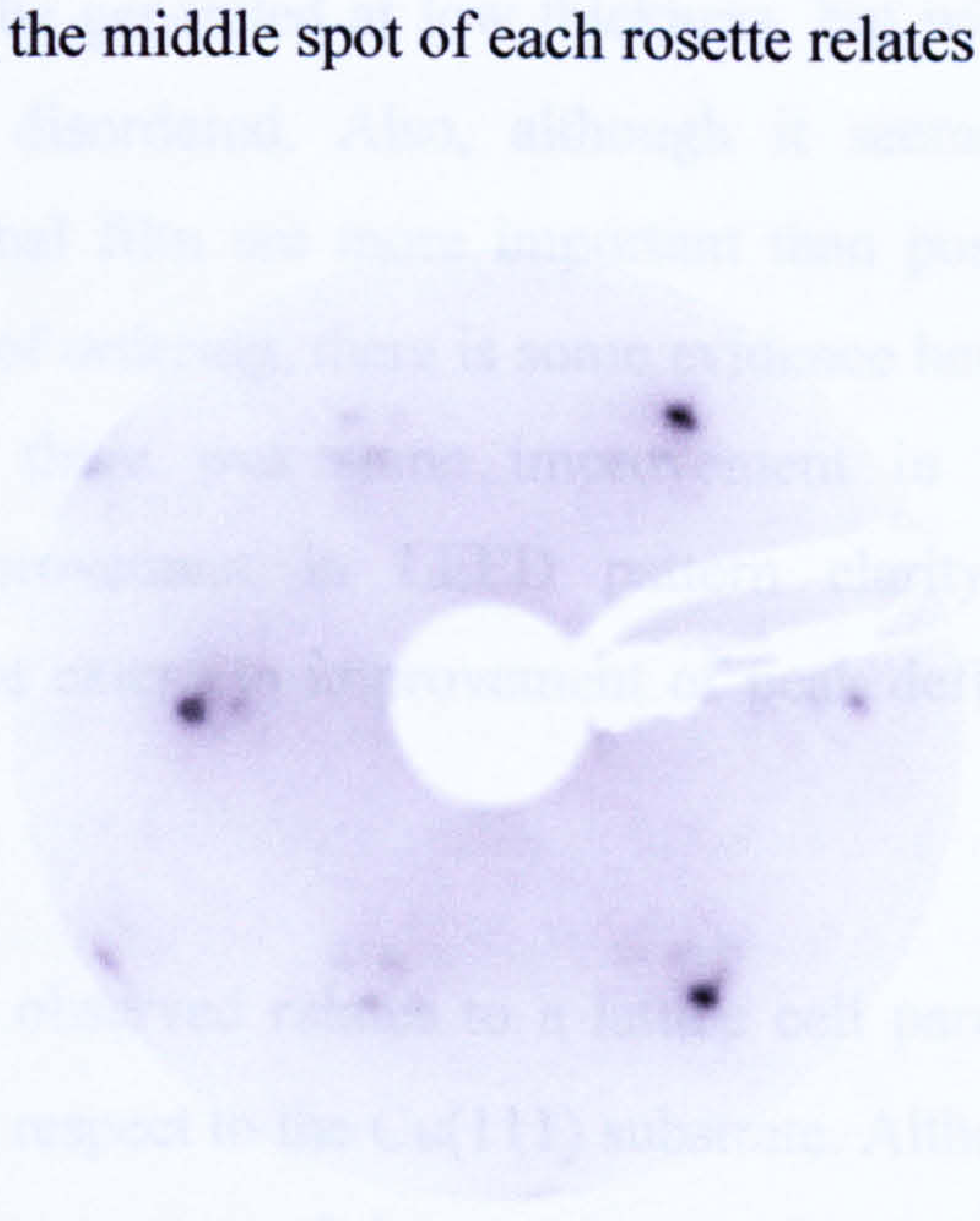

Figure 5.19: LEED pattern of film E after 1 cycle of growth with beam energy 115 eV

With further growth all the spots became fainter and fainter leading to a diffuse background upon which the spots were barely visible. There was no significant increase in the clarity of the LEED pattern as a result of the two further exposures to 40 L O_2 at 773 K. The film was then annealed in vacuum at 773 K, 823 K, 873 K and 923 K, each time for 5 minutes. No significant improvement to the LEED pattern was observed until the annealing treatment at 873 K and after annealing at 923 K, the pattern was somewhat clearer (see Figure 5.20).

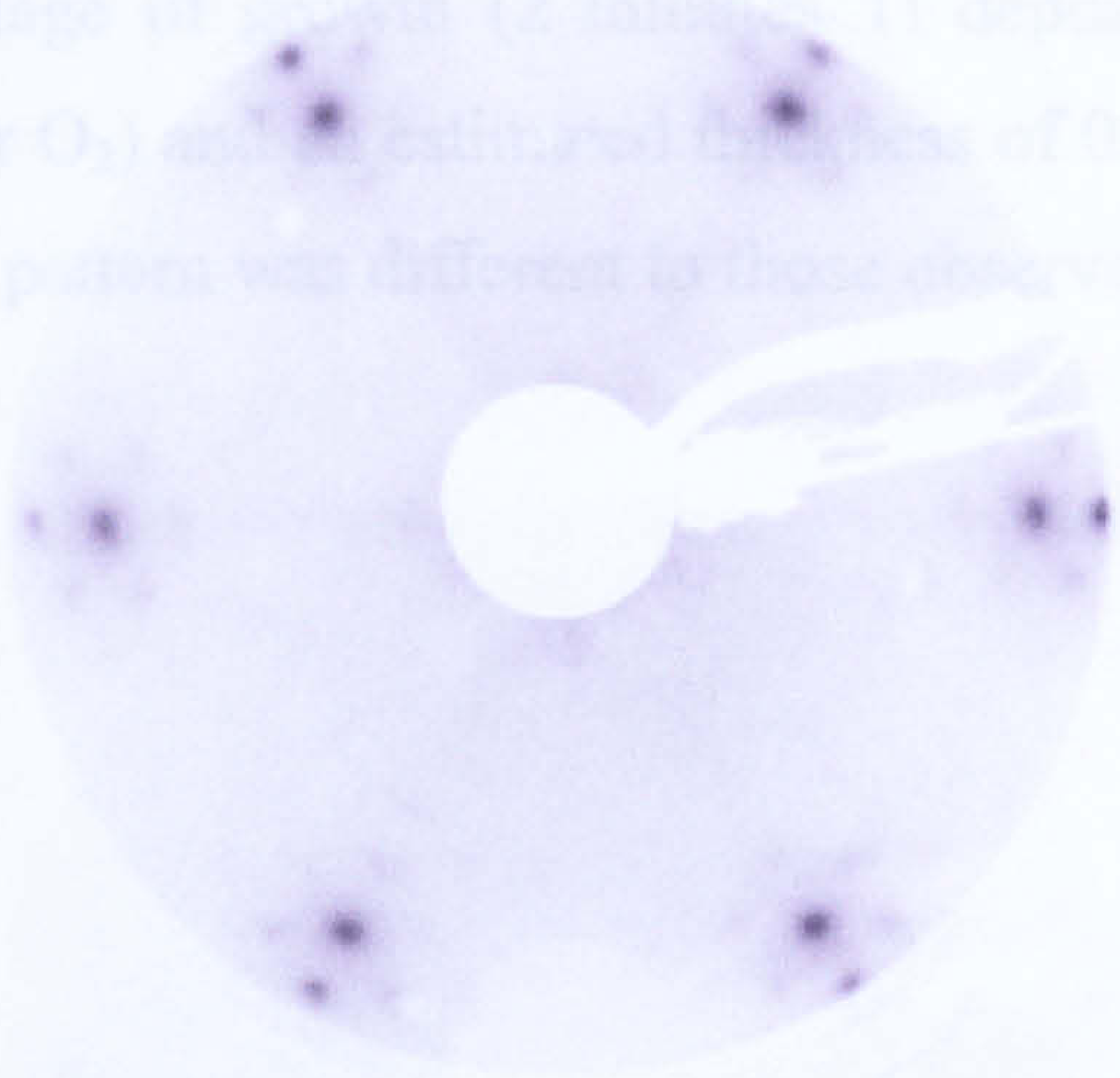

Figure 5.20: LEED pattern of film E after annealing at 923 K with beam energy 58 eV.

By this stage, however, a significant amount of film breakdown had occurred, with the estimated film thickness having decreased from 1.8 nm to 1.0 nm. This shows that ordered films can be generated at low thickness, but with increasing thickness they tend to become disordered. Also, although it seems that the preparation conditions of the original film are more important than post-growth treatments in determining the extent of ordering, there is some evidence here that after the steps of annealing in vacuum there was some improvement in LEED pattern clarity. Furthermore, this improvement in LEED pattern clarity coincides with film breakdown and to some extent to improvement of peak definition in the Ti 2p XP region.

The hexagonal pattern observed relates to a lattice cell parameter of 2.8 (±0.1) Å, which is 1.1 × 1.1 with respect to the Cu(111) substrate. Although this symmetry and structure does not relate to any of the commonly observed surfaces of rutile and anatase forms of TiO_2, hexagonal symmetry and lattice cell constants of 2.9 Å and

2.8 Å were found by Maeda et al and Wu et al, respectively, for TiO_x ultra-thin films on Cu(100).[17,19] So it seems that although an ordered structure can be generated at low thickness, this is due to the influence of the underlying substrate, and the oxide becomes disordered after the initial layers. Ideally ordered films with much greater thickness than 0.4 nm need to be grown in order to pursue further studies of the surface chemistry of the oxide.

Film F, which had been grown by oxidation during Ti deposition, exhibited a LEED pattern after the first stage of growth (2 minutes Ti deposition at 673 K under a pressure of 2×10^{-7} Torr O_2) and an estimated thickness of 0.7 nm (see Figure 5.21). Furthermore this LEED pattern was different to those observed previously.

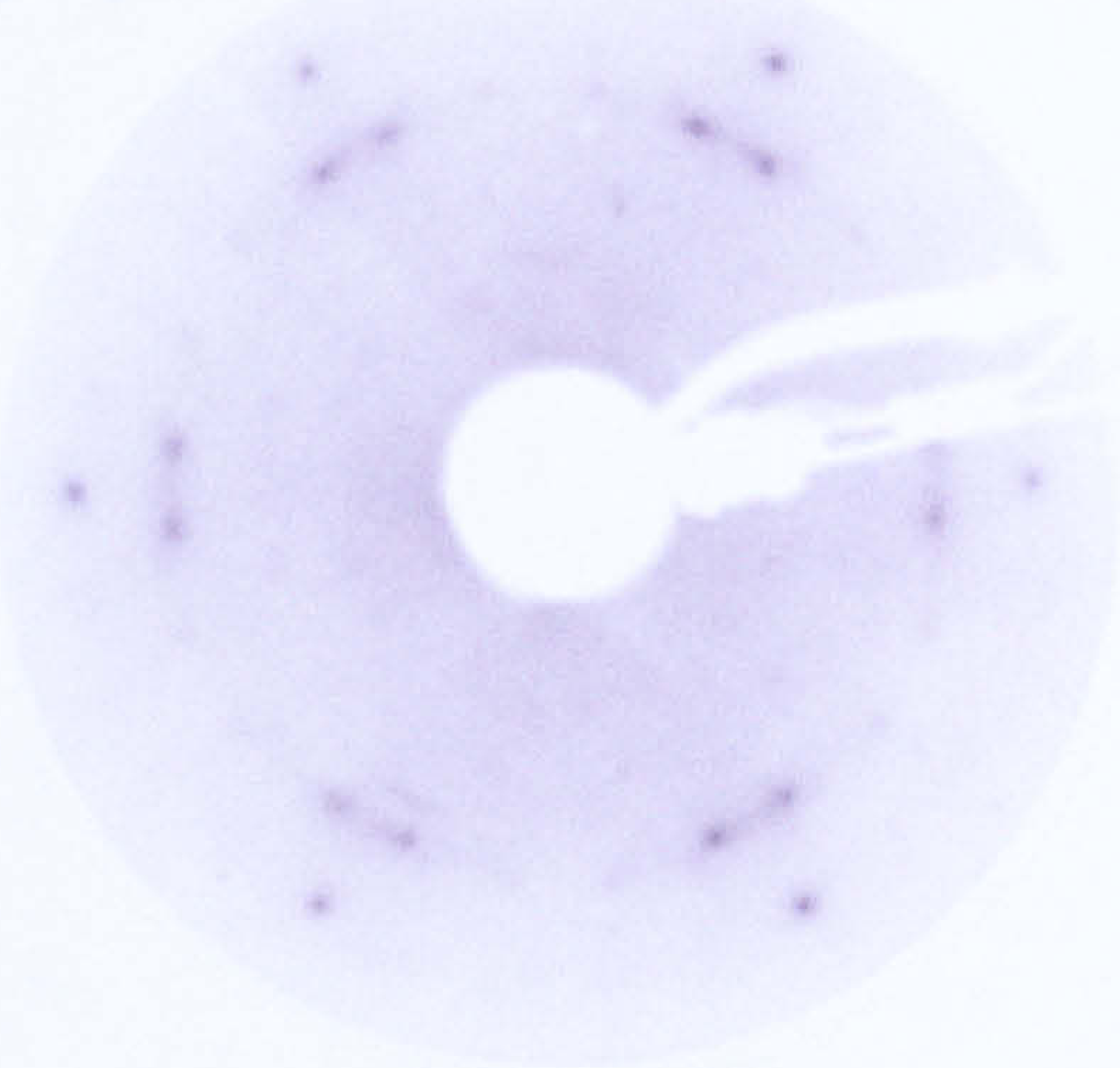

Figure 5.21: LEED pattern of film F with beam energy 77 eV

The debate here is whether the pattern observed after the first deposition relates to a crystal structure formed as a result of Ti diffusion into the substrate (at the elevated temperature), or a different structure of TiO_x produced as a result of the different preparation conditions (in particular oxidation exposure during the deposition and a partial pressure of O_2 four times higher than previously). Unfortunately the pattern is not clear enough to extract reliable structural information. After further deposition the structure reverted back to that previously observed with LEED, consisting of a faint hexagon of spots superimposed upon a diffuse background.

The ensuing post-growth exposure to O_2, in two 40 L steps at 773 K, resulted in some improvement of the LEED pattern clarity. There was no additional improvement after further annealing at 773 K and 823 K in vacuum however. The improvement in LEED pattern with the second deposition and the exposure to O_2 at 773 K is consistent with the observations discussed previously with respect to the findings of section 5.2 and 5.3. It seems that the diffusion of Ti into the substrate initially led to a different LEED pattern (perhaps a mixed oxide of Ti, Cu and O, or an oxide of Cu), but with subsequent deposition this was covered up resulting in the LEED pattern observed previously. The exposure to O_2 pulled the TiO_x to the surface explaining the improvement in LEED pattern clarity with these treatments. Once again the clarity of the LEED pattern coincides with how well-defined the peaks in the Ti 2p XP region are, since the films are better-defined in terms of Ti 2p region after the post-growth O_2 exposure, and this coincides with improvement in the LEED pattern obtained.

5.5 Angle-Resolved XPS

Angle-resolved XPS measurements were made on films E and F to see if different states were present at the surface of the oxide film compared to the bulk of the film. Measurements were made at the usual electron emission angle of 15° from the sample normal and at a grazing angle of 75° from the sample normal. Film E, which had been grown by oxidation at 773 K, was examined with angle-resolved XPS before any post-growth treatment. The intensity of the Cu $2p_{3/2}$ peak was seen to fall when measured at grazing emission angle, which is to be expected since the Cu substrate is covered by the oxide film. The Ti 2p and O 1s regions, however, did not change very much in intensity (see Figures 5.22a and 5.22b).

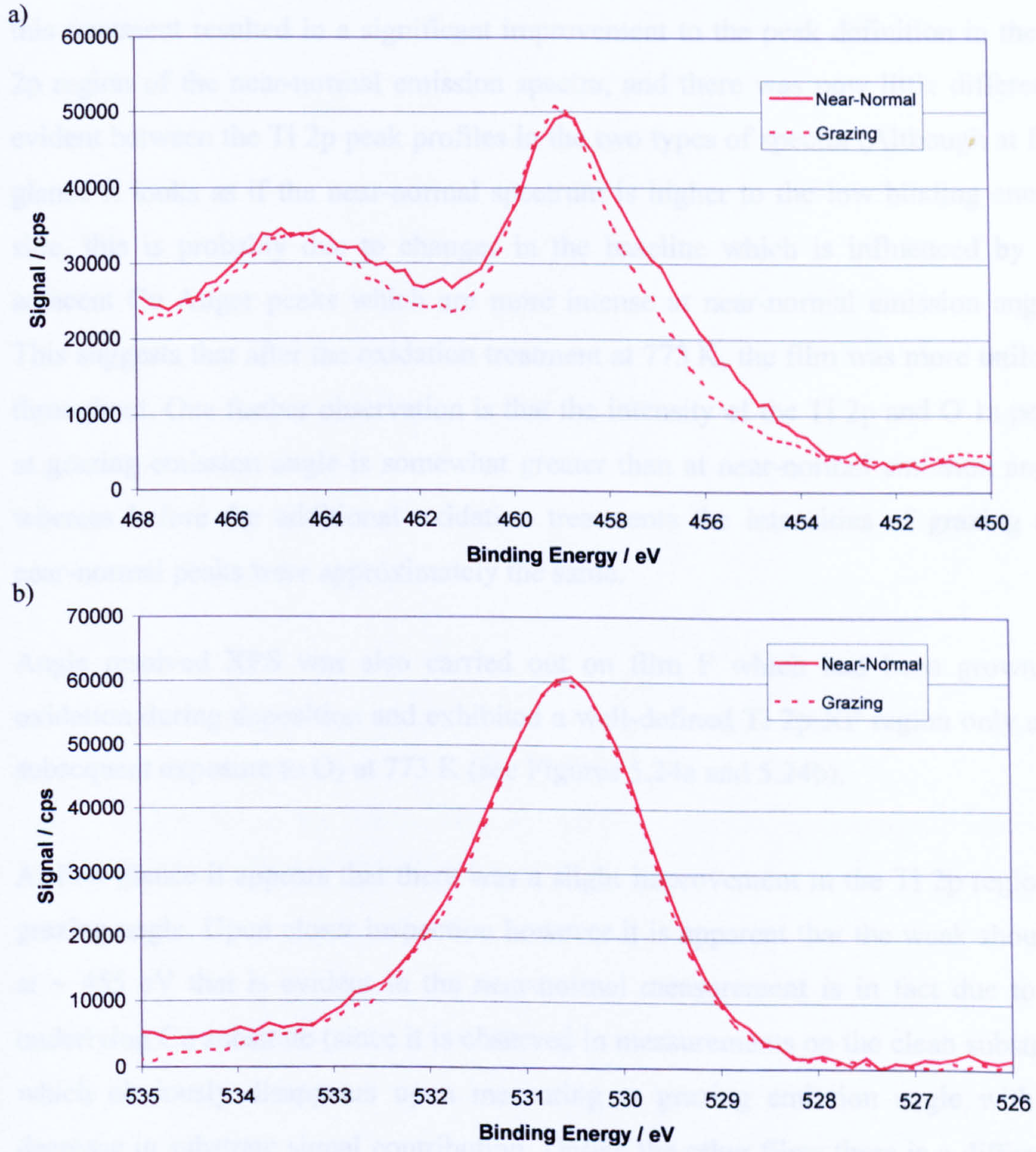

Figure 5.22: XPS data for film E at grazing and near-normal emission angles a) Ti 2p region; b) O 1s region

Asides from looking at changes in intensity and drawing conclusions about the proximity of different elements to the surface, the most interesting thing here is the effect on the Ti 2p peak profile. At grazing emission angle there is clearly an improvement in how well-defined the peaks in the Ti 2p region are, which indicates that there is a difference between TiO_x at the surface of the film and TiO_x deeper in the bulk of the film. This suggests that the oxide at the surface exhibits just one stoichiometry and is fully oxidised TiO_2, whereas in the sub-surface region there is more variation in the Ti oxidation state.

The angle-resolved XPS measurements were repeated after two cycles of 40 L O_2 exposure at 773 K (see Figures 5.23a and 5.23b). As previously noted in section 5.3 this treatment resulted in a significant improvement to the peak definition in the Ti 2p region of the near-normal emission spectra, and there was now little difference evident between the Ti 2p peak profiles in the two types of spectra (Although at first glance it looks as if the near-normal spectrum is higher to the low binding energy side, this is probably due to changes in the baseline which is influenced by the adjacent Cu Auger peaks which are more intense at near-normal emission angle). This suggests that after the oxidation treatment at 773 K, the film was more uniform throughout. One further observation is that the intensity of the Ti 2p and O 1s peaks at grazing emission angle is somewhat greater than at near-normal emission angle, whereas before the additional oxidation treatments the intensities of grazing and near-normal peaks were approximately the same.

Angle resolved XPS was also carried out on film F which had been grown by oxidation during deposition and exhibited a well-defined Ti 2p XP region only after subsequent exposure to O_2 at 773 K (see Figures 5.24a and 5.24b).

At first glance it appears that there was a slight improvement in the Ti 2p region at grazing angle. Upon closer inspection however it is apparent that the weak shoulder at ~ 455 eV that is evident in the near-normal measurement is in fact due to the underlying Cu substrate (since it is observed in measurements on the clean substrate) which obviously disappears upon measuring at grazing emission angle with the decrease in substrate signal contribution. Unlike the other films there is a difference in the O:Ti signal intensity ratio at grazing emission angle, which is seen to increase.

This may be indicative of O-termination, since the film is thought to be reasonably uniform in stoichiometry.

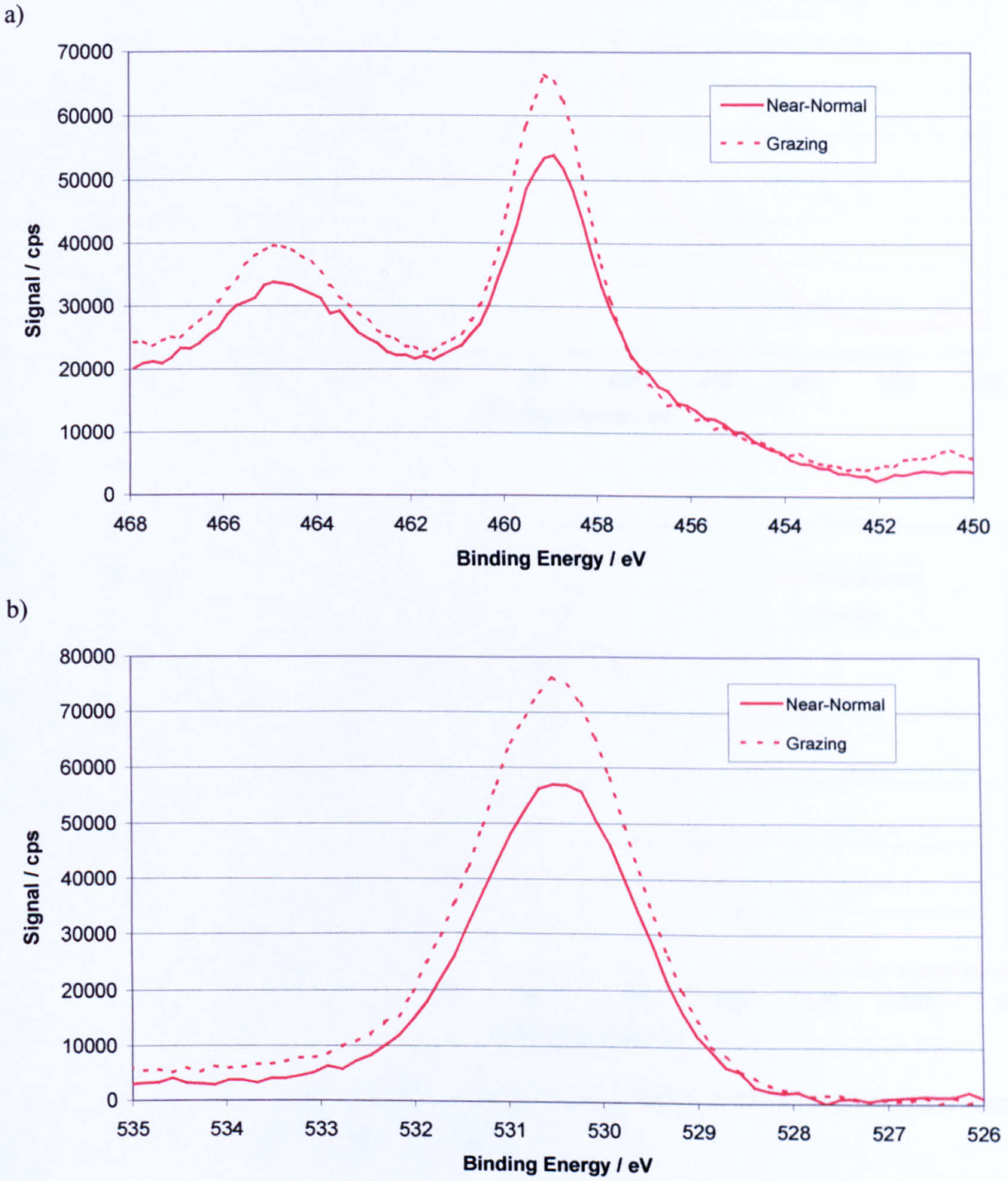

Figure 5.23: XPS data for film E (after additional exposure to O_2 at 773 K) at grazing and near-normal emission angles a) Ti 2p region; b) O 1s region

a)

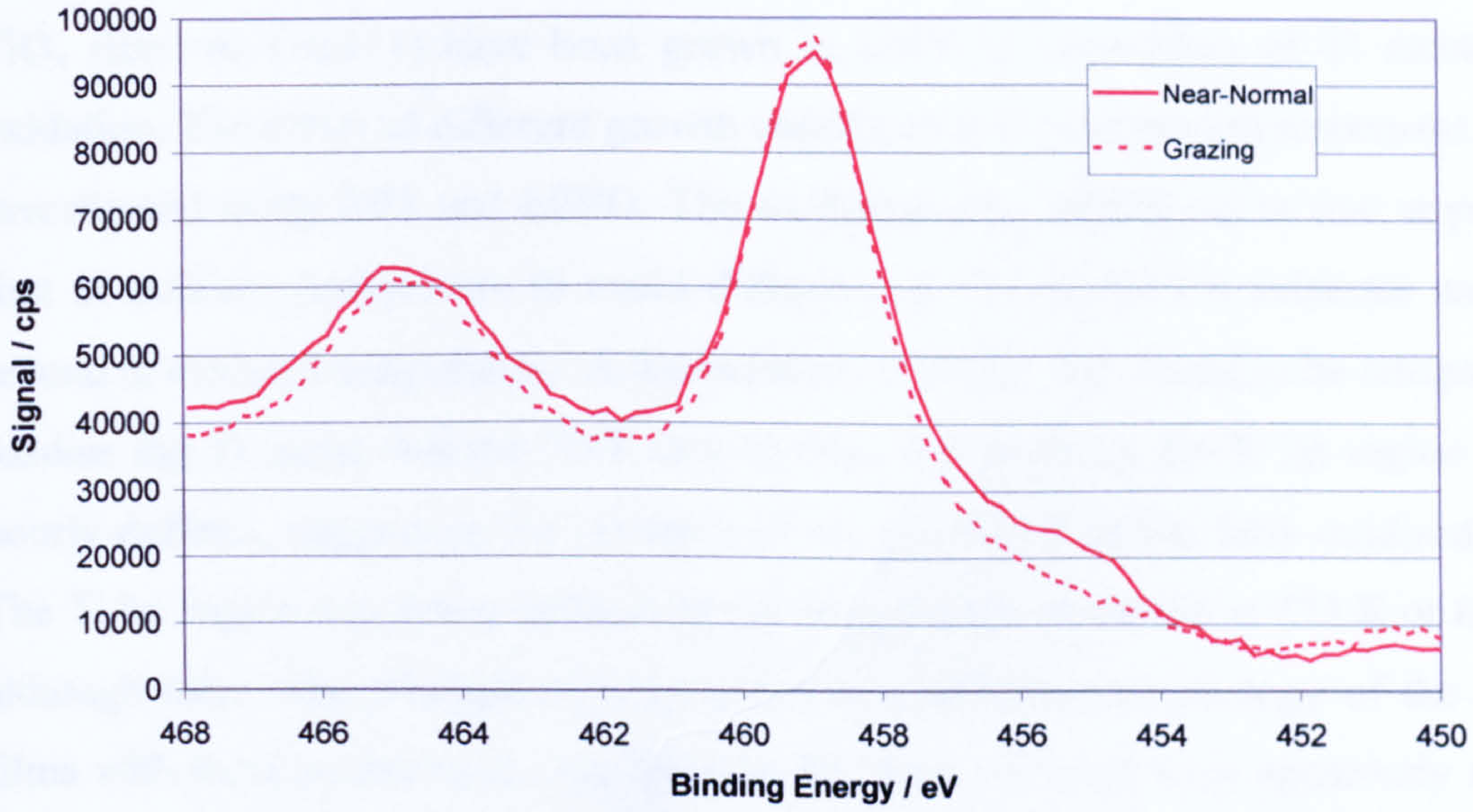

b)

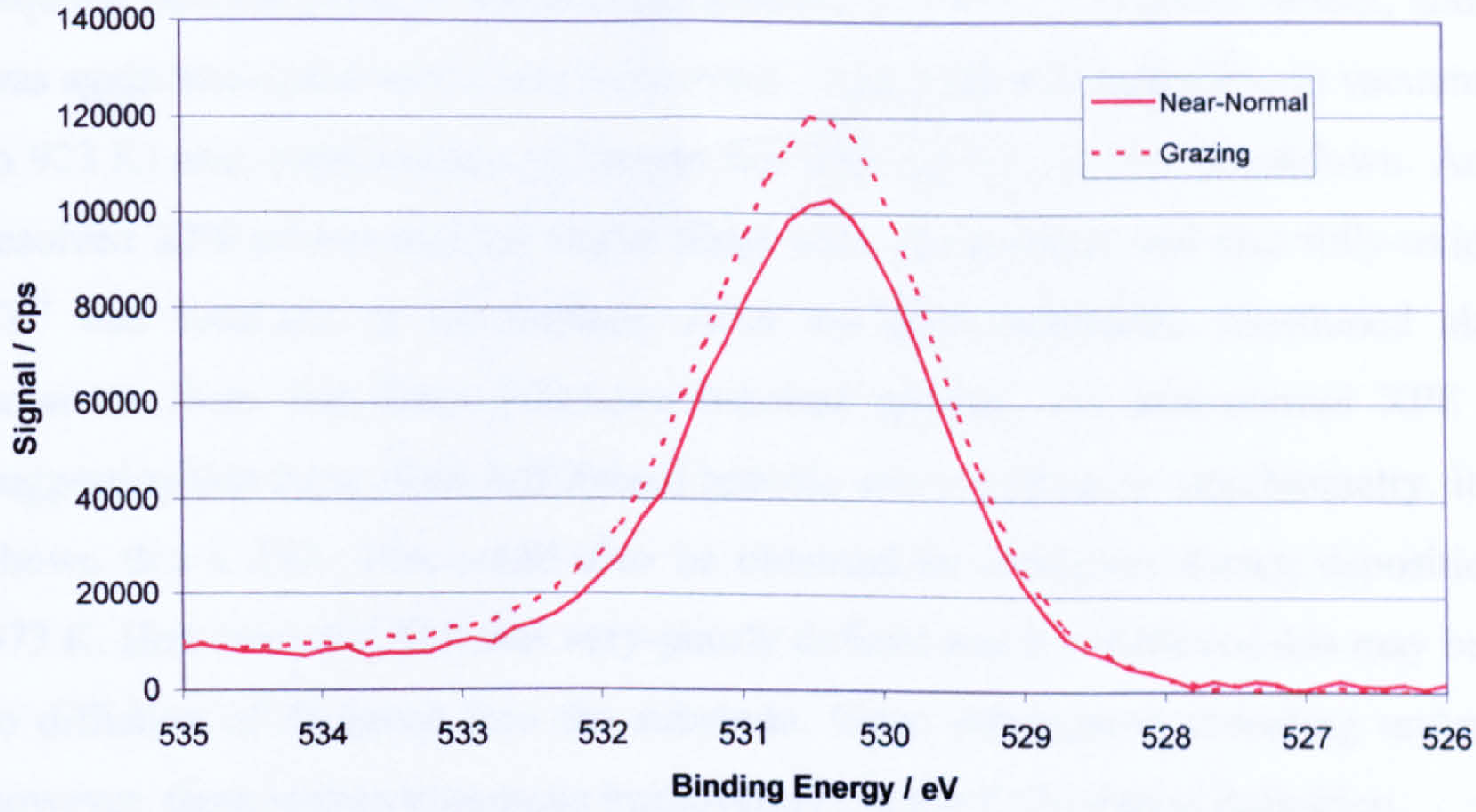

Figure 5.24: XPS data for film F (after additional exposure to O_2 at 773 K) at grazing and near-normal emission angles a) Ti 2p region; b) O 1s region

5.6 Summary

TiO_x films on Cu(111) have been grown in UHV by deposition of Ti metal and oxidation. The effect of different growth conditions and post-growth treatments were investigated using XPS and LEED. The oxidation was carried out in two steps, the first at ambient temperature to avoid diffusion of Ti into the Cu substrate and the second at elevated temperature. A temperature of 623 K was found to be adequate to oxidise the Ti metal, but the XPS data showed the peaks in the Ti 2p region to be poorly-defined, suggesting the presence of states other than the fully-oxidised Ti^{4+}. The Ti 2p region was better defined by carrying out the oxidation at 773 K or 823 K, although there was evidence of breakdown or a different morphology of the oxide films with these preparation conditions as the films obtained were apparently not as thick. Further oxidation treatments at elevated temperature (typically 823 K) were required of these films to improve the definition of the Ti 2p peaks further, and this was again associated with some breakdown. Following this, annealing in vacuum (up to 923 K) also improved the definition but with significant film breakdown. Angle-resolved XPS proves that the initial films were not uniform and that fully-oxidised Ti^{4+} was localised at the surface. After the post treatments mentioned above, however, there was little difference between grazing and near-normal XPS data suggesting that these films had indeed become more uniform in stoichiometry. It was shown that a TiO_x film could also be obtained by oxidation during deposition at 673 K. However, this film was very-poorly defined and it is believed this may be due to diffusion of Ti metal into the substrate. Upon subsequent annealing under O_2, however, there was an enormous improvement in the Ti 2p region definition.

Films grown by the two step oxidation procedure exhibited LEED patterns characteristic of a hexagonal surface structure, with a unit cell size of 2.8 (±0.1) Å. Above a film thickness of ~ 0.5 nm, though, the pattern became less clear suggesting the presence of disordered domains of the oxide. Substantial annealing of thicker films improved the LEED pattern clarity, but unfortunately only in conjunction with significant film breakdown. The film grown by oxidation during deposition possessed a different LEED pattern.

References

1 C.T. Cambell, *Surf. Sci. Rep.* 1997, **27**, 1

2 R.J. Lad, *Surf. Rev. Lett.* 1995, **2**, 109

3 U. Diebold, J.M. Pan and T.E. Madey, *Surf. Sci.* 1995, **333**, 845

4 G.C. Bond and D.T. Thompson, *Catal. Rev.-Sci. Eng.* 1999, **418**, 319

5 F. Cosandey and T.E. Madey, *Surf. Rev. Lett.* 2001, **8**, 73

6 X. Lai, T.P.S. Clair, M. Valden and D.W. Goodman, *Prog. Surf. Sci.* 1998, **59**, 25

7 L. Zhang, R. Persaud and T.E. Madey, *Phys. Rev. B,* 1997, **56**, 10549

8 F. Cosandey, R. Persaud, L. Zhang and T.E. Madey, *Mat. Res. Soc. Symp. Proc.* 1997, **440**, 383

9 C. Xu and D.W. Goodman, *Chem. Phys. Lett.* 1996, **263**, 13

10 U. Diebold, *Surf. Sci. Rep.* 2003, **48**, 53

11 C.H. Ao, S.C. Lee, J.Z. Ju and J.H. Zu, *Appl. Catal. B:Environ*, 2004, **54**, 41

12 A. Fujishima and K. Honda, *Nature*, 1972, **238**, 37

13 P.K. Dutta, A. Ginwalla, B. Hogg, B.R. Patton, B. Chwieroth, Z. Liang, P. Gouma, M. Mills and S. Akbar, *J. Phys. Chem.* 1999, **103**, 4412

14 F.A. Grant, *Rev. Mod. Phys.* 1959, **31**, 646

15 H. Selhofer, *Vacuum Thin Film*, 1999, 15

16 J.R. Sambrano, J. Andres, A. Beltran, F.R. Sensato, E.R. Leite, F.M.L.G. Stamato and E. Longo, *Int. J. Quantum Chem.* 1997, **65**, 625

17 T. Maeda, Y. Kobayashi and K. Kishi, *Surf. Sci.* 1999, **436**, 249

18 I. Vaquila, M.C.G. Passeggi and J. Ferron, *Phys. Rev. B*, 1997, **55**, 13925

19 Y.M. Wu and R.M. Nix, *J. Mat. Chem.* 1994, **4**, 1403

20 T.D. Cromer and K. Herrington, *J. American Chem. Soc.* 1955, **77**, 4708

21 K.M. Glassford,N. Troullier, J.L. Martins and J.R. Chelikowsky, *Solid State Communications* 1990, **76**, 635

22 C.J. Howard, T.M. Sabine and F. Dickson, *Actacrystallographica B,* 1991, **47**, 462

23 http://ruby.colorado.edu/~smyth/min/corundum.html

24 M. Ramamoorphy and D. Vanderbilt, *Phys. Rev. B*, 1994, **49**, 16721

25 H. Onishi, K.-I Fukui and Y. Iwasawa, *Bull. Chem. Soc. Jpn.* 1995, **68**, 2447

26 C.L. Pang, S.A. Haycock, H. Raza, P.W. Murray, G. Thornton, O. Gülseren,

R. James and D.W. Bullet, *Phys. Rev. B*, 1998, **58**, 1586

27 N.M. Harrison, X.G. Wang, J. Muscat and M. Scheffler, *Faraday Discuss. Chem. Soc.* 1999, **114**, 305

28 G. Charlton, P.B. Hoowes, C.L. Nicklin, P. Steadman, J.S.G. Taylor, C.A. Muryn, S.P. Harte, J. Mercer, R. McGrath, D. Norman, T.S. Turner and G. Thornton, *Phys. Rev. Lett.* 1997, **78**, 495

29 H.A. Al-Abadleh and V.H. Grassian, *Surf. Sci. Rep.* 2003, **52**, 63

30 H. Raza, C.L. Pang, S.A. Haycock and G. Thornton, *Appl. Surf. Sci.* 1999, **140**, 271

31 R.H. Tait and R.V. Kasowski, *Phys. Rev. B*, 1979, **20**, 5178

32 L.E. Firment, *Surf. Sci.* 1982, **116**, 205

33 G.E. Poirier, B.K. Hance and M. White, *J. Vac. Sci. Technol. B*, 1992, **10**, 6

34 C.N. Satterfield, *Heterogeneous Catalysis In Industrial Practice*, 2nd Ed. McGraw-Hill, Newyork, 1991

35 M. Lazzeri, A. Vittadini and A. Selloni, *Phys. Rev. B*, 2001, **63**, 155409

36 M. Lazzeri, A. Vittadini and A. Selloni, *Phys. Rev. B*, 2002, **65**, 119901

37 W. Hebenstreit, N. Ruzycki, G.S. Herman, Y. Gao and U. Diebold, *Phys. Rev. B*, 2000, **64**, R16344

38 V.E. Henrich and P.A. Cox, *The Surface Science of Metal Oxides, Cambridge University Press, Cambridge, 1994*

39 M.B. Hugenschmidt, L. Gamble and C.T. Campbell, *Surf, Sci.* 1994, **302**, 329

40 M.A. Henderson, *Surf. Sci.* 1996, **355**, 151

41 M.A. Henderson, *Langmuir*, 1996, **12**, 5093

42 S. Suzuki, K.-I Fukui, H. Onishi, T. Sasaki and Y. Iwasawa, *Stud. Surf. Sci. Catal.* 2001, **132**, 753

43 R.F. Nalewajski. A.M. Koester, T. Bredow and K. Jug, *J. Mol. Catal.* 1993, **82**, 407

44 A. Fahmi and C. Minot, *Surf. Sci.* 1994, **304**, 343

45 G.S. Herman, Z. Dohnalek, N. Ruzycki and U. Diebold, *J. Phys. Chem. B*, 2003, **107**, 2788

46 A. Vittadini, A.Selloni, F.P. Rotzinger and M. Grätzel, *Phys. Rev. Lett.* 1998, **81**, 2954

47 M.A. Henderson, W.S. Epling, C.L. Perkins, C.H.F. Peden and U. Diebold, *J. Phys. Chem. B*, 1999, **103**, 5328

48 W.J. Lo Y.W. Chung and G.A. Somorjai, *Surf. Sci*, 1978, **71**, 199

49 J.M. Pan, B.L. Maschhoff, U. Diebold and T.E. Madey, *J. Vac. Sci. Technol. A*, 1992, **10**, 2470

50 W. Göpel, G. Rocker and R. Feierabend, *Phys. Rev. B*, 1983, **28**, 3427

51 G. Rocker and W. Göpel, *Surf. Sci.* 1986, **175**, L675

52 G. Lu, A. Linsebigler and J.T. Yates Jr, *J. Phys. Chem.* 1994, **98**, 11733

53 A.N. Shulz, W.M. Hetherington III, D.R. Baer, L.Q. Wang and M.H. Engelhard, *Surf. Sci.* 1997, **392**, 1

54 L.Q. Wang, A.N. Shultz, D.R. Baer and M.H. Engelhard, *J. Vac. Sci. Technol. A*, 1996, **14**, 1532

55 J.A. Rodriguez, T. Jirsak, G. Liu, J. Hrbek, J. Dvorak and A. Maiti, *J. Am. Chem. Soc.* 2001, **123**, 9597

56 W.S. Epling, C.H.F. Peden, M.A. Henferson and U. Diebold, *Surf. Sci.* 1998, **412**, 333

57 K.E. Smith and V.E. Henrich, *J. Vac. Sci. Technol. A*, 1989, **7**, 1967

58 M.A. Barteau and D.P. Woodruff (Ed.), *The Chemical Physics of Solid Surfaces, vol. 9, Oxide Surfaces*, Elsevier, Amsterdam, 2001

59 S.A. Chambers, S. Thevuthasan, Y.J. Kim, G.S. Herman, Z. Wang, E. Tober, R. Ynzunza, J. Maorais, C.H.F. Peden, K. Ferris and C.S. Fadley, *Chem. Phys. Lett.* 1997, **267**, 51

60 A. Gutierrez-Sosa, P. Martinez-Escolano, H. Raza, R. Linsay, P.L. Wincott and G. Thornton, *Surf. Sci.* 2001, **471**, 163

61 B.E. Hayden, A. King and M.A. Newton, *J. Phys. Chem. B*, 1999, **103**, 203

62 M.A. Henderson, *J. Phys. Chem. B*, 1997, **101**, 221

63 H. Onishi, T. Aruga, C. Egawa and Y. Iwasawa, *Surf. Sci.* 1988, **193**, 33

64 M.A. Henderson, S. Otero-Tapia and M.E. Castro, *Faraday Discuss. Chem. Soc.* 1999, **114**, 313

65 G. Kresse and J. Hafner, *Phys. Rev. B*, 1993, **47**, 558

66 G.E. Mullenberg, *Handbook of X-ray Photoelectron Spectroscopy*, Perkin-Elmer, 1979

67 R. Gouttebaron, D. Cornelissen, R. Snyders, J.P. Dauchot, M. Wautelet and M. Hecq, *Surf. Inter. Anal.* 2000, **30**, 527

68 Q. Guo, W.S. Oh and D.W. Goodman, *Surf. Sci.* 1999, **437**, 49

Chapter 6:

Growth & Characterisation of $FeO_x/Cu(111)$ & $Ag/FeO_x/Cu(111)$

6.1 Literature Review of Fe_yO_x Surface Science Studies

Iron oxides have been the subject of much research interest as a result of their utilisation in a number of technologies and also their geochemical significance.

6.1.1 Motivation for Surface Science Studies

Iron oxides have found numerous applications in **heterogeneous catalysis**. For example, they are used in a range of important synthesis reactions in the chemical industry, both as catalysts and support materials. In the **dehydrogenation of ethyl benzene** to styrene in the presence of steam, a potassium-promoted iron oxide catalyst is used; however, unpromoted iron oxide has also been found to be active. In one comprehensive study[1] on (unpromoted) FeO(111), $Fe_3O_4(111)$ and α-$Fe_2O_3(0001)$ films grown on Pt(111), only α-$Fe_2O_3(0001)$ with surface defects was found to be active. The authors proposed a model of the reaction mechanism in which the active site consists of a regular acidic terrace site and a neighbouring defect site. It is believed that O anions with higher basicity are exposed at the defect sites, allowing deprotonation of the ethyl benzene molecule. The subsequent transfer of an electron from the reaction intermediate to an acidic Fe^{3+} site, may explain the inactivity of Fe_3O_4. Iron oxide is also a component of Fischer Tropsch catalysts for alcohol synthesis and pure iron oxide is used to catalyse the hydrogenation of acetic acid to acetaldehyde.[2]

Iron oxides have also been applied to the **catalytic removal of a variety of environmentally-unfriendly compounds**. Destruction of the common laboratory and industrial solvent carbon tetrachloride is of particular importance and the chemistry of CCl_4 on the $Fe_3O_4(111)$ selvedge of α-$Fe_2O_3(0001)$ has been investigated utilising TPD and XPS.[3,4] Silica-supported iron oxide has been found to be active in the selective oxidation of hydrogen sulphide to elemental sulfur.[5] The catalyst currently used is iron oxide/chromia supported on α-alumina. Furthermore iron oxides have been studied for their activity for selective catalytic reduction of NO_x when potassium-promoted,[6] as nanoparticles,[7] and when mixed with other oxides.[8] There may also be some relevance to the atmospheric chemistry of mineral dust in the troposphere (mostly SiO_2, but partly Fe_2O_3).[9] Continuing the environmental theme, partially reduced iron oxide surfaces can be used as sorbents of toxic metals ions, such as Cr(VI) in the form of chromate.[10]

There are a number of **other applications**, which warrant the study of iron oxide surfaces. Iron is a common component of construction materials and understanding the surface properties of iron oxides, in particular their interaction with water, is essential in corrosion control.[11] The magnetic properties of Fe_3O_4 (magnetite) has led to its utilisation in high-density magnetic recording media.[12] It is also found in a variety of electronic devices, including electromagnetic coils, microwave resonant circuits, computer memory cores[13] and spin electronics.[14]

FeO_x films have been grown and characterised on Cu(100),[15-20] Cu(110)[21-23] and Cu(111).[24] In the previous study on a Cu(111) substrate formation of Fe_2O_3 and Fe_3O_4 upon oxidation of deposited Fe was evidenced by AES, RHEED and LEED.

6.1.2 Bulk Structure

Iron oxide exists in a variety of stoichiometries, namely Fe_2O_3 (iron (III) oxide), Fe_3O_4 (iron(II, III) oxide) and FeO (iron (II) oxide) in order of decreasing oxidation state. The most stable and important phases are hematite (α-Fe_2O_3) and magnetite (Fe_3O_4), which occur naturally. Other forms include maghemite (γ-Fe_2O_3) and wustite (FeO). Hematite, α-Fe_2O_3, is isomorphous with corundum (α-Al_2O_3), which has the $R\bar{3}c$ (167) space group. This bulk structure can be envisaged as an approximately hexagonal close packed array of oxygen anions (O^{2-}), which possesses octahedral and tetrahedral holes. Two thirds of the octahedral holes are occupied by the iron cations (Fe^{3+}). An alternative perspective is to consider the structure as comprising pairs of face-sharing FeO_6 octahedra linked by edge-sharing, stacked along the *c*-axis (see Figure 6.1). The hexagonal lattice cell parameters have been determined by numerous research to be $a = b = 5.03$ Å, $c = 13.75$ Å.[25,26] Magnetite possesses an inverse spinel $Fe^{3+}(Fe^{2+}Fe^{3+})O_4$ structure, with space group $FD\bar{3}m$. This consists of a face-centred cubic array of oxygen anions with half the Fe^{3+} iron cations filling the tetraheral sites and half the Fe^{3+} cations filling the octahedral sites along with the Fe^{2+} cations. The cubic lattice cell parameters have been determined by numerous research to be $a = b = c = 8.40$ Å.[27]

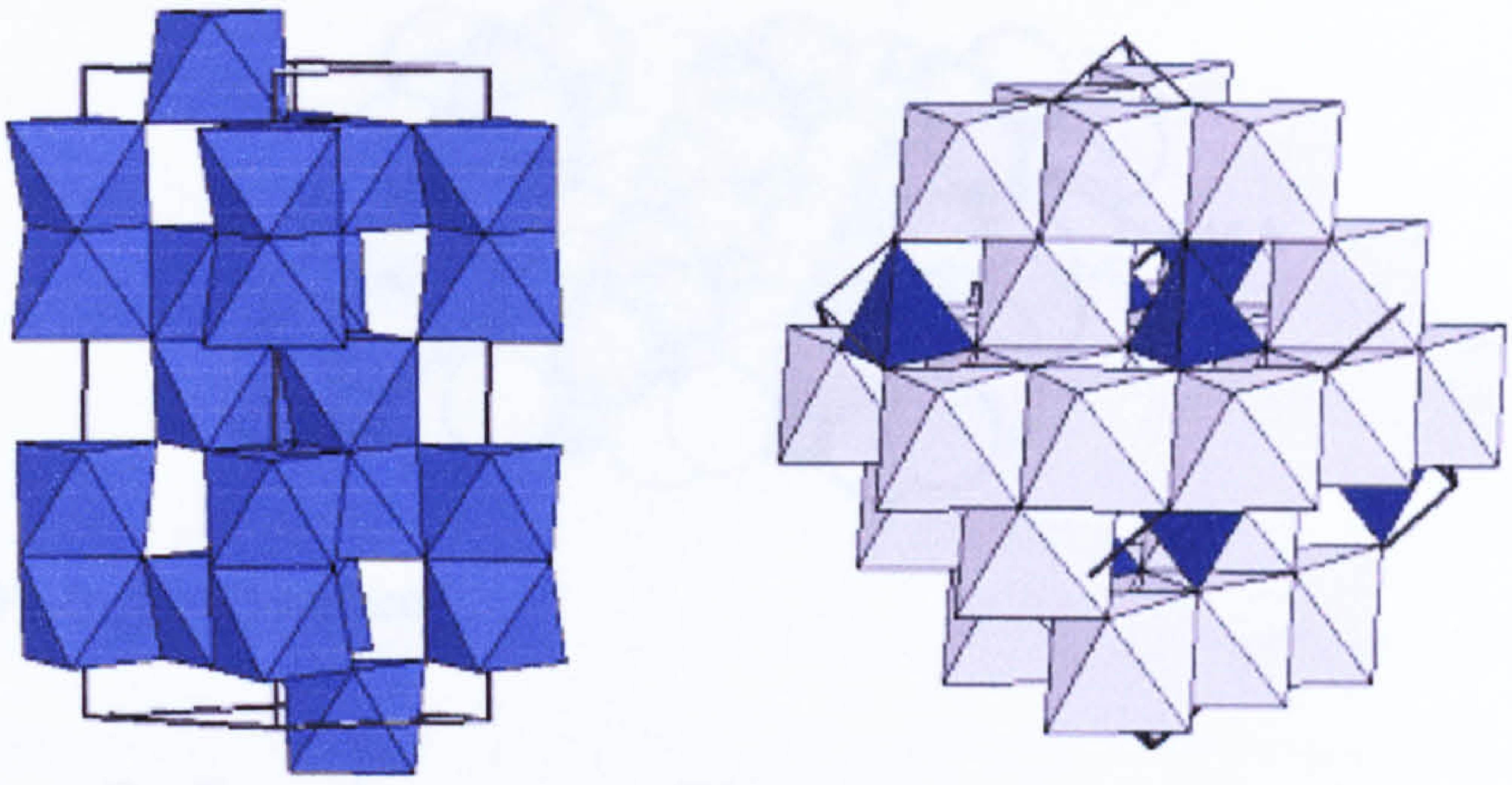

Figure 6.1: Unit cells of hematite (left) and magnetite (right)[28]

6.1.3 Surface Structure

The natural growth faces of α-Fe_2O_3 are the (0001) and $(\bar{1}012)$, of which the α-$Fe_2O_3(0001)$ surface is the most studied. Several researchers have observed the formation of Fe_3O_4 and FeO surface phases[29-30], but this partial reduction can be avoided by preparation in higher pressures of O_2.[31] Theoretical work[32] has predicted unreconstructed, strongly-relaxed Fe-terminated and O-terminated α-$Fe_2O_3(0001)$ surfaces depending on the pressure of O_2. This seems to be supported by empirical findings since both surfaces have been observed with STM.[31]

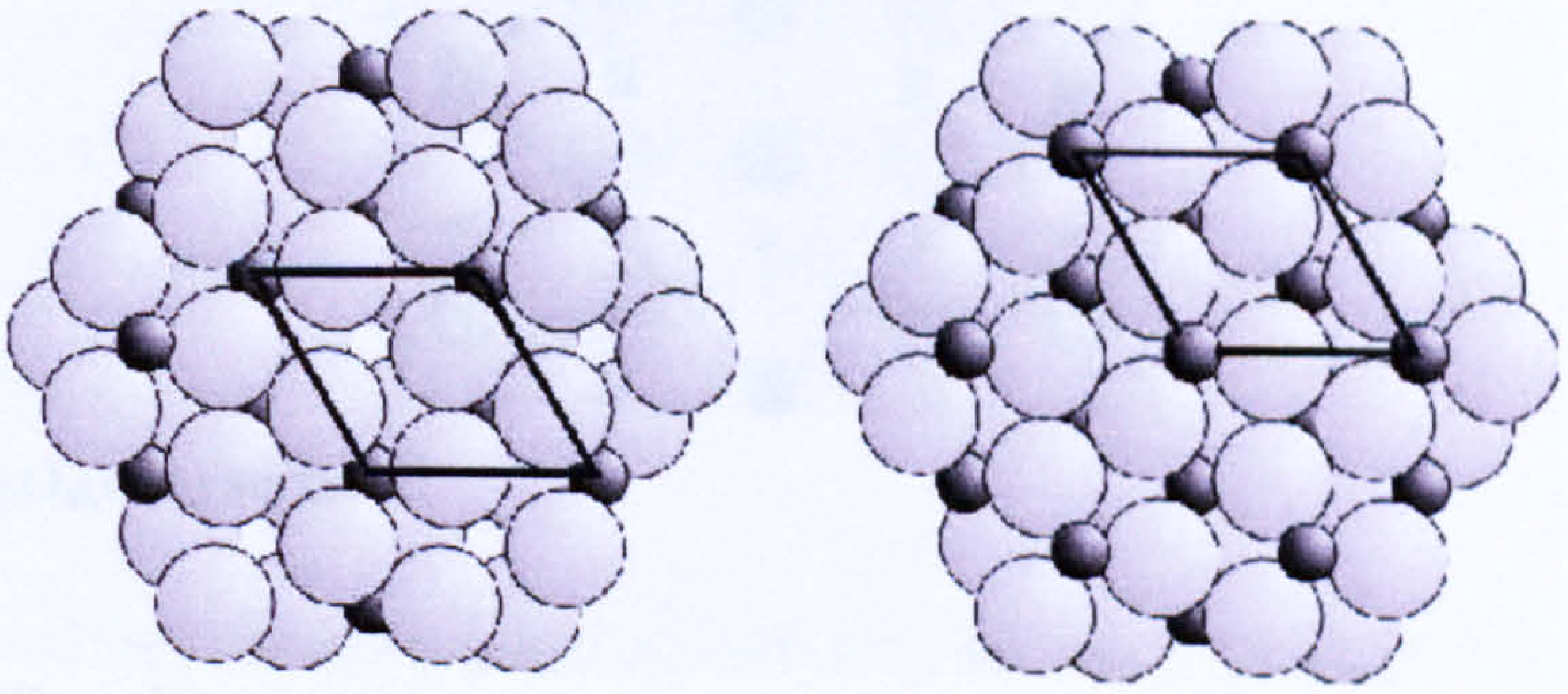

Figure 6.2: The α-$Fe_2O_3(0001)$ surface, O-terminated (left) and Fe-Terminated (right)[31]

The α-$Fe_2O_3(\bar{1}012)$ surface termination consists of a zigzag pattern of 3-fold co-ordinated oxide anions (compared to 4-fold in the bulk) and 5-fold co-ordinated iron cations (compared to 6-fold in the bulk).[33,34] The α-$Fe_2O_3(\bar{1}012)$ surface can exhibit either a (1 × 1) structure or (1 × 2) reconstruction.

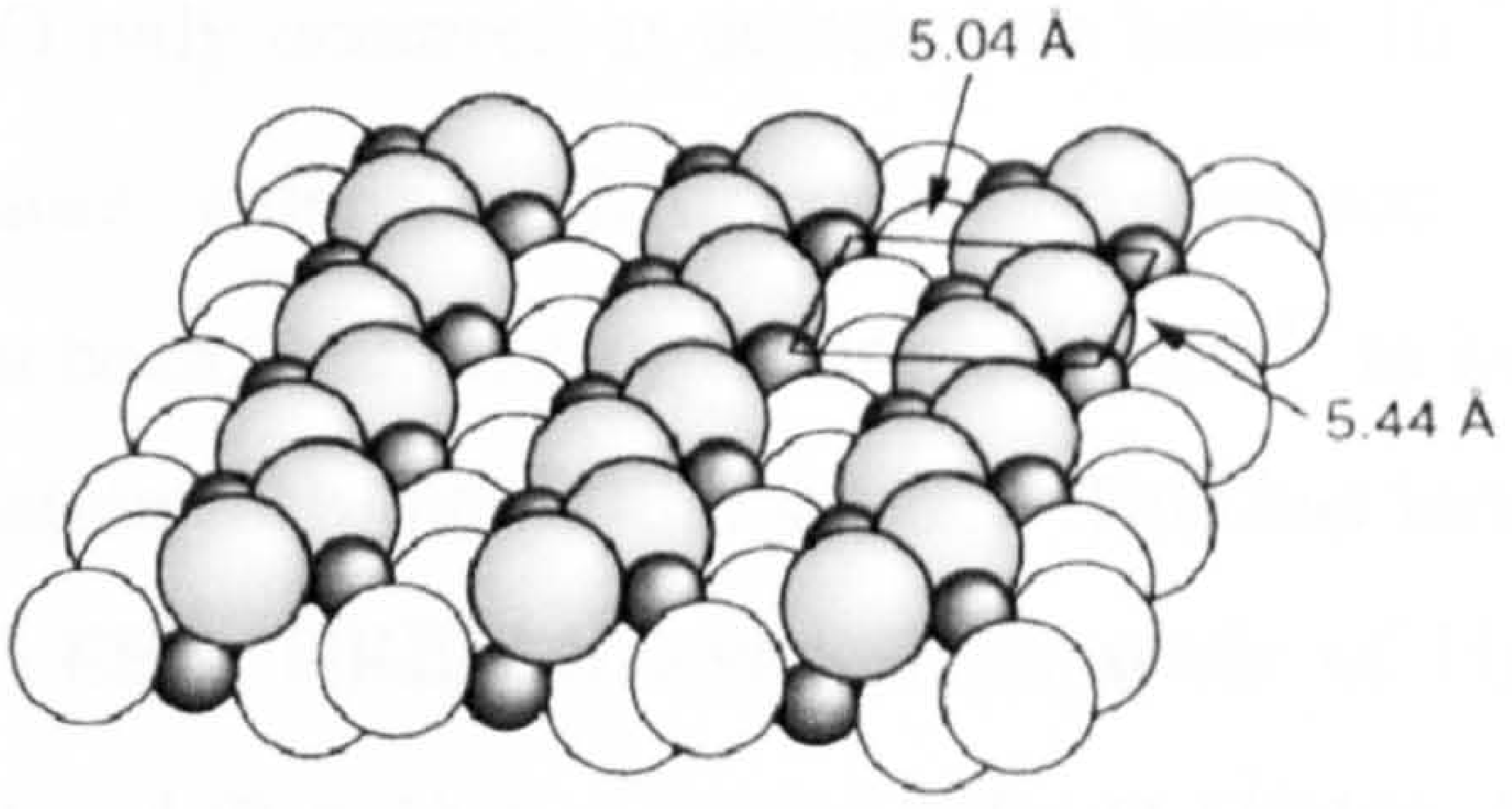

Figure 6.3: α-$Fe_2O_3(\bar{1}012)$ surface[33]

With regards to Fe_3O_4 surfaces, most of the work concerns the (001) surface[1,13,14,35,36] and the (111) surface, [1,37,38] which are the natural growth faces, although the (110) surface has also been studied.[39] The (001) surface consists of alternating A and B layers, the A-layer containing tetrahedrally co-ordinated Fe^{3+} ions, and the B-layer consisting of rows of octahedrally co-ordinated Fe^{3+} and Fe^{2+} ions surrounded by O^{2-} anions. The rows in successive B-layers are rotated 90° with respect to each other. Both A-terminated and B-terminated (001) surfaces have been observed and a (√2 × √2)R45° reconstruction has been widely reported.

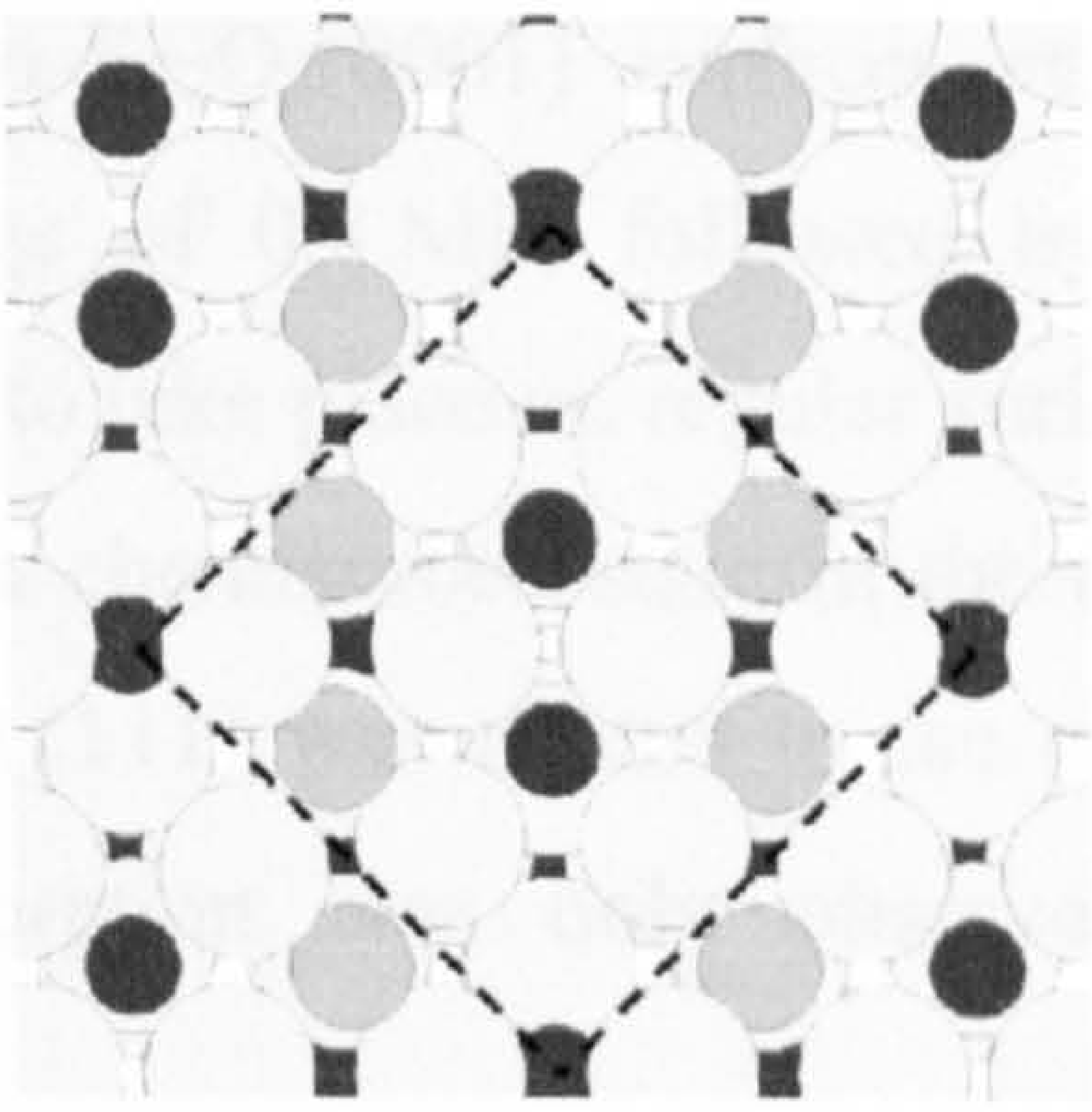

Figure 6.4: The $Fe_3O_4(001)$ surface[35]

6.1.4 Surface Chemistry

The interaction of well-defined iron oxide surfaces with **water** has attracted particular interest, since these interactions play a major role in catalysis and corrosion. It is known from early experiments[40] on powdered samples that water chemisorbs dissociatively resulting in a monolayer of hydroxyl groups. More recently a number of studies[10,41,42] concerning H_2O adsorption on α-$Fe_2O_3(0001)$ have been carried out. The general findings are that H_2O does not bind strongly with this surface and that dissociative adsorption is only favoured at higher pressures, as evidenced by UPS.[41,42] In particular one study[10] utilising PES found that dissociative chemisorption of H_2O only occurred at defect sites below 10^{-4} Torr, but that above this threshold pressure extensive hydroxylation occurred. The α-$Fe_2O_3(\bar{1}012)$ surface, however, has been predicted by theoretical work[43] to be much more reactive towards H_2O dissociation than the (0001) surface. This has indeed been found to be the case in a TPD, LEED, HREELS and SSIMS study of H_2O adsorption on the reconstructed (1 × 1) and (2 × 1) surfaces of α-$Fe_2O_3(\bar{1}012)$. Water dissociation on both surfaces resulted in terminal and bridging hydroxyl groups, with recombinative desorption occurring at 350 K and 400 K, respectively. Dissociative H_2O adsorption has also been observed on the $Fe_3O_4(111)$ surface[1] and the authors identified 3 species: dissociatively chemisorbed water, physisorbed monomeric water and hydrogen-bonded condensed ice.

Due to the application of iron oxides in ethyl benzene dehydrogenation to synthesise styrene, the adsorption of **ethyl benzene** and **styrene** on well-defined iron oxide surfaces has been studied. Experiments have been carried out on FeO(111), $Fe_3O_4(111)$ and α-$Fe_2O_3(0001)$ surfaces grown to 1-2 ML thickness on Pt(111).[1] On both the $Fe_3O_4(111)$ and α-$Fe_2O_3(0001)$ surfaces ethyl benzene was found to chemisorb up to a coverage of 0.8 ML, followed by a physisorbed layer. The chemisorption was believed to take place on regular surface sites and was not related to defects. The absence of a chemisorbed state in the case of FeO(111), suggested that chemisorption on $Fe_3O_4(111)$ was related to the exposed surface iron cations. Similarly, styrene chemisorption was only observed for $Fe_3O_4(111)$ and α-$Fe_2O_3(0001)$ surfaces.

The adsorption of **methanol** on α-$Fe_2O_3(0001)$ has been studied by HREELS[2] and CH_3OH was found to adsorb molecularly, desorbing between 140 K and 180 K.

With the potential application of iron oxides in the removal of chlorinated hydrocarbons, the surface reactions of **carbon tetrachloride** with iron oxides have prompted a number of studies recently.[44,45] Synchrotron XPS and TPD were used to study the interaction of CCl_4 with the $Fe_3O_4(111)$-(2 × 2) selvedge of α-$Fe_2O_3(0001)$ and CCl_4 was found to dissociate at 100 K resulting in chemisorbed Cl and CCl_2. At 275 K the adsorbed CCl_2 extracted lattice oxygen and desorbed as phosgene.

6.2 Growth, Thermal Stability and Ordering of FeO_x

In order to examine the interaction of molecules with iron oxide surfaces, it was first necessary to grow and characterise FeO_x films. Film A was generated by cycles consisting of Fe metal deposition (9.5 A for 90 s) followed by 20 L O_2 (5×10^{-8} Torr for 400 s) at ambient temperature and then a further 20 L O_2 at 673 K (see Figures 6.5a and 6.5b). In total 6 cycles were carried out (see Figures 6.6a and 6.6b). The thickness at this stage was estimated from the attenuation of the substrate photoelectron peak to be 2.0 nm.

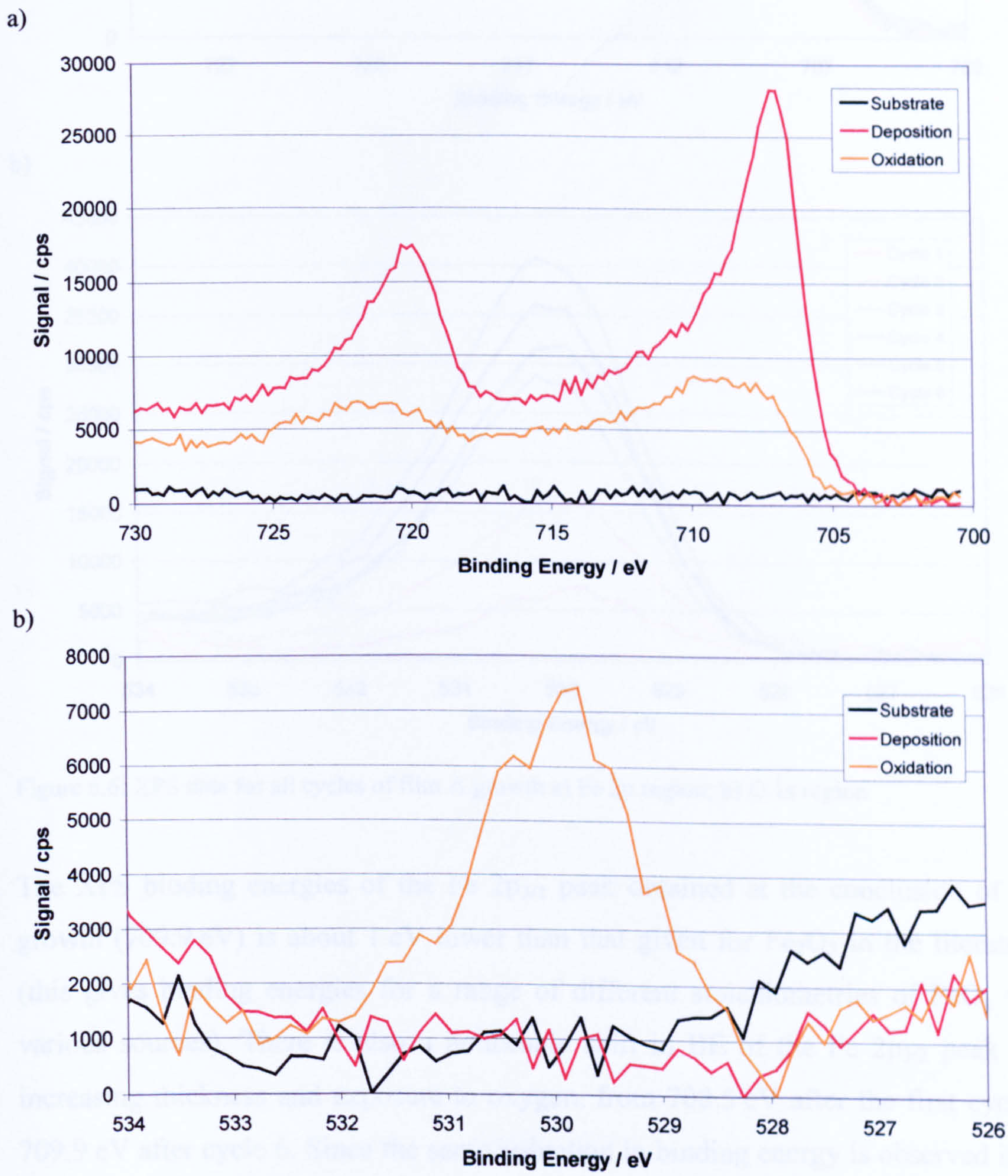

Figure 6.5: XPD data for cycle 1 of film A a) Fe 2p region; b) O 1s region;

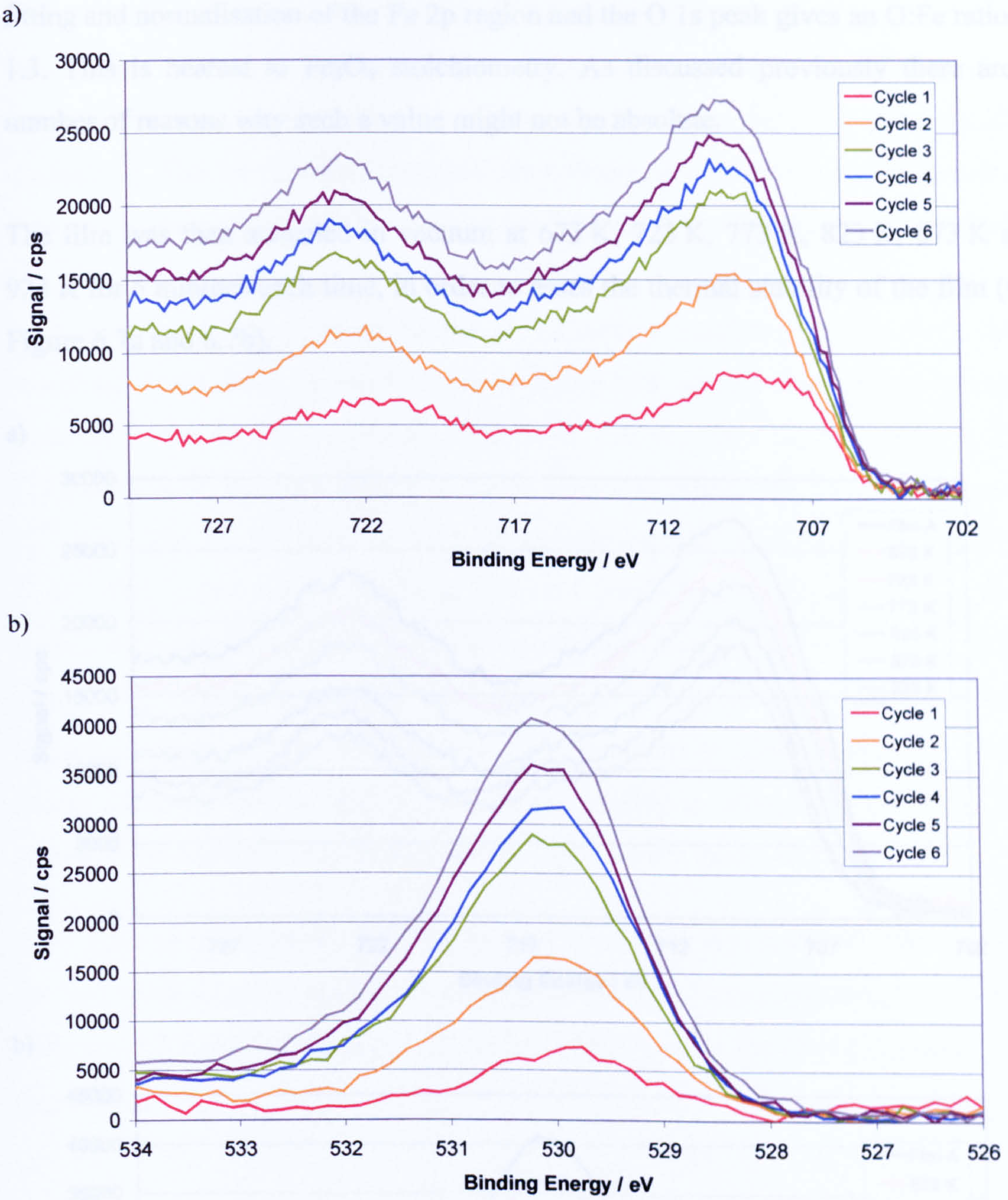

Figure 6.6: XPS data for all cycles of film A growth a) Fe 2p region; b) O 1s region

The XPS binding energies of the Fe $2p_{3/2}$ peak obtained at the conclusion of film growth (709.9 eV) is about 1 eV lower than that given for Fe_2O_3 in the literature[46] (this gives binding energies for a range of different stoichiometries of FeO_x from various sources). There is also a noticeable shift in BE of the Fe $2p_{3/2}$ peak with increasing thickness and exposure to oxygen, from 708.5 eV after the first cycle to 709.9 eV after cycle 6. Since the same reduction in binding energy is observed in the O 1s data at lower thickness, this is most likely due to the proximity to the metallic substrate, causing extra-atomic screening, rather than a real chemical shift. Peak fitting and normalisation of the Fe 2p region and the O 1s peak gives an O:Fe ratio of 1.3. This is nearest to Fe_3O_4 stoichiometry. As discussed previously there are a number of reasons why such a value might not be absolute.

The film was then annealed in vacuum at 673 K, 723 K, 773 K, 823 K, 873 K and 923 K for 5 minutes each time, in order to asses the thermal stability of the film (see Figure 6.7a and 6.7b).

a)

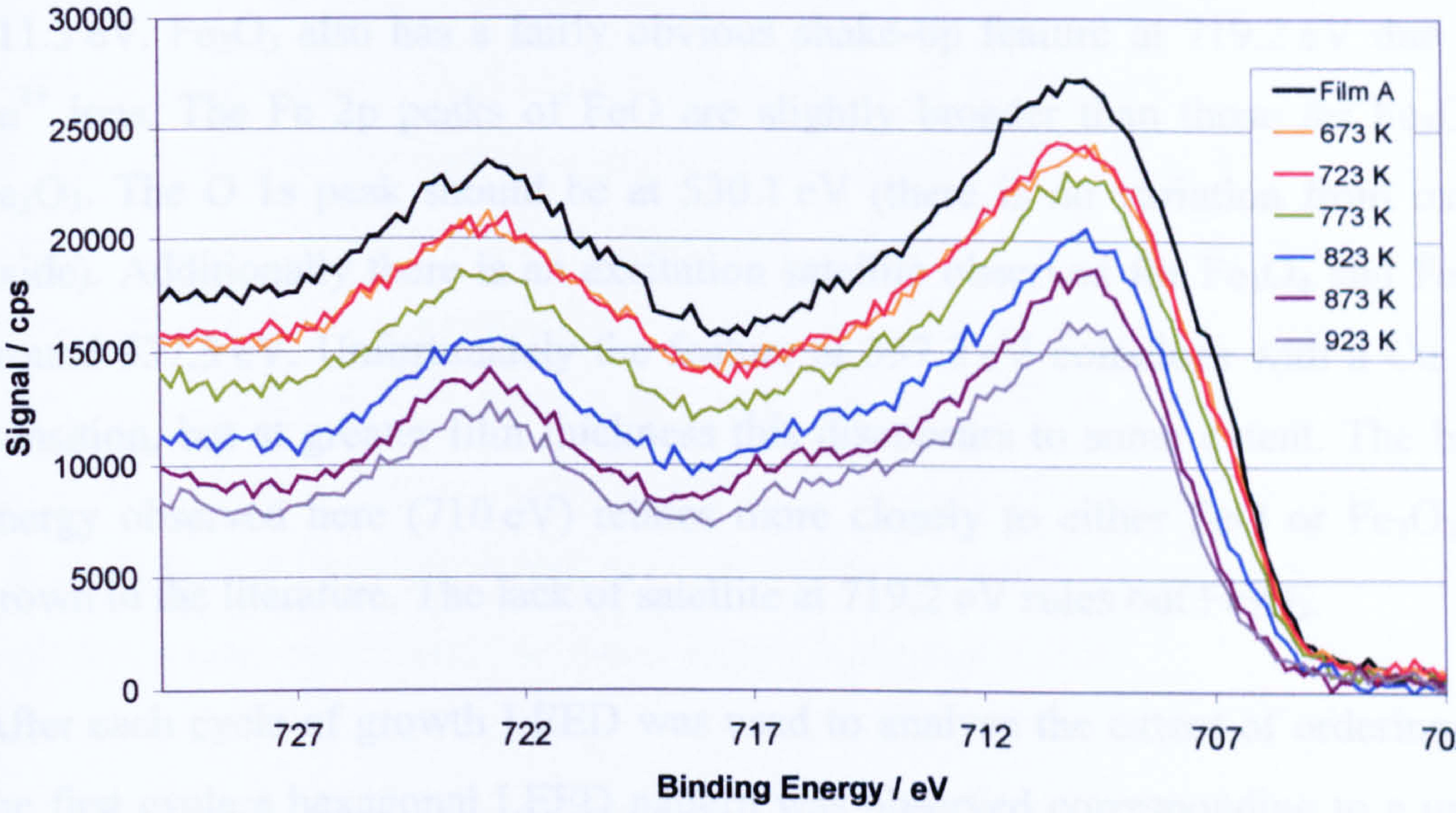

b)

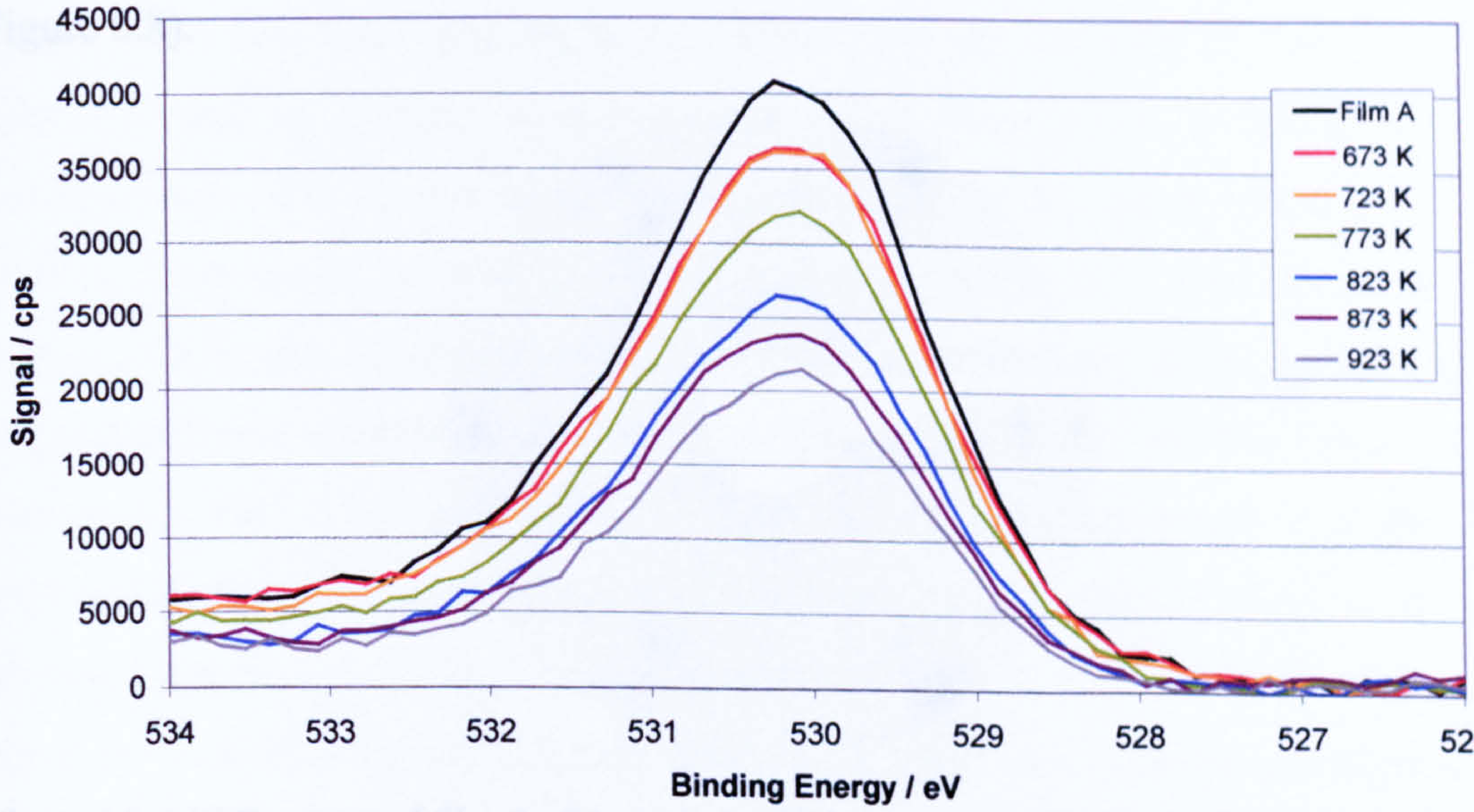

Figure 6.7: XPS data for the vacuum annealing of film A for 5 mins at each of the indicated temperatures a) Fe 2p region; b) O 1s region

The XPS data indicates that gradual breakdown of the FeO_x film occurs after annealing at 773 K or higher in vacuum (which may mean diffusion of Fe and O into the substrate or a morphological change in the film, such as 3D crystallite nucleation). This breakdown / morphological change is evident from reduction in the intensity of the Fe 2p and O 1s peaks and an increase in the intensity of Cu 2p peak.

It is possible to speculate as to the stoichiometry exhibited by the FeO_x films described above, from the features present in the XPS spectra. According to previous literature,[47] the Fe $2p_{3/2}$ peak for FeO is at 710 eV, whereas for Fe_2O_3 it is at 711.3 eV. Fe_2O_3 also has a fairly obvious shake-up feature at 719.2 eV due to the Fe^{3+} ions. The Fe 2p peaks of FeO are slightly broader than those for Fe_3O_4 and Fe_2O_3. The O 1s peak should be at 530.1 eV (there is no variation from oxide to oxide). Additionally there is an excitation satellite observed for Fe_3O_4 and Fe_2O_3 at around 537.3 eV. Unfortunately the feature at 537.3 eV coincides with a Cu Auger transition, but at greater film thickness this disappears to some extent. The binding energy observed here (710 eV) relates more closely to either FeO or Fe_3O_4 films grown in the literature. The lack of satellite at 719.2 eV rules out Fe_2O_3.

After each cycle of growth LEED was used to analyse the extent of ordering. After the first cycle a hexagonal LEED pattern was observed corresponding to a unit cell with, $a = 3.2$ Å (±0.1) which is 1.25 × 1.25 with respect to the Cu(111) substrate (see Figure 6.8).

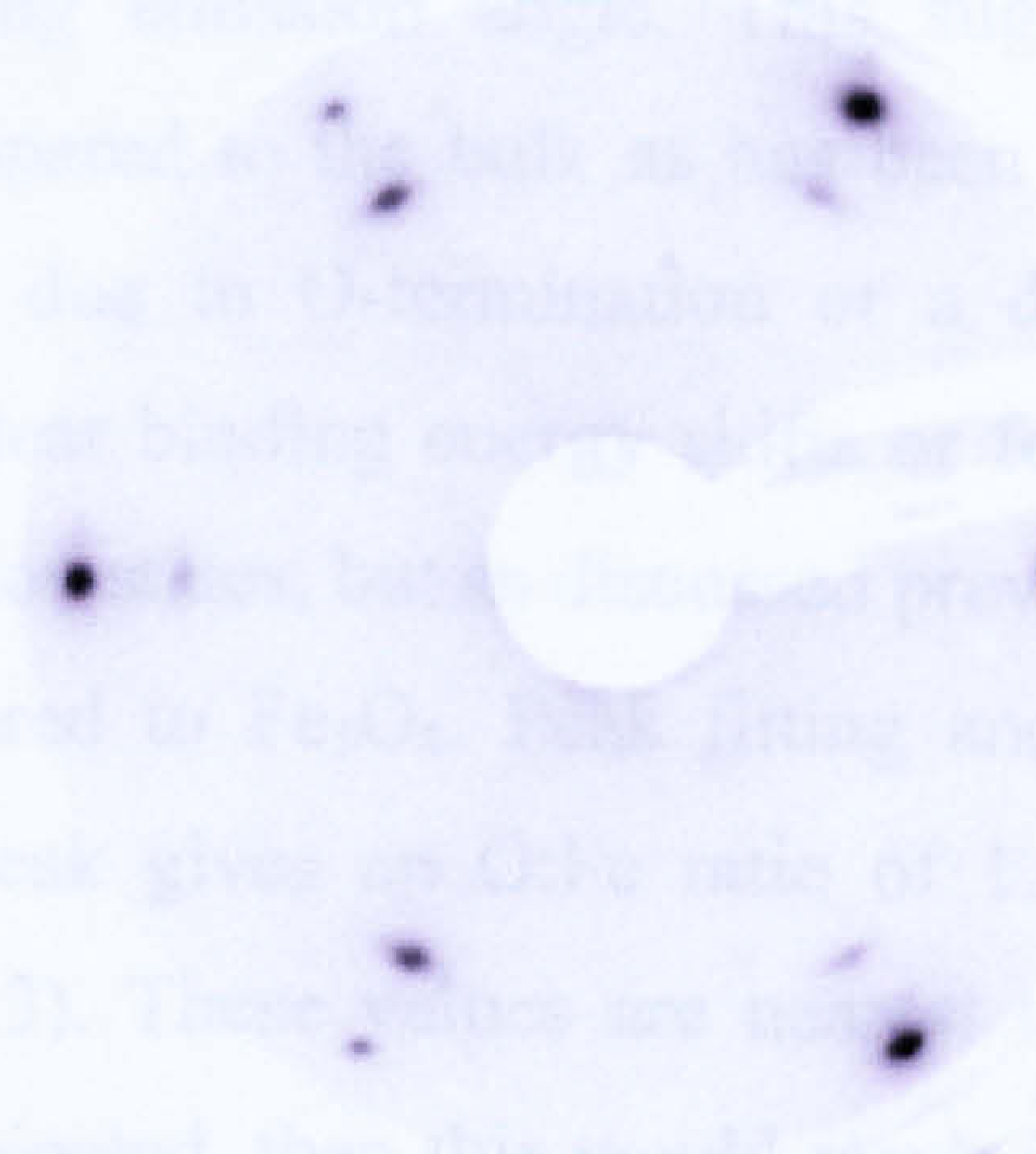

Figure 6.8: LEED pattern of film A after cycle 1 with beam energy 67 eV; the Cu(111) substrate spots are the outermost of the pair of spots

This pattern remained the same throughout the experiment, although the Cu spots became less clear with increased thickness, as would be expected. The value of 3.2 Å is in reasonable agreement with the value of 3.1 Å that would be expected for FeO(111) based upon the bulk cell constant. Lattice cell constants of 3.1 Å have also been observed for FeO(111)[1] grown on Pt. The slight difference compared to literature values could be due to electronic interaction between the substrate (Pt in the literature, Cu in this study).

In order to carry out an angle-resolved XPS study and to assess the reproducibility of these films, a new FeO_x film was grown. Film B was generated by deposition of Fe metal onto the cleaned Cu(111) substrate, followed by exposure to 5×10^{-8} Torr O_2 for 400 s (20 L) at ambient temperature and a further 20 L O_2 at 673 K (see Figures 6.9a and 6.9b). This procedure generated a film of 0.9 nm estimated thickness. Repeating this cycle a second time resulted in a film of 1.8 nm estimated thickness. After each cycle the XPS spectra for O 1s, Cu 2p3/2, C 1s and Fe 2p regions were recorded with an electron emission angle of 15° from the sample normal. After the 1.8 nm film had been generated, spectra were additionally recorded at more grazing emission angles of 45° and 75° (see Figures 6.10a and 6.10b)

Analysis of the collected data reveals no major differences between the Fe 2p and O 1s peaks for the FeO_x film at different emission angles, except a reduction in intensity for the most grazing angle. There was an increase in the O:Fe signal intensity ratio at grazing emission angle. This suggests a variation in surface concentration of O compared to the bulk as has been discussed before in AR-XPS studies. This could be due to O-termination or a different stoichiometry at the surface. There are no clear binding energy shifts or features in the Fe 2p region to suggest different oxidation states, but as discussed previously we don't expect a great change for FeO compared to Fe_3O_4. Peak fitting and normalisation of the Fe 2p region and the O 1s peak gives an O:Fe ratio of 1.4. This is close to the value obtained for film A (1.3). These values are nearest to Fe_3O_4 stoichiometry. If the films are indeed O-terminated, then this would result in a higher experimental value for the Fe:O ratio.

a)

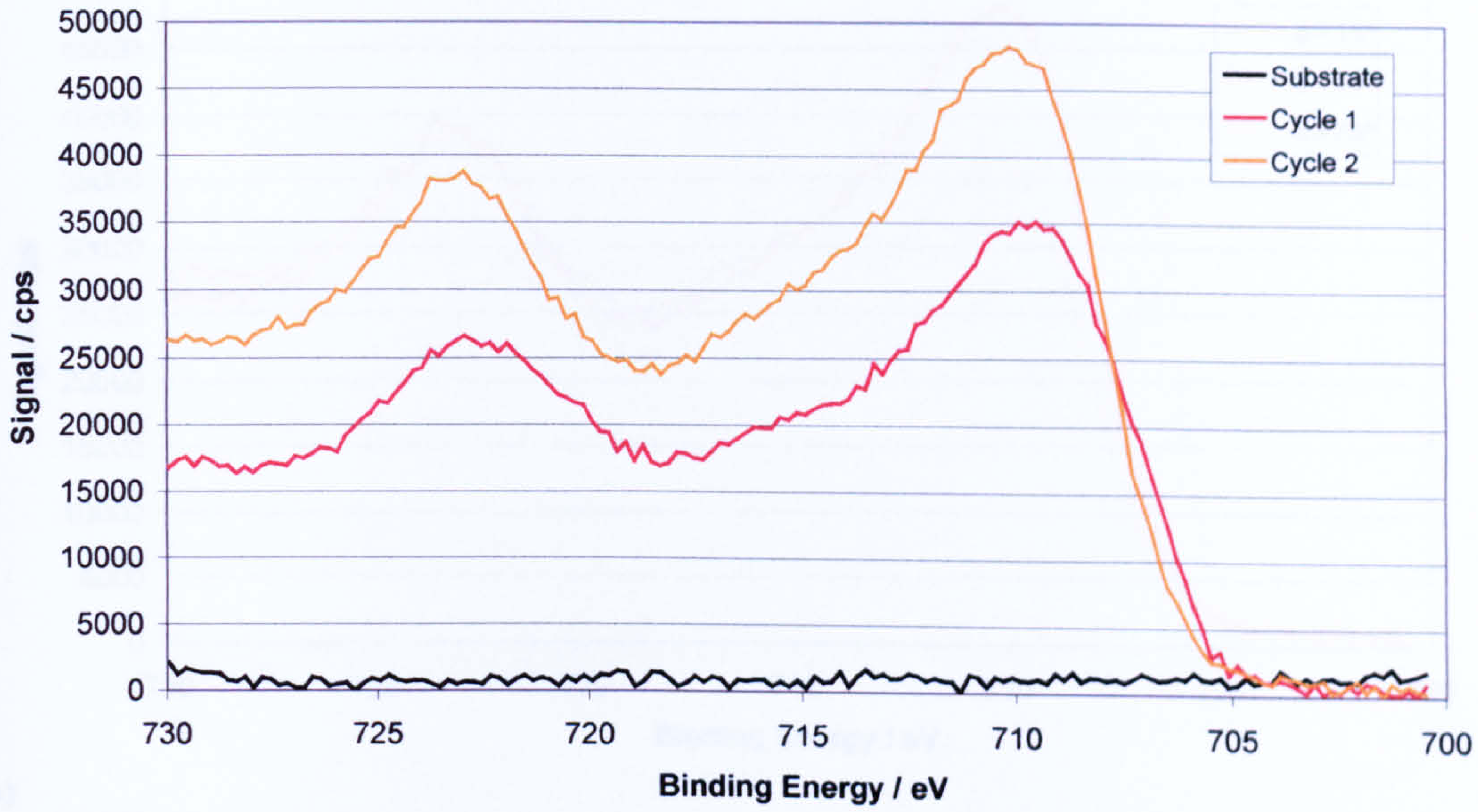

b)

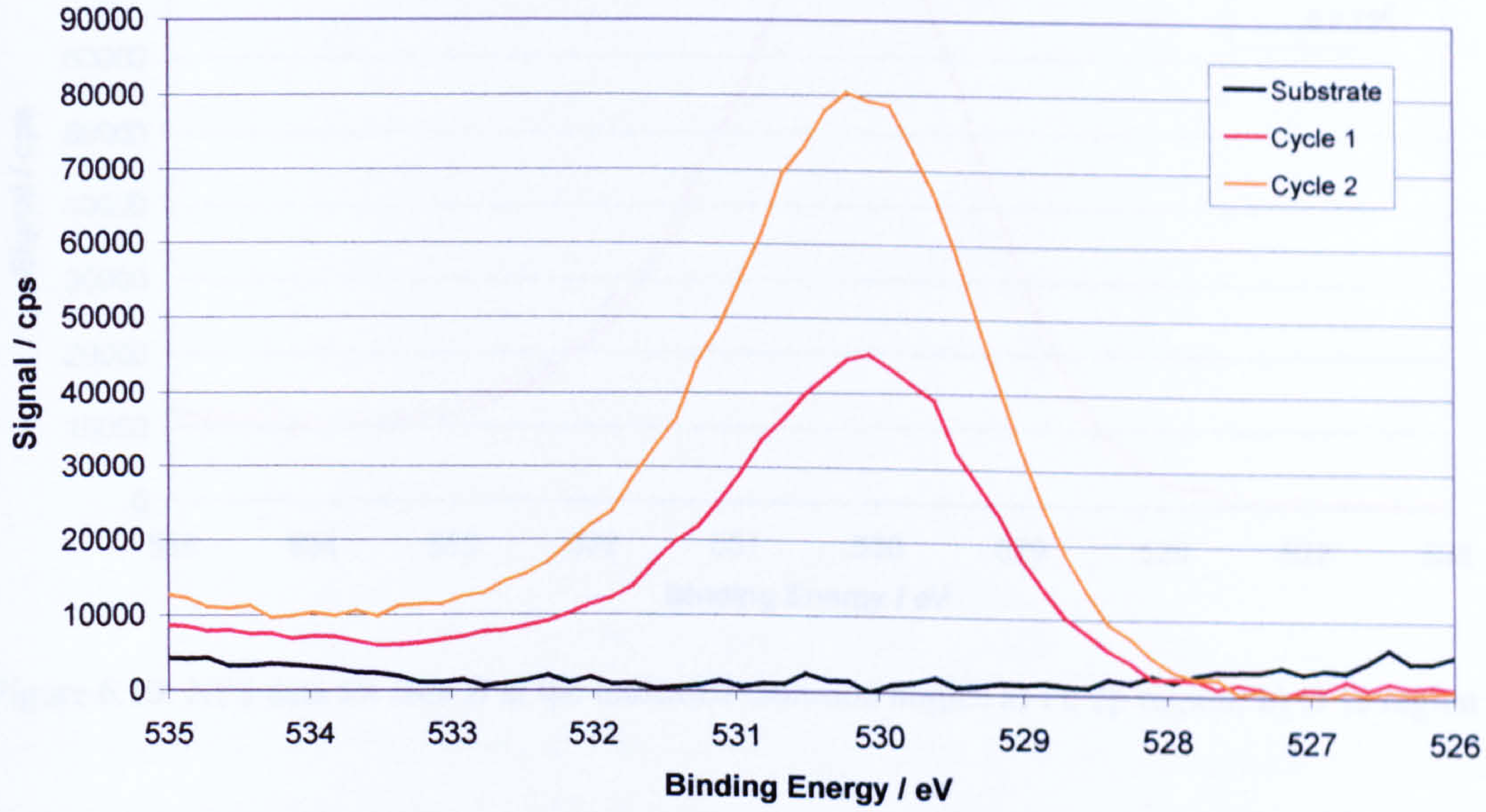

Figure 6.9: XPS data for growth of film B a) Fe 2p region; b) O 1s region;

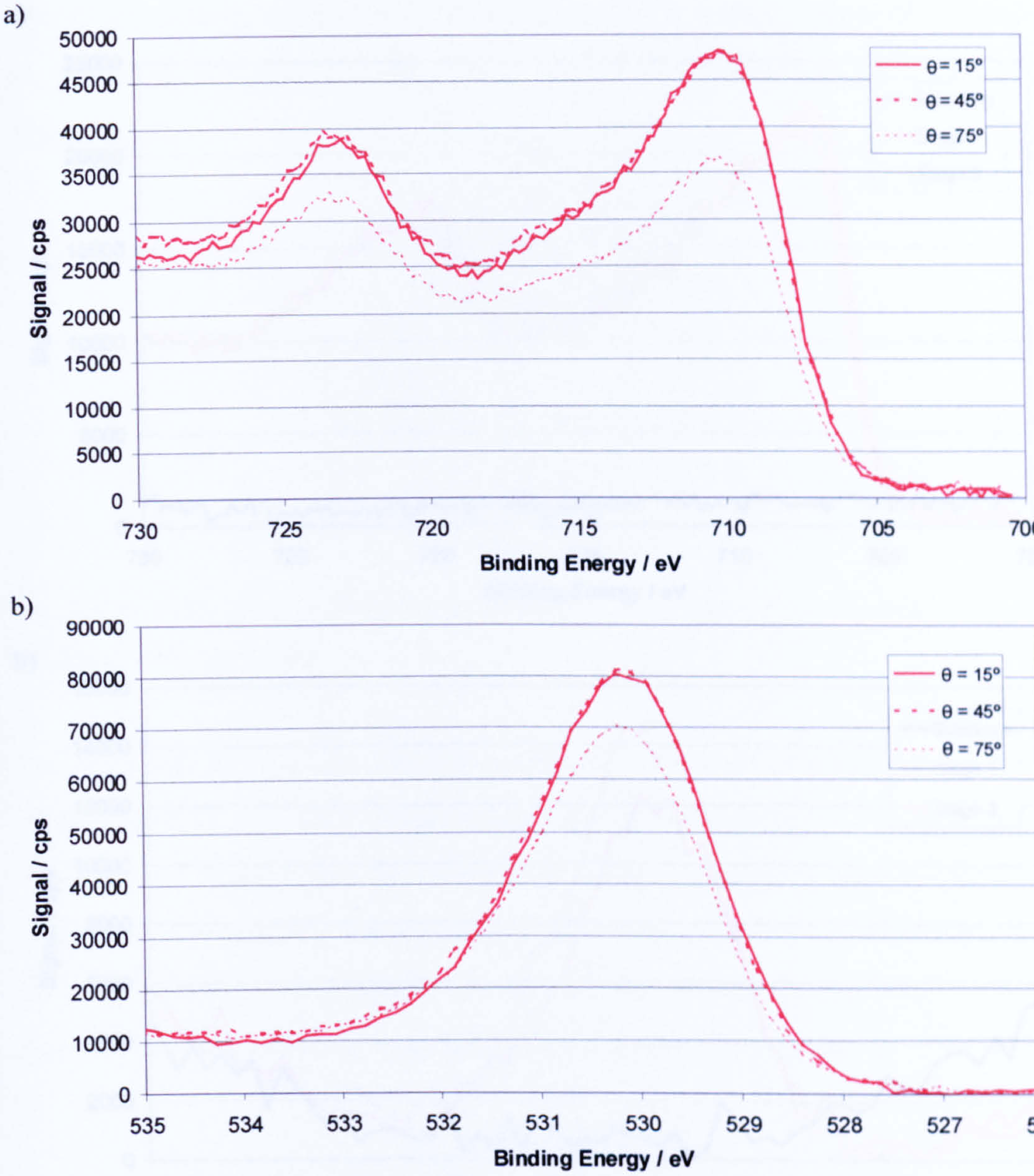

Figure 6.10: XPS data for film B at the indicated emission angles a) Fe 2p region; b) O 1s region

The next film grown, film C, was grown in a deliberate attempt to produce a film that was oxygen-deficient, so that the reactivity of such surfaces could be compared with those of more-oxidised surfaces. This film was generated by deposition of Fe metal (90 s at 9.5 A) onto the cleaned Cu(111) substrate, followed by exposure to 5 × 10^{-8} Torr O_2 for 100 s (5 L) at ambient temperature (stage 1) and a further 10 L O_2 at 673 K (stage 2). This procedure generated a film of 0.4 nm estimated thickness (see Figures 6.11a and 6.11b).

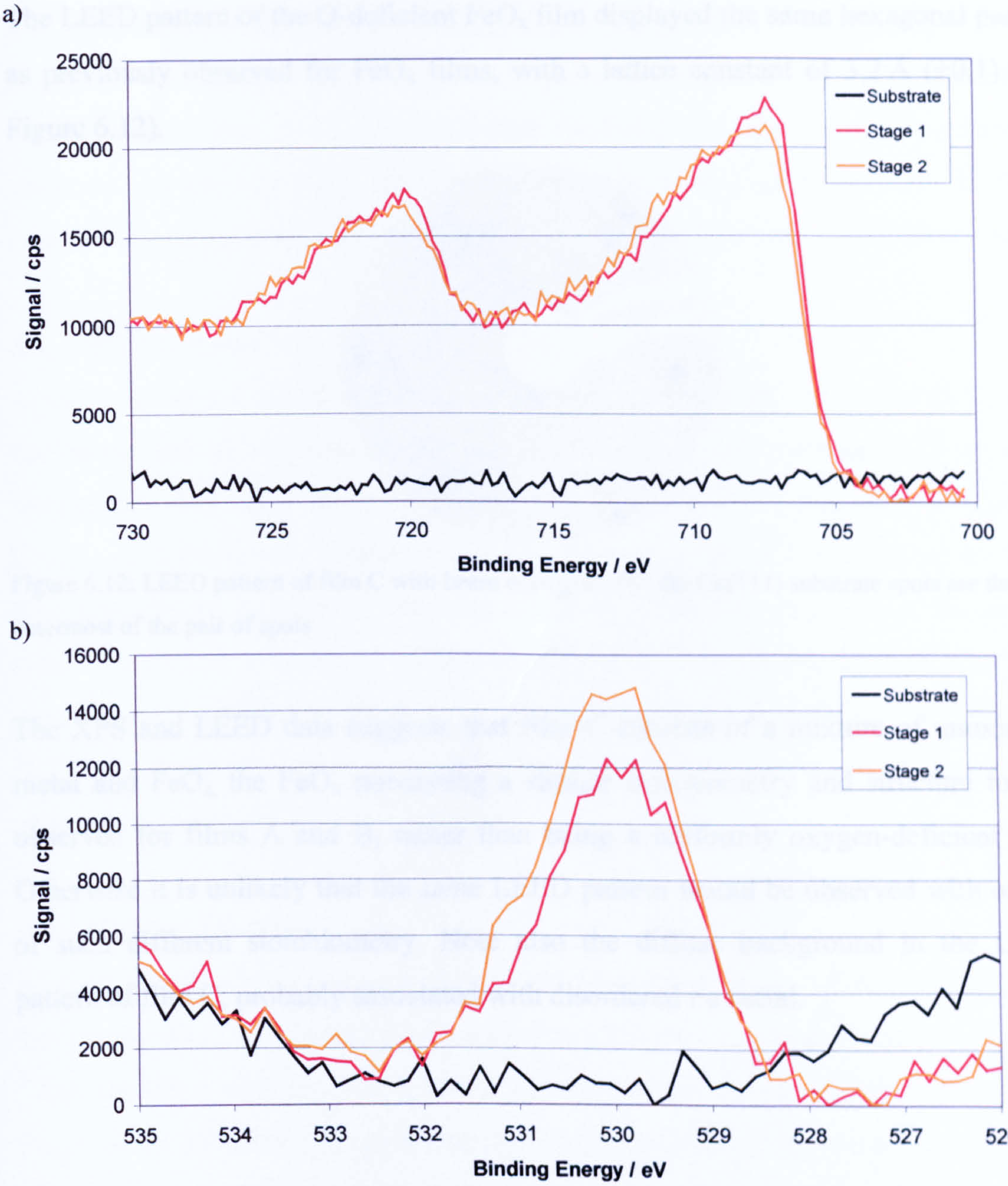

Figure 6.11: XPS data for growth of film C a) Fe 2p region; b) O 1s region; (Stage 1 = Fe metal deposition and oxidation with 5 L O_2 at room temperature; Stage 2 = Oxidation with 10 L O_2 at 673 K)

The XPS data, in particular that of the Fe 2p and O 1s regions, suggested that this film was indeed less-well oxidised than previously grown FeO_x films. This is on account of the Fe $2p_{3/2}$ peak maximum being at 707.5 eV with a shoulder at 709.9 eV, which suggests that there are portions of unoxidised Fe metal. Peak fitting and normalisation gives an O:Fe ratio of 0.7. This value is quite low (suggesting $FeO_{0.7}$ stoichiometry), but as previously discussed, these values may not be absolute. Also the O:Fe ratio is reduced by a factor of 2 compared to film A and film B.

The LEED pattern of the O-deficient FeO$_x$ film displayed the same hexagonal pattern as previously observed for FeO$_x$ films, with a lattice constant of 3.2 Å (±0.1) (see Figure 6.12).

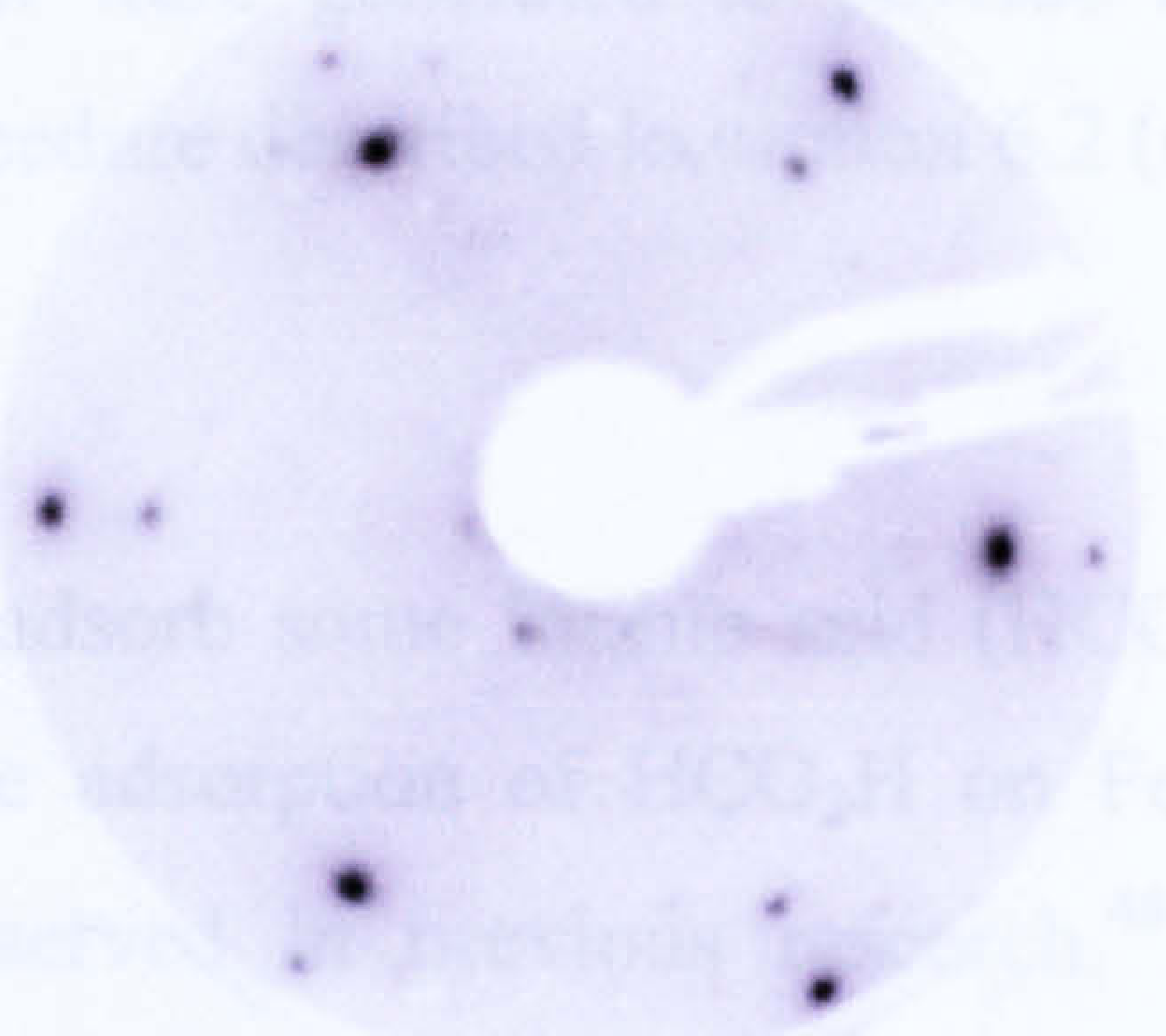

Figure 6.12: LEED pattern of film C with beam energy 67 eV; the Cu(111) substrate spots are the outermost of the pair of spots

The XPS and LEED data suggests that film C consists of a mixture of unoxidised metal and FeO$_x$, the FeO$_x$ possessing a similar stoichiometry and structure to that observed for films A and B, rather than being a uniformly oxygen-deficient film. Otherwise it is unlikely that the same LEED pattern would be observed with oxides of such different stoichiometry. Note also the diffuse background in the LEED pattern of film C, probably associated with disordered Fe metal.

6.3 Interaction of FeO_x with HCO_2H, CH_3OH, CO and C_3H_6

FTRAIRS was used as the primary instrumental technique to elucidate information on the interaction of small molecules with the FeO_x films generated. New films of thickness 1.4 nm – 1.8 nm were generated to provide a clean surface for these experiments, using the procedure described in section 6.2 (unless stated otherwise).

6.3.1 HCO_2H Adsorption

A test was carried out to adsorb some formic acid (HCO_2H) on a new FeO_x film. Molecular and dissociative adsorption of HCO_2H on Fe_2O_3 under UHV at room temperature has been observed in previous research.[48] Formic acid was dosed directly onto the sample to achieve a background pressure of 1×10^{-8} Torr for 100 s (this corresponds to a background exposure of 1 L, but the exposure at the sample would be around a factor of 10 greater due to the directional dosing). The mass spectrometer was used to check the purity of the formic acid. After adsorption the FT-IR spectrum showed no new absorption peaks, so no evidence of formic acid adsorption was observed.

6.3.2 CH_3OH Adsorption

Methanol is also known to adsorb on some iron oxide surfaces.[2] After flashing the sample to 673 K, the surface was exposed to CH_3OH at a dosing pressure of 1×10^{-7} Torr for 100 s, with the sample directly in front of the dosing tube of the leak valve. No evidence for methanol adsorption was observed in the IR spectrum.

An XPS investigation of CH_3OH adsorption was also carried out on a new film. Particular attention was paid to the O 1s and C 1s regions but additionally the Cu 2p and Fe 2p peaks were recorded. From the attenuation of the Cu 2p signal the oxide film thickness was estimated to be 1.4 nm. Each XPS spectrum was recorded at a grazing emission angle (75° from the sample normal) in addition to the usual 15° emission angle. After flashing the sample to 723 K and recording the "background" XP spectra, the sample was exposed to 1×10^{-7} Torr for 100 s as in the previous IR experiment (see Figure 6.13a, 6.13b, 6.14a and 6.14b).

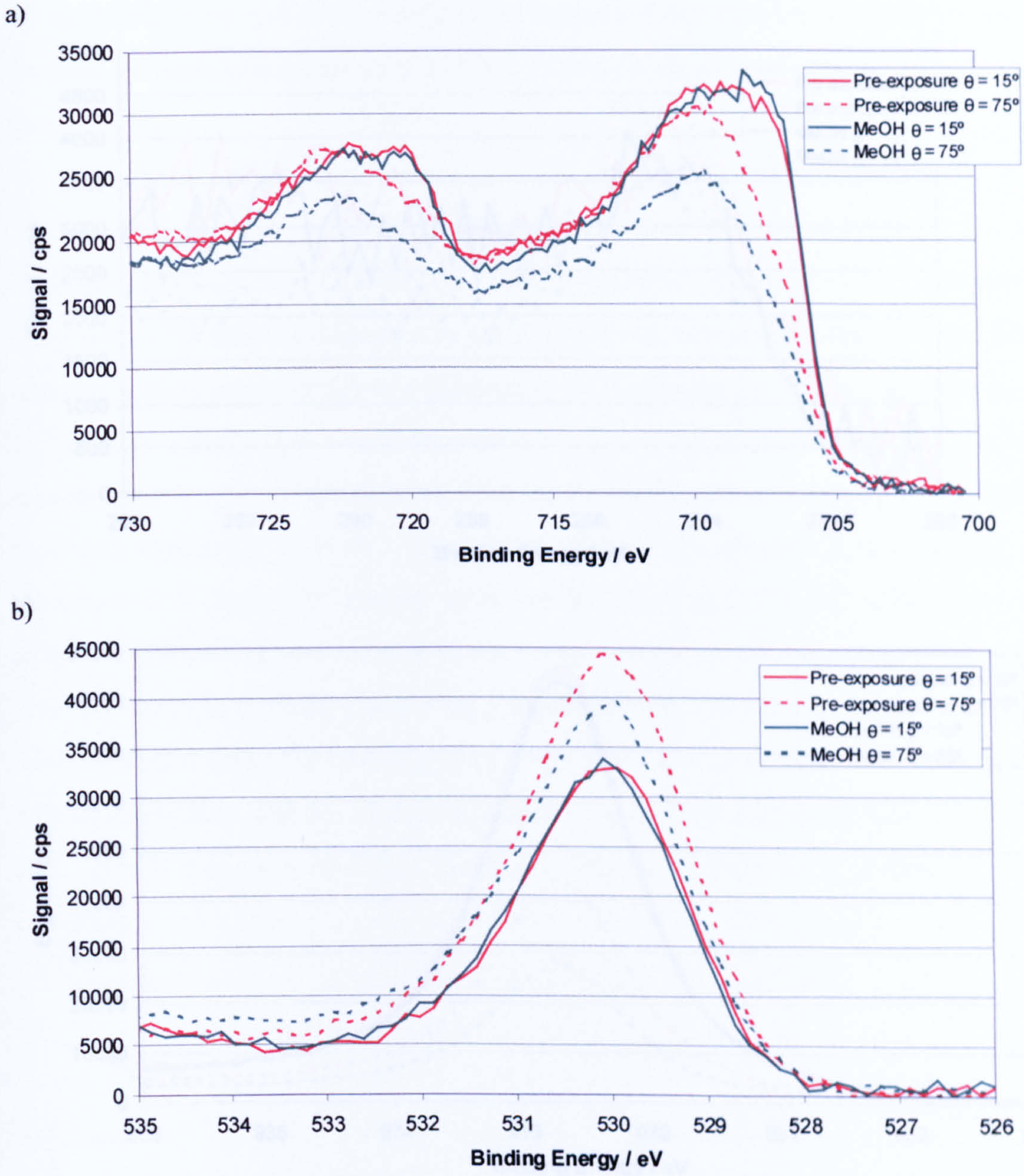

Figure 6.13: XPS data for CH_3OH adsorption at the indicated emission angles a) Fe 2p region; b) O 1s region

No unequivocal evidence of methanol adsorption was observed. Arguably there was a very slight increase in C 1s signal, in view of the greater decrease in all other peak intensities. In summary, although CH_3OH adsorption has been documented on α-$Fe_2O_3(0001)$,[2] the surface of the FeO_x films grown in this study appears to exhibit different surface chemistry and no adsorption is observed.

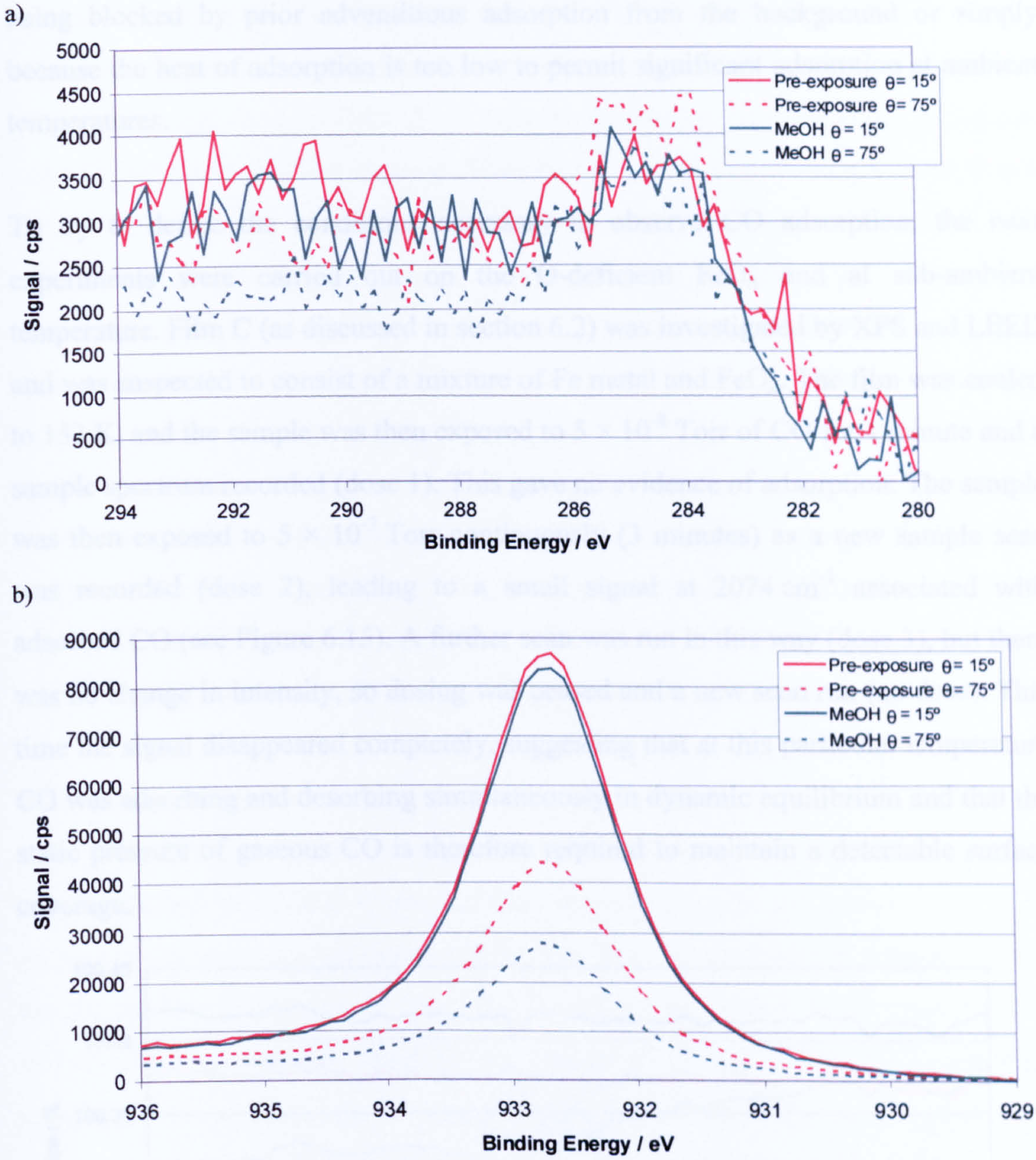

Figure 6.14: XPS data for CH_3OH adsorption at the indicated emission angles a) C 1s region; b) Cu $2p_{3/2}$ region

6.3.3 CO Adsorption

Firstly, CO adsorption was carried out at ambient temperature. A new FeO_x film was grown (as previously described) and exposed to 5×10^{-8} Torr CO for 1 minute. This did not result in any IR absorption peaks associated with CO adsorption, so the film was exposed to a further 5×10^{-7} Torr for 1 minute and a further sample scan run. Still no adsorption of CO was evident. The absence of any adsorption could be due to the surface being fully-oxygen terminated, the necessary adsorption sites having being blocked by prior adventitious adsorption from the background or simply because the heat of adsorption is too low to permit significant adsorption at ambient temperatures.

To try to define the conditions necessary to observe CO adsorption, the next experiments were carried out on the O-deficient FeO_x and at sub-ambient temperature. Film C (as discussed in section 6.2) was investigated by XPS and LEED and was suspected to consist of a mixture of Fe metal and FeO_x. The film was cooled to 153 K, and the sample was then exposed to 5×10^{-8} Torr of CO for 1 minute and a sample spectrum recorded (dose 1). This gave no evidence of adsorption. The sample was then exposed to 5×10^{-7} Torr continuously (3 minutes) as a new sample scan was recorded (dose 2), leading to a small signal at 2074 cm^{-1} associated with adsorbed CO (see Figure 6.15). A further scan was run in this way (dose 3), but there was no change in intensity, so dosing was ceased and a new scan run (no dose). This time the signal disappeared completely, suggesting that at this particular temperature CO was adsorbing and desorbing simultaneously in dynamic equilibrium and that the static pressure of gaseous CO is therefore required to maintain a detectable surface coverage.

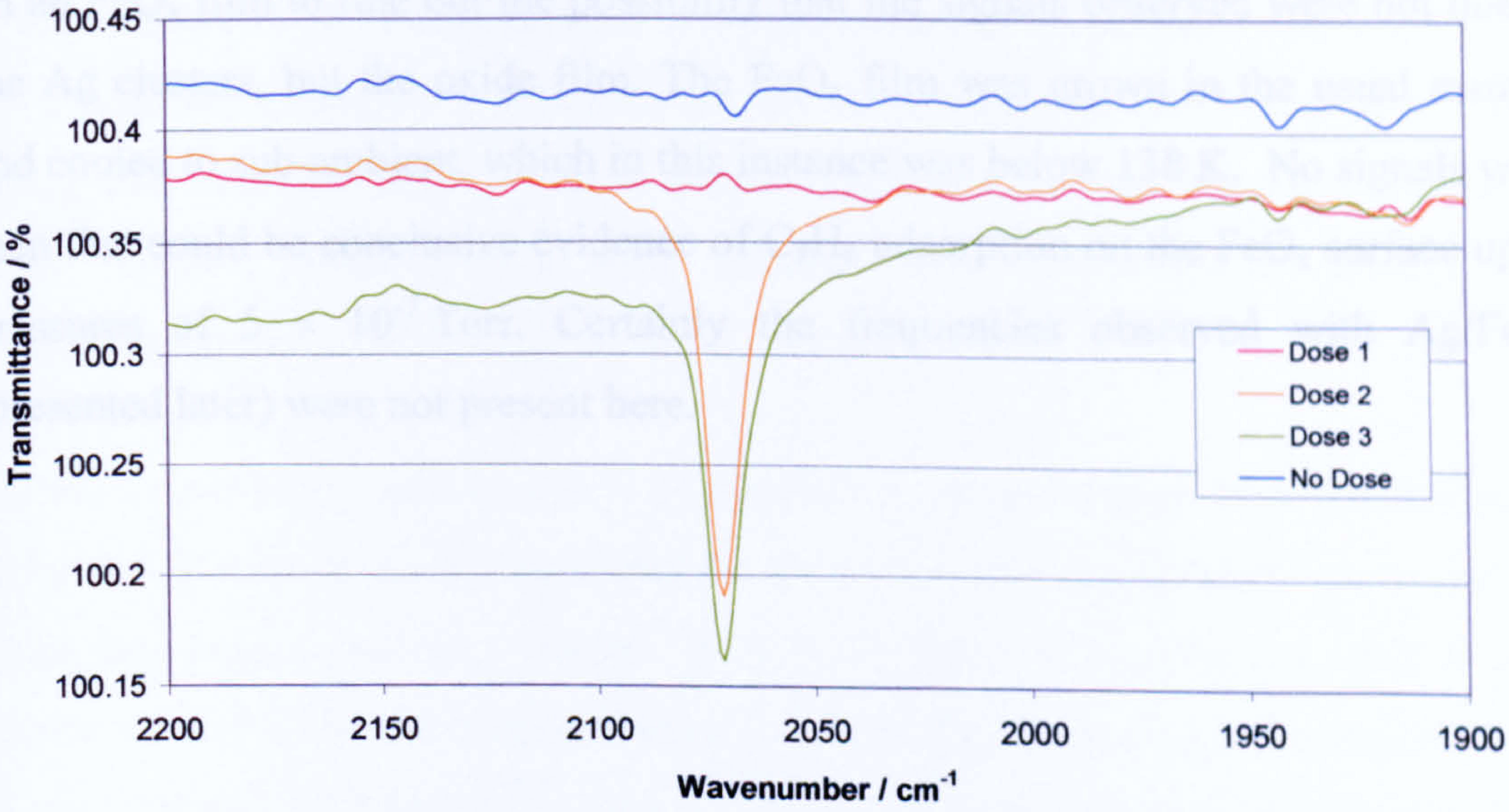

Figure 6.15: RAIRS spectra for CO adsorption on FeO_x (See accompanying text for explanation of gas exposures)

It is important to appreciate that this signal could have three origins. 1) CO adsorption on the O-deficient FeO_x film, 2) adsorption on exposed regions of the Cu substrate, 3) adsorption on unoxidised Fe metal. The signal at 2074 cm^{-1} is at exactly the same frequency as that observed in previous experiments in this project, where CO has been adsorbed on Cu(111) at these temperatures. At a thickness of 0.4 nm, some Cu substrate could be exposed. Moreover the frequency is thought to be to low for CO-oxide bonding. In conclusion, therefore, the most probable origin of this peak is adsorption of CO on a limited number of exposed Cu(111) sites.

Finally CO adsorption was investigated using a pre-sputtered FeO_x film, again at approaching 123 K. The FeO_x film was generated using the procedure described previously, then sputtered lightly (2 keV beam energy, ~ 10 μA for 60 s), in an attempt to expose surface Fe adsorption sites. The sample was then cooled down to approaching 123 K and exposed to 5×10^{-8} Torr CO for 1 minute. Dosing then continued at this pressure while running a sample scan which took 3 minutes, but no adsorption was observed. A second scan was recorded with the sample exposed to 5×10^{-7} Torr CO, however still no signal due to adsorbed CO was seen.

6.3.4 C_3H_6 Adsorption on $FeO_x/Cu(111)$

As will be discussed later in section 6.6, the interaction of C_3H_6 with FeO_x-supported Ag was studied by RAIRS. It was therefore important to also test adsorption of C_3H_6 on an FeO_x film to rule out the possibility that the signals observed were not due to the Ag clusters, but the oxide film. The FeO_x film was grown in the usual manner and cooled to sub-ambient, which in this instance was below 138 K. No signals were seen that could be conclusive evidence of C_3H_6 adsorption on the FeO_x surface up to pressures of 5×10^{-7} Torr. Certainly the frequencies observed with Ag/FeO_x (presented later) were not present here.

6.4 Literature Review of Metal Oxide-Supported Ag

Dispersed metals on well-defined metal oxides have been the focus of a large amount of research. In particular noble metals such as Pt, Au and Ag have received much attention.

The main reason for studying metal oxide-supported silver nanoparticles is as a model for heterogeneous catalysts, since these commonly consist of a dispersed noble metal on a metal oxide support. An important area of research for catalytic applications is orientated towards automobile emission control and alumina-supported silver has been found to possess catalytic activity for the oxidation of CO and hydrocarbons and the reduction of NO_x.[49] There are also a number of industrial reactions in which supported silver is known to be active, for example supported Ag is used for the highly-selective epoxidation of ethylene[50] and has also been tested for catalytic activity for hydrogenation.[51] Ag/Au bimetallic catalysts supported on α-Fe_2O_3 have also recently been found to be active for the water-gas shift reaction.[52] Other research motivations for studying metal oxide-supported Ag systems include the fabrication of new ceramic materials[53] and solid state gas sensors.[54]

A fair number of UHV surface science studies of metal oxide-supported Ag systems have been conducted as a result of the above applications and the need to better understand these systems. In particular the $TiO_2(110)$ surface has been used as an oxide support, probably as a result of this oxide surface already having been extensively studied.[53,55-57]

On the $TiO_2(110)$-(1 × 2) and (1 × 1) surfaces Ag clusters have been determined to grow as 3-D islands, nucleating along the step edges. No reaction between metal and oxide has been observed, however XPS shifts have been observed with smaller cluster sizes.[56] STM has been commonly utilised for elucidating information on Ag cluster size and morphology[50,53] and investigations have reported Ag cluster sizes of 1-20 nm. One STM study reports dispersed Ag particles deposited at room temperature on $TiO_2(110)$ to be remarkably stable, up to 900 K in vacuum[57] although Ostwald ripening has been observed to occur upon exposure to 10 Torr O_2.[50] In contrast it was found that an alumina support for Ag, reduces the reactivity of the metal clusters towards oxygen and hence cluster ripening is inhibited. Bimetallic nanoparticles have also received some attention. One group has studied Ag/Au nanoparticles supported on $TiO_2(110)$ using STM.[58]

Although α-Fe_2O_3 films containing dispersed Ag nanoparticles have been prepared by a sol-gel method[59] to the authors knowledge no study of Ag dispersed on a well-defined FeO_x surface under UHV conditions currently exists in the published literature.

6.5 Growth and Thermal Stability of Ag/FeO_x

In order to examine the interaction of small molecules with silver supported on iron oxide it was first necessary to grow and characterise the Ag/FeO_x system. Three metal-on-oxide systems of varying degrees of Ag loading were generated by growth of an FeO_x film as previously described in section 6.2 and then depositing Ag onto the oxide film. It was not possible to assess the extent of Ag loading from the attenuation of the oxide peaks, since with low loadings of Ag there was no attenuation of the Fe 2p or O 1s peaks upon Ag deposition. It should also be noted that as we anticipate the growth of silver clusters on the iron oxide surface, this method of thickness estimation is systematically flawed, as it is based upon the model of uniform layer growth. In order to provide the reader with an indication of the relative amounts of Ag in the different samples, the absolute signal of the Ag is quoted.

Sample A (Ag $3d_{5/2}$ peak height = 7 kcps) was grown by first generating the iron oxide support using two cycles of Fe deposition (100 s × 9.5 A), oxidation at ambient temperature (5×10^{-8} Torr for 400 s) and oxidation at 673 K (5×10^{-8} Torr for 400 s). This led to a well-defined FeO_x film with an estimated thickness of 2.2 nm. Ag was then deposited from the Ag deposition source (with a deposition source current of 13.25 A for 8 minutes). XPS data was recorded before and after Ag deposition (see Figure 6.16). In addition to the Ag 3d region, the Auger region Ag MVV was also recorded (920 eV – 880 eV). This was because according to literature values[46] only a negligible shift in binding energy is anticipated for Ag^0 to Ag^+ or Ag^{2+}. In the Auger region, however, a shift is expected. Unfortunately, for the amount of Ag deposited in this experiment, the Auger peak was not intense enough to see. Since there was no attenuation of the FeO_x signals, it was assumed that the thickness was under one monolayer, or that the Ag grew as 3-dimensional islands or clusters. One oddity here is that the signal for Fe 2p and O 1s actually increased after Ag deposition - indeed all peaks increase in intensity (including Cu $2p_{3/2}$). This could be explained by experimental error – after all it makes no sense that the underlying substrate signal would increase when depositing metal on top and these XPS intensities have been known to be inconsistent on occasions – however this same trend was observed consistently with all other Ag/FeO_x samples grown (including those not detailed in this report). One must therefore at least consider that there may be an underlying reason for this trend associated with structural changes upon deposition.

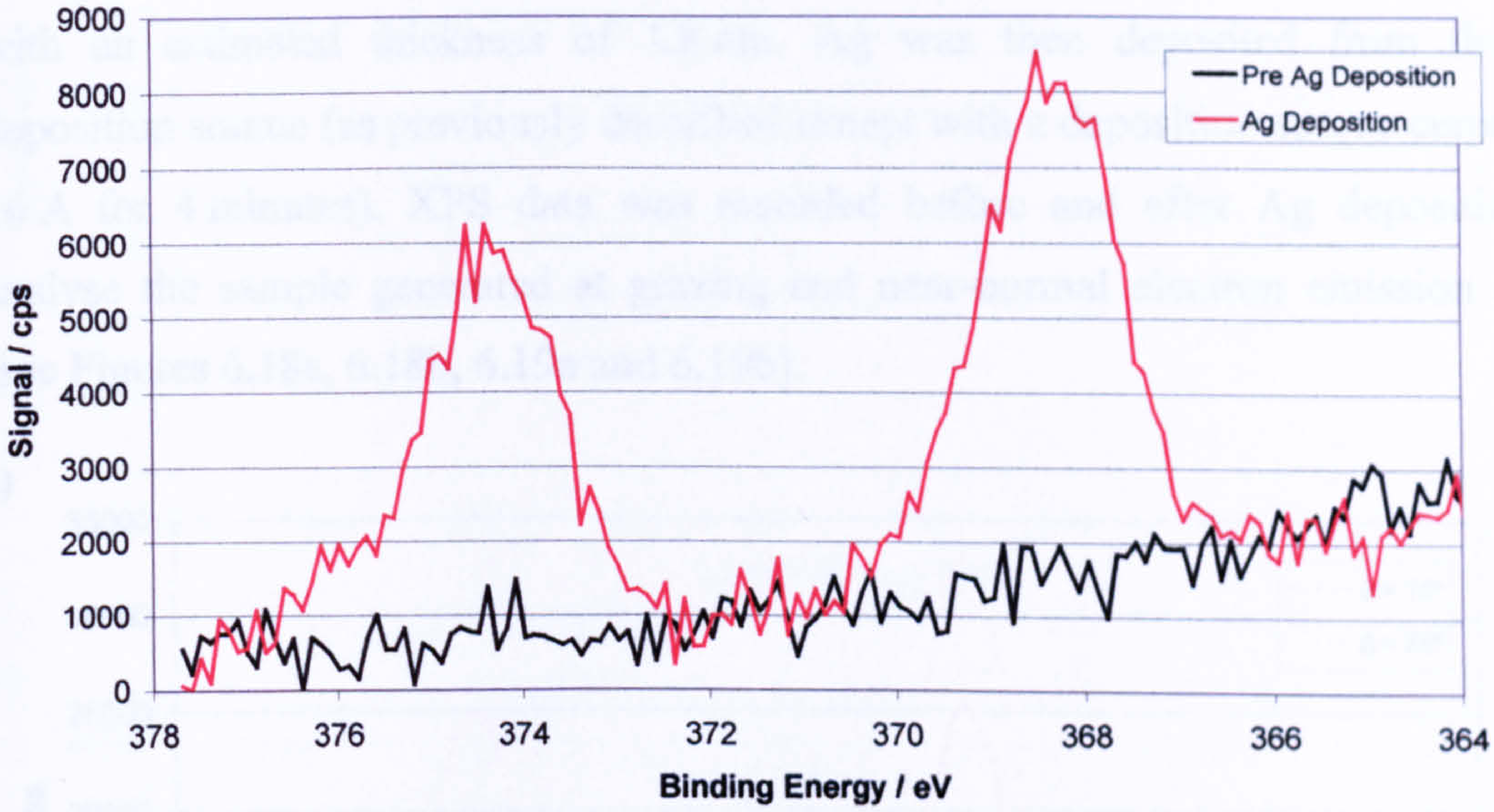

Figure 6.16: Ag 3d region for sample A

The Ag/FeO_x sample was then annealed for 2 minutes at various temperatures (473 K, 573 K, 673 K, 723 K and 773 K), each time recording XPS data to gauge the extent of breakdown (see Figure 6.17). At 673 K the Ag 3d doublet peak began to reduce in intensity and it was almost completely removed by heating to 773 K. There was no evidence of breakdown of the FeO_x support.

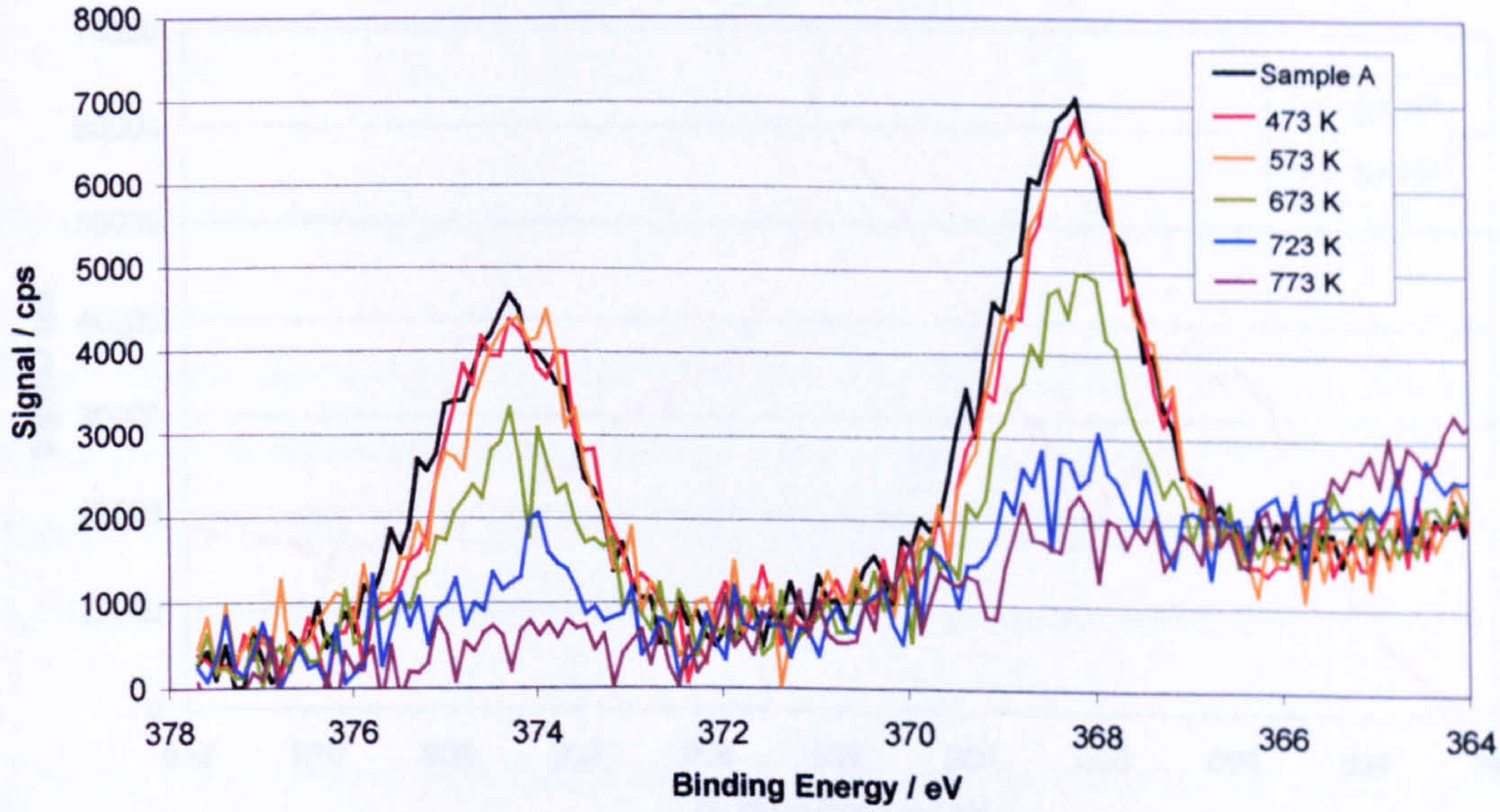

Figure 6.17: XPS data for vacuum annealing of sample A for 2 mins at each of the indicated temperatures (Ag 3d region)

Sample B (Ag $3d_{5/2}$ peak height = 25 kcps) was grown in the manner described previously. Firstly the FeO_x film was prepared using two cycles of Fe deposition (19.5 A for 100 s), oxidation at ambient temperature (5×10^{-8} Torr for 400 s) and oxidation at 673 K (5×10^{-8} Torr for 400 s). This led to a well-defined oxide film with an estimated thickness of 1.8 nm. Ag was then deposited from the Ag deposition source (as previously described except with a deposition source current of 16 A for 4 minutes). XPS data was recorded before and after Ag deposition to analyse the sample generated at grazing and near-normal electron emission angle (see Figures 6.18a, 6.18b, 6.19a and 6.19b).

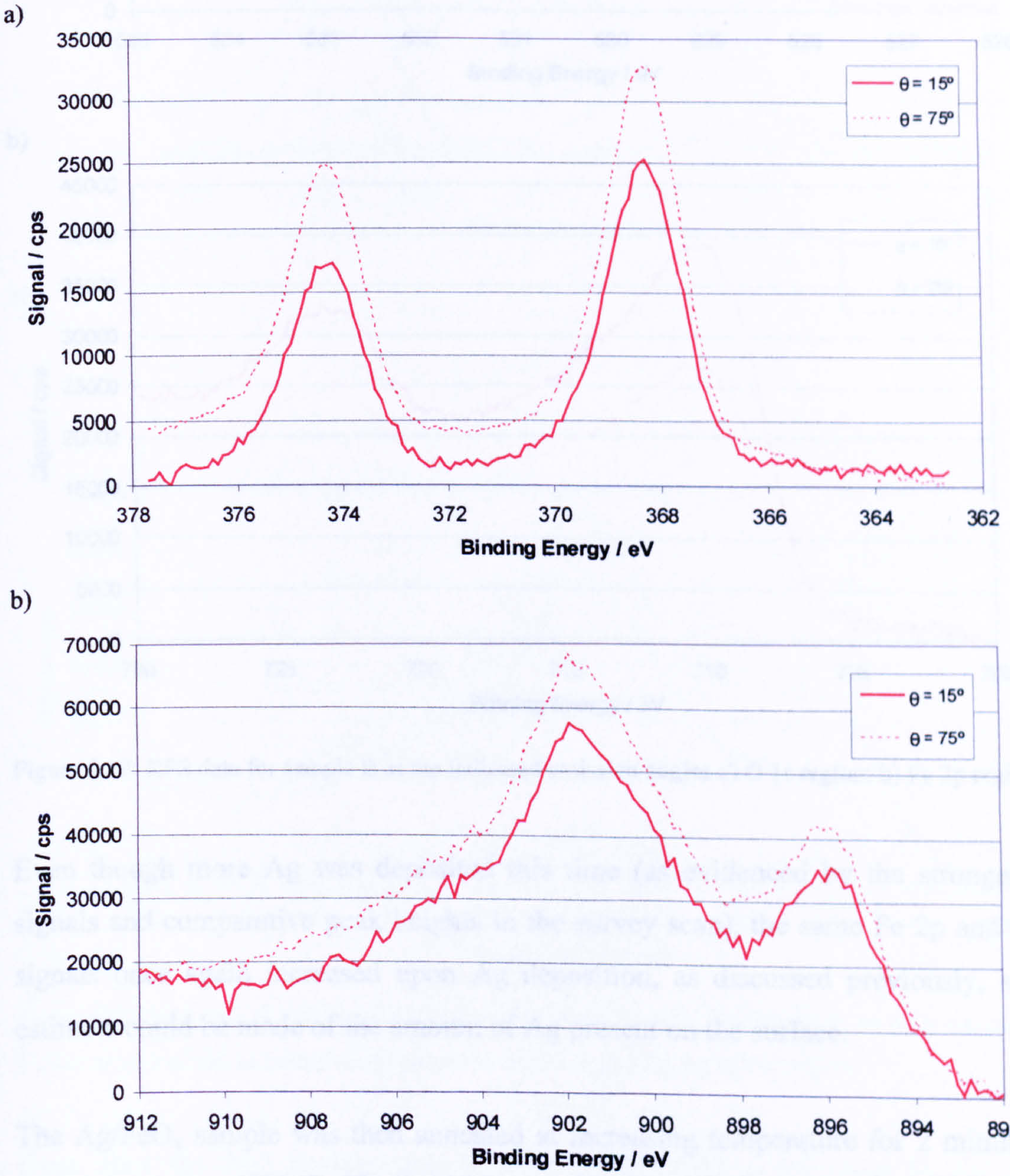

Figure 6.18: XPS data for sample B at the indicated emission angles a) Ag 3d region; b) Ag MVV (Auger) region

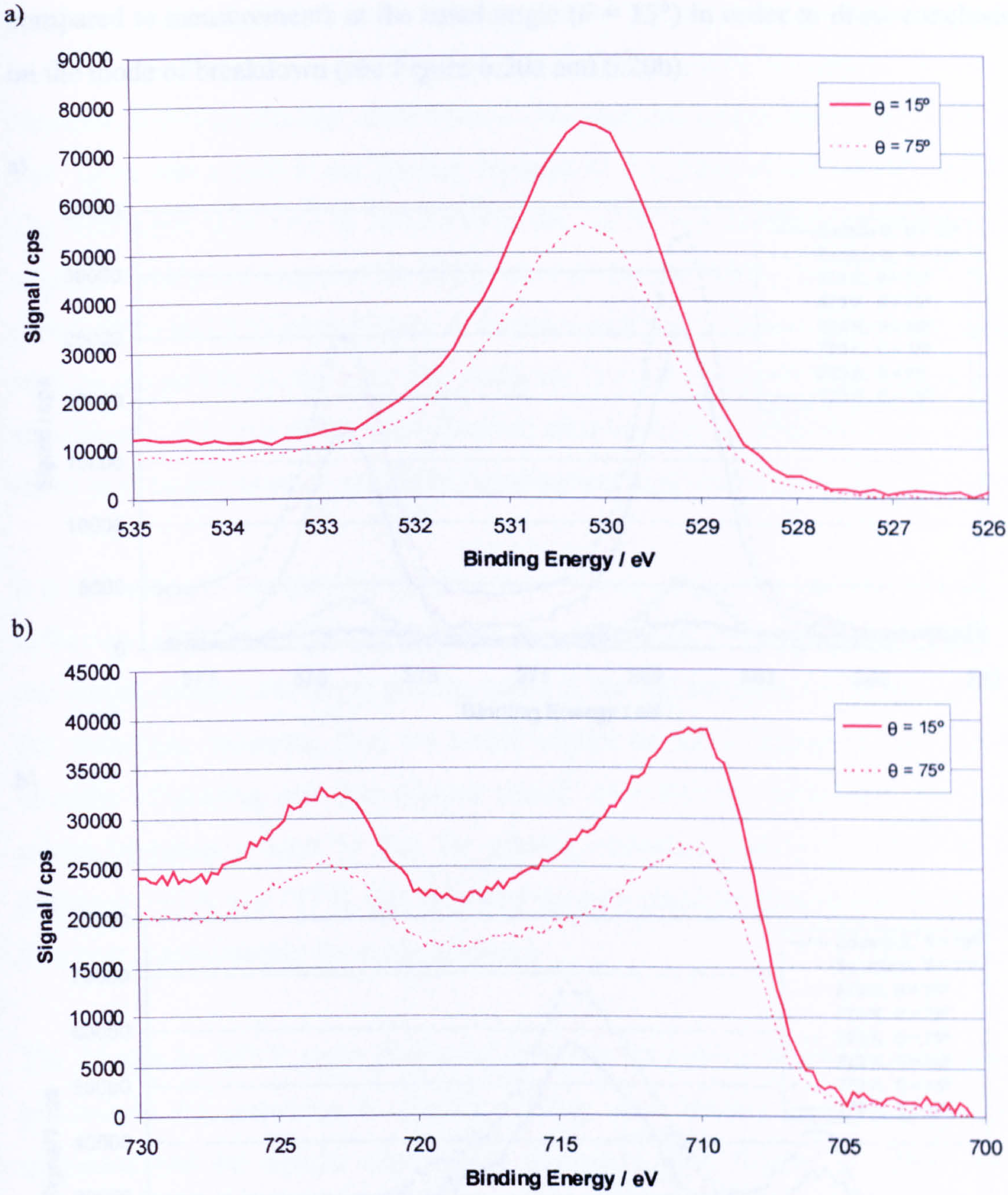

Figure 6.19: XPS data for sample B at the indicated emission angles a) O 1s region; b) Fe 2p region

Even though more Ag was deposited this time (as evidenced by the stronger Ag signals and comparative peak heights in the survey scan), the same Fe 2p and O 1s signals once again increased upon Ag deposition, as discussed previously, so no estimate could be made of the amount of Ag present on the surface.

The Ag/FeO_x sample was then annealed at increasing temperature for 2 minutes at each temperature (573 K, 673 K, 723 K and 773 K) each time recording XPS data to gauge the extent of breakdown. Grazing angle measurements (θ = 75°) were compared to measurements at the usual angle (θ = 15°) in order to draw conclusions on the mode of breakdown (see Figure 6.20a and 6.20b).

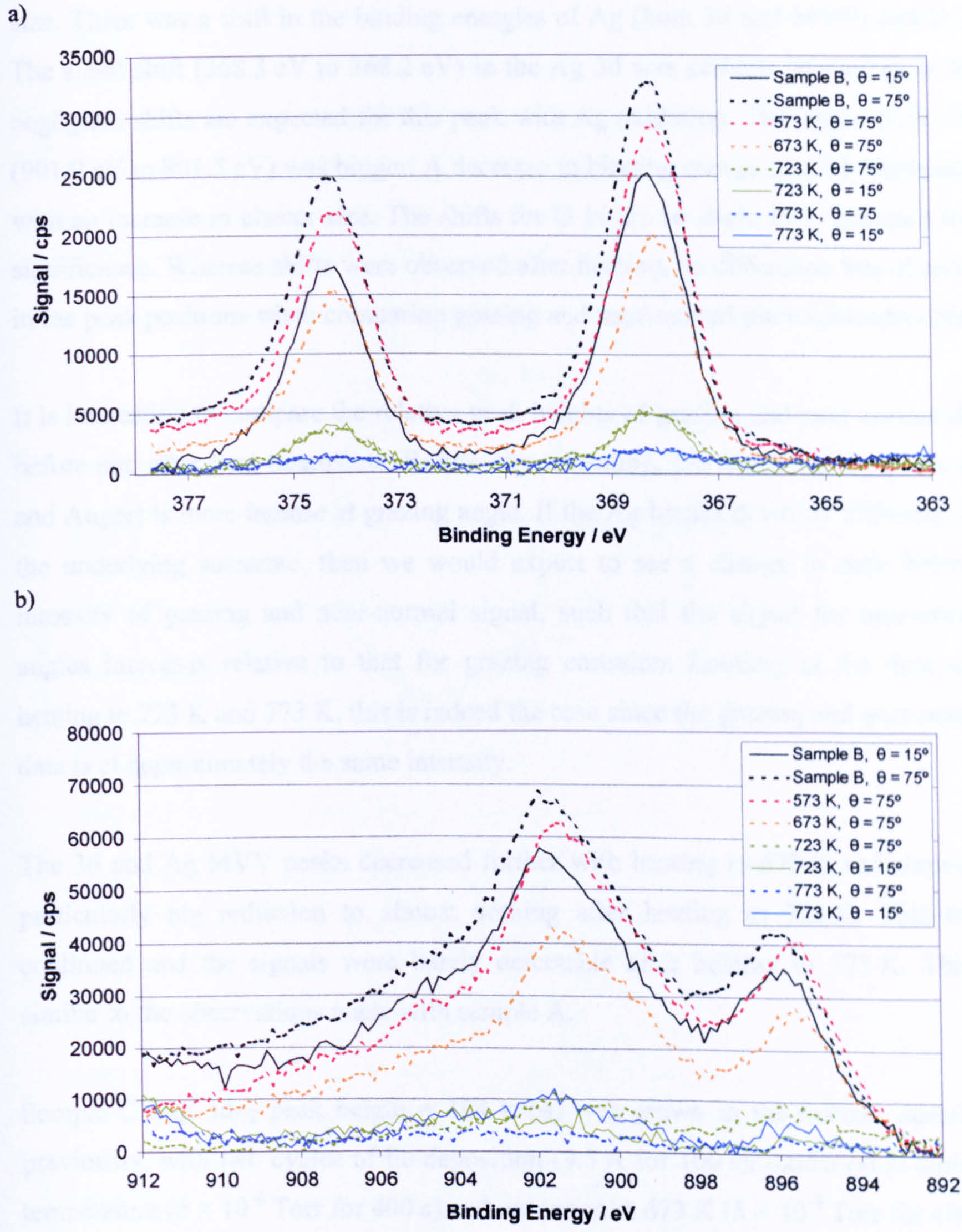

Figure 6.20: XPS data at grazing and near-normal emission angles for sample B, vacuum annealed for 2 mins at each of the indicated temperatures a) Ag 3d region; b) Ag MVV region

Even after the first heating step at 573 K, there was a reduction in Ag signal intensity. Strangely the signal for Fe 2p and O 1s also decreased after the first annealing step. It would be easy to dismiss this simply as experimental error – as was discussed in the case of changes before and after Ag deposition – however, as this occurred with annealing there may be an underlying reason for this to do with the structure of the metal/metal oxide system – for example an increase in the Ag cluster size. There was a shift in the binding energies of Ag (both 3d and MVV) and O 1s. The small shift (368.3 eV to 368.2 eV) in the Ag 3d was perhaps interesting in that negligible shifts are expected for this peak with Ag oxidation. The Auger peak shift (901.9 eV to 901.5 eV) was bigger. A decrease in binding energy could be associated with an increase in cluster size. The shifts for O 1s are so slight as to question their significance. Whereas shifts were observed after heating, no difference was observed in the peak positions when comparing grazing and near-normal photoemission data.

It is interesting to compare the relative peak heights of grazing and near-normal data before and after heat treatments. Before any annealing, the signal for Ag peaks (3d and Auger) is more intense at grazing angle. If the Ag breaks down by diffusing into the underlying substrate, then we would expect to see a change in ratio between intensity of grazing and near-normal signal, such that the signal for near-normal angles increases relative to that for grazing emission. Looking at the data after heating to 723 K and 773 K, this is indeed the case since the grazing and near-normal data is at approximately the same intensity.

The 3d and Ag MVV peaks decreased further with heating to 673 K and showed a particularly big reduction to almost nothing after heating to 723 K. This trend continued and the signals were barely detectable after heating to 773 K. This is similar to the observations made with sample A.

Sample C (Ag $3d_{5/2}$ peak height = 104 kcps) was grown in the manner described previously, with two cycles of Fe deposition (9.5 A for 100 s), oxidation at ambient temperature (5×10^{-8} Torr for 400 s) and oxidation at 673 K (5×10^{-8} Torr for 400 s). This led to a well-defined FeO_x film with an estimated thickness of 1.8 nm. Ag was then deposited from the Ag deposition source to give a much higher Ag loading (as previously described, except with 3 cycles with a deposition source current of 16 A for 4 minutes). XPS data was recorded before and after Ag deposition to analyse the sample generated (see Figures 6.21a, 6.21b and 6.21c).

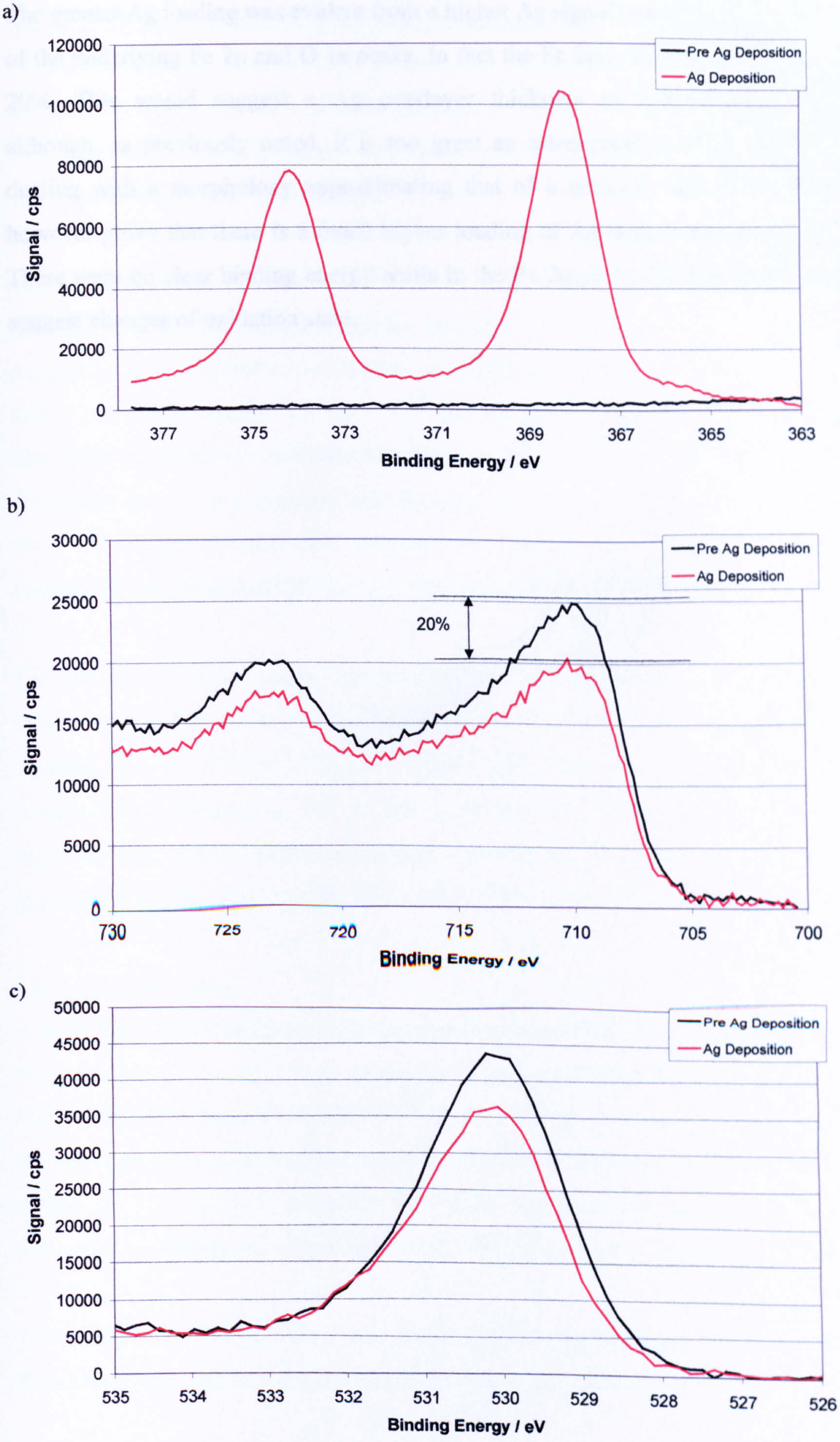

Figure 6.21: XPS data for film C a) Ag 3d region; b) Fe 2p region; c) O 1s region

The greater Ag loading was evident from a higher Ag signal intensity and attenuation of the underlying Fe 2p and O 1s peaks. In fact the Fe $2p_{3/2}$ peak was attenuated by 20%. This would suggest a Ag overlayer thickness of approximately 0.2 nm although, as previously noted, it is too great an assumption to make that we are dealing with a morphology approximating that of a uniform film. The data does however prove that there is a much higher loading of Ag than in samples A and B. There were no clear binding energy shifts in the Fe 2p or Ag 3d regions that would suggest changes of oxidation state.

6.6 Interaction of Ag/FeO_x with CO, N_2O and C_3H_6

FTRAIRS was used as the primary instrumental technique to provide information on the interaction of small molecules on the Ag/FeO_x samples generated. New samples were generated to provide a clean surface for these experiments, using the procedure described in section 6.2 (unless stated otherwise).

6.6.1 CO Adsorption

An FeO_x film was grown in the manner described previously, with two cycles of Fe deposition (100 s at 9.5 A), oxidation at ambient temperature (5×10^{-8} Torr for 400 s) and oxidation at 673 K (5×10^{-8} Torr for 400 s). This led to a well-defined film with an estimated thickness of 2.2 nm. Ag was then deposited from the Ag deposition source (as previously described except with a deposition source current of 16 A for 4 minutes). XPS data was recorded before and after Ag deposition to analyse the sample generated. The Ag $3d_{5/2}$ peak intensity was 11 kcps.

The sample was then cooled down to around 123 K and then flashed to room temperature and re-cooled. After running a background IR scan the sample was exposed to 5×10^{-8} Torr CO for 1 minute and then a sample scan run, whilst continuously exposing to CO at the same pressure (a further 3 minutes). No significant signal from surface adsorbates was seen, so this was repeated with a static pressure of 5×10^{-7} Torr CO, but still no signal due to CO adsorption was observed.

6.6.2 N_2O Adsorption

A fresh FeO_x film was grown in the manner described previously, with two cycles of Fe deposition (9.5 A for 100 s), oxidation at ambient temperature (5×10^{-8} Torr for 400 s) and oxidation at 673 K (5×10^{-8} Torr for 400 s). Ag was then deposited from the Ag deposition source (as previously described except with a deposition source current of 18.5 A for 5 minutes). XPS data was recorded before and after Ag deposition to analyse the sample generated. The Ag $3d_{5/2}$ peak intensity was 37 kcps.

The sample was then cooled to around 123 K. A background scan was run, and then N_2O dosed at a constant pressure of $\sim 5 \times 10^{-8}$ Torr and then $\sim 5 \times 10^{-7}$ Torr. No peaks were reproducibly observed which could be clearly attributed to adsorbed N_2O.

6.6.3 C_3H_6 Adsorption

A new FeO_x film was grown in the manner described previously, with two cycles of Fe deposition (9.5 A for 100 s), oxidation at ambient temperature (5×10^{-8} Torr for 400 s) and oxidation at 673 K (5×10^{-8} Torr for 400 s). Ag was then deposited from the Ag deposition source. This was done in 4 minute increments each time measuring XPS until the Fe 2p signal had been attenuated to 20-25%, which required three of these cycles. The Ag $3d_{5/2}$ peak intensity was 114 kcps and therefore this sample therefore had a much higher Ag loading than previous samples used in the adsorption experiments.

The sample was then cooled to around 123 K. A background was run and C_3H_6 then dosed onto the sample and sample spectra run (see Figure 6.22): A fixed exposure of 5 L at 5×10^{-8} Torr (dose 1), a constant pressure of 5×10^{-8} Torr (dose 2), a sample spectrum run with base pressure of $< 5 \times 10^{-9}$ Torr to see if anything desorbed (no dose), a fixed exposure of 5 L at 5×10^{-7} Torr (dose 3) and a constant pressure of 5×10^{-7} Torr (dose 4)

It is worth noting that after dosing at the higher pressure (5×10^{-7} Torr), the IR chamber pressure took a long time to reach optimum base pressure, such that the fixed exposure of 5 L at 5×10^{-7} Torr spectrum was effectively recorded with the sample exposed to a constant pressure of $\sim 5 \times 10^{-8}$ Torr of C_3H_6.

Peaks were observed at frequencies that related to previous research[60] 919 cm^{-1}, 908 cm^{-1}, 986 cm^{-1}. An absorption peak was also evident at 898 cm^{-1} (see Figure 6.22) which has not been reported in the aforementioned study on Ag(111). This may relate to Ag(110) or Ag(100), but no previous RAIRS studies on these surfaces could be found in the literature. The peak at 908 cm^{-1} was assigned to a state (so-called α_3) which desorbed at a temperature of 123 K which is not quite that achieved here. This may however reflect the higher exposure pressures used here compared to that study. The relative intensities of these signals change with different exposures.

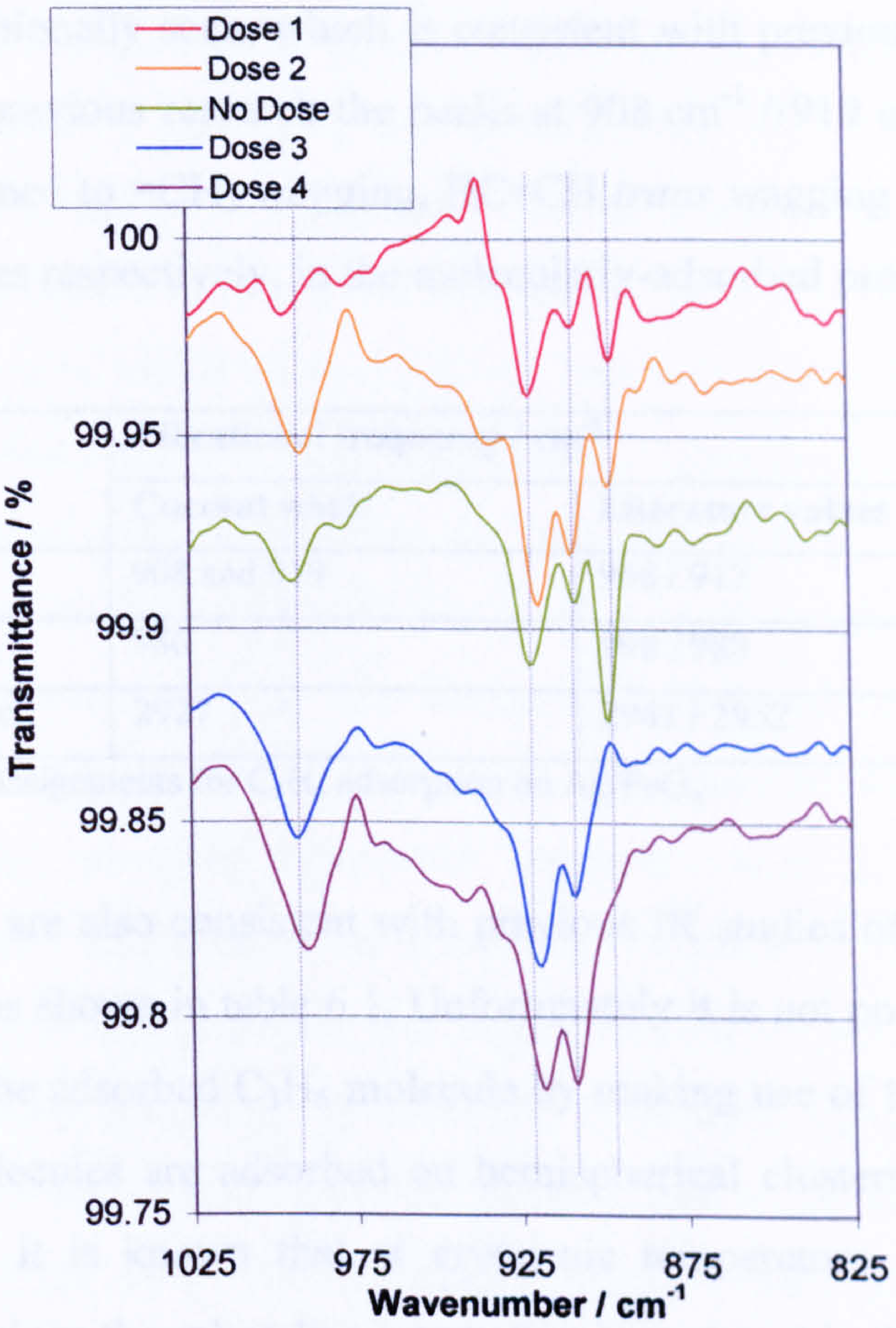

Figure 6.22: RAIRS spectra for adsorption of C_3H_6 on Ag/FeO_x (see accompanying text for explanation of gas exposures)

The same sample was flashed to 623 K and then re-cooled to bellow 143 K. The purpose was to remove any adsorbates and to change the morphology of the supported silver (the chosen temperature was based upon observations made during previous thermal stability experiments on Ag/FeO_x samples). Once cooled, a background spectrum was collected and C_3H_6 dosed onto the sample and following sample spectra run: after a fixed exposure of 5 L at 5×10^{-8} Torr, whilst exposing to a constant pressure of 5×10^{-8} Torr, after a fixed exposure of 5 L at 5×10^{-7} and whilst exposing to a constant pressure of 5×10^{-7} Torr.

Once again at higher pressures, it took a long time for the IR cell to return to its normal base pressure. The most significant observation is that although the peaks at 908 cm^{-1} and 919 cm^{-1} were again present, the peak at 898 cm^{-1} was not. This is interesting in terms of the previous discussion about the origin of this peak, which had not been observed on Ag(111) in a previous study. In these spectra a peak at 2927 cm^{-1} was additionally seen, which is consistent with previous observations on Ag(111).[60] In this previous research the peaks at 908 cm^{-1} / 919 cm^{-1}, 986 cm^{-1} and 2927 cm^{-1} are assigned to $=CH_2$ wagging, HC=CH *trans* wagging and asymmetrical methyl stretch modes respectively, in the molecularly-adsorbed propene.

Assignment	**Vibrational frequency / cm^{-1}**	
	Current work	**Literature values (solid[61] / gas[62])**
$=CH_2$ wagging	908 and 919	908 / 912
HC=CH *trans* wagging	986	998 / 980
CH_3 asymmetrical stretch	2927	2941 / 2952

Table 6.1: Vibrational assignments for C_3H_6 adsorption on Ag/FeO_x

These assignments are also consistent with previous IR studies of solid C_3H_6 [61] and gas phase C_3H_6,[62] as shown in table 6.1. Unfortunately it is not possible to determine the orientation of the adsorbed C_3H_6 molecule by making use of the dipole selection rule, since the molecules are adsorbed on hemispherical clusters rather than a flat surface. However, it is known that at cryogenic temperature alkenes chemisorb weakly, lying flat, since the π-bonding interaction is strongest in this geometry.[63]

In summary, there is reasonable confidence in the reproducibility of the peaks seen in the IR data associated with C_3H_6 adsorption. The exact patterns (*e.g.* interchange between peaks, relative peak intensities under different conditions/at different stages of adsorption are less sure and open to speculation. The problem is that the signals observed (about 0.05%) are very weak (as is a common problem in RAIRS). Added to this, there are some electrical oscillations in the base line which do not help.

6.7 Summary

FeO_x films on Cu(111) have been grown in UHV by deposition of Fe metal and oxidation. The growth of the films was characterised by XPS and LEED. The oxidation was carried out in two steps, the first at ambient temperature to avoid diffusion of Fe into the Cu substrate and the second at 673 K. XPS data evidenced oxidation of the Fe metal under these conditions and with successive cycles an oxide film of 2 nm estimated thickness could be generated. The absence of the XP satellite at 719.2 eV associated with Fe_2O_3, rules out fully oxidised Fe^{3+}. The XPS data is believed to be most consistent with FeO or Fe_3O_4. Angle-resolved XPS revealed a difference in O concentration at the surface which could be evidence of O-termination. Furthermore a clear LEED pattern was obtained without the need for post-treatment. The observed hexagonal structure, with a cell constant of 3.2 (±0.1) Å, is most consistent with an FeO(111) surface. The bulk value for FeO(111) is 3.1 Å and this value has also been observed for FeO(111) films grown on a Pt substrate. Upon annealing (up to 923 K) in vacuum, a gradual breakdown of the oxide film was observed. By reducing the exposure to O_2 in the preparation, it was possible to produce an oxygen–deficient film with a significantly reduced O:Fe ratio. This FeO_{x-y} film also exhibited a well-defined LEED pattern. It is believed that this film consists of portions of unoxidised metal rather than a uniformly O-deficient film. There was no FT-RAIRS evidence of HCO_2H adsorption on FeO_x and no FT-RAIRS or XPS evidence of CH_3OH adsorption either. Likewise there were no conclusive signs of CO adsorption on the FeO_x film or a pre-sputtered FeO_x film at – 423 K. A peak was observed in the FT-RAIRS spectrum following CO-adsorption on the oxygen-deficient FeO_{x-y} film at 153 K, but is thought to be associated with adsorption on the Cu substrate.

Ag clusters supported on FeO_x were grown by Ag deposition onto FeO_x films grown in the manner adopted in the previous section. Three systems of varying Ag loading were produced and analysed with XPS. The samples were stable up to 673 K in vacuum, but after annealing at 773 K the Ag signal had almost completely disappeared. Angle-resolved XPS data supports the theory that the Ag diffuses into the FeO_x at these temperatures. No FT-RAIRS evidence was found for CO or N_2O adsorption on this system at sub-ambient temperature. There was more success with

C_3H_6 adsorption at sub-ambient temperatures. Peaks were observed in the FT-RAIRS spectra which must relate to interaction with Ag, as they were not observed on FeO_x in a control experiment. Furthermore the frequencies are similar to those obtained in the literature for C_3H_6 adsorption on Ag(111), but there was an additional peak at a frequency not reported in current literature, which could be associated with adsorption on Ag(110), Ag(100) surfaces or special adsorption sites (such as corners or edges) which may also be present on the Ag clusters.

References

1 W. Weiss and W. Ranke, *Prog. Surf. Sci.* 2002, **70**, 1

2 Q. Guo, P.H. McBreen and P.J. Møller, *Surf. Sci.* 1999, **423**, 19

3 K. Adib, N. Camillone III, J.P. Fitts, K.T. Rim, G.W. Flynn, S.A. Joyce and R.M. Osgood Jr. *Surf. Sci.* 2002, **497**, 127

4 K. Adib, D.R. Mullins, G. Totir, N. Camillone III, J.P. Fitts, K.T. Rim, G.W. Flynn and R.M. Osgood Jr. *Surf. Sci.* 2003, **524**, 113

5 R.J.A.M. Terörde, P.J. van den Brink, L.M. Visser, A.J. van Dillen, and J.W. Geus, *Catal. Today*, 1993, **17**, 217

6 K. Kureti Shizbullah and W. Weisweiler, *Chem. Eng. Technol.* 2003, **26**, 1003

7 H.A. Al-Abadleh and V.H. Grassian, *Surf. Sci. Rep.* 2003, **52**, 63

8 G. Ramis, L. Yi, G. Busca, M. Turco, E. Kotur and R.J. Willey, *J. Catal.* 1995, **157**, 523

9 A.S. Goudie and N.J. Middleton, *Earth-Sci. Rev.* 2001, **56**, 179

10 P. Liu, T. Kendelewicz, G.E. Brown Jr. E.J. Nelson and S.A. Chambers, *Surf. Sci.* 1998, **417**, 53

11 R.K. Wild, D.R. Randall (Ed.) and W. Neagle (Ed.), *Surface Science Analysis and Applications*, Special Publication, Royal Society of Chemistry, London, 1990, p.73

12 J.C. Mallinson, *The Foundations of Magnetic Recording*, 2nd Ed, Academic Press, New York

13 B. Stanka, W. Hebenstreit, U. Diebold and S.A. Chambers, *Surf. Sci.* 2000, **448**, 49

14 S.F. Ceballos, G. Mariotto, K. Jordan, S. Murphy, C. Seoighe and I.V. Shvets, *Surf. Sci.* 2004, **548**, 106

15 H. Dendaas, O.L.J. Gijzeman and J.W. Geus, *Surf. Sci.* 1993, **285**, 15

16 L. Lozzi, M. Passacantando, P. Picozzi, S. Santuccis and H. Dendaas, *Surf. Sci.* 1995, **333**, 703

17 A.N. Koveshnikov, R.H. Madjoe, J. Karunamuni, R.L. Stockbauer and R.L. Kurtz, *J. Appl. Phys.* 2000, **87**, 5929

18 R.L Kurtz, J. Karunamuni, and R.L. Stockbauer, *Phys. Rev. B.* 1999, **60**, R16342

19 L. Scipioni and B. Sinkovic, *J. Appl. Phys.* 1996, 79, 4976

20 J. Karunamuni, R.L. Kurtz, R.L. Stockbauer, *Surf. Sci.* 1999, 442, 223

21 C. Pflitsch, R. David, L.K. Verheij and R. Franchy, *Surf. Sci.* 2001, 488, 32

22 C. Pflitsch, R. David, L.K. Verheij and R. Franchy, Appl. Phys. 2001, 90, 1215

23 E. Yagasaki and K. Kishi, *J. Electron. Spec. Rel. Phenomena*, 1994, 69, 133

24 C. Ruby, J. Fusy, Appl. *Surf. Sci.* 1996, 99, 393

25 L.W. Finger and R.M. Hazen, *J. Appl. Phys.* 1980, 51, 5362

26 V.A. Sadykov, L.A. Isupova, S.V. Tsybulya, S.V. Cherepanova, G.S. Litvak, E.B. Burgina, G.N. Kustova, V.N. Kolomiichuk, V.P. Ivanov, E.A. Paukshtis, A.V. Golovin and E.G. Avvakumov, *J. Solid State Chem.* 1996, 123, 191

27 F. de Boer, J.H. van Santen and E.J.W. Verwey, *J. Chem. Phys.* 1950, 18, 1032

28 http://ruby.colorado.edu

29 N.G., Condon, F.M. Leibsle, A.R. Lennie, P.W. Murray, D.J. Vaughan and G. Thornton, *Phys. Rev. Lett.* 1995, 75, 1961

30 N.G. Condon, F.M. Leibsle, A.R. Lennie, P.W. Murray, T.M. Parker, D.J. Vaughan and G. Thornton, *Surf. Sci.* 1998, 397, 278

31 Sh.K. Shaikhutdinov and W. Weiss, *Surf. Sci.* 1999, 432, L627

32 X-G. Wang, W. Weiss, Sh.K. Shaikhutnidov, M. Ritter, M. Petersen, F. Wagner, R. Schlögl and M. Scheffler, *Phys. Rev. Lett.* 1998, 81, 1038

33 M.A. Henderson, S.A. Joyce and J.R. Rustad, *Surf. Sci.* 1998, 417, 66

34 M. Gautier-Soyer, M. Pollak, M. Henriot and M.J. Guillet, *Surf. Sci.* 1996, 352, 112

35 S.A. Chambers and S.A. Joyce, *Surf. Sci.* 1999, 420, 111

36 J.R. Rustad, E. Wasserman and A.R. Felmy, *Surf. Sci.* 1999, 432, L583

37 J. Ahdjoudj, C. Martinsky, C. Minot, M.A. Van Hove and G.A. Somorjai, *Surf. Sci.* 1999, 443, 133

38 M. Ritter and W. Weiss, *Surf. Sci.* 1999, 432, 81

39 R. Jansen, V.A.M. Brabers and H. Van Kempen, *Surf. Sci.* 1995, 328, 237

40 Y.F.Y. Yao, *J. Phys. Chem.* 1965, 69, 3930

41 M. Hendewerk, M. Salmeron and G.A. Somorjai, *Surf. Sci.* 1986, 172, 544

42 R.L. Kurtz and V.E. Henrich, *Phys. Rev. B.* 1987, 36, 3413

43 E. Wasserman, J.R. Rustad, A.R. Felmy, B.P. Hay and J.W. Halley, *Surf. Sci.* 1997, **385**, 217

44 K.T. Rim, J.P. Fitts, T. Muller, K. Adib, N. Camillone, R.M. Osgood, S.A. Joyce and G.W. Flynn, *Surf. Sci*, 2003, **541**, 59

45 K. Adib, D.R. Mullins, G. Totir, N. Camillone, J.P. Fitts, K.T. Rim, G.W. Flynn and R.M. Osgood, *Surf. Sci.* 2003, **524**, 113

46 G.E. Mullenberg, *Handbook of X-ray Photoelectron Spectroscopy*, Perkin-Elmer, 1979

47 Th. Schedel–Niedrig, W. Weiss, and R. Schlögl, *Phys. Rev. B.* 1995, **52**, 17449

48 A. Glisenti, *J. Chem. Soc. Faraday Trans.* 1998, **94**, 3671

49 F. Bonet, S. Grugeon, R. Herra Urbina, K. Takaia-Elhsissen and J.M. Tarascon, *Solid State Sciences*, 2002, **4**, 665

50 X. Lai and D.W. Goodman, *J. Mol. Catal. A*, 2000, **162**, 33

51 S. Link, Z.L. Wang and M.A. El-Sayed, *J. Phys. Chem.* 1996, **103**, 363

52 A. Venugopal, J. Aluha and M.S. Scurrell, *Catal. Lett.* 2003, **90**, 1

53 A.R. Canário, E.A. Sanchez, Y. Bandurin and V.A. Esaulov, *Surf. Sci.* 2003, **547**, L887

54 U. Kimer, *Sens. Actuators B*, 1990, **1**, 103

55 D. Martin, J. Jupille and Y. Borensztein, *Surf. Sci*, 1998, **402**, 433

56 U. Diebold, *Surf. Sci. Rep.* 2003, **48**, 53

57 D.A. Chen, M.C. Bartelt, S.M. Seutter and K.F. McCarty, *Surf. Sci.* 2000, **464**, L708

58 A.K. Santra, F. Yang, D.W. Goodman, *Surf. Sci.* 2004, **548**, 324

59 A. Watanabe and H. Kozuka, *J. Phys. Chem. B*, 2003, **107**, 12713

60 W.X. Huang and J.M. White, *Surf. Sci.* 2002, **513**, 399

61 A.J. Barnes and J.D.R. Howells, *J. Chem. Soc. Faraday Trans.* 1973. 69. [illegible]

62 B.Silvi, P.Labarbe and J.P.Perchard, *Spectrochem. Acta A*. 1973. 29. 263

63 K.W. Kolasinski, *Surface Science Foundations of Catalysis and Nanoscience* [illegible]

Chapter 7:

Conclusions & Future Work

Chromium oxide, barium oxide, titanium oxide, iron oxide and silver dispersed on iron oxide were identified as technologically interesting systems with much scope for surface science study. Thin films of the oxides were grown on a Cu(111) substrate and characterised by XPS and LEED. After extensive investigation of the parameters required for optimised growth, well-defined films of CrO_x, TiO_x and FeO_x were obtained.

Well-defined CrO_x films (up to about 2 nm estimated thickness) were obtained by deposition of Cr metal followed by oxidation at 873 K. Alternatively annealing of a disordered film to 923 K in vacuum also led to a well-defined oxide. The LEED data was consistent with the $Cr_2O_3(0001)$ surface and XPS data suggested that the oxide is O-terminated. TiO_x films were obtained by deposition of Ti metal and oxidation at ambient temperature followed by further oxidation at 773 K-823 K. Films with an estimated thickness of < 0.5 nm were well-ordered, but above this thickness annealing only improved the LEED pattern to a limited extent. Well-defined FeO_x films (up to about 2 nm estimated thickness) were obtained by deposition of Fe metal followed by oxidation at ambient temperature and then additional oxidation at 673 K. Clear LEED patterns were observed without the need for further treatment. The XPS data was consistent with Fe_3O_4 or FeO stoichiometry. BaO_x films were grown by direct deposition of BaO onto the substrate. Despite a detailed investigation into the effect of different growth conditions and post-deposition treatments, only a very faint LEED pattern was obtained. The XPS data suggested the films possessed a complicated oxygen chemistry. In addition to the study of the pure oxide, model Ag/FeO_x catalysts were prepared by the growth of silver metal clusters on well-defined iron oxide films. These clusters were shown to be stable up to 673 K.

Having generated well-defined oxide films, the interaction of selected molecules with these surfaces was probed by RAIRS, TPD and XPS. There was no conclusive evidence of adsorption of H_2O, CH_3OH or CO_2 on the CrO_x surface, which is consistent with the proposition that the films obtained were O-terminated. There was also no conclusive evidence of HCO_2H, CH_3OH or CO adsorption on the FeO_x surface. Although the BaO_x films were not well-defined adsorption of CO_2 and CO was tested. There was clear evidence in XPS spectra of CO_2 adsorption, which is believed to form surface carbonate. Additionally there was some XPS evidence of an interaction with CO, which either adsorbs on or reduces the surface. The interaction of CO, N_2O and C_3H_6 with the dispersed silver metal on iron oxide system was probed by RAIRS at sub-ambient temperature. There was no conclusive evidence of CO adsorption. Some peaks in the RAIRS spectra may be evidence of N_2O adsorption. Most interestingly there was evidence of C_3H_6 adsorption and an additional peak not observed in published literature on the interaction of C_3H_6 with Ag(111). This peak may be due to C_3H_6 adsorption on other surfaces of the Ag clusters, or on corner/edge atoms.

There are many avenues for potentially interesting future work based on the studies described in this thesis:

1) Activation of the CrO_x surface. Some attempts were made to activate the CrO_x surface (which was believed to be O-terminated). A further idea would be to chemically reduce the surface under a pressure of CO at elevated temperature. If it is possible to active the CrO_x surface (without loss of order), then it would be possible to pursue the interaction of molecules with this surface.

2) Optimisation of the growth method for TiO_x to generate well-defined TiO_x films of greater thickness. The interaction of molecules with these well-defined TiO_x films could then be studied, including by RAIRS which cannot be readily applied to TiO_2 single crystal surfaces.

3) Further work is required to obtain well-defined BaO films. This may be possible by optimisation of the post depostion parameters or (more radically) by re-fabrication of the depostion source. It is possible that deposition of Ba metal followed by oxidation would be more effective at generating well-defined films. The interaction of molecules, such as NO_x, SO_2 and CO_2, with well-defined BaO films could then be studied.

4) Better characterisation of the silver clusters on iron oxide. In the absence of direct imaging techniques, it might be possible to gather some information by careful measurement of the intensity of the Fe 2p photoelectron peak (from the underlying FeO_x) at increasing amounts of silver deposition. There may be a

breakpoint that relates to a change in growth mode and Ag morphology. However, the application of STM would be the preferred approach.

5) The Ag/FeO$_x$ system is of particular interest since it models a real heterogeneous catalyst – this is an area that surface science has only recently turned attention towards. The experiments with C_3H_6 adsorption were promising but further work is needed here, both to characterise the interaction of the molecule with specific surface sites and to study its reactivity with other adsorbed species (*e.g.* surface oxygen).

There are many other metal on oxide systems that could be investigated. For example a UHV investigation of Pt/BaO would be of interest to the NO$_x$ storage/reduction technology. Such studies of systems which more closely align with those used in real industrial applications are the future of UHV surface science investigations in the catalytic field.